Investigation of subunits of the cytoplasmic dynein complex using novel mouse models

Thesis presented in partial fulfilment of the requirements for the degree of Doctor of Philosophy to the University College London

By

Anna Kuta

Department of Neurodegenerative Disease
Institute of Neurology
University College London

Mojej Rodzinie,

Z podziekowaniami za wsparcie
I wiare w moje mozliwosci

Declaration

I hereby declare that this thesis is my work and effort, and that it has not been submitted anywhere for any award. Wherever contributions of others are involved, every effort is made to indicate this clearly, with due reference to the literature, and acknowledgement of collaborative research and discussions.

Abstract

Cytoplasmic dynein is a multisubunit complex responsible for the transport of cellular components from the cell periphery towards the nucleus. The role of the dynein complex in vesicle trafficking, organelle positioning and chromosome segregation during mitosis has been extensively studied but still little is known of specific roles of distinct subunits of the complex. Cytoplasmic dynein is a dimeric complex consisting of heavy chains, intermediate chains, light intermediate chains and three light chains. In order to investigate the roles of the cytoplasmic dynein subunits, two mouse lines with chemically generated single point mutations in the intermediate chain 1 and 2 genes *(Dync1i1, Dync1i2)* were subjected to a behavioural analysis. The mouse line carrying a mutation in the intermediate chain 2 showed working memory deficits which suggested impairment in hippocampal functions.

In order to examine the effects of mutation at the cellular level primary mouse embryonic fibroblasts (MEFs) lines were derived from embryos carrying mutations in the intermediate chains and used as a model system. Cell functions, such as trafficking of epidermal growth factor (EGF) positive endosomes, Golgi assembly were examined. Furthermore, biochemical analyses were performed focused on the expression of dynein subunits and their assembly in the functional complex.

Alternative splicing is known to produce multiple isoforms of the intermediate chains. The analysis of various splice variants of these genes in a panel of mouse tissues resulted in detecting new isoforms which were compared with bioinformatics data available for human and rat thus establishing the splicing pattern of the mouse intermediate chains.

Legs at odd angles (*Dync1h1*^{Loa}) is another mutant mouse line carrying a point mutation in the dynein heavy chain which results in neurological defects. Here the effects of the *Loa* mutation in the trafficking of membranous organelles were investigated by an infection of cultured MEFs with *Salmonella enterica* serovar Typhimurium. Furthermore, upon the induction of a cellular stress the wildtype and the *Loa* homozygous cells showed significant differences in stress granule assembly suggesting the impairment in the stress signaling.

Table of contents

List of tables

List of figures

Abbreviations

5-FAM	5-Carboxyfluorescein
aa	Amino acid
AAA	ATPases associated with various cellular activities
Adar1	*Adenosine-deaminase RNA specific*
AKAP9 (AKAP450)	A-kinase anchor protein 9
ALS	Amyotropic lateral sclerosis
ANOVA	Analysis of variance
ARHGEF2 (LFC)	RHO/RAC guanine nucleotide exchange factor (GEF) 2
ARP1	Actin related protein 1
AS	Alternative splicing/splice site
ATP	Adenosine triphosphate
ATP2A3	ATPase Ca^{2+} pump 3
BCP	Bromo-chloro-propane
BICD	Bicaudal-D
BMP-2	Bone morphogenetic protein 2
BSA	Bovine serum albumin
BSN	Bassoon
BUB3	Budding uninhibited by benzimidazoles 3 homolog *(S. cerevisiae)*
CACNA1A/CACNA1B	P/Q-type/ N-type voltage-gated calcium channel
CALB1	Calbindin
CDC42	Cell division cycle 42 (GTP binding protein)
cDNA	Complementary DNA
CGE-LIF	Capillary gel electrophoresis with laser induced fluorescence
COL1A1	Collagen I
Cra1	*Cramping 1*
C_T	Threshold cycle
CV	Coefficient of variation
DAPI	4',6-diamidino-2-phenylindole
DCTN1	$P150^{Glued}$ subunit of dynactin
DEPC	Diethylpyrocarbonate
D-HPLC	Denaturing high pressure liquid chromatography
DIC (1/2), IC74	Antibodies against cytoplasmic dynein 1 intermediate chain 1 and 2
D-MEM	Dulbecco's Modified Eagle Medium
DMF	*N, N*-Dimethylformamide
DMSO	Dimethyl sulfoxide
DNA	Deoxyribonucleic acid
dNTP	Deoxyribonucleotide triphosphate
D-PBS	Dulbecco's phosphate buffer
DRG	Dorsal root ganglia
dSBMA	distal spinal and bulbar muscular atrophy
DTT	Dithiothreitol
Dync1h1	*Cytoplasmic dynein 1 heavy chain 1 gene*
DYNC1H1	Cytoplasmic dynein 1 heavy chain 1
Dync1i1, Dync1i2	*Cytoplasmic dynein 1 intermediate chain 1 and 2 genes*
DYNC1I1, DYNC1I2	Cytoplasmic dynein 1 intermediate chain 1 and 2
DYNC1LI1, DYNC1LI2	Cytoplasmic dynein 1 light intermediate chain 1 and 2
DYNC2	Cytoplasmic dynein complex 2
DYNC2H1	Cytoplasmic dynein 2 heavy chain 1
DYNLL 1/2	Cytoplasmic dynein 1 light chain LC8 family
DYNLRB 1/2	Cytoplasmic dynein 1 light chain Roadblock family
DYNLT 1/3	Cytoplasmic dynein 1 light chain Tctex-1 family
E 13.5	Embryonic day 13.5
EBSS	Earle's balanced salt solution

EDTA	Ethylenediaminetetraacetic acid
EGF	Epidermal growth factor
EGFR	Epidermal growth factor receptor
EIF2A	Eukaryotic translation initiation factor 2α
EIF2AK1 (HRI)	Eukaryotic translation initiation factor 2α kinase 1
EIF2AK2 (PKR)	Eukaryotic translation initiation factor 2α kinase 2
EIF2AK3 (PERK)	Eukaryotic translation initiation factor 2α kinase 3
ELAV1 (HuR)	ELAV (embryonic lethal, abnormal vision, Drosophila)-like 1
EMC	Extracellular matrix
EMPReSS	European Mouse Phenotyping Resource of Standardised Screens
ENU	*N*-ethyl-*N*-nitrosourea
ER	Endoplasmic reticulum
ERC	Endocytic recycling compartment
ERES	Endoplasmic reticulum exit site
ERGIC	ER-Golgi intermediate compartment
ES	Embryonic stem cells
ESRRB	Orphan nuclear steroid hormone receptor β
EST	Expressed sequence tag
EUCOMM	European Conditional Mouse Mutagenesis
EUMODIC	European Mouse Disease Clinic
EUMORPHIA	European Union Mouse Research for Public Health and Industrial Applications
F1, N1	Number of mouse generation intercrossed or backcrossed to inbred strain
FBS	Foetal bovine serum
fMRI	Functional magnetic resonanse imaging
G3BP	GTPase activating protein (SH3 domain) binding protein 1
GAPDH	Glyceraldehyde-3-phosphate dehydrogenase
GEF	Guanine nucleotide exchange factor
GFAP	Glial fibrillary acidic protein
GFP	Green fluorescent protein
GM130	Golgin A2 (GOLGA2)
GPHN	Gephyrin
GR	Glucocorticoid receptor
GRASP65	Golgi reassembly stacking protein 65
GTP	Guanidine triphosphate
GTST	Gene trap sequence tags
H&E	Haematoxylin and eosin
hASCs	Human adipose-derived stem cells
HEK293T	Human embryonic kidney cell line 293 transfected with SV40 T antigen
HeLa	Human cell line derived from cervical cancer taken from Henrietta Lacks
HEPES	4-(2-hydroxyethyl)-1-piperazineethanesulfonic acid
HPLC	High pressure liquid chromatography
HR	Homologous recombination
hSDFs	Human skin-derived fibroblasts
HTT	Huntingtin
ICCB	Intensity correlation coefficient based analysis
ICCS	Image cross-corelation spectroscopy
ICV	Individual isolated cage
IFN	Interferon
IFT	Intraflagellar transport
IKMC	International Knock-out Mouse Consortium
IMSR	International Mouse Strain Resource
iPS	Induced pluripotent stem cells
IQR	Interquartile range
IVF	In vitro fertilisation
KLF7	Krüppel-like factor 7

KO/KI	Knock out/knock in
KOMP	Knock-Out Mouse Project
LAMP-1	Lysosomal-associated membrane protein
LB	Luria Broth
LDS, SDS	Lithium, Sodium dodecylsulfate
LFA	Lipofectamine
Loa	*Legs at odd angles*
LRRK2	Leucine-rich repeat kinase 2
LSCM	Laser scanning confocal microscopy
LTR	Long terminal repeat
M	Molar concentration [mol/l]
m.o.i.	Multiplicity of infection
MaLR	Mammalian apparent LTR-retrotransposon
MAP2K1 (MEK1)	Mitogen-activated protein kinase kinase 1
MEFs	Mouse embryonic fibroblasts
MES	2-(N-morpholino) ethanesulfonic acid
MGI	Mouse Genome Informatics
MLC	Myosin light chain
MND	Motor neuron disease
MOPS	3-(N-morpholino) propanesulfonic acid,
MPD	Mouse phenome database
mPFC	Medial prefrontal cortex
MRPS18-2	Human mitochondrial ribosomal protein S18-2
MTOC	Microtubule organising centre
MTs	Microtubules
MVB	Multivesicular body
M_X, M_Y	Mander's colocalisation coefficient
MYH9	Myosin heavy chain 2A
MYO5A	Myosin VA
NC	Nocodazole
Nde1	*Nuclear distribution gene E 1*
Ndel1	*Nuclear distribution gene E-like 1*
NDN	Necdin
NDR	Novelty discrimination ratio
NF	Neurofilament
NGF	Neurotrophic growth factor
NHS, HS	Horse (normal) serum
NMJ	Neuromuscular junctions
NTRK2	Neurotrophic tyrosine kinase receptor, type 2
OD	Optical density
ORF	Open reading frame
PAFAH 1B (LIS1)	Platelet-activating factor acetylhydrolase subunit 1b (Lissencephaly 1)
PAGE	Polyacrylamide gel electrophoresis
PAK1	P21-activated kinase 1
PB	Processing body
PBS	Phosphate buffer saline
PCC	Pearson's correlation coefficient
PCLO	Piccolo
PCR	Polymerase chain reaction
PFA	Paraformaldehyde
Phyh	*Phytanoyl-CoA 2-hydroxylase*
PIK3	Phosphatidylinositol 3-kinase
PLEKHM2 (SKIP)	Pleckstrin homology domain containing, family M (with RUN domain) member 2 (SifA (Salmonella-induced filaments A) and kinesin-interacting protein)
POU5F1 (OCT-4)	POU domain, class 5, transcription factor 1 (octamer binding protein 4)

PPI	Pre-pulse inhibition/Protein-proximity index
PPP1R15A (GADD43)	Protein phosphatase 1, regulatory (inhibitor) subunit 15A
PVDF	Polyvinylidene fluoride
RAB GTPase	Member of RAS-oncogenic family
RAB11-FIP3	Rab11-family interacting protein 3
RAC1	RAS-related C3 botulinum substrate 1
RHO	Rhodopsin
RHOD	Rhod ras homolog gene family, member D
RILP	Rab7-interacting lysosomal protein
RIPA	Radioimmunoprecipitation assay
RNA	Ribonucleic acid
RNAPII	RNA polymerase II
RNP	Ribonucleoprotein
ROI	Region of interest
RPL13A	Ribosomal protein L13A
RT	Room temperature/ Reverse transcription
SA	Sodium arsenite
Saa1/2	*Serum amyloid A1/A2*
SCA5	Spinocerebral ataxia type 5
SCAMP2	Secretory carrier-associated membrane protein 2
SCAMP3	Secretory carrier-associated membrane protein 3
SCV	*Salmonella* containing vesicles
SD	Standard deviation of a mean
SEM	Standard error of a mean
SG	Stress granule
SHIRPA	**S**mithKline Beecham Pharmaceuticals; **H**arwell, MRC Mouse Genome Centre and Mammalian Genetics Unit; **I**mperial College School of Medicine at St Mary's; **R**oyal London Hospital, St Bartholomew's and the Royal London School of Medicine; **P**henotype **A**ssessment
SIFT	Sorting Intolerant From Tolerant
SKP2	S-phase kinase-associated protein 2
SMAD3	MAD (mothers against decapentaplegic, *Drosophila*) homolog 3
SNX4	Sorting nexin 4
SOP	Standard operating procedure
SOX2	SRY-box containing gene 2
SOX9	SRY-box containing gene 9
SPI-1	*Salmonella* pathogenicity island 1
SPI-2	*Salmonella* pathogenicity island 2
Swl	*Sprawling*
SYP	Synaptophysin
T3SS	Type III secretion systems
TARDBP (TDP43)	TAR DNA binding protein
TBE	Tris/ Borate/ EDTA
TBS	Tris buffered saline
TfnR	Transferrin receptor
TG	Thapsigargin
TGF-β	Transforming growth factor β
TGN	Trans-Golgi network
TIAL1 (TIAR1)	TIA1 cytotoxic granule-associated RNA binding protein-like 1
TLE-4	Transducing-like enhancer of split 4
TNFRSF11A (RANK)	Tumor necrosis factor receptor superfamily, member 11a (NFKB activator/osteoprotegerin)
TNFSF11 (RANKL)	Tumor necrosis factor ligand superfamily member 11 (receptor activator of NF-kappaβ ligand, osteoprotegerin ligand)
U2AF	U2 auxiliary factor

UPR	Unfolded protein response
VIM	Vimentin
WD	Protein domain usually 40 aa long containing a GH dipeptide 11-24 residues from its N-terminus and the WD dipeptide at its C-terminus; between GH and WD lies a conserved core which serves as a propeller-like platform
WT	Wildtype
WWC1 (KIBRA)	WW, C2 and coiled-coil domain containing 1
X-Gal	5-Bromo-4-chloro-3-indolyl b-D-galactopyranoside
YWHA (14-3-3)	Tyrosine 3-monooxygenase/tryptophan 5-monooxygenase activation protein
α-SMA	Smooth muscle α-actin
γ-TuRC	γ-tubulin ring complex

Acknowledgements

This thesis is a story of three and a half years spent working with the dynein intermediate chains and I'd like to aknowledge everyone whose help and advice made it possible. I'm most grateful to Lizzy for the opportunity to work with her, and her patience and precious advice. I'd also like to thank members of our group for creating a great atmosphere, especially Gareth Banks, who introduced me to the lab and was there to discuss both popculture and experiments. Furthermore, I am grateful to the staff of the MRC Prion Unit animal house for taking care of my mice.

I'd like to thank Abraham Acevedo-Arozena, Tom Ricketts and the staff of the Mary Lyon Centre at the MRC Harwell for maintaining mouse colonies and help with phenotyping. My work would also have been impossible without Rob Deacon and Sam Line, who spent lots of time characterising our mutant mice. Furthermore, I'd like to thank Mike Groves, Jackie Linehan and 'histology' group for their help with histological analysis.

I'd also like to appreciate Gipi Schiavo, Matthew Golding, Gavin Kelly, and Mike Mitchell from the CRUK, and the participants of the RTN 'ENDOCYTE' for stimutaling discussions and helpful comments. Phil McGoldrick, who spent a rotation feeding cells with EGF and taking hundreds of pictures. An adventure with *Salmonella* typhimurium was possible thanks to David Holden and his group, especially Kieran McGourty who prepared bacterial cultures and was there to answer all the silly questions. Furthermore, I'd like to thank Kevin Pfister and Majid Hafezparast for their contribution and helpful comments on the splicing project.

Tommy has seen the best and the worst of the process successfully distracting me with books, shows, wine fueled discussions about science, and being adorable. I'm sure it would have been much harder without him. And there's DrainCat too.

1. Introduction

1.1 Cytoplasmic dynein is a molecular motor

Living cells are dynamic with organelles being in a constant movement. The flow of membranous organelles and protein complexes is possible thanks to molecular motors (kinesin, dynein, and myosin) and their interactions with filamentous polymers (microtubules, F-actin) (Hirokawa *et al.*, 2010). Molecular motors convert the chemical energy derived from ATP hydrolysis into mechanical action, and precise spatial and temporal regulation of motor-based transport is essential to ensure efficient cargo delivery. While the actin cytoskeleton is crucial for processes in the sub-cortical region, the long-distance transport is mediated by motors associated with microtubules (MTs). A cell being a highly organised entity depends on kinesins and dyneins, which use energy to move along MTs thus preserving the spatial distribution of organelles and their structure. Although general features of transport mediated by the cytoplasmic dynein complex are the same in all cells, the polarisation often imposes specific adaptations on the transport machinery to maintain cell function (Yamada *et al.*, 2010). Furthermore, defects in motor-dependent transport are associated with a range of diseases, including neurodegeneration, tumorigenesis and developmental defects (Eschbach and Dupuis, 2011).

The characteristic morphology of neurons makes this type of cell a useful model to study mechanisms of a long range transport (Hirokawa *et al.*, 2010). There are well distinguished compartments in a neuronal cell: an axon often extending far from a cell body and a network of much shorter dendrites. The cytoplasmic dynein complex is involved in the minus-end directed movement along microtubules (MTs (-)) in both axon and dendrites. The dynein has been shown to transport signalling endosomes after stimulation with neurotrophic factors (Deinhardt and Schiavo, 2005; Gauthier *et al.*, 2004; Ha *et al.*, 2008), mediate stress signalling (Perlson *et al.*, 2009), transport receptor containing vesicles (e.g. AMPA) (Kapitein *et al.*, 2010), and many more cargoes. Nonetheless, both detailed mechanisms of cargo selection or their regulation are not well known.

1.2 Molecular organisation of the dynein complex

There are two known families of the dynein complexes: *(1)* axonemal dyneins driving intraflagellar transport (IFT) and movement of cilia, and *(2)* cytoplasmic dyneins. Analysis of the vertebrate genomic sequences revealed the presence of two gene families, which compose the cytoplasmic dynein complex (Pfister *et al.*, 2006). Cytoplasmic dynein complex 2 (DYNC2) is found in cilia together with axonemal dyneins, while cytoplasmic dynein complex 1 (DYNC1) is the one responsible for the dynamics of the intracellular components and will be discussed in detail. Cytoplasmic dynein is made up of several subunits forming a functional complex, which is a dimeric assembly of heavy, intermediate, light intermediate, and three classes of light chains (Figure 1.1).

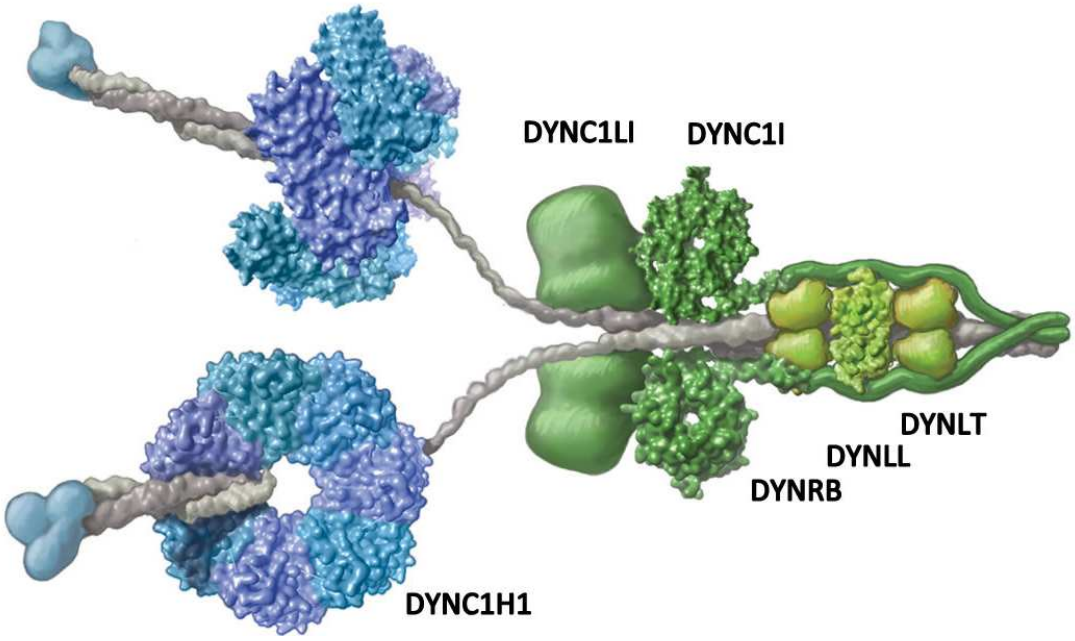

Figure 1.1. Structure of the cytoplasmic dynein complex
Representation of the complex with motor domain shaded blue, cargo binding domain marked in green; DYNC1H1 – heavy chains, DYNC1LI – light intermediate chains, DYNC1I – intermediate chains, DYNRB – light chains (Roadblock family), DYNLL – light chains (LC8 family), DYNLT – light chains (Tctex-1 family); reprinted with modifications from Cell vol. 112, Ronald D Vale, 'The Molecular Motor Toolbox for Intracellular Transport', p.14, © 2003, with permission from Elsevier

1.2.1 Cytoplasmic dynein heavy chain (DYNC1H1)

The cytoplasmic dynein heavy chain (DYNC1H1) is the largest subunit of the complex and is capable of generating mechanical force through ATP hydrolysis. Phylogenetic analyses suggest that heavy chain does not share origins with other motor proteins, kinesins and myosins (Spudich, 2011). It is built of over 4,600 residues and has a molecular weight of 530 kDa and was classified to a family of ATPases associated with various cellular activities (AAA), which feature a ring-shaped oligomeric structure (Hook and Vallee, 2006). The C-terminal motor domain contains six AAA^+ ATPase-like domains, however only four are catalytic. Additional structures, called 'linker' and 'stalk' have been implicated in the movement along microtubules. Both linker and catalytic domains are highly conserved (Hook and Vallee, 2006). The stalk contains a microtubule binding domain, whose affinity changes depending on the ATP-cycle (Figure 1.2) (Carter *et al.*, 2011). Furthermore, the linker extends over the AAA^+ domains, and was proposed to mediate the conformational changes during stepping. The N-terminal region called the 'tail', forms a platform where remaining subunits binds (Pfister *et al.*, 2006). Known mutations in the dynein heavy chain cause neurological deficits in heterozygous animals (*Dync1h1*$^{Mut/+}$) and lethality in homozygous (*Dync1h1*$^{Mut/Mut}$), as discussed in section 1.5.1.

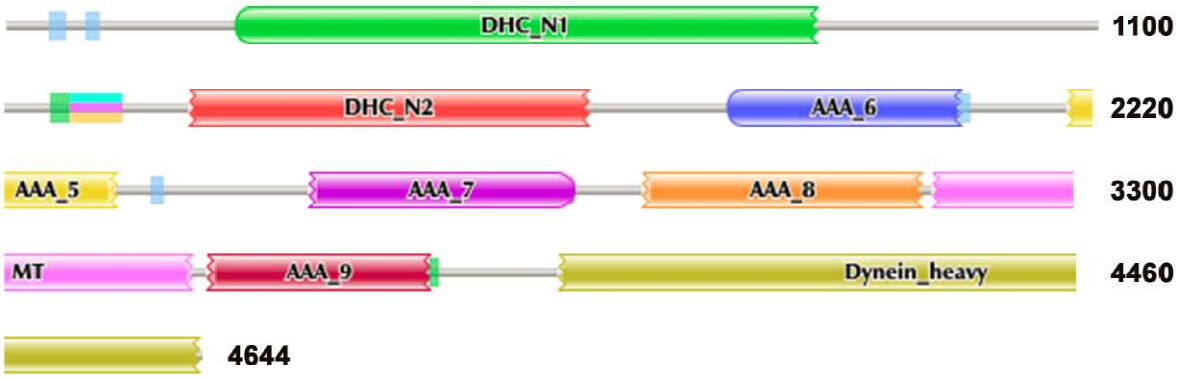

Figure 1.2. Organisation of domains of the cytoplasmic dynein heavy chain
Domains of the mouse DYNC1H1 (UniProt Q9JHU4) as annotated by Pfam 25.0 (Finn *et al.*, 2010); DHC_N1 – N-terminal region 1; DHC_N2 – N-terminal region 2; AAA_6 – hydrolytic ATP-binding site; AAA_5 – AAA domain; AAA_7 – P-loop containing motor region; AAA_8 - P-loop containing motor region; MT – microtubule binding stalk; AAA_9 – ATP binding motor region; Dynein_heavy – C-terminal region without P-loop (non-catalytic); for better visualisation divided into 4 parts running from: 1 – 1100, 1101 – 2220, 2221 – 3300, 3301 – 4460, and 4460 – 4644 amino acid, drawing is to scale; no splice variants are known

1.2.2 Cytoplasmic dynein intermediate chains 1 and 2 (DYNC1I1, DYNC1I2)

In the vertebrate genomes there are two genes encoding the dynein intermediate chains *(Dync1i1, Dync1i2)*. Protein sequences of both chains are highly similar (83%, BioEdit) and in the native complex these proteins are found as dimers (Pfister *et al.*, 2006). Intermediate chains function as an 'interaction hub' and are known to associate not only with heavy chains, but also with light chains (section 1.2.4), and adaptor complexes (section 1.3). This feature of the intermediate chains is characteristic for proteins containing WD domains, which form a structure known as a β–propeller (Figure 1.3) (Stirnimann *et al.*, 2010). WD domains are localised in the C-terminal region, while the helical N-terminal region forms a flexible structure, which adopts more helical conformation upon binding of the light chains (section 1.2.5) (Barbar, 2008).

Dynein intermediate chains are the most versatile subunits of the complex, due to their differential expression and posttranslational modifications. During transcription exons are alternatively spliced resulting in at least 6 isoforms of each gene (Chapter 6) (Kuta *et al.*, 2010). Furthermore, the expression pattern varies with DYNC1I1 found in the neural tissues and gonads, and DYNC1I2 localised in neural tissues except for one isoform. The only DYNC1I2 found in all mouse tissues was isoform DYNC1I2.C, which is the shortest variant known. The roles of distinct isoforms need to be determined, and the fact, that DYNC1I2.B was found to transport NTRK2-NGF vesicles suggests their significance in cargo selection (Ha *et al.*, 2008). In addition, phosphorylation of different residues of the intermediate chains was shown to regulate their interactions with the dynactin complex during trafficking of membranous organelles (Vaughan *et al.*, 2001), aggregation of pigment containing vesicles (Ikeda *et al.*, 2011), and segregation of chromatids (Whyte *et al.*, 2008).

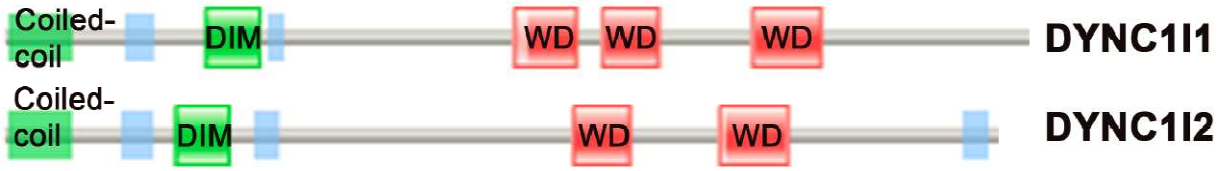

Figure 1.3. Organisation of domains of the cytoplasmic dynein intermediate chains
Domains of the mouse DYNC1I1 (upper panel, UniProt O88485, isoform DYNC1I1.B) and DYNC1I2 (lower panel, UniProt O88487, isoform DYNC1I2.B) as annotated by Pfam 25.0 (Finn *et al.*, 2010); DIM – dimerisation domain (green); WD – WD repeat; depending on a source there are from 2 to 7 WD repeats distinguished in the intermediate chains sequence (red); drawings are to scale and extend from amino acid 1 to 628 for DYNC1I1 and to 612 for DYNC1I2

1.2.3 Cytoplasmic dynein light intermediate chains (DYNC1LI1, DYNC1LI2)

Similarly to the intermediate chains, there are two genes known encoding dynein light intermediate chains 1 and 2 (*Dync1li1, Dync1li2*) (Pfister *et al.*, 2006). The N-terminal region binds to the heavy chains. In many experimental systems they were shown to interact directly with various proteins, supporting their role in cargo selection. The expression patterns of the light intermediate chains is not uniform, with *Dync1li1* transcripts detected mostly in neural tissues, heart, and kidney, whereas *Dync1li2* was present in brain, adipose tissue, muscle, spleen, testis, and bone (Gene Expression Atlas 11.04, http://www.ebi.ac.uk/gxa). Furthermore, light intermediate chains can also be phosphorylated (Pfister *et al.*, 2006).

DYNC1LI1 was shown to directly interact with pericentrin (Tynan *et al.*, 2000), RAB4A GTPase (Bielli *et al.*, 2001), and RAB11A – FIP3 (Horgan *et al.*, 2010b). DYNC1LIs were suggested to recruit the dynein complex to endosomal membranes thus increasing the accumulation of Transferrin (TfnR) in the perinuclear endosome recycling compartment (ERC) (Horgan *et al.*, 2010b). Furthermore, not only were those subunits involved in endosomal sorting, but they also clustered on the late endosomal and lysosomal membranes, where DYNC1LI1 recruits the dynein complex independently of both Rab7-interacting lysosomal protein (RILP) and dynactin (Tan *et al.*, 2011). Expression of the *Dync1li2* gene increased during neurite extension after growth factor stimulation (Angelastro *et al.*, 2000).

1.2.4 Cytoplasmic dynein light chains (DYNLT1, DYNLT2, DYNLRB1, DYNLTRB2, DYNLL1, DYNLL2)

Light chains are the only components of the dynein complex, which are also found to participate in processes different than dynein driven transport, and the same binding site is occupied by intermediate chains and competing interactors (Pfister *et al.*, 2006). They are found as homodimers *in vivo*, and it has been proposed, that they might act during dimerisation as stabilising partners (Barbar, 2008). An assembly of the cytoplasmic dynein complex is discussed in section 1.2.5.

DYNLT1 and DYNLT3 (known as Tctex-1 and Rp3 respectively) bind directly to the intermediate chains. They were detected in most of mouse tissues examined, including brain, lung colon, heart, pancreas in case of the DYNLT1, and brain, lung, kidney, liver in case of the DYNLT3 (Gene Expression Atlas 11.04, http://www.ebi.ac.uk/gxa). A body of evidence points towards specific functions of these subunits during mitosis and assembly of the mitotic spindle, although DYNLT1 was proposed to be involved in dynein independent pathways (Chuang *et al.*, 2005). In developing neurons, DYNLT1 determines the orientation of the mitotic spindle via interactions with RHO/RAC guanine nucleotide exchange factor (GEF) 2 (ARHGEF2, LFC) (Gauthier-Fisher *et al.*, 2009), whereas DYNLT3 interacts with a mitotic spindle checkpoint protein BUB3 (Budding uninhibited by benzimidazoles 3 homolog *(S. cerevisiae))* (Lo *et al.*, 2007a). Furthermore, the expression of the DYNLT1 was elevated in neuronal progenitors and young neurons (Dedesma *et al.*, 2006), while DYNLT3 strongly marked populations of mature neurons (Chuang *et al.*, 2001).

In growth cones of hippocampal neurons high levels of DYNLT1 were found to correlate with up-regulation of the RAS-related C3 botulinum substrate 1 (RAC1) signalling. A family of small GTPases (Rhod ras homolog gene family, member D (RHOD)) activates RAC1, which results in rearrangements of the actin cytoskeleton. In order to maintain the signalling, GTPases require activity of the guanidine exchange factor (GEF). A known RHOD/RAC1 specific GEF is ARHGEF2 (LFC), which was also found on the Golgi membrane and in the growth cones (Conde *et al.*, 2010). DYNLT1 competed with tyrosine 3-

monooxygenase/tryptophan 5-monooxygenase activation protein (YWHA/ 14-3-3) for the ARHGEF2 binding site, thus decreasing its activity (Meiri *et al.*, 2009).

Among cargos specific for DYNLT1 was C-terminal domain of rhodopsin (RHO) (Tai *et al.*, 1999), RAB3D GTPase (Pavlos *et al.*, 2011), and voltage gated calcium channels type P/Q and N (CACNA1A/CACNA1B respectively) (Lai *et al.*, 2005). In bone-desorbing osteoclasts RAB3D GTPase localised on the exocytic vesicles and the DYNLT1 binding was dependent on the GTP-GDP cycle, suggesting involvement of the dynein complex in the recycling of the RAB3D vesicles to the cell centre. Similarly, DYNLT1 was found important in the sorting and trafficking of the calcium dependent channels in the hippocampal neurons.

DYNLRB1 and DYNLRB2 (Roadblock) bind in the intermediate chains also as a dimer, however not much is known about their functions. The expression pattern differs between tissues, with DYNLRB1 found in brain, lung, heart, kidney, and DYNLRB2 detected in trachea, lung, but not brain (Gene Expression Atlas 11.04, http://www.ebi.ac.uk/gxa). DYNLRB1 is enriched on the Golgi complex membranes where it interacts with RAB6 GTPase (Wanschers *et al.*, 2008). There are three isoforms of the RAB6 known, which are involved in exocytosis and vesicle transport from Golgi apparatus towards the plasma membrane. DYNLRB1 is found to bind in a GTP-GDP dependent manner, similarly to the association observed for the RAB3 and DYNLT1. Likewise, RAB6 was proposed as a regulator of the exocytic pathway (Grigoriev *et al.*, 2007)

On the other hand, DYNLRB2 was found in the complexes with SMAD family member 3 (SMAD3) only, and it was phosphorylated after stimulation with transforming growth factor β (TGF-β) (Jin *et al.*, 2009).

Finally, light chains DYNLL1 and DYNLL2 (LC8 family) are loosely associated with the dynein complex and can be found as a free pool in the cytoplasm (Lo *et al.*, 2007b). They were observed interacting with bassoon (BSN) and piccolo (PCLO) in the synaptic compartment (Fejtova *et al.*, 2009), P21-activated kinase 1 (PAK1) (Vadlamudi *et al.*, 2004), myosin VA (MYO5A) (Espindola *et al.*, 2000), and many more proteins. They were proposed to act on a structural level by triggering the dimerisation of the intermediate chains (Barbar, 2008).

1.2.5 Assembly of the dynein complex

Cytoplasmic dynein is a complex made up of six different subunits, which are often expressed in many isoforms, thus greatly increasing the number of possible pools of the dynein complexes (King *et al.*, 2002). However, there are few mechanisms known, that tightly control distinct pools of the complexes - for example differential expression patterns of various subunits, their modifications - and an assembly of the dynein complex.

Apart from the heavy chains, often at least two variants of intermediate, light intermediate, and light chains can be expressed in the same tissue, and they have distinct structural characteristics. Dynein functions as a dimeric complex, and the dimerisation modes of various subunits have been studied, showing that *in vivo* DYNC1I1 and DYNC1I2 isoforms formed homo- and heterodimers (Myers *et al.*, 2007), while DYNC1LIs were observed as homodimers only. Similarly, only homodimers of DYNLT1 or DYNLT3 were capable of binding to the intermediate chains (homo- and heterodimers), while all variants of the intermediate chains associated with both, homo- and heterodimers of the DYNLL1/DYNLL2 and DYNLRB1/DYNLRB2 (Table 1.1) (Ilangovan *et al.*, 2005; Myers *et al.*, 2007). Furthermore, all the subunits, except for the DYNLL, were detected only in the holocomplex (Myers *et al.*, 2007).

Table 1.1. Summary of dimerisation modes
Preferences of subunits of the dynein complex to form homo- or heterodimers marked as '+' or '-'; chains found as homodimers only shaded

	DYNC1H1	**DYNC1I1** **DYNC1I2**	**DYNC1LI1** **DYNC1LI2**	**DYNLT1** **DYNLT3**	**DYNLRB1** **DYNLRB2**	**DYNLL1** **DYNLL2**
Homodimers	+	+	+	+	+	+
Heterodimers	-	+	-	-	+	+

Biochemical and structural studies allowed further insight into the molecular dynamics of dynein complex assembly. Native dynein complex can be fractionated into two distinct subcomplexes, which might correspond to separate assembly processes (King *et al.*, 2002). One pool consists of the heavy chains with bound intermediate chains, while intermediate and light chains constitute a second subcomplex. Association of the DYNC1LI homodimers is regulated by phosphorylation and can be abolished by dephosphorylating the light intermediate chains (Deng *et al.*, 2010). The assembly of the intermediate chains with dimers of three classes of light chains is a more complicated process involving conformational changes. The N-terminal region of free DYNC1Is is unstructured and dimerisation is initiated by binding dimeric DYNLTs or DYNLLs (Hall *et al.*, 2009). Association of the first dimer greatly enhances binding of the second pair of light chains (Figure 1.4). Upon dimerisation intermediate chains undergo a structural transition, resulting in formation of two extended β-sheets on the interface of bound DYNLTs and DYNLLs. Furthermore, this stage of the assembly changes the conformation of the intermediate chains in the distant region and a helical structure can be distinguished. Subsequently, a dimer of the DYNLRB is recruited to the intermediate chains (Nyarko and Barbar, 2011). Binding of the DYNLRBs is regulated by phosphorylation, and two phosphorylated residues were identified. Moreover, the region of interactions with the DYNC1Is is bigger than in case of the light chains, and it spans 27 and 22 residues respectively (Hall *et al.*, 2010). Interestingly, the intermediate chains undergo another conformational shift, and binding of the DYNLRBs destroys the helix induced by the DYNLTs/DYNLLs. As a result, the subcomplex of the intermediate and light chains forms elongated and flexible scaffold, with unordered region of the DYNC1Is between DYNLLs and DYNLRBs (Nyarko and Barbar, 2011).

Light chains were found to associate slightly more strongly with the complexes formed with DYNC1I1 than with DYNC1I2 (King *et al.*, 2002). Furthermore, interactions with both heavy chains and $P150^{Glued}$ were disrupted in the intermediate chains lacking light chain binding domains (King *et al.*, 2003). All these observations suggest an existence of a precise mechanism regulating the assembly of the subunits in a functional dynein complex.

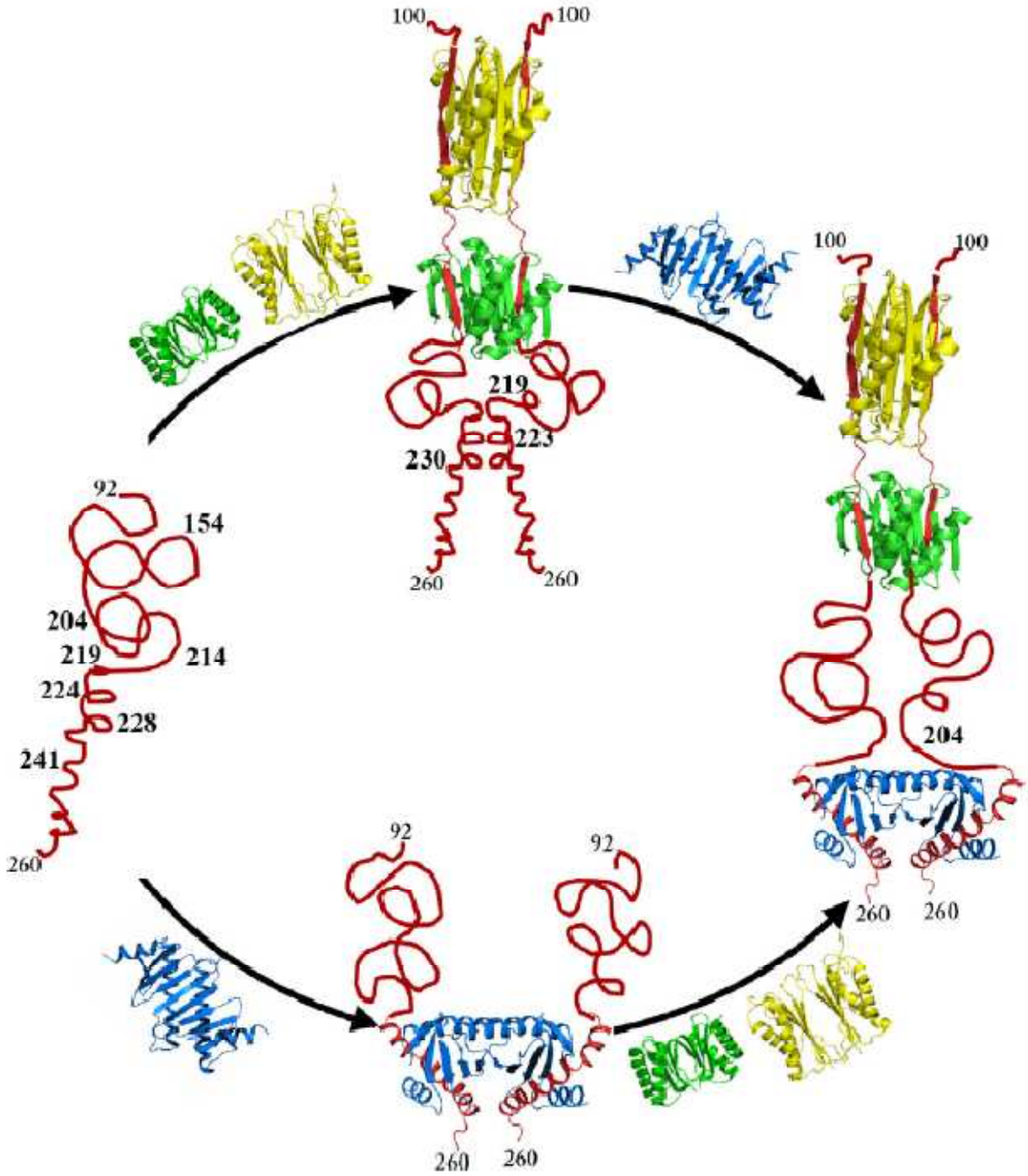

Figure 1.4. Model summarizing the light chains-dependent association of the intermediate chains
N-terminal region of the intermediate chains shown as an unstructured fragment (red) which undergoes a structural shift and a helix formation upon binding of the dimeric DYNLTs (yellow) and DYNLLs (green); in case of binding of the DYNLRBs (blue) only intermediate chains are separated; assembly of all the light chains results in an elongated structure, where DYNC1Is can associate; numbers correspond to residues crucial for the assembly of the functional complex;
This research was originally published in J Biol Chem., Nyarko A and Barbar E, 'Light chain-dependent self-association of dynein intermediate chain' 2011, vol. 286 p9. 1556-66 © 2011 by The American Society for Biochemistry and Molecular Biology, Inc.

1.3 Complexity of adaptors – who keeps dynein at bay?

Motility of the cytoplasmic dynein is often an outcome of interactions between many complexes, and their versatility reflects numerous cellular functions. Apart from adenoviruses, which leave early endosomes and bind directly to dynein via intermediate and light intermediate chains, the dynein complex does not interact directly with cargo, thus additional complexes serve as adaptors (Bremner *et al.*, 2009). There are many adaptor complexes known, which regulate the recruitment of the cytoplasmic dynein complex and cargo transport along microtubules, and those interacting directly with the intermediate chains will be mentioned.

1.3.1 Dynactin complex

The dynactin complex mediates cargo binding and promotes the activity of the cytoplasmic dynein. It is built from several subunits, out of which DCTN1 ($P150^{Glued}$) interacts directly with the dynein intermediate chains (Pfister *et al.*, 2006). It contains a CAP-Gly domain which interacts directly with microtubules, while a basic domain increases dynein processivity via stabilising the motor on the MTs (Culver-Hanlon *et al.*, 2006). Few single point mutations in the *DCTN1* gene were found in patients diagnosed with motor neuron disease (MND) (Munch *et al.*, 2004; Puls *et al.*, 2003). The dynactin complex binds EB1 at the tips of growing MTs and it is released after phosphorylation of its $P150^{Glued}$ subunit (Schuster *et al.*, 2011). Moreover, the recruitment of the dynein complex to endosomal membranes seems to be sequential; first the dynactin complex associates with cargo membranes via interactions with regulatory complexes (RAB GTPases) and then by actin-related protein (ARP1) binding to β-III-spectrin (Holleran *et al.*, 2001). A missense mutation in β-III-spectrin (L253P), causative of spinocerebral ataxia type 5 (SCA5), has been recently shown to disrupt release of plasma membrane proteins from the Golgi complex due to loss of its interactions with the ARP1 subunit of dynactin (Clarkson *et al.*, 2010). Furthermore, the $P150^{Glued}$ subunit of dynactin was found to accumulate in the ERC (Chen *et al.*, 2008), interact with SEC23 on vesicles budding from ER (Watson *et al.*, 2005), associate with RAB7 via RILP during maturation of late endosomes

(Jordens *et al.*, 2001); while p50/DYNAMITIN interacted with RAB6 and BICAUDAL-D during exocytosis (Akhmanova and Hammer, III, 2010).

1.3.2 Huntingtin

Another dynein adaptor is Huntingtin (HTT), which was observed associated with various vesicular organelles (Caviston *et al.*, 2007). HTT is expressed in all the tissues examined, and the highest levels of the *Htt* transcript were noted for brain and testis (Dixon *et al.*, 2004). In addition three splice variants were detected in mouse tissues (Schmitt *et al.*, 1995). Predicted HTT protein structure resembles that of a molecular scaffold, which can be incorporated in lipid membranes. The HTT is known to directly interact with the N-terminal region of the intermediate chains of the dynein complex (Caviston *et al.*, 2007) and indirectly with kinesins, myosins, and RAB5. Furthermore, removal of HTT in HeLa cells resulted in mislocalisation of endosomal compartments (early, recycling, late, lysosomal), which were clustered in the actin rich cortical area. Whereas cells lacking cytoplasmic dynein heavy chain (DYNC1H1) also displayed a dispersed phenotype yet the vesicles were mostly associated with MTs (Caviston *et al.*, 2011). Interestingly, expression of the full length HTT restored the retrograde endosomal transport, which supports the model of HTT acting as a scaffold on the endosomal membrane (Caviston and Holzbaur, 2009). Moreover, endogenous HTT was shown to be a key component responsible for smooth transition of newly formed vesicles from actin to microtubule cytoskeleton. Finally, while HTT stimulated the dynein dependent movement, it had no effect on kinesin-1.

1.3.3 NUD family (NDE1, NDEL1, LIS1)

In recent years more attention has been directed at a family of genes first described in *Aspergillus sp.* called nuclear distribution (*Nud*). Mammalian homologs include platelet-activating factor acetylhydrolase subunit 1b/Lissencephaly 1 (*Pafah1b/Lis1,* homolog of *NudF*), nuclear distribution gene E (*Nde1*), and nuclear distribution gene E-like 1 (*Ndel1*) (Lam *et al.*, 2010). Both NDE1 and NDEL1 dimerise and bind dynein intermediate chains upon phosphorylation of the C-terminal domain and form scaffold for a dimer of LIS1

interacting with AAA domains of the heavy chains (Zylkiewicz *et al.*, 2011). As a result, the 'tail' of the dynein complex is 'cross-linked' by a symmetric heterotetramer.

NDE1, NDEL1, and LIS1 were originally observed in the kinetochore complex, and recently they were shown to regulate dynein driven trafficking of the membranous organelles (Lam *et al.*, 2010). NDEL1 localised to the membranes of the Golgi complex and was essential for cargo binding and dynein transport. Furthermore, depletion of LIS1 resulted in dissociation of the intermediate chains from membranous organelles.

1.4 Mutagenesis as a way to study gene function

Information about an organism is stored in its DNA and genetic mutants have proved very useful in learning about functions of cellular components. The popularity of the laboratory mouse (*Mus musculus*) in biological research is reflected by a number of resources available, such as well characterised inbred strains, complete sequences of a mouse genome, and diversity of genetic manipulations successfully applied ((Nguyen and Xu, 2008) and references therein). Furthermore, rodents and humans share physiological pathways and developmental mechanisms, thus so far a mouse is the best animal model to study humans disorders.

1.4.1 Introduction of changes in genomic DNA

Although naturally occurring mutants were at the foundation of genetics, over decades it became possible to manipulate genetic information, thus establishing lines of mutant organisms. In mouse, mutations can be described as randomly spread throughout the genome or targeted to a specific locus (Hardy *et al.*, 2010).

1.4.1.1 Random mutagenesis

Random mutagenesis is often achieved by insertion of parts of DNA or by using chemical agents. Mammalian transposons constitute naturally occurring genetic elements capable of self-excision and insertion. Mobilisation of a transposon often results in the deletion of a part of a surrounding DNA, while insertion of a transposon within a gene may disrupt its architecture (Hardy *et al.*, 2010). Although insertional mutations were known to

sometimes result in incomplete loss of function phenotypes, gene trap cassettes based on transposable elements have been used to create a library of mouse embryonic stem (ES) cell lines carrying mutations in single genes. For example, a reference library of gene trap sequence tags (GTST) from insertional mutations was generated by The German Genetrap Consortium (GGTC) (http://www.genetrap.de), with 2910 new clones released (April 2011).

Many disorders described in humans are caused by single point mutations, and chemical mutagenesis (e.g. with *N*-ethyl-*N*-nitrosourea, ENU) has been shown to generate useful models recapitulating complex phenotypes observed in clinical conditions (Acevedo-Arozena *et al.*, 2008). When used in doses high enough to overcome DNA repair mechanisms, ENU alkylates DNA bases in a random fashion, thus introducing single point mutations throughout a genome (Nolan, 2000). As a result, a broad range of mutations can be observed, including not only missense changes (64%), but also affecting splicing (26%) or causing premature termination (10%). Chemical mutagenesis displays high rate of changes with expected 1 mutation per 1.01 Mb of genomic DNA or 1.82 Mb of coding sequence depending on the dose used (Keays *et al.*, 2006). An advantage of ENU induced mutations is that they are distributed across both coding and non-coding regions of the genome, therefore assumptions of the type of mutation and of causative gene function are avoided (Ching *et al.*, 2010). Furthermore, a panel of animals carrying allelic mutations can be analysed , so giving an 'allelic series' which may provide new insight into gene function (Nolan *et al.*, 2002). On the other hand, effects of the mutagen can depend on a mouse strain used, and usually several changes per a genome can be expected. A commonly used procedure involves induction of mutations in the premeiotic spermatogonia and analysis of the progeny of mutagenised male, but mutagenesis can be also carried out in embryonic stem (ES) cells (Acevedo-Arozena *et al.*, 2008).

1.4.1.2 Transgenesis

1.4.1.2.1 Transgenic mice

In the conventional approach, DNA from a gene of interest in a vector is introduced into a fertilised oocyte which was then implanted into a pseudopregnant female. The transplanted embryos develop to term and then the animals are screened for the presence of the transgene (Hardy *et al.*, 2010). Although this approach is popular and for example is used to model dominant disease, it is impossible to predict the integration site, orientation of the transgene or its copy number (Ohtsuka *et al.*, 2010). Furthermore, the chromatin rearrangements or silencing of the exogenous DNA often affect the expression of the transgene.

1.4.1.2.2 Gene targeted mice

A different approach, gene targeting, overcomes the above problems that may arise with transgenic animals created by pronuclear injection. Because homologous recombination (HR) is a preferable mechanism of DNA repair in the ES cells, development of ES cell based protocols allowed precise targeting by the DNA introduced on specially designed vectors. ES clones which have undergone HR can then be selected and injected into host blastocysts, which are then implanted into pseudopregnant females. These chimeric embryos come to term and result in chimeric mice (Hardy *et al.*, 2010). If the homologously recombined ES cell component is in the gonads of the chimeric mice, they may be bred to produce gene targeted animals. Although generation of chimeric mice and germ-line transmission of the targeted allele are limiting steps, this approach gained in popularity as only one copy of the mutation is introduced in the original locus. Thus, a range of manipulations can be achieved, including knock out (KO), knock in (KI), conditional and inducible mutations.

1.4.2 Phenotypic analysis of mutant mice

Phenotyping of a mutant animal is usually the final goal of most projects that use mouse genetics, therefore accurate characterisation should be a priority. There are two main approaches applied when working with mutant animals: a phenotype-driven screen

followed by mapping of the genetic locus which segregates with the phenotype (forward genetics), which is often applied in random mutagenesis programs. Alternatively, changes in a gene of interest are introduced and the phenotype of mutant animals is characterised (reverse genetics) (Nolan *et al.*, 2002). Both approaches have been successfully applied in the ENU-mutagenesis programs and are briefly described in the following paragraphs.

In the phenotype based screens of ENU-treated animals, mutagenised males are mated with wildtype females and the progeny (G1) are tested. The phenotypically aberrant animals identified in this round of testing carry dominant mutations. In order to detect phenotypes caused by recessive alleles intercrossing of other generations (G2, G3), which are subjected to analysis, is necessary; in either case the inheritance of the phenotype is also tested to ensure the phenotype arises form a germ-line mutation rather than a sporadic defect. One of the advantages of the phenotype based approach is that no assumptions are made about genes or pathways affected. Even though studies have reported that only approximately 25% of ENU induced mutations are dominant alleles (Brown and Nolan, 1998), high-throughput phenotype based studies have resulted in identifying many mutant mouse lines (Acevedo-Arozena *et al.*, 2008). Furthermore, ENU mutagenesis has been shown successful in analysis of modifiers of the known phenotype.

Taking the second approach, the genotype based approach, an archive of mutated DNA made from F1 mutant males can be screened in order to identify mutations in a specific gene. The method has gained on popularity thanks to the availability of the whole genome sequencing, genome-wide association studies, and applying a range of techniques to detect potential mutations (Acevedo-Arozena *et al.*, 2008). Once a mutation in a specific DNA sample is identified, the equivalent frozen sperm sample can be used for IVF and the mouse rederived. In this way a panel of allelic mutations can be found fairly quickly and animals can be rederived to be phenotyped.

Both approaches broaden our understanding of a gene's function by using standardised phenotyping regimes suitable for mouse. Standardising is essential, especially in case of complex traits or mild phenotypes, e.g. behaviour is very sensitive to various factors (Crawley, 2008). On the other hand high-throughput screens, when thousands of

individuals are analysed, require robust yet sensitive tests in order to yield good quality data (Brooks and Dunnett, 2009). Nevertheless, before performing behavioural tests several things should be considered. Decades of mouse breeding resulted in the generation of over 450 inbred strains, which due to their genetic background, often show different performances in various tasks (Phenome Database, http://www.phenome.jax.org). An appropriate inbred strain with moderate behavioural phenotypes should be then chosen when breeding a cohort of mutant mice that will be behaviourally tested; it is also beneficial to characterise effects of a mutation in a genetic context of at least two inbred strains. As an animal itself constitutes a very complex system a phenotype observed can be caused by many factors which should be taken into account while performing behavioural tasks. Thus in order to avoid misinterpretation of results, observations of general health of an animal are often included in a phenotyping pipeline, e.g. many neurological disorders affect locomotor ability. Moreover, performing several tests measuring the same behaviour (e.g. anxiety, memory) helps to discriminate even mild phenotypes. Finally, when a mouse is subjected to a series of various tasks, they should be carried out starting from the least stressful (Crawley, 2008).

Appropriate data analysis is extremely important and for example, Karp and colleagues (Karp *et al.*, 2010) discuss issues of variation between mice and an appropriate statistical validation of results. Most of the data obtained during phenotyping have hierarchical structure (e.g. genotype /treatment → animal → measurements) which should be taken into account; the authors propose 3-level random effect nested analysis of variance (ANOVA) with adjustments for multiple trials as a robust and powerful test.

One of the first protocols designed for phenotyping of large cohorts of mice was SHIRPA (**S**mithKline Beecham Pharmaceuticals; **H**arwell, MRC Mouse Genome Centre and Mammalian Genetics Unit; **I**mperial College School of Medicine at St Mary's; **R**oyal London Hospital, St Bartholomew's and the Royal London School of Medicine; **P**henotype **A**ssessment), which consisted of over 40 quantitative measurements (Rogers *et al.*, 1997). Initially SHIRPA was designed into three stages: (1) observation of basic health and animal performance (e.g. gait, overall appearance), (2) behavioral and pathological (e.g.

locomotor activity), and (3) more specific and invasive investigations such as behavioural tasks (e.g. anxiety, learning). The SHIRPA protocol was successful in characterizing behavioral traits in inbred strains (Rogers *et al.*, 1997), and adapted for long time observations of progressive neurological phenotypes (Lalonde *et al.*, 2004; Rogers *et al.*, 2001).

1.4.2.1 The MRC Mammalian Genetics Unit, Harwell, ENU mutagenesis programme

ENU mutagenesis, as mentioned before, is a powerful tool and a set of mutant animals can be generated in a short time. On the other hand numerous cohorts of mice need to be tested in a high-throughput manner before a specific phenotype may be detected (Acevedo-Arozena *et al.*, 2008). MRC Mammalian Genetics Unit, Harwell, UK is one centre generating novel mutant mouse lines in an ENU mutagenesis programme. A robust pipeline aimed to identify mutation-related phenotypes in all areas examined was applied in a screen of over 26000 mutagenised F1 mice (Nolan *et al.*, 2000). The primary screen consisted of sets of non-invasive tests which were performed sequentially: at weaning mice were assessed for developmental dysmorphologies, followed by modified SHIRPA, and biochemical analysis of blood. Nolan and colleagues (2000) reported dominant alleles having given rise to diverse phenotypes at a level of 2%. Following primary screens secondary phenotyping is designed for a specific area; for instance neurological deficits can be characterised with the SHIRPA protocol (as mentioned), long time behavioural observation coupled with computer based video analysis (Jhuang *et al.*, 2010), or tests scoring social interactions (Silverman *et al.*, 2010).

1.4.2.2 Data capture

The high-throughput ENU screens, of which the programme at MRC Harwell is just one, generate huge amount of data which need to be managed so that they are easily accessible. Therefore, in many European centers several projects have been initiated in order to provide the community with standardised procedures and accessible data, including EUMORPHIA (http://www.eumorphia.org), EMPReSS (http://empress.har.mrc.ac.uk), and EuroPhenome (http://www.europhenome.org). The main purpose of the

EUMORPHIA (European Union Mouse Research for Public Health and Industrial Applications) project was to develop new approaches in mouse mutagenesis and phenotyping, thus establishing EMReSS (European Mouse Phenotyping Resource of Standardised Screens) (Brown *et al.*, 2005). The EMPReSS database contains sets of individual standard operating procedures (SOPs) applicable in various phenotyping screens. Because the main objective was to provide robust yet sensitive protocols which would produce comparable results, the EMPReSS procedures were validated by screening four inbred mouse strains (Mandillo *et al.*, 2008). Moreover, EMPReSS slim phenotyping pipelines were designed to describe a comprehensive multi-system phenotypic pipeline and were used in primary high-throughput screens performed by the EUMODIC (European Mouse Disease Clinic) consortium (Gates *et al.*, 2010). The visual representation of a timescale of tests included in two EMPReSS slim pipelines is presented in Figure 1.5. Finally, all the data obtained from various screens are deposited in the EuroPhenome database (Mallon *et al.*, 2008); at present characteristics of 266 mutant and 44 inbred mouse strains can be accessed (March 2011).

Another resource initiated by the Jackson Laboratory is the Mouse Phenome Database (http://phenome.jax.org), in which genotypic and phenotypic data of inbred mouse strains are collected (Grubb *et al.*, 2009). Apart from versatile characteristics of mouse lines deposited by researchers, the database provides detailed protocols used in each study and informatics tools for data exploration, analysis and comparison. At present (March 2011) the MPD contains data from 118 phenotype strain survey projects and information of over 600 inbred strains.

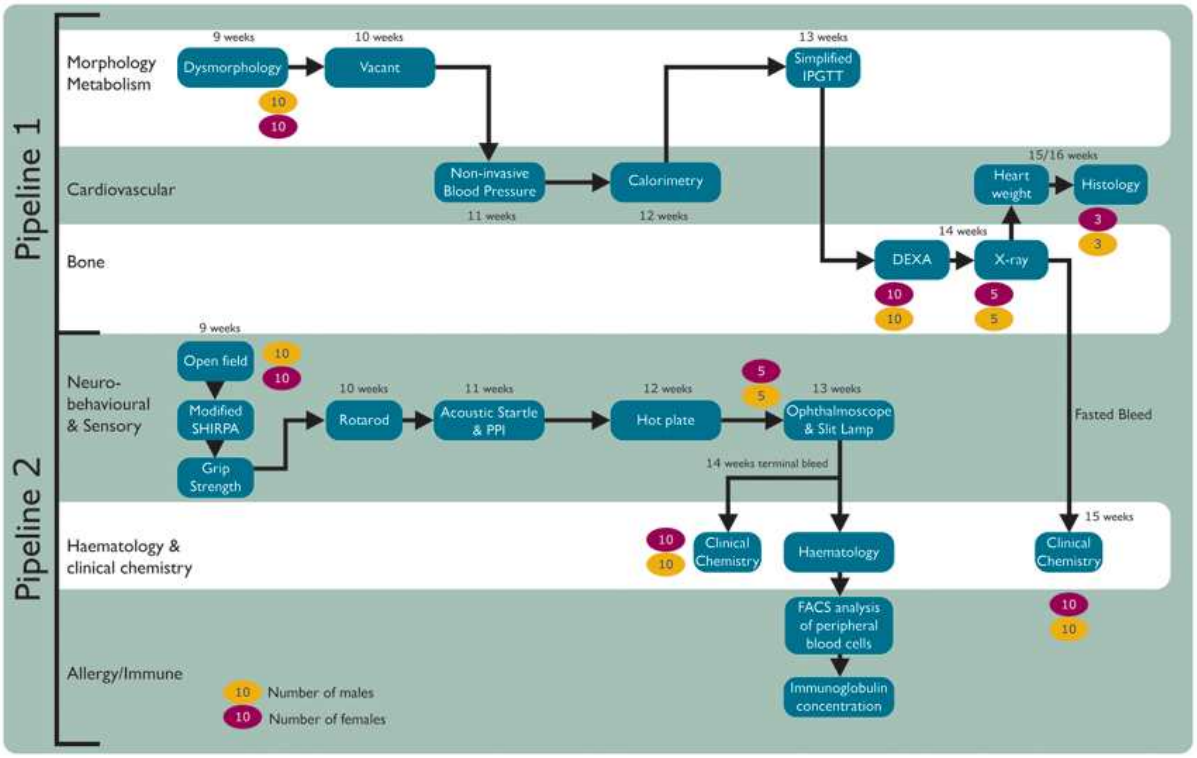

Figure 1.5. Simplified representation of Empress slim pipelines
EUMODIC screens consist of several tests covering various areas of animal physiology and behavior; they are performed on age-matched cohorts of 10 male and 10 female mice in a weekly intervals (the age of mice marked above each test); IPGTT - intra-peritoneal glucose tolerance test, DEXA – bone densitometry, PPI – pre-pulse inhibition, FACS – fluorescence – activated cell sorting.

1.5 Phenotypes of animal models carrying mutations in the cytoplasmic dynein and dynactin complexes

The cytoplasmic dynein complex is crucial for cell functioning and survival, as it participates in a range of cellular processes. Analysis of phenotypes of mouse models carrying mutations in the genes of the dynein complex is invaluable source of knowledge, giving insight into functions of the cytoplasmic dynein in a context of different tissues and developmental stages, and of the whole animal.

1.5.1 Mutant lines in the cytoplasmic dynein heavy chain *(Dync1h1)*

1.5.1.1 Dync1h1^{tm1Noh} mouse

There is one mouse line known carrying a targeted mutation resulting in a *null* allele of the dynein heavy chain (*Dync1h1^{tm1Noh}*) (Harada *et al.*, 1998). Lack of the heavy chain in the homozygous animals *Dync1h1$^{-/-}$* resulted in lethality of 8.5 days old embryos, while heterozygous mice *Dync1h1$^{+/-}$* were indistinguishable from their wildtype *Dync1h1$^{+/+}$* littermates. When cultured *in vitro*, homozygous *Dync1h1$^{-/-}$* embryonic cells failed to proliferate and blastocysts died after few days. On the cellular level, complete disruption of the heavy chain caused fragmentation of Golgi apparatus and mislocalisation of the endosomal compartment to the cell periphery.

1.5.1.2 Loa mouse (Legs at odd angles)

A founder of the *'Legs at odd angles' (Loa)* mutant mouse line was identified in the screen of ENU-mutagenised animals (Hafezparast *et al.*, 2003). It displayed abnormal body posture, limb grasping, reduced grip strength. A missense point mutation was found in the *Dync1h1* gene resulting in the amino acid substitution F508Y which is a causative of neurological deficits in heterozygous *Dync1h1$^{Loa/+}$* mice (Figure 1.6). Although homozygous *Dync1h1$^{Loa/Loa}$* animals were born, they died in late gestation or just after birth.

Detailed analysis of the heterozygous *Dync1h1$^{Loa/+}$* animals revealed sensory neuropathy associated with degeneration of muscle spindles and neurons in lumbar dorsal root ganglia (DRGs) (Chen *et al.*, 2007). Furthermore, in sciatic nerve two distinct populations of retrogradely transported endosomes were observed, where a slower component corresponded to impaired axonal transport in sensory neurons (Bilsland *et al.*, 2010). Biochemical analysis of a single motors revealed impairment in coordination between motor domains of the heavy chains, resulting in marked decrease in run length and velocity of a single run (Ori-McKenney *et al.*, 2010). Effects of the impairment in the function of heavy chain were also observed in adipose tissue. Heterozygous *Dync1h1$^{Loa/+}$* animals differed in adiposity and cold tolerance, features associated with impaired

lipolysis and morphological abnormalities in brown fat tissue (Eschbach *et al.*, 2011). This phenotype was caused by deficits in norepinephrin release and signalling.

The effects of mutation were pronounced in cells and tissues isolated from homozygous *Dync1h1*$^{Loa/Loa}$ animals, including defects in migration of neuronal populations in hindbrain, branching and elongation of peripheral nerves, and delays in reassembly of the Golgi complex (Hafezparast *et al.*, 2003). Furthermore, the mutation affected dynamics of the interactions between different subunits of the complex (Deng *et al.*, 2010).

1.5.1.3 Cra1 mouse (Cramping 1)

The *'Cramping 1' (Cra 1)* mouse line was created in an ENU-mutagenesis experiment, and carries a point mutation changing tyrosine to cysteine (Y1055C) (Figure 1.6) (Hafezparast *et al.*, 2003). The mutation is allelic to *Dync1h1*^{Loa}, and *Dync1h1*^{Cra1} animals have similar characteristics as the *Dync1h1*^{Loa} animals, including embryonic lethality of homozygous *Dync1h1*$^{Cra1/Cra1}$ mice and neuronal phenotypes in heterozygous *Dync1h1*$^{Cra/+}$ animals. Sensory neuron degeneration was observed in heterozygous (*Dync1h1*$^{Cra1/+}$) mice, while motor neurons were unaffected (Dupuis *et al.*, 2009). Furthermore, developmental defects in assembly of synapses were proposed to reflect structural defects of neuromuscular junctions (NMJ) (Courchesne *et al.*, 2011). Finally, heterozygous *Dync1h1*$^{Cra/+}$ mice recapitulated the adipose tissue phenotype observed in the *Dync1h1*$^{Loa/+}$ animals.

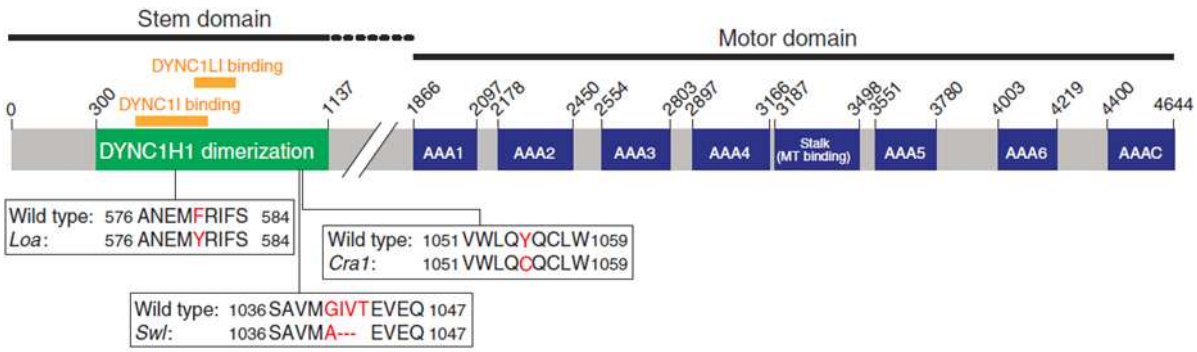

Figure 1.6. Protein map of the cytoplasmic dynein heavy chain showing the location of the mutations *Loa, Cra1* and *Swl*

The motor domain consists of the six known AAA-ATPase domains (AAA 1 to 6) and an unrelated seventh domain (AAAC); the microtubule-binding domain lies between AAA4 and AAA5; the N-terminal region protein contains the intermediate (DYNC1I), light-intermediate (DYNC1LI) and heavy (DYNC1H1); adapted from Banks and Fisher (2008) © 2008 by BioMed Central

1.5.1.4 Swl mouse (Sprawling)

The *'Sprawling' (Swl)* mutant was generated via radiation induced mutagenesis and carries a 9 bp deletion (GIVT1040A) within the dimerisation domain of the heavy chain (Figure 1.6) (Chen *et al.*, 2007). Mutation causes neurological deficits in heterozygous *(Dync1h1$^{Swl/+}$)* animals, and embryonic lethality of the homozygous *Dync1h1$^{Swl/Swl}$*. Heterozygous *Dync1h1$^{Swl/+}$* animals can be identified by an unsteady gait, and decrease in the grip strength of hind limbs. This behaviour results from a neuropathy of sensory neurons and degeneration of muscle spindles in hind limbs. Detailed histological analysis showed decrease in number of proprioceptors and sensory neurons located in the DRG. At the same time peripheral and spinal motor neurons were not affected.

1.5.2 *Dync1li1^{N235Y}* mouse

A reverse genetics approach was employed to identify a single point mutation in the cytoplasmic dynein light intermediate chain 1 (*Dync1li1*) in the genomic DNA isolated from ENU mutagenised animals in the MRC Harwell archive. Mutant mouse line was rederived and detailed phenotype of homozygous *Dync1li1$^{N235Y/N235Y}$* animals assessed (Banks *et al.*, 2011). Interestingly, mutant animals displayed phenotypes distinct from the mouse lines carrying mutations in the dynein heavy chain. *Dync1li1$^{N235Y/N235Y}$* animals showed increased levels of anxiety along with lower spontaneous locomotor activity and subtle gait impairment. Histological analysis revealed abnormal dendrite outgrowth and migration pattern of the cortical neurons, while dendrite branching was enhanced in sensory neurons. On the cellular level, impairment of housekeeping functions of the dynein complex was observed, namely EGF trafficking and Golgi complex reassembly.

1.5.3 *P150^{Glued}* transgenic models

A single point mutation (G59S) in *DYNACTIN 1* (*DCTN1/P150^{Glued})* was described in a family with distal spinal and bulbar muscular atrophy (dSBMA, previously classified as motor neuron disease, MND) (Chevalier-Larsen *et al.*, 2008; Puls *et al.*, 2003). Since then, two different transgenic mouse lines carrying G59S were described showing distinct phenotypes.

Transgenic mouse lines expressing human cDNA of *DCTN1*^{G59S} under a control of motor neuron specific promoter were compared with lines transgenic for a wildtype of the *DCTN1* (Chevalier-Larsen *et al.*, 2008; Laird *et al.*, 2008). Animals carrying mutant transgene displayed late onset progressive muscle weakness although whether their lifespan was affected needs to be clarified (Chevalier-Larsen *et al.*, 2008). Furthermore, expression of the human DCTN1^{G59S} caused distal degeneration associated with axonal swelling and changes in the NMJs. Although axonal transport was not impaired, there were enlarged tertiary lysosomes and cytoplasmic granules observed in neuronal cells, suggesting impairment in vesicular transport and degradation.

Alternative mouse models carrying the same mutation but in the mouse *Dctn1* gene were created by applying the targeted mutagenesis approach (Lai *et al.*, 2007). Established mouse lines had the wildtype allele replaced by mouse mutant alleles *(Dctn1*^{G59S} – amino acid substitution*, Dctn1*$^{\Delta 2\text{-}3}$ - deletion of exons 2 and 3, *Dctn1*^{neo} – knock-out allele*)*, which inhibited embryogenesis of homozygous animals *(Dctn1*$^{G59S/G59S}$*, Dctn1*$^{\Delta 2\text{-}3/\Delta 2\text{-}3}$*).* Although levels of wildtype DCTN1/P150^{Glued} in spinal cord protein lysates were lower by 50% in animals heterozygous for each of the alleles, the structure of the dynactin complex was not affected. Furthermore, only *Dctn1*$^{G59S/+}$ animals developed neurological deficits similar to motor neuron disease. There was no impairment in locomotor performance except for shortening of the stride length in the *Dctn1*$^{G59S/+}$ males. In addition, structural abnormalities of the NMJs were observed with accumulation of neurofilaments (NFs) and synaptophysin (SYP). Finally, number of motor neurons in the lumbar spinal cord was lower in the heterozygous *Dctn1*$^{G59S/+}$ animals.

1.5.4 Summary of dynein and dynactin mouse mutants

This summary of known mouse models mutant in the dynein/dynactin complexes suggests that there is a crucial role of retrograde transport in the neuronal cells. Interestingly, phenotypes associated with the cytoplasmic heavy chain *(Dync1h1*) and dynactin 1 (*Dctn1*) mutant alleles had dominant pattern of inheritance, which supports their critical role for the activity of the cytoplasmic dynein complex.

Table 1.2. Summary of mouse model mutant in the cytoplasmic dynein and dynactin complexes
Abbreviations used: *Dync1h1* – cytoplasmic dynein heavy chain 1, *Dctn1* – dynactin 1 ($P150^{Glued}$), *Dync1li1* – cytoplasmic dynein light intermediate chain 1, MNJ – neuromuscular junction, MN – motor neuron, NF – neurofilament, SYP – synaptophysin

Mouse model	Gene and mutation	Behavioural phenotype	Histological phenotype	Cellular phenotype
Dync1h1^{tm1Noh}	*Dync1h1,* knock-out allele	Homozygotes embryonic lethal		Homozygous embryos fail to proliferate Disruption of Golgi apparatus
Dync1h1^{Loa}	*Dync1h1,* F508Y mutation	Homozygotes die before/after birth Abnormal gait and performance on locomotor tasks	Sensory neurons neuropathy Abnormal adiposity Defects in neuronal migration	Delayed retrograde axonal transport Delay in reassembly of Golgi apparatus Impaired interactions between subunits
Dync1h1^{Cra1}	*Dync1h1,* Y1055C mutation	Homozygotes embryonic lethal	Sensory neurons neuropathy Abnormal adiposity Defects in neuromuscular junctions	
Dync1h1^{Swl}	*Dync1h1,* GIVT1040A deletion	Homozygotes embryonic lethal Unsteady gait, decrease in grip strength	Sensory neurons neuropathy Muscle spindles degeneration	
Dync1li1^{N235Y}	*Dync1li1,* N235Y mutation	Homozygotes show increased anxtiety, gait impairment	Abnormal dendrite architecture and neuronal migration	Impaired EGF trafficking, Golgi complex assembly
DCTN1^{G59S}	DCTN1, human transgene with G59S mutation	Muscle weakness	Distal degeneration with axonal swelling Ambormalities in NMJs	Enlarged tertiary lysosomes and cytoplasmic granules
Dctn1^{G59S}, *Dctn1*$^{\Delta 2\text{-}3}$	*Dctn1,* targeted mutation	Homozygotes embryonic lethal Neurological defects Gait abnormalities	Degeneration of MN in lumbar spinal cord	Accumulation of NFs and SYP

1.6 Project outline

Activity of cytoplasmic dynein complex is indispensable for cell function and survival, however there are still many unanswered questions regarding cargo assembly, roles of the individual subunits, and regulation of the complex. A great part of our knowledge about the dynein complex comes from studies employing cellular models, which although very useful, are not devoid of limitations. Many isoforms of the subunits are expressed in a tissue specific manner, which is difficult to replicate in a cell line. Furthermore, many reports come from studies, in which specific subunits were depleted often resulting in disruption of the whole dynein complex. However, many diseases associated with impairment of the intracellular transport are caused by point mutations.

With the above considerations in mind, we decided to use a mouse genetics approach to investigate the function of the cytoplasmic dynein intermediate chains. We chose these subunits, as being in the heart of the dynein complex they form a platform where many accessory complexes and cargos are known to bind. Using a reverse-genetics approach we performed a screen of the MRC Harwell DNA archive isolated from ENU-mutagenised mice. The screen resulted in detection of two mice heterozygous for coding point mutations in the intermediate chains 1 and 2. Mouse lines were rederived and colonies established in order to characterise phenotype of the mutant animals. The presented work was focused on:

- Behavioural analysis of mouse lines carrying mutations in the intermediate chains 1 and 2 *(Dync1i1^{G482D}, Dync1i2^{T172I}).*
- Investigation of the effects of the mutations on the housekeeping functions of the dynein complex using cellular models.
- Comparison of response to stress between cell lines carrying mutations in the intermediate *(Dync1i1^{G482D} Dync1i2^{T172I})* and heavy chains *(Dync1h1^{Loa}).*
- Detailed analysis of the alternative splicing of the dynein intermediate chains 1 and 2 (*Dync1i1*, *Dync1i2*) in mouse tissues.

2. Methods

2.1 Experimental animals

The animal experiments described were carried out under the "Guidance on Operation of Animals (Scientific Procedures Act 1986) March 2000" and Home Office Project license No. 30/2290. All mice were housed in a controlled environment in the animal facility on site (Table 2.1).

Table 2.1. Controlled environment details of animal housing

Isolation and conditioning	Ventilated racking
Cage type	ICV (individual isolated cage), Tecniplast
Bedding	Grade 5, dust-free, autoclaved wood bedding (Datastand Diet Service UK)
Diet	RM1, RM3, 2919
Room temperature	19- 23°C
Room humidity	55 ± 10%
Ventilation	60-70 m^3/h

The *Dync1i1*^{G482D} and *Dync1i2*^{T172I} mutant mice were rederived at the MRC Mammalian Genetics Unit, MRC Harwell, UK. The point mutations resulted from the treatment of BALB/c males with an *N*-ethyl-*N*-nitrosourea (ENU) as described in Nolan, 2000. After recovery males were mated to C3H/HeH females in order to produce F1 (C3H/HeH x BALB/c) progeny. Subsequently frozen sperm samples with the identified mutation of interest were used for *in vitro fertilisation* (IVF) with C57BL/6J females. The animals carrying the mutations in the cytoplasmic dynein intermediate chains 1 and 2 (*Dync1i1*^{G482D} or *Dync1i2*^{T172I}) were used as founders of the colonies and treated as generation N0.

C57BL/6J mice were provided by Harlan Laboratories.

2.1.1 Breeding protocols

Mutant *Dync1i1*$^{G482D/+}$ and *Dync1i2*$^{T172I/+}$ animals were backcrossed to C57BL/6J mice with the aim of producing congenic strains or intercrossed to produce homozygous mutant animals. Furthermore, a colony of double heterozygous *Dync1i1*$^{G482D/+}$ *Dync1i2*$^{T172I/+}$ animals on a C57BL/6J background was established at the MRC Mammalian Genetics Unit, MRC Harwell, UK.

Mutant *Dync1h1*^{Loa} mouse line (Hafezparast *et al.*, 2003) was established as congenic line and maintained by crossing to C57BL/6J mice.

Timed matings were set up with a purpose of collecting embryos at a certain age. Copulation plug checking was carried out in the morning as mating usually occurred during the dark cycle in the evening. When a plug was present a male was removed from the cage and the date was recorded as day E0.5; otherwise the animals were left together to mate.

2.1.2 Genotyping protocol

DNA was extracted from ear biopsies collected from post-weaning pups as described in 2.3.1. The single point mutations introduce or destroy sequences recognizable by restriction enzymes, thus routine genotyping was performed by PCR and subsequent digestion with a restriction enzyme. The details of the DNA amplification, restriction digest, and primer sequences are shown in Table 2.2 and Appendix 10.12.1 respectively. The digested PCR products were visualised on an agarose gel (section 2.3.6) together with samples isolated from animals of known genotype. Depending on the genotype of animal distinctive patterns of bands were observed as summarised in Table 2.3.

Table 2.2. The summary of genotyping protocol
Cycling steps (denaturation of a template, annealing of primers, and extension of a product) marked in grey

Mouse line	*Dync1i1*^{G482D}	*Dync1i2*^{T172I}	*Dync1h1*^{Loa}
PCR Mix	5 µl MegaMix Gold 1 µl 10µM primer mix 1 µl DNA 3 µl H_2O	8.5 µl MegaMix Blue 1.0 µl 5µM primer mix 0.5 µl DNA	10 µl MegaMix Gold 1 µl 5µM primer mix 1 µl DNA 8 µl H_2O
Thermal cycling program	95°C for 2 min	95°C for 2 min	95°C for 5 min
	94°C for 30 s 57°C for 30 s } 35 cycles 72°C for 45 s	94°C for 30 s 60°C for 30 s } 35 cycles 72°C for 45 s	94°C for 30 s 58°C for 30 s } 35 cycles 72°C for 45 s
	72°C for 5 min	72°C for 5 min	72°C for 5 min
Restriction digest (added to the PCR reaction)	3.0 µl NEB Buffer 4 0.5 µl MboII 16.5 µl H_2O Incubated at 37°C for 2 hours	3.0 µl NEB Buffer 1 0.5 µl Tsp45I 0.3 µl BSA 16.2 µl H_2O Incubated at 65°C for 2 hours	3.0 µl NEB Buffer 1 0.5 µl RsaI 6.5 µl H_2O Incubated at 37°C for 2 hours

Table 2.3. The summary of the pattern of the restriction digest
Wildtype allele denoted as *Gene*$^{+/+}$, heterozygous as *Gene*$^{Mut/+}$, homozygous as *Gene*$^{Mut/Mut}$

Mouse line	***Dync1i1*^{G482D}**		
Genotype Bands (bp)	*Dync1i1*$^{+/+}$ 325	*Dync1i1*$^{G482D/+}$ 325, 246, 79	*Dync1i1*$^{G482D/G482D}$ 246, 79
Mouse line	***Dync1i2*^{T172I}**		
Genotype Bands (bp)	*Dync1i2*$^{+/+}$ 149, 121	*Dync1i2*$^{T172I/+}$ 270, 149, 121	*Dync1i2*$^{T172I/T172I}$ 270
Mouse line	***Dync1h1*^{Loa}**		
Genotype Bands (bp)	*Dync1h1*$^{+/+}$ 322, 226	*Dync1h1*$^{Loa/+}$ 322, 226, 187, 135	*Dync1h1*$^{Loa/Loa}$ 226, 187, 135

2.1.3 Phenotyping protocols

Behavioural phenotyping of the wildtype and *Dync1i1*$^{G482D/G482D}$ female littermates, wildtype and *Dync1i2*$^{T172I/T172I}$ female littermates was carried out at the Department of Experimental Psychology, University of Oxford by Dr Robert Deacon and Dr Samantha Line. The tests performed were:

Accelerating rotarod

Mice were placed on the rotarod whilst it was rotating at 4 revolutions per min (rpm). If the animal fell off the rod before 10 sec had elapsed, the test was restarted (if the animal fell three times, the test was ended and a score of 4 rpm was recorded). After 10 sec at 4 rpm, the rod began to accelerate at 20 rpm/min. The speed at which the rod was rotating when the animal fell off was recorded. If an animal held on to the rod and made a full revolution, it was considered to have fallen off, and the speed of rotation was recorded. The rotarod was built in-house and similar to the Ugo Basile model (7650).

Multiple Static Rods

The multiple static rods consisted of three horizontal bars attached to a shelf at one end. Animals were placed on the distal end of the first (widest) rod facing away from the shelf and the time taken for them to turn 180° (orient) and walk from the far end of the rod to the shelf (traverse) was recorded.

Wheel running

Mice were singly housed in a cage containing a running wheel (Bio-Serv Fast-Trac wheel attached to a mouse igloo) attached to a pedometer. After 24 hour the distance run, average speed and maximum speed were recorded. Testing was performed for 5 days.

Food consumption

Mice were housed individually with accesses to food (standard laboratory chow, PCD Mod; Special Diet Services, Witham, Essex, United Kingdom) and water *ad libitum*. Consumption of food and water was measured over a period of 3 days.

Glucose preference

Mice were housed individually with access to food *ad libitum*, and were provided with both water and 7.5% (w/v) glucose solution. The bottles were weighed after 24 hours and the ratio of glucose: water consumption was calculated. The test was performed on 4 consecutive days.

Locomotor Activity

Animals were placed in individual chambers for 23 hours and their locomotor activity was recorded. Testing was begun at 1 pm, with the dark phase from 7 pm to 7 am.

Burrowing

Test for burrowing was performed as described in Deacon (2006b). Briefly, mice were placed in burrows filled with 200 g of food pellets. After 1 or 3 hours the burrows were weighted and the difference from the starting weight was a measure of displaced material. Two tests were performed.

Nesting

The quality of nests built overnight was assessed in a scale from 1 to 5 as described in Deacon (2006a).

Successive alleys

The successive alleys apparatus consisted of four increasingly anxiogenic, linearly connected wooden alleys. Each alley was 45 cm in length. The alleys had the following dimensions: alley 1 = 9 cm wide, 29 cm-high walls, painted black; alley 2 = 9 cm wide, 2.5 cm-high walls, painted grey; alley 3 = 6.7 cm wide, 0.5 cm-high walls, painted white; alley 4 = 5 cm wide, 0.3 cm-high walls, painted white. A 2 cm step down led from alley 2 to alley 3, with a further 0.5 cm step down between alleys 3 and 4. The apparatus was elevated 1 m above the floor in a well-lit laboratory. Mice were placed individually at the closed end of Alley 1, facing the wall. Each trial lasted for 300 sec (5 min) and for each section the total time spent in each Alley, and the numbers of entries were recorded.

Light/Dark Box

The light/dark box task was also a test of anxiety-like behaviour. Animals were placed in the dark compartment and measurements for the latency to emerge, the number of entries to the light area and the time spent in the light area were recorded over 5 minutes.

Spontaneous alternation

Spontaneous alternation was assessed in a gray, wooden, enclosed T-maze. On each trial, the mouse was placed into the start arm facing the end wall and allowed to enter a goal arm of its own choice. The mouse was confined in the chosen goal arm for 30 sec, then placed back at the beginning of the start arm and allowed a free choice of either goal arm. Whether or not the mouse alternated was recorded. Two trials were performed per day for six days.

Sanderson Y-maze

Detailed description of a test and analysis can be found in Sanderson *et al.*, 2009. The Y-maze test consisted of training phase and a novelty preference test. During the 2 min long training mice were allowed to explore freely 2 arms of the maze (called Start and Other arm) while third arm (called Novel) was blocked. Subsequently, mice received a novelty preference test, during which animals were allowed to explore 3 arms (Start, Other, and Novel). The exploratory behaviour was assessed for 2 min, when the time spent in each arm and numbers of entries were recorded.

CatWalk XT

Mice were allowed to walk spontaneously up and down the glass CatWalk XT walkway while images were collected by a video camera placed below. Four crosses of the walkway were analysed for each animal and the data averaged. A number of parameters were examined, including regularity, base of support, size of paw prints, step phase, and speed of a swing.

2.1.4 Collection of mouse tissues

Animals were culled according to Schedule 1, which methods included exposure to CO_2 or cervical dislocation ("Guidance on Operation of Animals (Scientific Procedures Act 1986) March 2000").

2.1.4.1 Tissue harvesting

Embryonic tissues were used for the extraction of total RNA and cell cultures of primary embryonic fibroblasts. Timed matings were set up as described in section 2.1.1; embryos were harvested at day E13.5 (preparation of mouse embryonic fibroblasts – section 2.6.1) or E17.5 (RNA extraction – section 2.2.2).

For RNA extraction embryonic brain and spinal cord were collected. Furthermore, a set of tissues was collected from 6-8 weeks old C57BL/6J mice (brain, spinal cord, ovary, testis, spleen, lungs, kidney, heart, intestine, muscle, liver) and brains from adult mice dissected into cortex, cerebellum, brain stem, hippocampus and olfactory bulbs. Immediately after collecting tissues were transferred into RNase-free 1.5 ml tubes (Biopur, Eppendorf) and immersed in RNAlater reagent (Qiagen) in order to minimize RNA degradation. Tissues were stored at 4°C overnight and transferred to -80°C the next day. Similarly, neuronal tissues (spinal cord, cortex, and hippocampus) were collected from 12-13 weeks old wildtype and *Dync1i2*$^{T172I/T172I}$ male and female mice and processed according to the RNA extraction protocol (section 2.2.2).

2.1.4.2 Histological protocols

Histological analysis of whole brains was performed in collaboration with Prof. Sebastian Brandner and Jacqueline Linehan (Institute of Neurology, UCL). Whole brains from 6 months old wildtype and *Dync1i2*$^{T172I/T172I}$ female littermates were removed and fixed in 4% PFA/PBS by immersion. Tissues were then prepared prior to analysis as described in Wadsworth *et al.*, 2008. The sagittal brain sections were stained with haematoxylin and eosin (H&E) and antibodies against glial fibrillary protein (GFAP), calbindin (CALB1).

2.2 General RNA protocols

All the procedures were carried out in RNase-free conditions: reagents based on DEPC-treated water (Invitrogen) and RNAZap (Ambion) to clean all the surfaces and equipment were used.

2.2.1 Total RNA extraction using TRIreagent

Muscle and liver were found to be difficult to extract RNA from due to: *(1)* fibrous nature and an abundance of proteins, and *(2)* high content of lipids. Therefore TRIreagent (Ambion) was used and the extraction protocol was modified.

Tissues were homogenized on ice in TRIreagent (1 ml per 30 mg tissue) using a Dounce Tissue Grinder, homogenates were centrifuged in 15 ml Falcon tubes at 4°C for 30 min at 5000 x g. Cleared supernatant was transferred to a fresh tube and RNase-free Mussel Glycogen (Sigma-Aldrich) was added to a final concentration 250 µg/ml. After 5 min of incubation 0.1 ml bromo-chloro-propane (BCP, Sigma-Aldrich) per 1 ml TRIreagent was added, the mixture was shaken vigorously and incubated for 2-3 min at room temperature. Another centrifugation step followed (4°C for 30 min at 5000 x g) which resulted in separation of lysate into 3 phases. The upper aqueous phase containing RNA was carefully transferred to a fresh tube and 0.3 ml isopropanol (IPA) and 0.2 ml high salt solution (0.8 M sodium citrate, 1.2 M sodium chloride) per 1 ml TRIreagent were added. Samples were incubated for 10 min at room temperature. After centrifugation step (4°C for 30 min at 5000 x g) RNA precipitated at the bottom of the tube and was washed with 75% ethanol (VWR), volume equal to TRIreagent, and centrifuged (4°C for 30 min at 5000 x g). Supernatant was removed; another portion 75% ethanol was added (1 ml) and transferred with the pellet to an RNase-free 1.5 ml tube (Biopur, Eppendorf). Resuspended RNA was centrifuged at room temperature for 5 min at 14000 x g and supernatant carefully removed. The RNA pellet was air dried and resuspended in RNase-free water.

2.2.2 Total RNA isolation and RNA clean-up using RNeasy columns

RNeasy Mini Kit (Qiagen) was used to extract total RNA from tissues, unless stated otherwise, according to manufacturer's instructions with additional on-column DNase I digest (RNase-free DNase Set, Qiagen). The detailed protocol and working principle can be obtained online from http://www1.qiagen.com/Products /RnaStabilizationPurification/ RNeasySystem/ RNeasyMini.aspx?rp=1000291&rpg=0#Tabs=t2. Briefly, tissues were weighed and homogenized on ice in RLT buffer supplemented with β-mercaptoethanol (Sigma-Aldrich) using Dounce Tissue Grinder (Wheaton Industries INC, VWR). The amount of lysate corresponding to 30 mg tissue was transferred onto QIAshredder column (Qiagen) and centrifuged while the remaining lysate was stored in a Biopur tube (Eppendorf) in -80°C. The detailed procedure is presented in Table 2.4. Total RNA was eluted with 60 µl pre-warmed (65°C) RNase-free water and stored in -80°C for further application.

Furthermore, total RNA extracted with TRIreagent (section 2.2.1) was cleaned and treated with DNase following the manufacturer's protocol provided with the RNeasy Mini Kit. Briefly, 100 µg total RNA in a volume of 100 µl was mixed with 350 µl RLT buffer and 250 µl 100% ethanol. Samples were mixed and applied on an RNeasy column, centrifuged for 15s at 14000 x g. The filtrate was reapplied on the column and centrifuged once more. The washing steps, DNase digest, and elution are the same as described above.

Table 2.4. Details of RNA extraction from mouse tissues

	Tissue	Weight [mg]	RTL volume - homogenate	Volume of lysate used in extraction	Comments
1	Brain	200	3 ml	500 µl	Half used
2	Spinal cord	100	2 ml	500 µl	
3	Ovary	80-90	2 ml	500 µl	Both used
4	Testis	80-90	2 ml	500 µl	One used
5	Spleen	120	3 ml	600 µl	QIAshredder
6	Lung	160	3 ml	600 µl	QIAshredder
7	Kidney	120	3 ml	600 µl	One used, QIAshredder
8	Heart	120	3 ml	600 µl	QIAshredder
9	Intestine	400	4 ml	600 µl	QIAshredder
10	Muscle	150		TRIreagent – whole tissue	
11	Liver	200		TRIreagent – whole tissue	
12	Embryo	200	3 ml	600 µl	QIAshredder
13	Embryonic brain	30	1 ml	500 µl	QIAshredder
14	Em. spinal cord	10	1 ml	500 µl	QIAshredder
15	Cortex	120	2 ml	600 µl	QIAshredder
16	Cerebellum	50	1 ml	500 µl	QIAshredder
17	Brain stem	40	1 ml	500 µl	QIAshredder
18	Hippocampus	20	1 ml	500 µl	QIAshredder
19	Olfactory bulbs	10-20	1 ml	500 µl	QIAshredder

2.2.3 RNA precipitation and storage

Purified total RNA was used in downstream reactions and prepared for storage. It has been shown that RNA is best preserved as ethanol precipitate or suspended in formamide (Chomczynski, 1992). Therefore 3 volumes 100% ethanol, 0.1 volume 3M sodium acetate and 20 µg RNase-free Mussel Glycogen were added to each RNA sample and incubated overnight at -80°C. Subsequently samples were centrifuged at 4°C for 30 min at 14000 x g. Supernatant was carefully removed and washing with ice-cold 75% ethanol followed. After another centrifugation step supernatant was removed, the RNA pellet air dried and transferred to -80°C for long-term storage.

2.2.4 RNA quantification

Quantity and purity of RNA were determined using a NanoDrop® ND-1000 Spectrophotometer (Labtech) by measuring absorbance at 260 nm and 280 nm (OD_{260}, OD_{280}). The instrument was blanked against water and UV measurements of 1.4 µl RNA

samples were taken using the NanoDrop® software. Ratio values of $OD_{260/280}$ and RNA concentrations (OD_{260} 1.0 = 40 µg/ml RNA) were automatically computed by software. RNA purity was assessed by $OD_{260/280}$ ratio, with acceptable values above 1.9.

2.3 General DNA protocols

2.3.1 DNA isolation

Genomic DNA

Genomic mouse DNA was isolated from ear biopsies and used in the subsequent reactions. Tissue samples were incubated in 75 µl NaOH extracting solution (25 mM NaOH, 0.2 mM EDTA) at 98°C for 1 hour. After the incubation 75 µl Tris neutralisation buffer (40 mM Tris-HCl, pH 5.5) was added to each sample, briefly mixed and centrifuged at room temperature for 5 min at 14000 x g. The resulting supernatant was used directly in the genotyping PCR (section 2.1.2).

DNA isolation from cultured cells

DNeasy Blood & Tissue Kit (Qiagen) was used in order to extract genomic DNA from cultured mouse embryonic fibroblasts (section 2.6.1) following manufacturer's protocol. Purified DNA was then used in the genotyping PCR (section 2.1.2). DNA concentration was measured and samples were stored at -80°C.

Plasmid DNA

Plasmid DNA was isolated from *Escherichia coli* (*E. coli*) using a GenElute Plasmid Miniprep Kit (Sigma-Aldrich) and following the manufacturer's protocol. Cells were grown overnight in LB medium supplemented with 50 µg/ml kanamycin and 5 ml suspension were used in a single plasmid preparation. Briefly, cells were lysed; DNA was bound to a silica membrane, washed, and eluted with water. DNA concentration was measured and samples were stored at -80°C.

2.3.2 DNA quantification

Quantity and purity of DNA were determined using a NanoDrop® ND-1000 Spectrophotometer (Labtech) by measuring absorbance at 260 nm and 280 nm (OD_{260}, OD_{280}). The instrument was blanked against water and UV measurements of 1.4 µl DNA samples were taken using the NanoDrop® software operating on the computer. $OD_{260/280}$ ratio and RNA concentrations (OD_{260} 1.0 = 50 µg/ml dsDNA) were automatically computed by software. DNA purity was assessed by $OD_{260/280}$ ratio, with acceptable values between 1.7 – 2.0.

2.3.3 Reverse Transcription (RT)

All the reactions were performed on a DNA Engine Tetrad 2 Peltier Thermal Cycler (BioRad Laboratories).

AccuScript High Fidelity Reverse Transcriptase (Stratagene) was used in order to synthesize full length cDNA of mouse cytoplasmic dynein intermediate chain 1 and 2 from different tissues, and was chosen due to its high accuracy (http://cp.literature.agilent.com /litweb/pdf/TB108_71067.pdf). The Reverse Transcriptase (RT) reaction was set up as described in Table 2.5. The master mix containing RNA, oligo-dT primer, dNTPs and RT buffer was incubated at 65°C for 5 min and cooled to allow primer annealing, reactions were supplemented with DTT and *AccuScript HF RT* to the final volume 20 µl; negative control reactions were also prepared where the addition of the reverse transcriptase was omitted. Complementary DNAs were produced at 42°C for 45 min. Prepared cDNAs were diluted 1:10 and aliquots used in downstream reactions.

QuantiTect Reverse Transcription Kit (Qiagen) was used in order to prepare cDNAs for the Real-Time PCR (section 2.3.9). The detailed protocol and working principle can be obtained online from http://www.qiagen.com /products /pcr /quantitectpcrsystems/ quantitectrevtranscriptionkit .aspx#Tabs=t1. Following the manufacturer's instructions, 500 ng of total RNA extracted from neuronal tissues of the wildtype (*Dync1i2*$^{+/+}$) and homozygous *Dync1i2*$^{T172I/T172I}$ mice were used in a single reaction. The negative reactions, containing only RNA and reaction buffer were also prepared.

2.3.4 Polymerase Chain Reaction (PCR)

All the reactions were performed on a DNA Engine Tetrad 2 Peltier Thermal Cycler (BioRad Laboratories). A list of primers used in different applications is described in an Appendix 10.12.

PfuUltra High Fidelity DNA polymerase

In order to amplify full length cDNA of mouse *Dync1i1* and *Dync1i2* the *PfuUltra* HF DNA polymerase (Stratagene) was used according to the protocol in Table 2.5.

MegaMix Gold

MegaMix Gold (Microzone) is a ready to use double concentrated mix with optimized Hot-Start *Taq* DNA polymerase, anti-*Taq* DNA polymerase monoclonal antibodies, 400 µM dNTPs, and 6mM $MgCl_2$, in buffer with stabilizer. The reactions were set up as in Table 2.5, the annealing temperature depended on primers used.

Multiplex PCR Kit

Multiplex PCR Kit (Qiagen) provides Master Mix with Hot-Start *Taq* DNA polymerase and a unique PCR buffer containing the novel synthetic Factor MP. Thus, specifically bound primers are stabilized and an efficient extension of all primers in the reaction without optimization is enabled (details can be found at http://www.qiagen.com /products /pcr /multiplexpcrsystem /multiplexpcr .aspx#Tabs=t1). Reaction conditions used are described in Table 2.5.

Table 2.5. PCR protocols and conditions

Component	Final amount per reaction	Volume per reaction	Step	Tempera-ture (°C)	Duration	
Reverse Transcription (RT)						
Total RNA	400 ng					
10x RT buffer		2.0 µl				
Oligo dT primer	25 ng/µl					
dNTP mix	4 mM					
DTT	10 mM					
AccuScript HF RT		1.0 µl				
Nuclease-free H_2O		Up to 17 µl				
***PfuUltra High Fidelity* PCR**						
cDNA template		1.0 µl	Initial denaturation	95°C	1 min	
10x RT buffer		2.5 µl				
Primers	0.4 µM		Denaturation	95°C	30 s	} 35 times
dNTP mix	8 mM		Annealing	58°C	30 s	
$MgCl_2$	1 mM		Elongation	68°C	3 min	
PfuUltra HF		0.5 µl	Final elongation	68°C	10 min	
Nuclease-free H_2O		Up to 25 µl				
MegaMix Gold						
cDNA/DNA template		0.25 - 1.0 µl	Initial denaturation	95°C	3 min	
MegaMix Gold		5.0 µl	Denaturation	94°C	30 s	} 35 times
Primers	0.25 µM		Annealing	52 - 60°C	10 s	
			Elongation	72°C	1 - 2 min	
Nuclease-free H_2O		Up to 25 µl	Final elongation	72°C	10 min	
Multiplex PCR Kit						
cDNA template		1.0 µl	Initial denaturation	95°C	15 min	
Master Mix		10.0 µl	Denaturation	94°C	30 s	} 35 times
Primers	0.25 µM		Annealing	52 - 60°C	90 s	
Q solution		2.0 µl	Elongation	72°C	1 min	
Nuclease-free H_2O		Up to 20 µl	Final elongation	72°C	10 min	

2.3.5 PCR product purification with ethanol/salt precipitation

In order to remove the excess of primers and salts from PCR products, amplified DNA was precipitated by adding 0.1 volume 3 M sodium acetate, 0.1 volume 125 mM EDTA and 2 volumes 100% ethanol. Samples were mixed briefly, incubated at room temperature for 15 min, then centrifuged at 4°C for 30 min at 3000 x g. Solvent was initially removed by a gentle inversion of the tube, followed by further removal of any residual solvent by placing the tube inverted on absorbent tissue paper. The DNA pellet was washed with 4 volumes 70% ethanol and centrifuged for 15 min at 2000 x g. The solvent was removed as before and samples were left to air dry. Clean DNA was resuspended in nuclease-free water.

Alternatively PCR products were purified using QIAquick PCR Purification Kit (Qiagen) according to manufacturer's instructions.

2.3.6 Agarose gel electrophoresis

Appropriate volumes and concentration (%w/v) of agarose gels were prepared by dissolving agarose in 1x TBE buffer (National Diagnostic) and microwaving at high power for 1-2 minutes. The gel solution was allowed to cool slightly before the addition of ethidium bromide to final concentration 0.5 µg/ml (Sigma-Aldrich). The gel solution was then poured into a gel casting tray and left at room temperature for 30-40 min to solidify. Prior to electrophoresis DNA samples were mixed with DNA loading buffer (1:5). Electrophoresis was carried out in 1x TBE buffer at 7 V/cm at room temperature. Gels were visualised and imaged on a UV transilluminator and digital imaging system (BioRad Laboratories).

2.3.7 DNA Sequencing

Automated sequencing was carried out with the BigDye Terminator Ready Reaction Kit (Applied Biosystems) on a 3130XL Genetic Analyser (Applied Biosystems). Prior to sequencing reactions, unbound primers, primer dimers and unused nucleotide triphosphates were removed from the template PCR products using one of the methods

described in section 2.3.5. Sequencing PCRs were set up as follows:

Component	Final concentration per reaction	Volume per reaction
DNA template	30 – 50 ng	
Better Buffer		5.0 µl
Primers	0.25 µM	
BigDye Terminator		1.0 µl
Nuclease-free H_2O		Up to 15 µl

Conditions of the sequencing PCR cycling program and run parameters were:

Step	Temperature (°C)	Duration	
Denaturation	96°C	30 s	} 30 times
Annealing	50°C	15 s	
Elongation	60°C	3 min	

Parameter	Setting
Length of detector	50 cm
Polymer/gel type	POP7
Sampling rate	2.801 Hz
Injection time	7 s

Fluorescently labeled PCR products were purified by ethanol/salt precipitation and resuspended in 20 µl Hi-Di Formamide (Applied Biosystems). Before the sequencing analysis samples were incubated at 95°C for 5 min and immediately cooled on ice for several minutes. The chromatograms were analysed using Sequence Analysis 5.2 (Applied Biosystems) and BioEdit Sequence Alignment Editor v5.0.9.

2.3.8 Fragment analysis

The automated fragment analysis system uses capillary array electrophoresis to perform fragment size separation of fluorescently labeled DNA samples and calculates their sizes based on an internal standard. For fragment analysis reverse primers (section 10.12.4) were conjugated with 5-Carboxyfluorescein (5-FAM) and Multiplex PCRs were run. DNA concentration was measured and subsequently 100 ng DNA were suspended in 9 µl Hi-Di Formamide together with 0.5 µl GeneScan – Liz 1200 Size Standard (Applied Biosystems) as an internal standard. Before analysis samples were incubated at 95°C for 5 min and immediately cooled on ice for several minutes. The chromatograms obtained were

analyzed using Gene Mapper software (Applied Biosystems). Run modules on the 3130XL Genetic Analyser were as follows:

Parameter	Setting
Length of detector capillary	50 cm
Polymer/gel type	POP7
Run voltage	8500
Injection voltage	1800
Injection time	7 s
Temperature	60°C
Laser power	15

2.3.9 Quantitative Real-Time PCR (qRT-PCR)

Complement DNA was prepared as described in section 2.3.3. The cDNA was diluted 1:4 in water and this dilution was used for the template in qRTPCR reactions, which were run using Power SYBR PCR master mix (Applied Biosystems) on a 7500 Fast Real-Time PCR System (Applied Biosystems). The primers were used in reactions were: *Dync1li1* (For and Rev), *Dynlt1* (For and Rev), *Dynlt3* (For and Rev), *Dynll1* (For and Rev) *Dynll2* (For and Rev) (Appendix 10.12.5).

Ribosomal protein L13A (RPL13A) was used as the reference gene. Each reaction was run in triplicate per trial and on three independent trials. The $\Delta\Delta C_T$ of each reaction was calculated as a comparison with the average wildtype ΔC_T.

2.4 Plasmid cloning

2.4.1 Adding 3' A-overhangs

TOPO TA (Invitrogen) technology requires the presence of a terminal adenosine nucleotide in the PCR product. *PfuUltra* HF DNA polymerase lacks the terminal deoxynucleotidyltransferase (TdT) activity, which is characterized by the addition of non template-directed nucleotide(s) at the 3´ end of PCR-generated fragments (Hu, 1993). Thus, 3' A-overhangs were added to the purified PCR products (section 2.3.5) prior to the cloning reaction using *Taq* DNA polymerase. The protocol was as below and samples were incubated at 72°C for 10 min and used directly in cloning reaction.

Component	Final concentration per reaction	Volume per reaction
DNA	500 ng	
10x Reaction buffer		5.0 µl
dATPs	0.5 mM	2.5 µl
Taq DNA polymerase		0.5 µl
Nuclease-free H_2O		Up to 50 µl

2.4.2 TOPO TA cloning

TOPO TA Cloning Kit for Sequencing (Invitrogen) was used to generate clones of the mouse full length *Dync1i1* and *Dync1i2* cDNA. Samples from brain and spinal cord were prepared as described above and 4 µl DNA were ligated into pCR4-TOPO® vector (Invitrogen) according to manufacturer's instructions.

2.4.3 Transforming competent cells

TOP10 *E. coli* chemically competent cells were transformed with 6 µl of ligation reaction according to the manufacturer's protocol. Clones were selected on Luria Broth Agar (Sigma-Aldrich) plates containing 50 µg/ml kanamycin. Additionally, 40 µl 20 mg/ml stock solution of X-Gal (Sigma-Aldrich) in DMF (Sigma-Aldrich) was spread on each plate to facilitate the selection of transformants. Plates were incubated overnight at 37°C and single colonies selected the next day for further expansion in antibiotic supplemented Luria Broth (Sigma-Aldrich).

2.4.4 Analysing transformants

Bacterial colonies which remained white in the presence of the X-Gal were inoculated on a 96-well plate in 200 µl LB with 50 µg/ml kanamycin and incubated at 37°C with shaking. Cell suspension was left at 37°C for 2 hours in order to initiate bacterial growth and then used as a template in a PCR based screen. Inserts were amplified in 30 µl reaction using MegaMix Gold (section 2.3.4) and the vector specific primer pair M13F – M13R (Appendix 10.12.2). The PCR products were run on a 0.7% agarose gel; DNA was purified by ethanol/salt precipitation and sequenced.

2.4.5 Glycerol stocks

Colonies selected for further expansion were grown overnight in 5 ml LB containing 50 µg/ml kanamycin, at 37°C with shaking at 250 rpm. The following day 800 µl of the culture was mixed with 200 µl of autoclaved glycerol (Sigma), mixed and stored in -80°C.

2.5 General protein protocols

2.5.1 Total protein extraction from mouse tissue

Mice were culled by a cervical dislocation, brains were extracted from skulls, weighed, and homogenised in ice-cold 0.1% Triton X-100/TBS (50 mM Tris-HCl, 150 mM NaCl, pH 7.6) buffer supplemented with Halt Protease and Phosphatase Inhibitor Cocktail (Thermo Scientific) (10% w/v). The homogenate was centrifuged at 4°C for 20 min at 14 000 x g, supernatant transferred to a fresh cooled 1.5 ml tube, and protein concentration measured as described in section 2.5.3.

2.5.2 Total protein extraction from cultured cells

Cells were counted (section 2.6.2.2) and seeded on 6-well plates (Corning). Plates were placed on ice, culturing medium aspirated and cells were washed with 1 ml ice cold D-PBS (without Ca^{2+}/Mg^{2+}). Depending on density of a culture, 200 µl (MEFs) or 500 µl (HEK293T, section 2.6.7) RIPA buffer (50 mM Tris-HCl pH 7.5, 150 mM NaCl, 1% deoxycholate, 0.1% SDS, 1% NP-40) supplemented with Halt® Cocktail was applied per well and cells were scraped with a sterile cell scraper. The lysate was transferred into a sterile chilled 1.5 ml tube and 0.5 µl Benzonase (Roche) was added in order to shear genomic DNA. Samples were incubated on ice for 15 min, centrifuged at 4°C for 15 min at 14 000 x g, and supernatant transferred to a fresh chilled 1.5 ml tube. The concentration of protein was measured (section 2.5.3); samples were stored at -80°C.

2.5.3 Protein quantification

Protein concentration was measured using DC Protein Assay (Bio-Rad) in microplate format following manufacturer's instructions. Briefly, samples were prepared in triplicate (5 µl per well) on a 96-well plate, incubated with relevant reagent and absorbance at 650 nm was measured. BSA at known concentrations (0.2, 0.4, 0.6, 0.8, 1.0, 2.0 mg/ml) was used as a protein standard and the concentration of protein in the samples was calculated from a standard curve. Prepared lysates were used in western blotting (section 2.5.4).

2.5.4 Western blotting

Protein separation and transfer onto polyvinylidene fluoride membranes (PVDF, ImmobilonP, Milipore) were performed using NuPAGE electrophoresis system and following manufacturer's instructions; all the details can be found in the 'NuPAGE Technical Guide' (Invitrogen). In order to detect phosphorylated proteins buffers based on TBS were used instead of PBS.

2.5.4.1 Protein denaturation

Protein samples were mixed with NuPAGE LDS Sample Buffer (4x, Invitrogen) containing NuPAGE Reducing Agent (10x, Invitrogen) or 2% β-mercaptoethanol, heated at 70°C for 10 min, and loaded on a polyacrylamide gel.

2.5.4.2 Polyacrylamide gel electrophoresis (Nu-PAGE)

Proteins were separated using 4-12% NuPAGE Novex Bis-Tris precast gels (1.5 mm thick, Invitrogen) and NuPAGE MOPS SDS Running Buffer (20x, Invitrogen). Electrophoresis was performed at 160 V for 60-90 min. SeeBlue Plus2 Pre-Stained Standard (Invitrogen) was loaded together with samples in order to facilitate visualisation.

2.5.4.3 Protein transfer

Immediately after the electrophoresis proteins were transferred to pre-wet PVDF membrane using XCell II Blot Module (Invitrogen). The cassette was filled with 1x NuPAGE Transfer Buffer (20x, Invitrogen) containing 20% methanol and transfer was carried out for 2 hours at 35 V.

2.5.4.4 Immunodetection

After the transfer PVDF membranes were dried and blocked in 5% HS/TBS or 5% BSA/PBS buffer for 1 hour at room temperature. Primary antibodies (Appendix 10.11) were diluted in 5% HS/TBS or 5% BSA/0.05% Tween-20/PBS and incubated at 4°C overnight. Membranes were washed several times in relevant buffers containing 0.05% Tween-20 and incubated with infrared IRDye - labeled secondary antibodies (LI-COR) diluted in 5% HS/0.05% Tween-20/TBS or 5% BSA/0.05% Tween-20/PBS for 1 hour. After washing membranes were kept in TBS or PBS and imaged using Odyssey system (LI-COR). During all the steps membranes were kept on a horizontal shaker.

2.5.4.5 Image acquisition and analysis (Odyssey)

Membranes were visualised using Odyssey Imager (LI-COR), which allowed detection of a fluorescent signal in the near infra-red range of spectrum. The intensity settings where adjusted for individual channels in order to achieve an optimal signal.

2.6 Mammalian cell culture

2.6.1 Isolation of mouse embryonic fibroblasts (MEFs)

The protocol used for the isolation of mouse primary fibroblasts has been modified from Reznikoff *et al.* (1973). A pregnant female was sacrificed at day E13.5 *post coitum* by cervical dislocation, embryos were separated and kept in Leibovitz's L-15 GlutaMAX I medium (Gibco, Invitrogen) on ice prior to processing. Head and visceral organs were removed and remaining tissues were minced using razorblades and suspended in 1.5 ml 0.05% Trypsin (Gibco, Invitrogen) in Dulbecco's PBS (with Ca^{2+}/Mg^{2+}) supplemented with DNase I (200U, Invitrogen). Tissues were incubated at 37°C for 20 min, transferred into 4 ml warm culturing medium (D-MEM GlutaMAX I supplemented with 10% FBS and 1/100 (v/v) penicillin/streptomycin). Remaining pieces of tissue were allowed to settle to the bottom of a 15 ml Falcon tube while cell suspension was transferred into cell culture flasks and plated as P0 (P75, Nunc). Fresh medium was added the next day, and cells were split when grown to subconfluency (section 2.6).

2.6.2 Culturing condition

All procedures were carried out in a tissue culture hood with aseptic technique. Unless stated otherwise, medium and supplements used throughout culture were ordered from Gibco, Invitrogen:

- Dulbecco's Modified Eagle Medium (D-MEM with GlutaMAX I, 4500 mg/L D-Glucose, Sodium Pyruvate)
- 10% Fetal Bovine Serum (Qualified, preferentially from Australia or New Zealand).

Cells routinely were cultured in P75 flasks (Nunc) and grown in a DH Autoflow Air-Jacketed Incubator (Nuaire) at 37°C in a humid environment and 5% CO_2.

2.6.2.1 Cell splitting

Cultured cell grew in monolayer and the level of confluency was assessed qualitatively under a phase contrast microscope (Olympus CK40); cells were split 1:3 (MEFs) or 1:5 (HEK293T) once they grew to subconfluency. All the buffers were used pre-warmed to 37°C. First medium was removed by aspiration and cell layer was washed gently with Dulbecco's PBS (without Ca^{2+}/Mg^{2+}). Subsequently cells were incubated with TrypLE Express for 3-4 min at 37°C and once detached, as visible 'cloudy' suspension, warm full D-MEM was added in order to dilute TrypLE Express. The surface of the flask was gently washed with medium and the cells were transferred to a sterile Falcon tube. At this stage cells were counted and seeded on sterile glass coverslips for immunofluorescence based experiments (sections from 2.6.3 to 2.6.6), 6-well plates (Corning) for protein extraction (section 2.5.2), plated on a new flask at appropriate density, or frozen.

2.6.2.2 Cell counting

Harvested cells were counted using Bright-Line Hemacytometer (Warner-Lambert Technologies) with the improved Neubauer rulings. Briefly, ruling pattern covers 9 mm^2, boundary lines are the main lines in the groups of 3. The central square millimeter is ruled into 25 groups of 16 small squares, each group separated by triple lines, the middle one of which represents the boundary. The ruled surface is 0.10 mm below the cover glass, so that the volume over each of the 16 small squares is 0.00025 mm^3 (Figure 2.1).

Cell suspension was thoroughly mixed and 20 µl was applied on the counting chamber. The cells were counted using a phase contrast microscope at magnification 100x and the number of cells observed in 4 large corner squares, each corresponding to 1 mm^2, was recorded. In case of a diluted sample, when fewer than 100 cells were observed, additional squares were taken into account (more details can be found on http://www.ruf.rice.edu /~bioslabs /methods /microscopy /cellcounting.html). The density of the culture, expressed as the number of cells per ml, was calculated as follows:

$$density = \frac{number - of - cells - counted}{number - of - squares - counted} \times 10^4 \times (dilution)$$

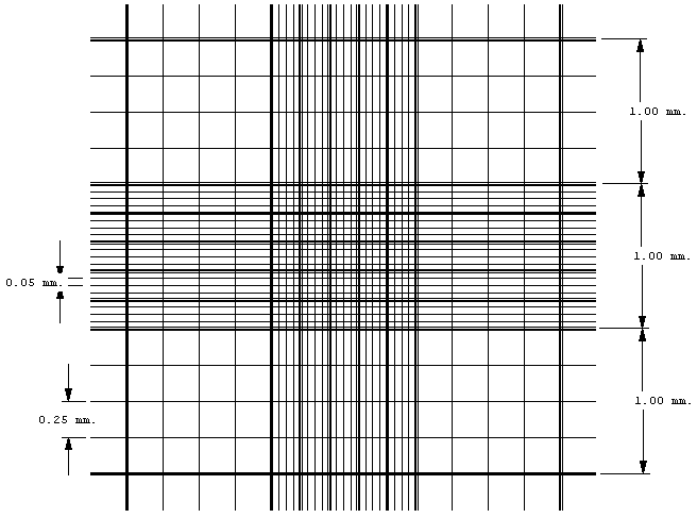

Figure 2.1. A pattern of an improved Neubauer ruling
The area is marked by triple boundary lines which mark area of 1 mm^2; single lines divide the area further into squares of 0.0625 mm^2 and 0.0025 mm^2; adapted from http://www. hausserscientific.com/ hausserbrightlinedirect.htm

2.6.2.3 Cell freezing and storage

A frozen stock of MEFs was prepared with cells at a second passage (P2). Cells were harvested as described above and centrifuged for 5 min at 230 x g. Supernatant was gently removed and cell pellet was reconstituted in cold freezing mix containing FBS/DMSO in ratio 9:1. Cell suspension was transferred to 1.8 ml cryogenic vials (Corning) as 1 ml aliquots containing between $5x10^6$ – 10^7 cells. The cryovials were placed in 'Mr. Frosty' (Nalge Nunc) and stored in the - 80°C overnight. The cryo-freezing container filled

with isopropanol allowed freezing the cells slowly by reducing the temperature at approximately 1°C per minute. For long term storage frozen vials were transferred to liquid nitrogen tank.

2.6.2.4 Cell thawing

Frozen vials were removed from liquid nitrogen storage and thawed quickly (1-2 min) in a 37°C water bath. Once thawed, cells were resuspended in few ml warm medium and pelleted by centrifugation for 5 min at 230 x g. The supernatant containing DMSO was aspirated and cells were gently resuspended in fresh medium and plated on P75 culture flask (Nunc).

2.6.3 Golgi complex reassembly after microtubule disruption

Mouse embryonic fibroblasts (MEFs) were seeded on sterile glass coverslips (12 mm diameter, 1.5 mm thick, VWR) placed in a 24-well plate (TTP). In order to obtain the optimal level of confluency (approximately 70%) cells were counted and 4 x 10^4 cells were plated per each coverslip. The next day standard medium was replaced with standard D-MEM containing 15 mM HEPES (Gibco, Invitrogen) and the cells were left on ice for 30 min. Subsequently, the medium was replaced with D-MEM-HEPES containing 10 µg/ml nocodazole (Sigma – Aldrich) and cells were returned to the incubator for 3 hours. Cells were washed 3 times with the standard medium, fixed at 0 min or returned to the incubator for a recovery. Nocodazole treated and untreated control cells were fixed after 20 min, 50 min and processed as described in section 2.6.8.

2.6.4 EGF uptake assay

MEFs were seeded on glass coverslips in 4-well plates. Before experiment, fibroblasts were washed with D-PBS (without Ca^{2+}/Mg^{2+}) and incubated in serum-free D-MEM for 2 hours at 37°C. After starvation cells were stimulated with 50 ng/ml Alexa Fluor 555 conjugated EGF (Molecular Probes, Invitrogen) in the serum-free D-MEM supplemented with 0.1% BSA (Sigma – Aldrich) for 1 hour at 4°C. The medium was replaced with fresh serum-free D-MEM and the EGF – AF 555 trafficking was followed at 37°C over the time course. Before fixing cells were washed with ice-cold D-PBS (without Ca^{2+}/Mg^{2+}) and fixed

at 0 min, 15 min, 30 min, 45 min, and 60 min after the EGF – AF 555 internalization. Coverslips were processed as described in section 2.6.8.

2.6.5 Infection with *Salmonella enterica* ser. Typhimurium

All the experiments were carried out in collaboration with Prof. David Holden at Imperial College London and detailed description of bacterial strains used and culturing conditions can be found in Beuzon *et al.*, 2000 and Guignot *et al.*, 2004.

Briefly, on a day before the infection MEFs were seeded on sterile round coverslips (12 mm diam., VWR), 2 x 10^4 cells per a coverslip; WT and *SifA*$^-$ strains were grown in LB supplemented with appropriate antibiotics. The next day bacteria were diluted in fresh LB and cultured at 37°C with shaking to an OD_{600} between 1.8 – 2.0. Prior to infection standard D-MEM was replaced with EBSS (Sigma – Aldrich) and 2.5 µl bacterial suspension were added per well. The infection was allowed to proceed for 15 minutes at 37°C in 5% CO_2. The cells were washed 3 timed with standard D-MEM containing 100 µg/ml gentamicin and incubated for 1 hour in D-MEM with 100 µg/ml gentamicin, after which time the concentration of antibiotic was decreased to 20 µg/ml gentamicin in standard D-MEM. Eight hours post infection cells were washed with D-PBS (without Ca^{2+}/Mg^{2+}), fixed, and processed for immunofluorescence (section 2.6.8).

2.6.6 Induction of stress granules

Fibroblasts were seeded on sterile round coverslips (12 mm diam., VWR), 4 x 10^4 cells per a coverslip. The next day cells were washed with standard D-MEM and incubated at 37°C in 5% CO_2 for 1 hour or 45 min in D-MEM containing 1 µM thapsigargin (Calbiochem) or 200 µM sodium arsenate (SA, VWR) respectively. Cells were washed with D-PBS (without Ca^{2+}/Mg^{2+}) and fixed or 50 µg/ml emetine (Sigma – Aldrich) was added and cells were incubated for another hour, washed with D-PBS (without Ca^{2+}/Mg^{2+}), and fixed.

2.6.7 Plasmid transfection of HEK293T

HEK293T (ATCC® number: CRL-11268™) were derived from HEK293 cell line, which was generated by transformation of human embryonic kidney (HEK) cell cultures with sheared adenovirus 5 DNA (Sena-Esteves *et al.*, 1999). Those cells (kind gift from Ms Astrid Authier, UCL) were cultured as described (section 2.6.2) and used to express isoforms of dynein intermediate chains fused with green fluorescent protein (GFP) (kind gift from Dr M. Hafezparast, University of Sussex). 48 hours before transfection with adequate plasmid DNA cells were split 1:5, seeded into 6-well plates (Corning) and cultured in standard D-MEM. Lipofectamine 2000 (LFA, Invitrogen) and plasmid DNAs were made up in 50 µl Opti-MEM I Reduced Serum Medium (Gibco, Invitrogen) in ratio 3 µg DNA per 10 µl LFA. After 5 min incubations DNA and LFA were mixed together (100 µl final volume) and incubated for 20 min at room temperature to form DNA:LFA complexes. Transfection mix was added to wells; the medium was replaced after 4 hours and cells were cultured for 48 hours before protein extraction (section 2.5.2).

2.6.8 Immunofluorescence

Although general principles of staining cells with antibodies prior to a fluorescence microscopy analysis were followed, the particular steps differed depending on antibody used or cell structures of the interest. Therefore, the details of each staining are summarised in Table 2.6 while the dilutions of antibodies can be found in Appendix 10.11. Briefly, at the end of each experiment MEFs grown on glass coverslips were washed with D-PBS (without Ca^{2+}/Mg^{2+}), fixed, washed, permeabilised in order to expose intracellular structures. Then cells were blocked in buffers containing serum proteins, stained with primary antibodies against a target protein, washed at least twice, incubated with secondary antibodies conjugated with fluorescent dyes (Alexa Fluor, Rhodamine Red-X), washed again, and mounted on microscope slides. During incubation steps coverslips were kept in a humidified chamber in order to minimize evaporation. Slides were analysed as described in section 2.7, and kept at -20°C. Phosphate buffer saline (PBS) was used in washing steps and to prepare solutions, unless stated otherwise.

Table 2.6. The detailed protocol of immunostaining of cultured mouse embryonic fibroblasts, reagents used and time of each step are specified

Headings correspond to experiments carried out as described in sections 2.6.3, 2.6.4, 2.6.5, and 2.6.6; EGF – epidermal growth factor, PFA – paraformaldehyde, RT – room temperature, AF – Alexa Fluor dye, PBS – phosphate buffer saline, D-PBS – Dulbecco's PBS (without Ca^{2+}/Mg^{2+}), BSA – bovine serum albumin, NHS – normal horse serum, RR-X – Rhodamine Red-X, DAPI – 4',6-diamidino-2-phenylindole (DNA stain), NaN_3 – sodium azide, host species annotated as follows: (d) – donkey, (g) – goat, (m) – mouse, (r) – rat, (rb) – rabbit, æ – denotes an antigen for secondary antibody; N/A – not applicable; h – hours

Step	Cytoplasmic dynein	Golgi complex reassembly	EGF uptake	*Salmonella* Typhimurium	Stress granules
Fixative	-20°C methanol 10 min at RT	-20°C methanol 10 min at RT	4% PFA/PBS 10 min at RT	4% PFA/PBS 15 min at RT	4% PFA/PBS 15 min at RT
Permeabi-lising buffer			0.1% Triton X-100/ PBS, 5 min at RT	0.1% saponin/PBS 5 min at RT	-20°C methanol 10 min at RT
Blocking buffer	5% HS (NaN_3)/ PBS, 1 h at RT	5% HS(NaN_3)/ PBS, 1 h at RT	1% BSA/PBS 30 min at RT		5% HS (NaN_3)/ PBS, 1 h at RT
Primary antibody (targeted to)	(m)IC74, (rb) DIC1, (rb) DIC2(60) in 0.1% saponin / 10% NHS/PBS 2 h at RT	(rb) GIANTIN in 0.1% saponin /10% NHS/PBS 2 h at RT	(m) α-TUBULIN AF 488 in 1% BSA/PBS 45 min at RT	(r) LAMP-1 (m) GM130 in 0.1% saponin / 10% NHS/PBS 2 h at RT	(m) G3BP (g) TIAL1 in 5% NHS/D-PBS 2 hours at RT
Washing buffer	0.1% saponin/ PBS	0.1% saponin/ PBS	PBS	0.1% saponin/ PBS	PBS
Secondary antibody (species and dye)	d-æ-m AF 633 d-æ-rb AF 546 in 0.1% saponin / 10% NHS/PBS 45 min at RT	d-æ-rb AF 546 in 0.1% saponin / 10% NHS/PBS 45 min at RT	N/A	d-æ-r RR-X d-æ-m AF 647 in 0.1% saponin / 10% NHS/PBS 45 min at RT	d-æ-m AF 488 d-æ-g AF 546 in 0.05% saponin / 5% NHS/PBS 45 min at RT
Washing buffer	0.1% saponin /PBS, PBS	0.1%saponin /PBS, PBS	N/A	0.1% saponin /PBS PBS, H_2O	PBS H_2O
Additional staining	(m) α-tubulin AF 488 in D-PBS 45 min at RT	(m) α-tubulin AF 488 in D-PBS 45 min at RT	DAPI/PBS 5 min at RT	N/A	N/A
Washing buffer	PBS, H_2O	PBS, H_2O	PBS	N/A	N/A
Mounting	ProLong Gold Antifade + DAPI	ProLong Gold Antifade + DAPI	Dako Fluorescence Mounting Medium	Mounting medium	ProLong Gold Antifade + DAPI

2.7 Data acquisition and analysis

2.7.1 Epifluorescence microscopy

Cellular phenotypes were observed and scored blindly using fluorescence microscopes (BX50 Olympus, Axioplan 2, Zeiss) equipped with relevant filters.

2.7.2 Laser scanning confocal microscopy (LSCM)

Confocal fluorescent images were acquired with a Zeiss LSM 510 META confocal microscope equipped with 4 lasers: diode (405 nm) 25 mW, Argon (458, 477, 488, 514 nm) 30 mW, HeNe1 laser (543 nm) 1 mW; HeNe2 laser (633 nm). Depending on the fluorescent dyes applied a signal from four channels could be viewed using Plan-Neofluar 40x/1.3 Oil DIC, and Plan-Apochromat 63x/1.4 Oil DIC objectives after applying immersion oil (IMMERSOL 518F, Zeiss). All the pictures used in further analysis were taken with a resolution of 1024 x 1024 pixels.

2.7.3 Colocalisation analysis using Volocity®

Volocity® software (Perkin Elmer, version 5.5) was used to measure the colocalisation as an overlap of intensities of 2 fluorescence markers. In order to obtain more accurate values images were processed using built-in Volocity Quantitation tasks:

- Find objects using intensity ('Green' channel corresponding to MTs staining)
- Exclude objects smaller that 1000 μm^2
- Fill holes in objects
- Make ROIs from objects
- Remove noise from objects (median filter with 'fine' matrix)

Images were then cropped (segmentation) and tresholded Pearson's correlation and Mander's coefficients were calculated as described in Barlow *et al.* (2010).

2.7.4 CellProfiler image-based analysis

Digital fluorescence images obtained with a laser scanning confocal miscroscope (LSCM) were analysed with CellProfiler software (v1.0.5122) (Carpenter *et al.*, 2006;Vokes and Carpenter, 2008). 'LSM' images were converted to 8-bit 'tiff' files; different settings were used depending on the structures of interest as presented below.

Golgi complex reassembly

Membranes of the Golgi stacks were identified as objects positive for staining with anti-giantin antibodies based on the intensity of a fluorescent signal and their parameters measured.

EGF uptake analysis pipeline

All the pictures representing distinct timepoints were analysed using the same settings: endosomes labelled with fluorescent EGF-AF 555 were identified based on intensity of the signal and their parameters measured. Due to a weak signal from the membrane bound EGF-AF 555 (cells imaged at 0 min) the threshold values of intensity were decreased to 0.19 as marked in blue (*). Furthermore, in order to measure the rate of displacement of EGF-AF 555 containing endosomes a ratio was measured between the number of perinuclear objects to total number of objects in a cell; a boundary of the perinuclear region was marked at a distance equal to a radius of a nucleus as marked in green (**).

Detection of stress granules

Cytoplasmic stress granules were identified as objects positive for staining with anti-G3BP antibodies (stress granules marker) based on the intensity of a fluorescent signal and their parameters measured.

Table 2.7. Detailed protocol of image analysis using CellProfiler (nex page).

Pipeline module	Analysis parameters	Golgi complex	EGF	Stress granules
Load Images	Load files	Text – Regular expression	Text-Exact match	Text-Exact match
	Call images within CellProfiler	OrigBlue	OrigBlue	OrigBlue
	Type of files	Individual images	Individual images	Individual images
Color To Gray	Call the image to be converted to Gray	OrigBlue	OrigBlue	OrigBlue
	Convert the color image	Split	Split	Split
	SPLIT options: call the image that was red/ green/ blue	OrigRed/ OrigGreen/ OrigBlue	OrigRed/ OrigGreen/ OrigBlue	OrigRed/ OrigGreen/ OrigBlue
Identify Primary Automatic	Call the images to process	OrigBlue	OrigBlue	OrigBlue
	Call the objects identified by this module	Nuclei	Nuclei	Nuclei
	Typical diameter of objects, in pixel units	100, 1000	20, 300	50, 1000
	Discard objects outside the diameter range	Yes	Yes	Yes
	Try to merge too small objects with nearby larger objects	Yes	Yes	Yes
	Discard objects touching the border of the image	Yes	Yes	Yes
	Select an automatic thresholding method	Robust Background Global	Otsu Adaptive	Otsu Adaptive
	Threshold correction factor	1	1	1
	Lower and upper bounds on threshold, in the range [0,1]	0.3, 1	0.1, 1	0.2, 1
	Size of smoothing filter, in pixel units		10	10
	Suppress local maxima within this distance		10	10
	Fill holes in identified objects	Yes	Yes	Yes
Identify Secondary	Call the primary objects to create secondary objects around	Nuclei	Nuclei	Nuclei
	Call the objects identified by this module	Cells	Cells	Cells
	Method to identify the secondary objects **	Propagation	Propagation/ Distance-B	Propagation
	Call the images to be used to find the edges of the secondary objects	OrigGreen	OrigGreen	OrigRed
	Select an automatic thresholding method	Otsu Global	Otsu Global	Otsu Global

	Threshold correction factor Lower and upper bounds on threshold, in the range [0,1] For PROPAGATION/DISTANCE, enter the regularization factor/ number of pixels by which to expand the primary objects	1 0.05, 1 5	1/ 1 0.05, 1/ 0.05, 1 5/ Nuclear radius	1 0.05, 1 5
Identify Tertiary Subregion	Call the larger identified objects Call the smaller identified objects Call the new subregions	Cells Nuclei Cytoplasm	Cells Nuclei Cytoplasm	Cells Nuclei Cytoplasm
Crop	Call the image to be cropped Call the cropped image For RECTANGLE + ELLIPSE, shape to crop into The cropping pattern - each image cycle cropped	OrigRed Cropped Cytoplasm	OrigRed Cropped Cytoplasm Individually	OrigGreen Cropped Cytoplasm Individually
Identify Primary Automatic	Call the images to process Call the objects identified by this module Typical diameter of objects, in pixel units Discard objects outside the diameter range Try to merge too small objects with nearby larger objects Discard objects touching the border of the image Select an automatic thresholding method Two-class or three-class thresholding Minimize the weighted variace Assign pixels in the middle intensity class to Threshold correction factor Lower and upper bounds on threshold, in the range [0,1] Method to distinguish clumped objects Method to draw dividing lines between clumped objects Size of smoothing filter, in pixel Suppress local maxima within this distance	Cropped Golgi 12, 500 Yes Yes No Otsu Global Three classes Yes Foreground 1 0.3, 1 Laplacian of Gaussian Propagate 8 10	Cropped Vesicles 2,50 Yes No No Otsu Adaptive 1 0.25, 1 / 0.19, 1* Intensity Intensity 1 2	Cropped SG 10, 100 Yes Yes No Otsu Adaptive 1 0.26, 1 Intensity Intensity 2 1
Measure Object Area Shape	Call the objects to measure	Nuclei, Golgi	Nuclei, Vesicles	SG
Export To Excel	Objects to export	Golgi, Image	Nuclei, Vesicles	SG

2.7.5 Statistical analysis

Statistical analysis of data was performed using GraphPad Prism v5.02 for Windows (GraphPad Software, San Diego California USA, www.graphpad.com). Depending on the structure of data, results were presented as mean value and standard error (SEM), a mean and standard deviation (SD), or median with interquartile range (IQR). All the tests reported two-tailed p-value; the difference was considered statistically significant for $p< 0.05$.

Categorical data (sections 3.4.2, 3.4.3, and 4.4.4.2) were analysed in a format of a contingency table and two-sided p-values were reported with Fisher's exact (for 2x2 tables) or Chi-squared (χ^2) (2x4 tables) test. In addition, the distribution of genotypes was analysed with Chi-square (χ^2) test by comparison of observed to expected frequencies. This option was available from GraphPad QuickCalcs (http://secure. graphpad.com /quickcalcs/index.cfm). The test combines the observed and expected values into a variable, Chi-square (χ^2). The Chi-square (χ^2) is calculated by squaring the difference between observed and expected values for each category and dividing it by the expected value; final operation is the sum of the resulting divisions $((\text{Observed} - \text{Expected})^2 /\text{Expected})$. The reported two-tailed p value with N-1 degrees of freedom expresses whether the data observed are sampled from the expected distribution.

Dependence of two variables was measured by calculating Pearson correlation coefficient (r). The correlation coefficient quantifies the direction and magnitude of correlation ranging from 1.0 (perfect correlation) to -1.0 (lack of correlation). In addition, squared coefficient (R^2) was also calculated, which corresponds to a fraction of the variance in X that can be explained by variation in Y (the fraction of the variance in the two variables that is 'shared').

3. Characterisation of mutant mouse lines carrying single point mutations in the cytoplasmic dynein intermediate chains 1 and 2 (*Dync1i1*^{G482D} and *Dync1i2*^{T172I})

3.1 Introduction

A genes' function can be studied by analysing a phenotype of mutant organisms. Thus functions of the cytoplasmic dynein intermediate chains 1 and 2 in mouse were investigated by a genotype driven approach: single point mutations causing amino acid change in *Dync1i1* and *Dync1i2* genes were identified, mutant mouse lines established, and their behavioural phenotype assessed.

The MRC Mammalian Genetics Unit, Harwell, UK is one of the centres which has a large-scale ENU mutagenesis program. The archives of DNA and frozen sperm isolated from the F1 male progeny of mutagenised mice have been established which enabled genotype-based screens for ENU-induced mutations (Nolan *et al.*, 2002). Currently the archive consists of over 10,000 DNA samples from individual mice; mutant lines that have been characterized can be found in the MouseBook database (http://www.mousebook.org).

To identify mutations in the *Dync1i1* and *Dync1i2,* denaturing HPLC screening of the DNA archive was performed by Dr Gareth T. Banks as previously described (Quwailid *et al.*, 2004). Briefly, genomic samples of mutagenised DNA were used as templates to amplify regions of exonic sequences, which then were analysed for the presence of heteroduplex regions indicating a potential mutation. Identified samples were then sequenced in order to confirm the nucleotide change. Subsequently, mutant mouse lines were rederived at the MRC Harwell.

3.2 Identification of a missense point mutation in the cytoplasmic dynein intermediate chain 1

A substitution was identified in exon 14 of the *Dync1i1* gene (MGI: 107743): G to A in position 1628 (ENSMUST00000115555, Ensembl NCBI m37) which causes a glycine to aspartic acid change in the protein at residue 482 (ENSMUSP00000111217, Ensembl NCBI m37). The novel allele was annotated as *Dync1i1*^{G482D} and was not found in any of the inbred mouse strains (NCBI refSNP). The mutation was predicted to lie within the 5th WD domain and a conservation profile was analysed using Jalview 2.6.1 (Waterhouse *et al.*, 2009). Representative protein sequences were acquired from GenBank (except for *Mus musculus)* and aligned using the MUSCLE algorithm (Edgar, 2004) (Figure 3.1). Because in the vertebrate lineage whole genome duplication occurred ('2R'), there are 2 genes coding intermediate chains 1 and 2 and the protein sequences of DYNC1I1 are highly similar amongst the vertebrates (Pfister *et al.*, 2006). Furthermore, conservation and alignment quality scores for each residue in the alignment, and the consensus sequence were calculated. The value of conservation was expressed as a number of physico-chemical properties of each amino acid, which were conserved: the higher the score the more conserved residue (Livingstone and Barton, 1993). The alignment quality rated the likelihood of observing a mutation in the particular position (from 0 to 1). Furthermore, potential effects of the mutation on protein function were calculated using a 'Sorting Intolerant From Tolerant' algorithm (SIFT Blink, http://sift.jcvi.org) (Kumar *et al.*, 2009). Briefly, position-specific scoring matrices (PSI-BLAST) were used to score sequence homology and the best BLAST hits from each organism were retrieved in order to build a multiple sequence alignment. Based on gathered data substitution matrices were calculated for each amino acid in the query sequence.

Glycine at position 482 could be found in most of the taxonomic groups (from vertebrates to fungi), and in all the sequences aligned but the *Drosophila* homologue cDIC. A value of the conservation score was average (4 out of 11) while the alignment quality was scored over 0.68. The G482D mutation causes a change of glycine, classified as 'tiny' and 'hydrophobic' into 'small' and 'negatively charged' aspartic acid (Livingstone and Barton,

1993). Furthermore, 85 homologous sequences (median conservation value 2.92) were retrieved by SIFT Blink, and G482D substitution was predicted to affect protein function.

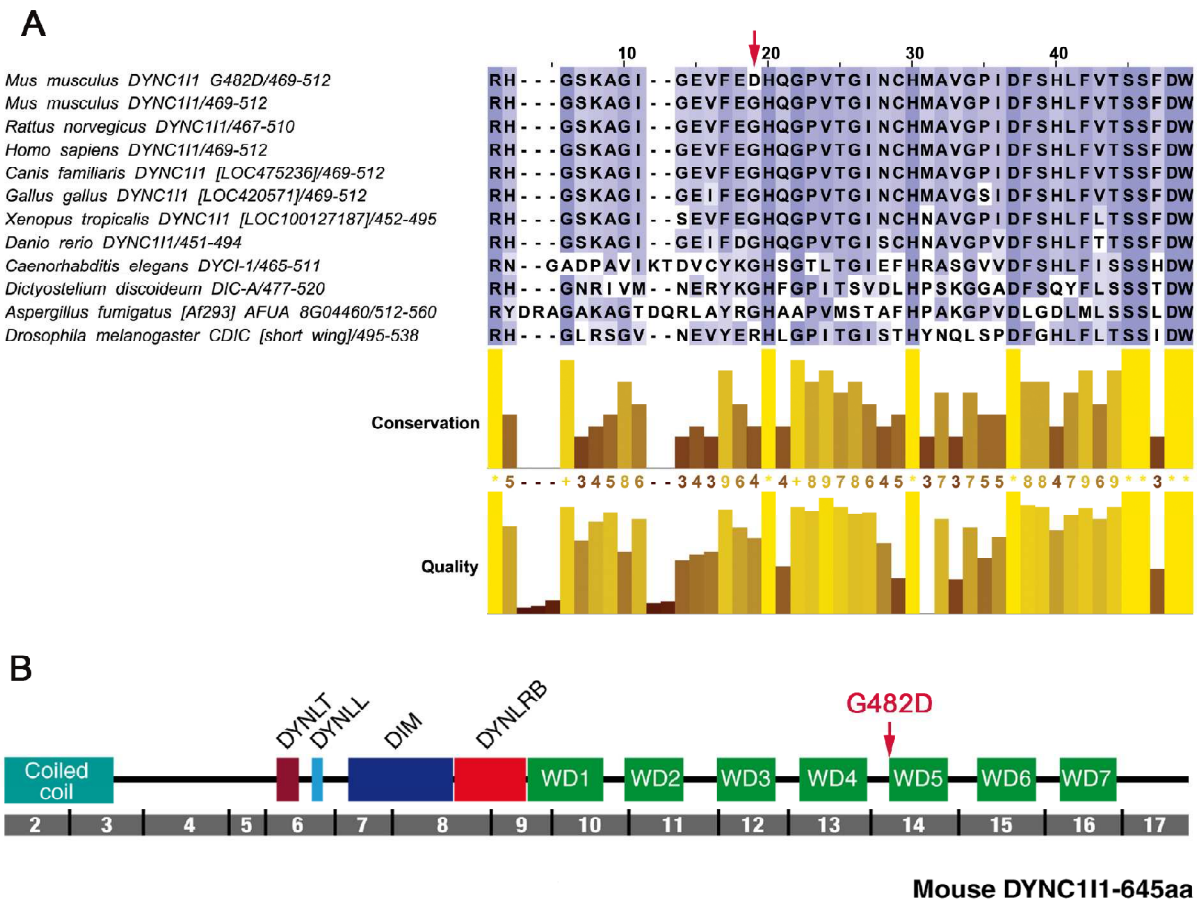

Figure 3.1. Bioinformatics analysis of DYNC1I1 protein sequence

A. An alignment of representative sequences of cytoplasmic dynein intermediate chain 1 generated by Jalview 2.6, annotated by a species name and gene/protein symbol followed by amino acids displayed; residues and corresponding histograms shaded based on their conservation; the ENU induced mutation in the mouse sequence marked with an arrow; sequences aligned retrieve from GenBank except for mouse: *Mus sp*. (mouse) ENSMUSP00000111217, *Rattus sp* (rat) NP_062107, *Canis sp*. (dog) XP_850340 - predicted in locus LOC475236, *Homo sp*. (human) NP_004402, *Gallus sp.* (chicken) XP_418672 – predicted in locus LOC420571, *Xenopus sp*. (frog) NP_001106382 – hypothetical locus LOC100127187, *Danio sp*. (zebra fish) NP_001073459, *Drosophila sp*. (fruit fly) NP_477075, *Caenorhabditis sp*. (nematode) NP_501038, *Dictyostelium sp*. (amoeba) XP_640973; *Aspergillus sp.* (fungus) XP_747253 – predicted locus AFUA_8G04460

B. Schematic representation of mouse DYNC1I1 protein (isoform A); protein domains marked as blocks, numbered exons marked in grey, position of the G482D mutation marked with arrow; DYNLT – binding region of Tctex-1 dynein light chain, DYNLL – binding region of LC8 dynein light chain, DIM – intermediate chain dimerisation domain, DYNLRB – binding domain of Roadblock dynein light chain, WD domains marked in green

3.3 Identification of a missense point mutation in the cytoplasmic dynein intermediate chain 2

Another coding mutation from the ENU-treated DNA archive was identified in an exon 7 of the *Dync1i2* gene (MGI: 107750). The mutation changes C in position 664 into T (NM_001198872, GenBank), and causes substitution of threonine with isoleucine in position 172 (NP_001185801, GenBank), thus the novel allele was annotated *Dync1i2*^{T172I}. This substitution was not found in genomic sequences of the known mouse strains (NCBI refSNP). The new mutation was predicted to change threonine located in the dynein light chain LC8 binding domain (DYNLL) (Nyarko and Barbar, 2011) and this region of the intermediate chain was analysed *in silico*. The multiple alignments of representative protein sequences showed high similarity of the DYNC1I2 sequence within the vertebrates, but not with other taxonomic groups (Figure 3.2).

Based on the alignment generated with the MUSCLE algorithm, threonine 172 is well conserved in vertebrates. However, there are dynein intermediate chain sequences obtained from 2 fungi (*Laccaria bicolor, Coprinopsis cinerea*, order *Agaricales*), which contain isoleucine in the corresponding position. The value of the conservation score was average (5 out of 11) while the alignment quality was scored 0.49. The T172I mutation causes a change of threonine, classified as 'small' and 'hydrophobic' into 'aliphatic' and 'hydrophobic' Isoleucine (Livingstone and Barton, 1993). Moreover, 80 homologous sequences deposited in the GenBank (median conservation value 2.95) were retrieved by SIFT Blink (http://sift.jcvi.org), and the T172I substitution was predicted to be a tolerated variant.

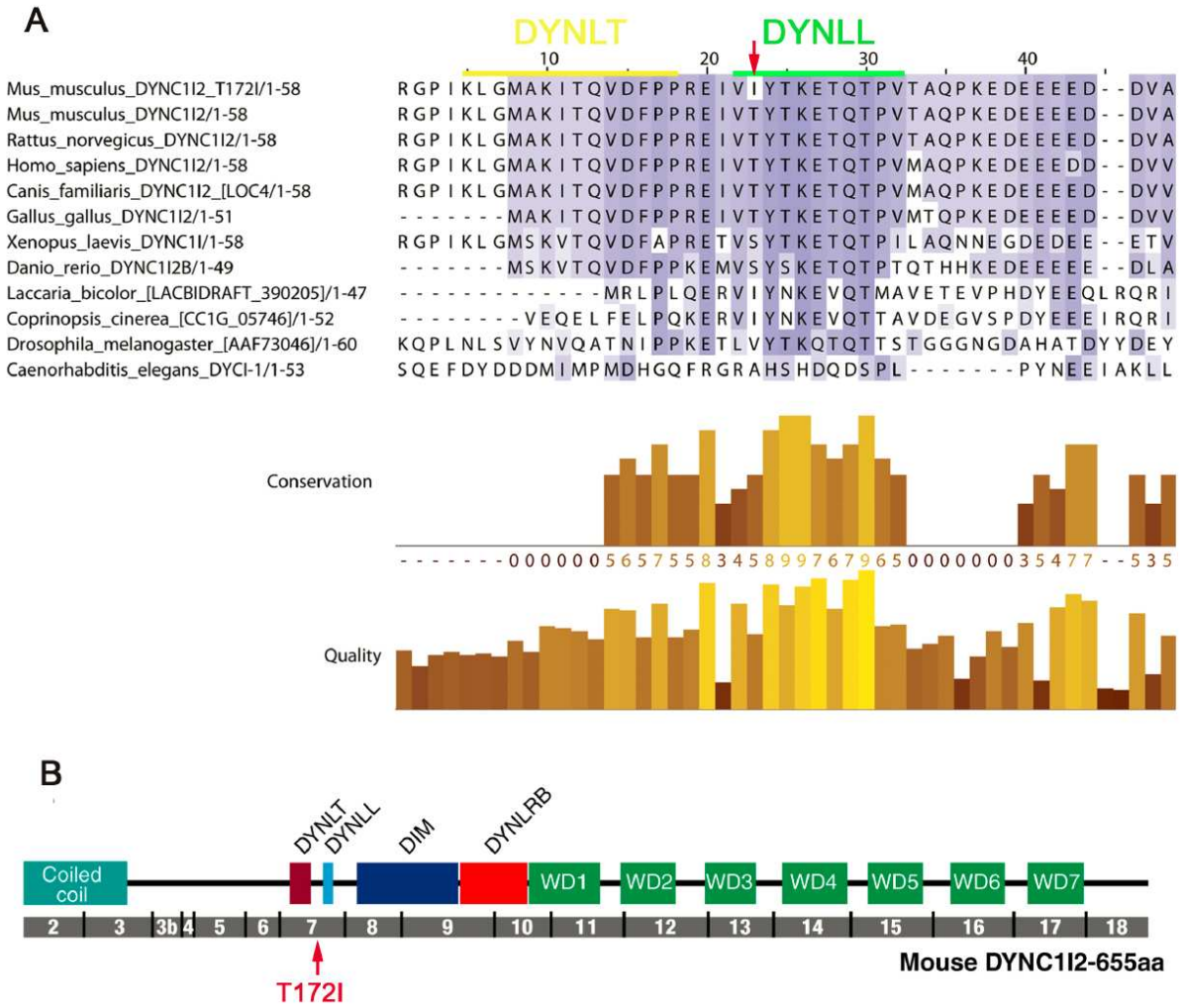

Figure 3.2. Bioinformatics analysis of DYNC1I2 protein sequence

A. An alignment of representative sequences of cytoplasmic dynein intermediate chain 2 generated by Jalview 2.6, annotated by a species name and a gene/protein symbol, amino acids displayed correspond to a light chain binding domain; residues and plots shaded based on their conservation; the ENU induced mutation in the mouse sequence marked with an arrow; sequences aligned retrieve from GenBank: *Mus sp*. (mouse) NP_001185801, *Rattus sp* (rat) NP_446332, *Homo sp*. (human) NP_001369, *Canis sp*. (dog) XP_859859 - predicted in locus LOC478797, *Gallus sp*. (chicken) NP_001006519, *Xenopus sp*. (frog) AAH86292 – due to discrepancy either gene nor locus are known, *Danio sp.* (zebra fish) XP_690115 – there are 2 loci annotated as *Dync1i2*, *Aspergillus sp*. (fungus) XP_747253 – predicted locus AFUA_8G04460, *Coprinopsis sp.* (fungus) XP_001831675, *Laccaria sp.* (fungus) S238N-H82 XP_001883758, *Drosophila sp.* (fruit fly) AAF_73046, *Caenorhabditis sp*. (nematode) NP_501038; light chains binding sites marked with yellow (DYNLT) and green (DYNLL) as in Nyarko and Barbar, 2011

B. Schematic representation of mouse DYNC1I2 protein (isoform D); protein domains marked as blocks, numbered exons marked in grey, position of the T172I mutation marked with arrow; DYNLT – binding region of Tctex-1 dynein light chain, DYNLL – binding region of LC8 dynein light chain, DIM – intermediate chain dimerisation domain, DYNLRB – binding domain of Roadblock dynein light chain, WD domain marked in green

3.4 Results

3.4.1 Breeding and maintenance of the *Dync1i1*^{G482D} mutant mouse line

A mouse line carrying a coding mutation identified in the *Dync1i1* gene was rederived by IVF. The heterozygous mice (*Dync1i1*$^{G482D/+}$) were bred to C57BL/6J mice in order to produce a congenic line, or intercrossed to produce progeny. The wildtype (*Dync1i1*$^{+/+}$) and homozygous (*Dync1i1*$^{G482D/G482D}$) littermates were subsequently tested for any phenotypic differences (section 3.4.4). The genotyping of pups was performed 3 weeks after birth (after weaning) by PCR and restriction digest as described (section 2.1.2). Due to space limitations the *Dync1i1*^{G482D} mutant mouse line was established and maintained by Dr A. Acevedo-Arozena at the MRC Mammalian Genetics Unit, Harwell, UK. Thus, no detailed data regarding the inheritance of this mutation are available.

3.4.2 Breeding and maintenance of the *Dync1i2*^{T172I} mutant mouse line

The colony of *Dync1i2*^{T172I} mice was kept at the MRC Prion Unit animal facility in controlled conditions. The colony was founded by heterozygous (*Dync1i2*$^{T172I/+}$) animals rederived by IVF of C57BL/6J oocytes with sperm from C3H/HeH x BALB/c male (F1 progeny, section 2.1.1). Because of the mixed genetic background the 'founders' were annotated as generation N0. The genotyping of all progeny was performed 3 weeks after birth (post weaning), thus any cases of pup lethality were not detected. The *Dync1i2*^{T172I} colony was bred in 2 regimes:

- backcrossing heterozygous (*Dync1i2*$^{T172I/+}$) animals with mice from C57BL/6J stock in order to segregate other point mutations and obtain a homogenous genetic background (up to N5),
- intercrossing heterozygous (*Dync1i2*$^{T172I/+}$) animals in order to produce cohorts of wildtype (*Dync1i2*$^{+/+}$) and homozygous (*Dync1i2*$^{T172I/T172I}$) mice.

3.4.2.1 C57BL/6J backcross

We chose to breed the mutant line with a C57BL/6J inbred strain, which is well characterised and widely used. In addition, the C57BL/6J strain was classified as good breeder producing from 3 to 7 pups per litter (http://www.jax.org). The generations were numbered with each cross to C57BL/6J mouse, and starting from generation N5 mice were considered congenic, containing only 3% of paternal BALB/c DNA ($0.5^5 = 0.03125$; Keays *et al.*, 2006).

The transmission of the *Dync1i2*^{T172I} allele was analysed in cohorts consisting of animals at N1, N5, and N7 and its distribution tested with Chi-square (χ^2) test (GraphPad, section 2.7.5). The detailed summary is shown in Table 3.1. There were 29 mice (14 males, 15 females, p=0.8527) obtained from 5 litters in the first backcross (generation N1), which gave on average 5.8 pups per litter. The distribution of the genotypes was as expected for an independently segregating allele (1:1), and 16 wildtype (*Dync1i2*$^{+/+}$) and 13 heterozygous (*Dync1i2*$^{T172I/+}$) animals were weaned (p=0.5775).

Further breeding brought 74 mice from 12 litters at N5 with the average size of 6.2 pups. There was no difference in the sex ratio (36 males, 38 females, p=0.8162), but the number of wildtype (*Dync1i2*$^{+/+}$, n=27) mice was lower compared with heterozygote (*Dync1i2*$^{T172I/+}$, n=47, p=0.0201). However, the disproportion was observed neither in any other generation, nor when both the gender and the genotype were taken into account (p=0.1285).

Furthermore, at N7 there were 29 mice born in 4 litters, which corresponded to 7.2 pups per litter. As before, both parameters tested did not differ from expected frequencies: there were 17 males and 12 females weaned (p=0.3532), out of which 12 carried wildtype allele (*Dync1i2*$^{+/+}$) and 17 were heterozygous (*Dync1i2*$^{T172I/+}$) (p=0.3532).

The increase in the number of pups born in following generations may be the result of removing other random mutations, which might affect fertility or embryogenesis.

Table 3.1. Summary of the mutant *Dync1i2*^{T172I} allele distribution and litter statistics calculated for backcrosses to the C57BL/6J strain

Numbers of mice weaned in each generation (N1, N5, N7) split by genotype and gender; the distribution analysed with Chi-square (χ^2) test, df=1; genotypes correspond to wildtype (*Dync1i2*$^{+/+}$) and heterozygous (*Dync1i2*$^{T172I/+}$) animals; in case of statistically significant difference at N5 the expected number of pups given in brackets; for **p<0.05 in bold**

Generation	Genotype	Males	χ^2, p	Females	χ^2, p	Mice	χ^2, p	Litter size
N1	*Dync1i2*$^{+/+}$	8	0.2860	8	0.0670	16	0.3100	5.8
	Dync1i2$^{T172I/+}$	6	0.8527	7	0.7963	13	0.5775	
N5	*Dync1i2*$^{+/+}$	14	1.7780	12	3.7890	26 (37)	5.4050	6.2
	Dync1i2$^{T172I/+}$	22	0.1824	25	0.0516	47 (37)	**0.0201**	
N7	*Dync1i2*$^{+/+}$	7	0.5290	5	0.3330	12	0.8620	7.2
	Dync1i2$^{T172I/+}$	10	0.4669	7	0.5637	17	0.3532	

3.4.2.2 Intercross

A group of mice was bred by crossing heterozygous (*Dync1i2*$^{T172I/+}$) mice in order to produce cohorts of wildtype (*Dync1i2*$^{+/+}$) and homozygous (*Dync1i2*$^{T172I/T172I}$) littermates, which were used in phenotyping (sections 3.4.4 and 3.4.4.4) and molecular analysis (sections 2.6.1, 4.4.3 and 6.4.2). Mice intercrossed came from various generations and the inheritance of the *Dync1i2*^{T172I} mutation was analysed at N0 (colony founders), N5, and N7. Assuming a Mendelian distribution of alleles, 3 classes of genotypes were expected to segregate in ratio 1:2:1, corresponding to wildtype (*Dync1i2*$^{+/+}$), heterozygous (*Dync1i2*$^{T172I/+}$), and homozygous (*Dync1i2*$^{T172I/T172I}$) animals (Table 3.2).

Cohort at N0 was bred by crossing mice rederived by IVF thus there was a high proportion of C3H/HeH x BALB/c genetic material. There were 136 mice born and weaned from 20 litters, which corresponds to 6.8 pups per litter on average. The gender ratio did not vary from normal (p=0.1227) with a small dominance of females (n=77) over males (n=59). The distribution of genotypes was as expected: 27 wildtype (*Dync1i2*$^{+/+}$), 79 heterozygote (*Dync1i2*$^{T172I/+}$), and 30 homozygote (*Dync1i2*$^{T172I/T172I}$) mice (p=0.1579). However, when only females were compared there were more heterozygous (*Dync1i2*$^{T172I/+}$) and fewer wildtype (*Dync1i2*$^{+/+}$) animals (p=0.0464). The trend however, was not observed in other cohorts thus it was not considered relevant. Those mice were selected for a long time observation experiment, as described in 3.4.2.3.

A larger cohort, which consisted of 204 animals, was bred by crossing heterozygous (*Dync1i2*$^{T172I/+}$) animals at N5. There were 38 litters, with the average of 5.4 pups per litter. The equal numbers of males (n=102) and females (n=102) were weaned (p=1.000), the genotype ratios were also normal (p=0.5059), with 44 wildtype (*Dync1i2*$^{+/+}$), 105 heterozygous (*Dync1i2*$^{T172I/+}$), and 55 homozygous (*Dync1i2*$^{T172I/T172I}$) animals. That cohort was regarded as congenic and subjected to a battery of behavioural test (sections 3.4.4 and 3.4.4.4).

The last set of intercrosses produced 53 animals at N7. There were 9 litters born with the average of 5.8 pups per litter, consisting of 26 males and 27 females (p=0.8907). As previously, the allele distribution in the cohort followed the classic 1:2:1 pattern: for 16 wildtype (*Dync1i2*$^{+/+}$), 20 heterozygous (*Dync1i2*$^{T172I/+}$), and 17 homozygous (*Dync1i2*$^{T172I/T172I}$) animals the reported value of p=0.1992. Although there seemed to be a disproportion of genotypes between females, more mice would be required to confirm this observation. The cohort was sacrificed and samples collected for further analysis (sections 2.1.4.1 and 6.4.2).

We also showed that homozygous (*Dync1i2*$^{T172I/T172I}$) mice at N1 were fertile and 1 litter of 8 pup was produced.

Table 3.2. Summary of the mutant *Dync1i2*^{T172I} allele distribution and litter statistics for intercrosses
Numbers of mice weaned in each generation (N0, N5, N7) split by genotype and gender; the distribution analysed with Chi-square (χ^2) test, df=2, genotypes correspond to wildtype (*Dync1i2*$^{+/+}$), heterozygous (*Dync1i2*$^{T172I/+}$), and homozygous (*Dync1i2*$^{T172I/T172I}$) animals; in case of a noticeable difference at N0 the expected number of pups given in brackets; for **p<0.05 in bold**

Generation	Genotype	Males	χ^2, p	Females	χ^2, p	Mice	χ^2, p	Litter size
N0	*Dync1i2*$^{+/+}$	15	0.0510	12 (19.2)	6.1430	27	3.6910	6.8
	Dync1i2$^{T172I/+}$	30	0.9749	49 (38.5)	**0.0464**	79	0.1579	
	Dync1i2$^{T172I/T172I}$	14		16		30		
N5	*Dync1i2*$^{+/+}$	23	0.3530	21	1.1180	44	1.3620	5.4
	Dync1i2$^{T172I/+}$	52	0.8382	53	0.5719	105	0.5059	
	Dync1i2$^{T172I/T172I}$	27		28		55		
N7	*Dync1i2*$^{+/+}$	7	0.6920	9	3.000	16	3.2260	5.8
	Dync1i2$^{T172I/+}$	11	0.7074	9	0.2231	20	0.1992	
	Dync1i2$^{T172I/T172I}$	8		9		17		

3.4.2.3 Long term observation experiment

In order to investigate effects of the *Dync1i2*^{T172I} mutation on survival of animals long term observation was carried out until mice reached the age of over 24 months. An experimental cohort consisted of 13 wildtype (*Dync1i2*$^{+/+}$), 10 homozygous (*Dync1i2*$^{T172I/T172I}$) males, 11 wildtype (*Dync1i2*$^{+/+}$) females, and 12 homozygous (*Dync1i2*$^{T172I/T172I}$) females, all at N0. The mice were kept undisturbed and any events of death or sickness were noted. During the course of the experiment 11 out of 24 wildtype (*Dync1i2*$^{+/+}$) mice died, out of which 6 were males, 5 females. It was noted that first deaths were amongst males at age of 220 days, while all the wildtype females lived over 400 days. This phenomenon might have been caused by fighting or increased level of stress, which is quite common for male mice. Amongst homozygous (*Dync1i2*$^{T172I/T172I}$) mice, only 5 out of 22 died by the end of the experiment, out of which 2 were males and 3 were females. Similar to the wildtype cohort, mutant *Dync1i2*$^{T172I/T172I}$ males were noted to die slightly earlier than *Dync1i2*$^{T172I/T172I}$ females.

The results of the aging experiment were analysed in GraphPad using Kaplan-Meier survival plot, on which the fractional survival (Y) was depicted as a function of time (Days) (Figure 3.3). The survival curves were compared with Log-rank (Mantel-Cox) and Gehan-Breslow-Wilcoxon tests, when the latter gave more weight to deaths at early time points; the details are shown in Table 3.3. The survival of the wildtype (*Dync1i2*$^{+/+}$) animals did not differ from homozygous (*Dync1i2*$^{T172I/T172I}$), although the trend towards longer lifespan was observed in the cohort of mutant mice (p=0.0790). However, it was less distinct when males and females were compared separately, thus in order to validate this differences a larger cohorts would need to be observed for a longer period of time.

In conclusion, the lifespans of the wildtype (*Dync1i2*$^{+/+}$) and homozygous (*Dync1i2*$^{T172I/T172I}$) littermates were comparable with the median lifespan reported for inbred strains: 908/914 days (males/females respectively) for C57BL/6J, 707/785 days (males/females) for BALB/cByJ, and 714/659 (males/females) for C3H/HeJ (Yuan *et al.*, 2009). Furthermore, the survival curves might be affected by the presence of additional ENU-induced mutations (generation N0).

Table 3.3. The summary of the long term observation of aged cohorts of wildtype (*Dync1i2*$^{+/+}$) and homozygous (*Dync1i2*$^{T172I/T172I}$) mice

Numbers of mice annotated as **Dead** or **Alive** at the end of the experiment, split by genotype and gender; the survival curves compared with 2 tests (details above), reported values of Chi-square (χ^2) df=1; genotypes correspond to wildtype (*Dync1i2*$^{+/+}$), and homozygous (*Dync1i2*$^{T172I/T172I}$) animals

Genotype			Males	Females	Total Mice
Dead	*Dync1i2*$^{+/+}$		6	5	11
	Dync1i2$^{T172I/T172I}$		2	3	5
Alive	*Dync1i2*$^{+/+}$		7	6	13
	Dync1i2$^{T172I/+}$		8	9	17
Log-rank (Mantel-Cox) test		χ^2	1.6630	1.7970	3.0860
		p	0.1972	0.1801	0.0790
Gehan-Breslow-Wilcoxon test		χ^2	1.6920	1.4590	3.5420
		p	0.1933	0.2271	0.0598

Figure 3.3. Kaplan-Meier survival curves of wildtype (*Dync1i2*$^{+/+}$) and homozygous (*Dync1i2*$^{T172I/T172I}$) mice (next page)

Survival represented as percent of alive animals as a function of time (Days); a horizontal red line at Y=50; n – number of animals (next page)

A. The survival curve of wildtype (*Dync1i2*$^{+/+}$) and homozygous (*Dync1i2*$^{T172I/T172I}$) males, the median lifespan of males from inbred strains marked with vertical lines: BALB/cByJ – red, C3H/HeJ – black
B. The survival curve of wildtype (*Dync1i2*$^{+/+}$) and homozygous (*Dync1i2*$^{T172I/T172I}$) females; the median lifespan of females from inbred strains marked with vertical lines: BALB/cByJ – red, C3H/HeJ – black
C. The survival curve of wildtype (*Dync1i2*$^{+/+}$) and homozygous (*Dync1i2*$^{T172I/T172I}$) animals

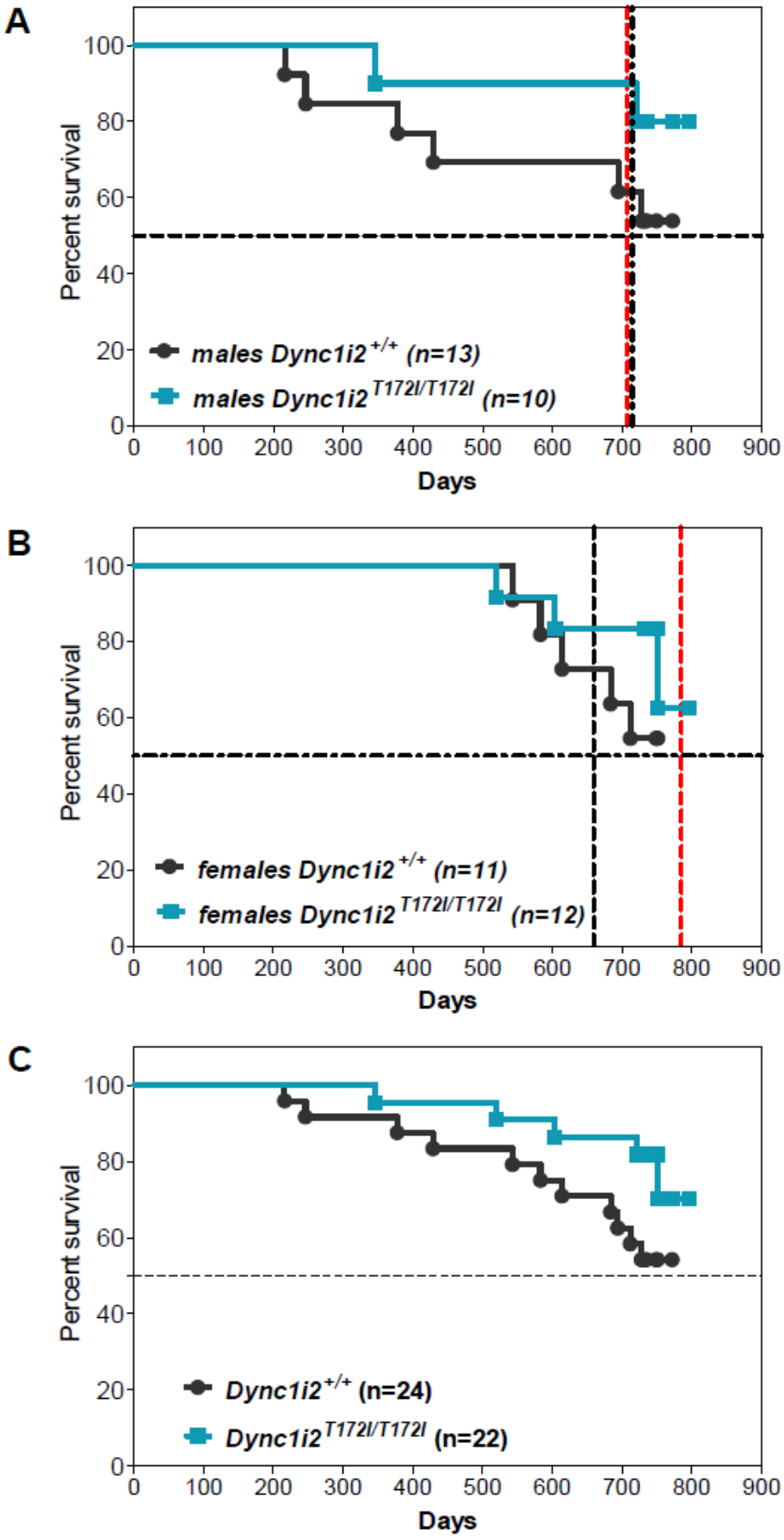
A
Percent survival
Days
males Dync1i2 +/+ (n=13)
males Dync1i2 T172I/T172I (n=10)
B
Percent survival
Days
females Dync1i2 +/+ (n=11)
females Dync1i2 T172I/T172I (n=12)
C
Percent survival
Days
Dync1i2 +/+ (n=24)
Dync1i2 T172I/T172I (n=22)

3.4.3 Breeding of double heterozygous mutant mice (*Dync1i1*$^{G482D/+}$ *Dync1i2*$^{T172I/+}$)

In addition to mutant lines carrying single mutations (*Dync1i1*^{G482D}, *Dync1i2*^{T172I}) a cohort of 10 male and 10 female double heterozygous mice (*Dync1i1*$^{G482D/+}$ *Dync1i2*$^{T172I/+}$) was established at MRC Harwell, which then were timed mated. Embryos harvested at E13.5 – 14.5 were used to prepare MEF cell lines, DNA from remaining tissues was extracted and genotyping performed following standard protocol (section 2.1.2). There were 92 embryos collected from 9 litters, with an average of 10 embryos per litter. The genotypes of pups were expected to segregate as independent alleles (1:1:2:2:4:2:2:1:1) and all 9 genotypes were observed (Table 3.4). The Chi-square (χ^2) equaled 9.696 and the two-tailed p value with 8 degrees of freedom equaled 0.2870. Thus the presence of both alleles (*Dync1i1*^{G482D} and *Dync1i2*^{T172I}) did not affect fertility or early embryogenesis of mutant animals. On the other hand, in case of mild or low penetrance phenotype a bigger sample would be required. The cell lines homozygous for one or both mutations were used as a model to study the effects of mutations in the cytoplasmic dynein intermediate chains on a cellular level (section 4.1).

Table 3.4. Distribution of progeny genotypes from double heterozygous matings (*Dync1i1*$^{G482D/+}$ *Dync1i2*$^{T172I/+}$)

Genotypes are organized by allele of each gene; there were 92 pups and all 9 genotypes observed; expected numbers based on ratio of independently segregating alleles in brackets; in bold marked numbers of embryos/cell lines with the genotypes of interest: wildtype (*Dync1i1*$^{+/+}$ *Dync1i2*$^{+/+}$), *Dync1i1*^{G482D} homozygous (*Dync1i1*$^{G482D/G482D}$ *Dync1i2*$^{+/+}$), *Dync1i2*^{T172I} homozygous (*Dync1i1*$^{+/+}$ *Dync1i2*$^{T172I/T172I}$), double homozygous (*Dync1i1*$^{G482D/G482D}$ *Dync1i2*$^{T172I/T172I}$)

Allele	*Dync1i1*$^{+/+}$		*Dync1i1*$^{G482D/+}$		*Dync1i1*$^{G482D/G482D}$	
Dync1i2$^{+/+}$	**6**	**(5.75)**	10	(11.5)	**2**	**(5.75)**
Dync1i2$^{T172I/+}$	20	(11.5)	21	(23)	9	(11.5)
Dync1i2$^{T172I/T172I}$	**6**	**(5.75)**	12	(11.5)	**6**	**(5.75)**

3.4.4 Behavioural phenotypes of the *Dync1i1*^{G482D} and *Dync1i2*^{T172I} mouse lines

Detailed behavioural phenotyping of *Dync1i1*^{G482D} and *Dync1i2*^{T172I} mutant mouse lines was performed by Dr Robert Deacon and Dr Samantha Line at Department of Experimental Psychology, University of Oxford. All the tests were performed blind to genotype on age-matched littermates. Two phenotyping cohorts consisted of:

- 10 wildtype (*Dync1i1*$^{+/+}$), 10 homozygous (*Dync1i1*$^{G482D/G482D}$) females at N4 C57BL/6J background
- 14 wildtype (*Dync1i2*$^{+/+}$), 14 homozygous (*Dync1i2*$^{T172I/T172I}$) females at N5 C57BL/6J background.

Few of the tests performed required prolonged periods of time when mice were transferred to individual cages, therefore females were chosen over males in order to avoid fighting often observed in males which were rehoused (Deacon *et al.*, 2002). A variety of tests was used to assess motor function and coordination, general metabolic performance, species specific behaviour, anxiety-like behaviour, and learning and memory. The specific behaviour may be affected by many factors and at least two tests for similar behaviour were performed; their outcomes are grouped as mentioned.

3.4.4.1 Analysis of motor function and coordination

The motor performance of mutant mouse lines was tested on accelerating rotarod, multiple static rods, and during voluntary wheel running.

The accelerating rotarod is a simple task commonly used to detect any neurological deficits, which would affect a coordination or muscle function. However, any differences in fatigue or body weight may affect the outcome (Brooks and Dunnett, 2009).

The *Dync1i1*^{G482D} and *Dync1i2*^{T172I} mice were tested on the accelerating rotarod at the age of 14 months old and the speed of the rod when an animal fell was recorded. The performance of the *Dync1i1*$^{G482D/G482D}$ mice (14.4 ± 1.4 rpm) was comparable with the wildtype (*Dync1i1*$^{+/+}$) littermates (15.5 ± 1.4 rpm) (p=0.5567). Similarly, *Dync1i2*$^{T172I/T172I}$

mice fell at the same speed as wildtype (*Dync1i2*$^{+/+}$) littermates (p=0.7853). The detailed measurements and statistical analysis are summarised in Table 3.5 and Figure 3.4A.

Multiple static rods are used to detect defects in coordination and balance. The test consists of three horizontal bars, each thinner than the previous. Time, in which an animal turns (**Orient**) and runs to a shelter (**Traverse**) gives a measure of the overall performance. At the same time posture or use of tail can be observed and noted (Mattsson *et al.*, 1997).

In a sequence of three rods the performance of *Dync1i1*$^{G482D/G482D}$ females (n=10) did not vary from wildtype *Dync1i1*$^{+/+}$ littermates (n=10), neither in the time to turn around (Orient, p=0.1068), nor in the time to walk from the far end of the rod to the shelf (Traverse, p=0.5210). However, mutant *Dync1i1*$^{G482D/G482D}$ mice turned faster on the wider rod (Rod1) than wildtype *Dync1i1*$^{+/+}$ (unpaired *t*-test with Welch's correction, p=0.0319).

The task did not show differences in *Dync1i2*$^{T172I/T172I}$ females (n=14) when compared with wildtype *Dync1i2*$^{+/+}$ littermates (n=14) in turning time (Orient, p=0.8814) and crossing time (Traverse, p=0.2610). The mutant *Dync1i2*$^{T172I/T172I}$ animals were on average slightly faster on wide rods (Rod 1, Rod 2).

Interestingly though, the multiple static rods revealed that *Dync1i2*^{T172I} cohort was much slower at leaving rods than a cohort of the *Dync1i1*^{G482D} mice: it took 53.9 ± 13.2 s for wildtype *Dync1i2*$^{+/+}$ to cross the rod while the mean time of wildtype *Dync1i1*$^{+/+}$ mice was 8.6 ± 2.8 s. The reason for this discrepancy might be the origin of those colonies or underlying genetic variation (sections 3.4.1 and 3.4.2). The detailed measurements and statistical analysis are summarised in Table 3.5 and Figure 3.4B.

Table 3.5. Performance of the *Dync1i1*^{G482D} and *Dync1i2*^{T172I} mice in motor tasks

Measurements from each task shown as mean ± SEM (standard error of the mean); on the left (vertical) shown the task performed, the results of statistical analysis shaded; genotypes annotated as follows: wildtype *Dync1i1*$^{+/+}$, homozygous *Dync1i1*^{G482D} (*Dync1i1*$^{G482D/G482D}$), wildtype *Dync1i2*$^{+/+}$, homozygous *Dync1i2*^{T172I} (*Dync1i2*$^{T172I/T172I}$); n - number of animals tested except for: *n=8, **n=13, ***n=12; rpm – rotations per minute, s – seconds, a.u. – arbitrary units; F(DFn, DFd) – F ratio calculated for DFn: degrees of freedom for the numerator, DFd: degrees of freedom for the denumerator; RM ANOVA – repeated measures analysis of variance; $ - in addition turning on Rod1 was tested with umpaired *t*-test with Welch's correction for unequal variance; for **p<0.05 in bold**

Task			*Dync1i1*$^{+/+}$ n=10	*Dync1i1*$^{G482D/G482D}$ n=10	*Dync1i2*$^{+/+}$ n=14	*Dync1i2*$^{T172I/T172I}$ n=14	Statistics
Rotarod [rpm]			15.5 ± 1.4	14.4 ± 1.4	12.9 ± 1.9	13.5 ± 1.3	Unpaired *t*-test
			p=0.5567		p=0.7853		
Multiple Static Rods	Rod 1 [s]	Orient$	13.6 ± 3.6	4.2 ± 1.1	16.7 ± 8.1	16.6 ± 8.1	Two-way RM ANOVA
			p=0.0319				
		Traverse	8.6 ± 2.8	6.4 ± 1.3	53.9 ± 13.2	32.6 ± 10.7	
	Rod 2 [s]	Orient	7.2 ± 2.1	9.0 ± 2.2	8.4 ± 3.4	7.9 ± 3.9	
		Traverse	3.9 ± 0.6	3.5 ± 0.5	28.1 ± 9.8	16.0 ± 3.9	
	Rod 3 [s]	Orient	19.9 ± 4.5	12.8 ± 2.8	20.1 ± 3.8	18.4 ± 3.8	
		Traverse	9.9 ± 1.3	9.4 ± 2.2	53.3 ± 11.1	53.1 ± 9.6	
		Orient	F(1, 36)=2.8810, p=0.1068		F(1, 52)=0.0227, p=0.8814		
		Traverse	F(1, 36)=0.4285, p=0.5210		F(1, 52)=1.3200, p=0.2610		
Wheel running	Day 1 [a.u.]	Distance	7.9 ± 2.9	5.0 ± 2.0	7.0 ± 1.7**	8.9 ± 2.4***	Two-way RM ANOVA
		Speed	1.8 ± 0.4	1.2 ± 0.3	1.7 ± 0.3	1.7 ± 0.3	
		Max speed	12.4 ± 1.1	11.4 ± 2.3*	13.1 ± 0.8	13.2 ± 1.3	
	Day 2 [a.u.]	Distance	16.4 ± 2.5	11.3 ± 2.5	9.2 ± 1.4**	8.7 ± 2.0***	
		Speed	3.3 ± 0.2	2.5 ± 0.4	2.7 ± 0.2	2.4 ± 0.3	
		Max speed	13.1 ± 0.9	12.6 ± 2.0*	15.2 ± 0.6	14.8 ± 0.7	
	Day 3 [a.u.]	Distance	20.5 ± 2.1	14.5 ± 1.8	13.6 ± 1.9**	14.4 ± 3.3***	
		Speed	4.0 ± 0.2	3.5 ± 0.3	3.3 ± 0.2	3.0 ± 0.3	
		Max speed	14.4 ± 0.7	13.8 ± 1.4*	13.9 ± 0.5	13.4 ± 0.9	
	Day 4 [a.u.]	Distance	26.4 ± 2.2	17.5 ± 2.9	17.4 ± 2.3**	16.6 ± 2.7***	
		Speed	4.5 ± 0.2	3.8 ± 0.4	3.7 ± 0.3	3.5 ± 0.3	
		Max speed	13.5 ± 0.8	12.9 ± 1.1*	15.4 ± 0.5	12.4 ± 0.8	
	Day 5 [a.u.]	Distance	31.5 ± 3.2	23.4 ± 4.0	21.0 ± 3.3**	20.6 ± 3.1***	
		Speed	4.8 ± 0.2	4.2 ± 0.4	3.9 ± 0.3	3.9 ± 0.3	
		Max speed	13.5 ± 0.4	11.6 ± 1.1*	14.9 ± 0.6	12.8 ± 0.9	
	Days 1-5 [a.u.]	Distance	F(1, 72)=3.8160, p=0.0665		F(1, 92)=0.0050, p=0.9444		
		Speed	F(1, 72)=3.9680, p=0.0618		F(1, 92)=0.1709, p=0.6832		
		Max speed	F(1, 64)=0.6828, p=0.4208		F(1, 92)=4.0230, p=0.0568		
		Total distance	102.7 ±11.4	71.8 ± 10.9	68.1 ± 9.1	69.2 ± 12.3	Unpaired *t*-test
			p=0.0665		p=0.9444		

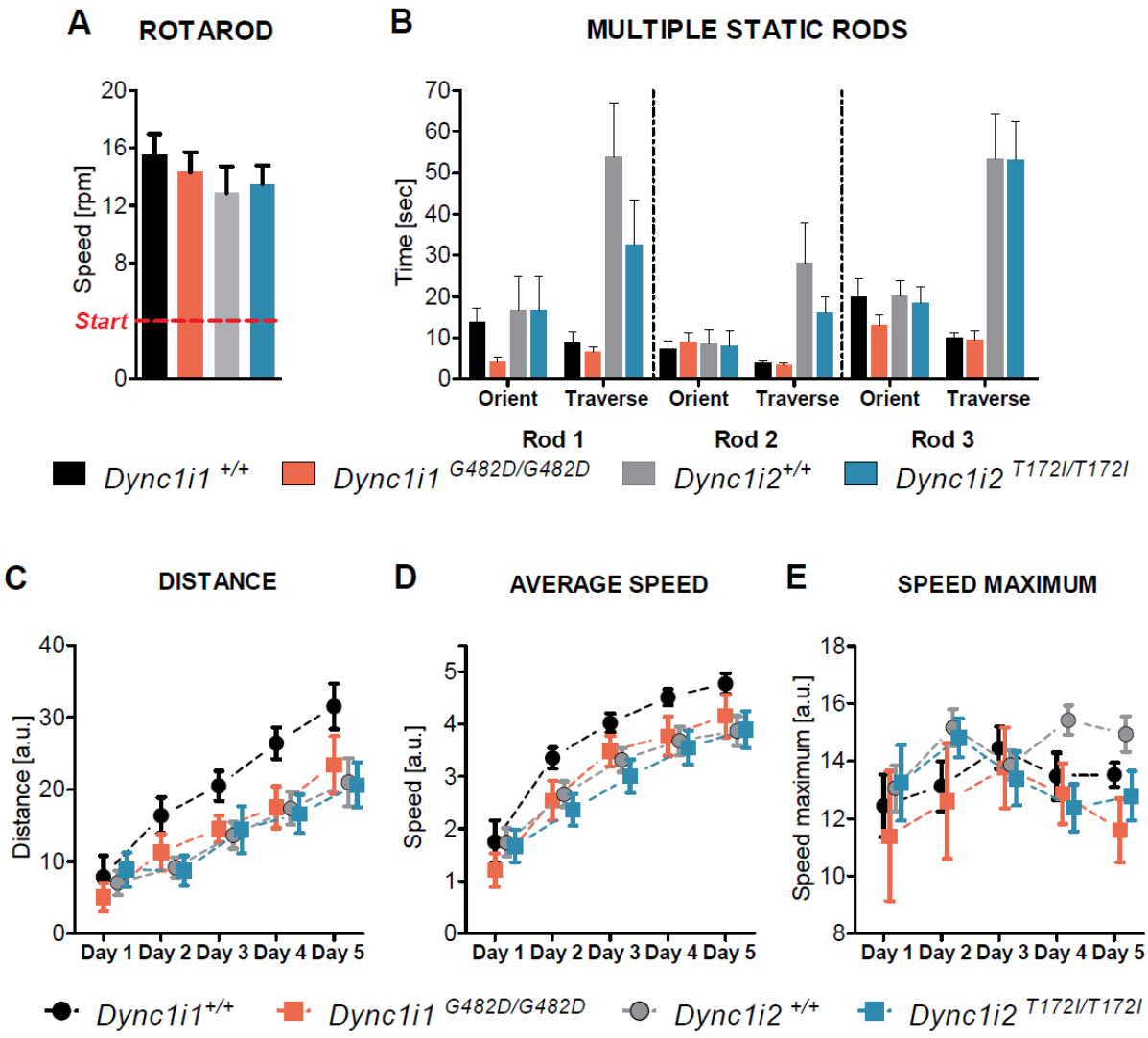

Figure 3.4. Performance of the *Dync1i1*^{G482D} and *Dync1i2*^{T172I} mouse lines in motor tasks
Results plotted as means ± SEM (standard error of the mean), colours correspond to: wildtype *Dync1i1*$^{+/+}$ (black), homozygous *Dync1i1*$^{G482D/G482D}$ (red), wildtype *Dync1i2*$^{+/+}$ (grey), homozygous *Dync1i2*$^{T172I/T172I}$ (blue), rpm – rotation per minute, sec – time in seconds, a.u. – arbitrary units; common legend for A-B and C-D-E
Performance on an accelerating rotarod, the speed [rpm] at which a mouse fell recorded, at Y=4 ('Start') marked the speed at the beginning of the test

A. Time taken to turn (Orient) and cross (Traverse) on a sequential static rods
B. Running wheel: distance run recorder for 5 days
C. Running wheel: average speed of running recorded for 5 days
D. Running wheel: maximum speed of running recorded for 5 days

Wheel running measures voluntary locomotor activity of an animal, and because it takes place in a home cage anxiety levels are usually reduced. Furthermore, data acquisition is often automated, thus increasing the quality and accuracy of a measurement (Brooks and Dunnett, 2009). Mice can run long distance (e.g. approximately 5 km/day for C57BL/6J), and 'pleasure' of running can be also involved in the final outcome (R. Deacon, personal communication). The animals were housed in cages equipped with a running wheel for 5 consecutive days and pedometer readings were taken daily; the distance and speed were measured in arbitrary units, relative to number of wheel turns.

Each day of the testing period (Days 1 – 5) *Dync1i1*$^{G482D/G482D}$ mice ran less (p=0.0665) and slower (p=0.0618) when compared with wildtype *Dync1i1*$^{+/+}$. The mean maximum speed was also reduced in the mutant *Dync1i1*^{G482D} cohort, yet the trend was not clear (p=0.4208). Furthermore, the total distance run within 5 day also reflected worse than in wildtype *Dync1i1*$^{+/+}$ (102.7 ± 11.4 a.u.) performance of the *Dync1i1*$^{G482D/G482D}$ mice (71.8 ± 10.9 a.u.) (p=0.0665).

In a cohort of the *Dync1i2*^{T172I} mice 1 wildtype and 2 homozygous animals did not run during the testing period, thus they were not included in the final results. There were no differences observed between wildtype *Dync1i2*$^{+/+}$ and homozygous *Dync1i2*$^{T172I/T172I}$ mice, neither in the distance run each day (p=0.9444) nor in the average speed (p=0.6832). On the 4th and 5th day the maximum speed of *Dync1i2*$^{T172I/T172I}$ animals decreased more than expected (p=0.0568), yet more data would be required as to the nature of a sudden change. The detailed measurements and statistical analysis are summarised in Table 3.5 and Figure 3.4 C-F.

In summary, in both cohorts a daily increase in a distance run can be observed, which might reflect the learning process. Furthermore, the static rods and running wheel were sensitive to detect the variation in performance of wildtype (*Dync1i1*$^{+/+}$ and *Dync1i2*$^{+/+}$) animals from 2 cohorts.

3.4.4.2 Food and water consumption

General metabolic functions were assessed by monitoring the food, water intake, and glucose preference; the measurements were recorded for a period of 7 consecutive days. Mice were weighed several times over a period of 6 months, from 14 months to 20 months of age, and the feeding behaviour was assessed in both cohorts at 20 months of age. For each animal the amount of food eaten was recorded every day for 3 days and calculated by *(1)* adding all the measurements and comparing total amount of food eaten (in grams) and by *(2)* correcting the total amount of eaten food for a body weight according to an equation: $Food_{corr} = \frac{total\ \ food\ \ eaten\ [g]}{weight^{0.72}\ [g]}$. The amount of water consumed, was similarly calculated either as *(3)* sum of water drunk within 3 days (in grams) or *(4)* as a corrected for body weight ratio: $Water_{corr} = \frac{total\,water\,drunk\,[g]}{weight\,[g]}$. The double calculations were performed in order to examine any possible interaction or influence of a body weight on feeding. Subsequently, the cages were equipped with an additional solution of 7.5% (w/v) glucose, which was closely monitored for another 4 days. The preference for glucose was calculated twice and expressed as ratios: *(5)* total amount of glucose solution drunk for 4 days (in grams) to body weight: $Glucose_{weight} = \frac{total\,glucosedrunk\,[g]}{weight\,[g]}$, and as *(6)* amount of glucose solution drunk daily to daily intake of water: $Glucose_{water} = \frac{averageglucosedrunk\,per\,day\,[g]}{averagewaterdrunk\,per\,day\,[g]}$. The summary with statistical analysis is shown in Table 3.6.

There were no differences in body weight between wildtype *Dync1i1*$^{+/+}$ (n=10) and mutant *Dync1i1*$^{G482D/G482D}$ littermates (n=10,) (p=0.6966), and both groups increased body mass at the age between 17 and 19 months by 6 grams on average (Figure 3.5 A). At the age of 14 and 19 months the wildtype *Dync1i1*$^{+/+}$ mice weighed 20.4 ± 0.6 g and 26.8 ± 0.7 g respectively; these results were slightly lower than data collected for aged C57BL/6J females (25,0 ± 2.1 g at 12 months, 27.8 ± 4.0 g at 18 months; Project 'Yuan1' 2007, MPD27012, MDP27013). Furthermore, the mean food consumption corrected for body weight was nearly equal (p=0.8719), with wildtype *Dync1i1*$^{+/+}$ ratio of 1.06 ± 0.07 and

1.04 ± 0.08 calculated for homozygous *Dync1i1*$^{G482D/G482D}$ females (Figure 3.5 B,C). Similarly, the relative amount of water drunk within 3 days was comparable, with mean value of 0.43 ± 0.04 for *Dync1i1*$^{+/+}$ and 0.41 ± 0.04 for *Dync1i1*$^{G482D/G482D}$ (p=0.5741) (Figure 3.5 D,E). Finally, *Dync1i1*$^{G482D/G482D}$ females displayed a trend in drinking more 7.5% glucose solution (daily consumption in relation to water: 3.68 ± 0.39) than wildtype *Dync1i1*$^{+/+}$ littermates (2.87 ± 0.30) (p=0.1192) (Figure 3.5F,G).

The wildtype *Dync1i2*$^{+/+}$ (n=14) females did not vary from homozygous *Dync1i2*$^{T172I/T172I}$ (n=14) littermates in body weight (p=0.5109), yet they were slightly heavier than the *Dync1i1*^{G482D} mice at the same age. There was also gain in a body mass observed between 17 and 19 months of age (from 23.6 ± 0.6 g to 27.1 ± 0.7 g in *Dync1i2*$^{+/+}$), reaching expected weight for 18 months old C57BL/6J females (27.8 ± 4.0 g) (Figure 3.5A). Furthermore, both groups consumed the same amounts of food when corrected for weight (*Dync1i2*$^{+/+}$: 1.07 ± 0.06 and *Dync1i2*$^{T172I/T172I}$*:* 1.08 ± 0.08, p=0.9981) (Figure 3.5 B,C). Neither the amount of water drunk differed when corrected for weight (*Dync1i2*$^{+/+}$: 0.48 ± 0.03 and *Dync1i2*$^{T172I/T172I}$: 0.45 ± 0.03, p=0.4330) (Figure 3.5 D,E). In addition, daily consumption of 7.5% glucose solution did not vary between wildtype *Dync1i2*$^{+/+}$ (3.37 ± 0.32) and homozygous *Dync1i2*$^{T172I/T172I}$ (3.92 ± 0.28) animals (relative to water drank daily, p=0.2135) (Figure 3.5 F,G). On the other hand, mice from the *Dync1i2*^{T172I} cohort seemed to prefer glucose solution more than the *Dync1i1*^{G482D} mice, which might be related to their higher body mass.

In summary, the mutant lines displayed similar feeding behaviour and body mass. Moreover, the weight of an animal should be taken into account during analysis of metabolic performance, especially when investigating nutrient preferences.

Table 3.6. Food and water consumption in the *Dync1i1*^{G482D} and *Dync1i2*^{T172I} cohorts

Results are shown as mean ± SEM (standard error of the mean); on the left measurements performed over the period of 3 (food, water) or 4 (glucose) days, the results of statistical analysis for each category shaded; genotypes annotated as follows: wildtype (*Dync1i1*$^{+/+}$), homozygous *Dync1i1*^{G482D} (*Dync1i1*$^{G482D/G482D}$), wildtype (*Dync1i2*$^{+/+}$), homozygous *Dync1i2*^{T172I} (*Dync1i2*$^{T172I/T172I}$); numbers in brackets correspond to calculation used (see paragraph); n - number of animals tested; weight, amount of food eaten and water drunk in grams [g]; F(DFn, DFd) – F ratio calculated with ANOVA when DFn: degrees of freedom for the numerator, DFd: degrees of freedom for the denumerator; RM ANOVA – repeated measures analysis of variance

Measurement		***Dync1i1*$^{+/+}$ n=10**	***Dync1i1*$^{G482D/G482D}$ n=10**	***Dync1i2*$^{+/+}$ n=14**	***Dync1i2*$^{T172I/T172I}$ n=14**	***Statistics***
Weight [g]	14 months	20.4 ± 0.6	20.3 ± 0.7	22.8 ± 0.4	23.7 ± 0.9	Two-way RM ANOVA
	17 months	20.9 ± 0.6	21.1 ± 0.6	23.6 ± 0.6	24.4 ± 1.0	
	19 months	26.8 ± 0.7	26.4 ± 0.8	27.1 ± 0.7	27.9 ± 1.5	
	20 months	28.3 ± 0.9	27.1 ± 1.0	27.9 ± 0.7	29.1 ± 1.7	
		F(1,54)= 0.1570, p=0.6966		F(1,78) =0.4443, p=0.5109		
Food consumption [g] [Day 1-3] *(1)*		11.3 ± 0.7	10.8 ± 0.7	11.5 ± 0.6	11.5 ± 0.7	Unpaired *t*-test
		p=0.6849		p=0.9941		
Food consumption corrected for weight [Day 1-3] *(2)*		1.06 ± 0.07	1.04 ± 0.08	1.07 ± 0.06	1.08 ± 0.08	
		p=0.8719		p=0.9981		
Water consumption [g] [Day 1-3] *(3)*		11.6 ± 0.9	10.5 ± 0.7	13.0 ± 0.9	12.2 ± 0.7	Unpaired *t*-test
		p=0.3333		p=0.4739		
Water consumption corrected for weight [Day 1-3] *(4)*		0.43 ± 0.04	0.41 ± 0.04	0.48 ± 0.03	0.45 ± 0.03	
		p=0.5741		p=0.4330		
Glucose 7.5% /weight [Day 1-4] *(5)*		1.59 ± 0.13	1.96 ± 0.24	2.05 ± 0.16	2.28 ± 0.16	Unpaired *t*-test
		p=0.1964		p=0.3054		
Glucose 7.5% /water [Mean per day] *(6)*		2.87 ± 0.30	3.68 ± 0.39	3.37 ± 0.32	3.92 ± 0.28	Unpaired *t*-test
		p=0.1192		p=0.2135		

Figure 3.5. Food, water, and glucose consumption in the *Dync1i1*^{G482D} and *Dync1i2*^{T172I} mouse lines (next page)

Results plotted as means ± SEM, colours correspond to: wildtype *Dync1i1*$^{+/+}$ (black), homozygous *Dync1i1*$^{G482D/G482D}$ (red), wildtype *Dync1i2*$^{+/+}$ (grey), homozygous *Dync1i2*$^{T172I/T172I}$ (blue), combined legends for B-G; all measurements in grams [g]

A. Body weight recorded over the period of 6 months, red lines mark an average body weight reported for 12 - 18 months old C57BL/6J females (25.0 g – 27.8 g), m.o. – months old
B. Mean amount of food eaten during the period of 3 days
C. Mean amount of food eaten during the period of 3 days corrected for body weight
D. Mean amount of water drunk during the period of 3 days
E. Mean amount of water drunk during the period of 3 days corrected for body weight
F. Mean amount of 7.5% (w/v) glucose solution consumed during 4 days related to body weight
G. Mean daily consumption of 7.5% (w/v) glucose solution related to water drunk per day

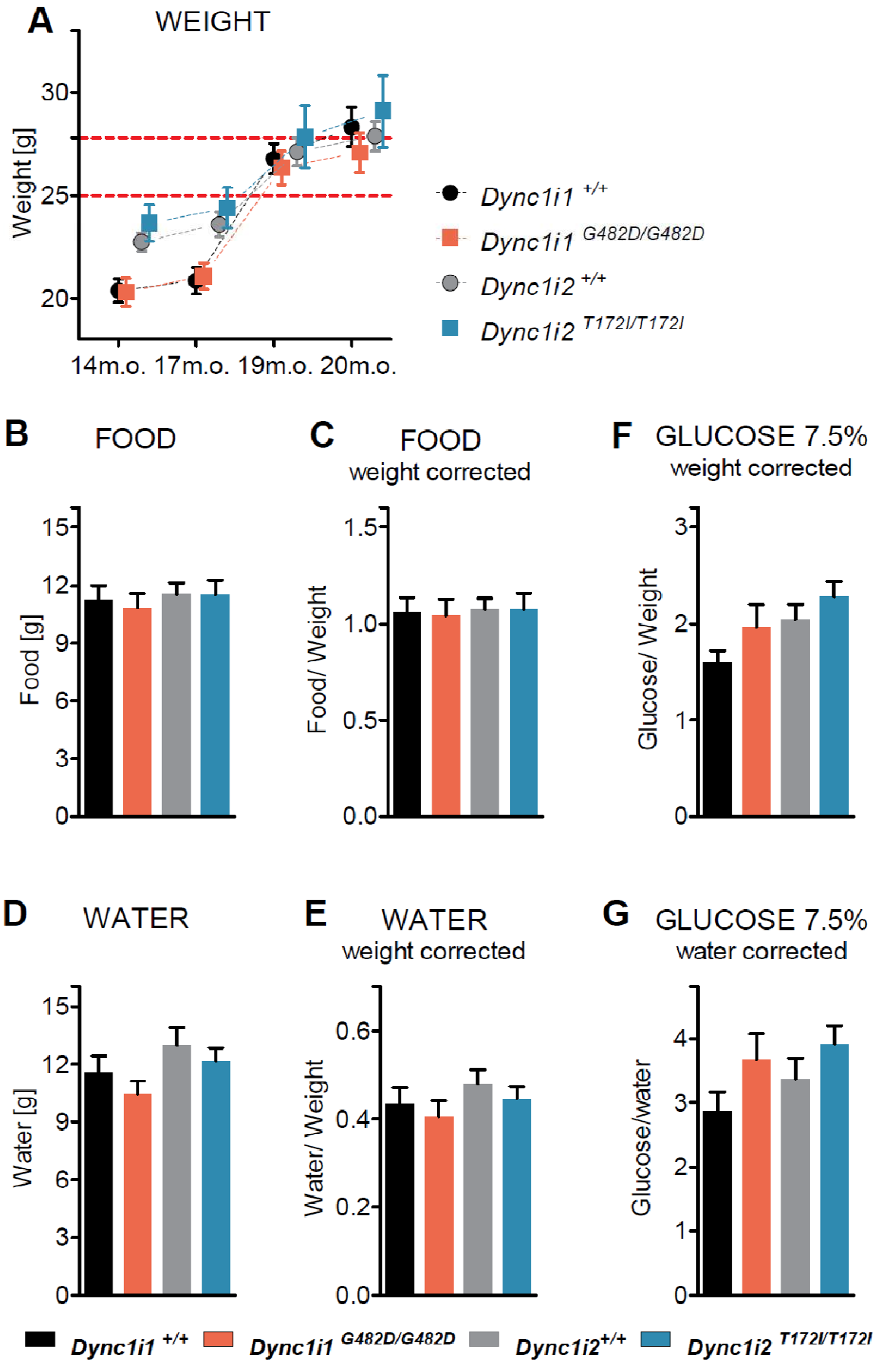
A
WEIGHT
Weight [g]
30
25
20
14m.o. 17m.o. 19m.o. 20m.o.
Dync1i1 +/+
Dync1i1 G482D/G482D
Dync1i2 +/+
Dync1i2 T172I/T172I
B
FOOD
Food [g]
15
12
9
6
3
0
C
FOOD
weight corrected
Food/ Weight
1.5
1.0
0.5
0.0
F
GLUCOSE 7.5%
weight corrected
Glucose/ Weight
3
2
1
0
D
WATER
Water [g]
15
12
9
6
3
0
E
WATER
weight corrected
Water/ Weight
0.6
0.4
0.2
0.0
G
GLUCOSE 7.5%
water corrected
Glucose/water
4
3
2
1
0
Dync1i1 +/+
Dync1i1 G482D/G482D
Dync1i2+/+
Dync1i2 T172I/T172I

3.4.4.3 Species specific behaviour

Mice display many behaviours specific for rodents, e.g. grooming, eating movements, food hoarding, burrowing, nesting etc. Those characteristics can be easily tested, and it has been reported that the outcome of rodent activities is related to integrity of the hippocampus and prefrontal cortex (Deacon and Rawlins, 2005). Accordingly, locomotor activity, nesting, and burrowing were assessed in the *Dync1i1*^{G482D} and *Dync1i2*^{T172I} mice.

Locomotor activity of individual animals was monitored for 23 hours with a 12 hours long dark phase (time points 7 – 19h), which allowed us to compare the patterns of circadian activity. The activity counts were expressed in arbitrary units. Mice are nocturnal thus the activity counts increased in the dark phase and were low in the presence of light (representative data in Table 3.7).

On overall, wildtype *Dync1i1*$^{+/+}$ (n=6) and homozygous *Dync1i1*$^{G482D/G482D}$ (n=7) mice did not display different patterns of the circadian rhythm (p=0.9136) (Figure 3.6 A).

There were also no differences observed between wildtype *Dync1i2*$^{+/+}$ (n=14) and homozygous *Dync1i2*$^{T172I/T172I}$ (n=14) females (p=0.7217), which were mostly active during the dark phase (Figure 3.6 B).

Table 3.7. Representative activity scores obtained for *Dync1i1*^{G482D} and *Dync1i2*^{T172I} cohorts
The activity scores at different phase of the test are shown as mean ± SEM (standard error of the mean); genotypes annotated as follows: wildtype *Dync1i1*$^{+/+}$, homozygous *Dync1i1*^{G482D} (*Dync1i1*$^{G482D/G482D}$), wildtype *Dync1i2*$^{+/+}$, homozygous *Dync1i2*^{T172I} (*Dync1i2*$^{T172I/T172I}$); shaded measurements taken during the dark phase, n - number of animals tested; number in brackets correspond to a test time point, see Figure 3.6; h – hours; all the scores shown in arbitrary units

Measurement point	***Dync1i1*$^{+/+}$** **n=6**	***Dync1i1*$^{G482D/G482D}$** **n=7**	***Dync1i2*$^{+/+}$** **n=14**	***Dync1i2*$^{T172I/T172I}$** **n=14**
2h before dark phase **(5)**	169.0 ± 60.8	129.6 ± 41.8	129.9 ± 25.5	122.3 ± 41.4
2h of dark phase **(9)**	701.7 ± 151.5	764.6 ± 108.9	686.5 ± 38.6	667.9 ± 49.4
2h before light phase **(17)**	373.4 ± 139.4	355.7 ± 128.3	271.5 ± 57.4	393.0 ± 63.3
2h of light phase **(21)**	187.2 ± 65.0	70.6 ± 21.9	91.5 ± 15.7	85.47 ± 12.4

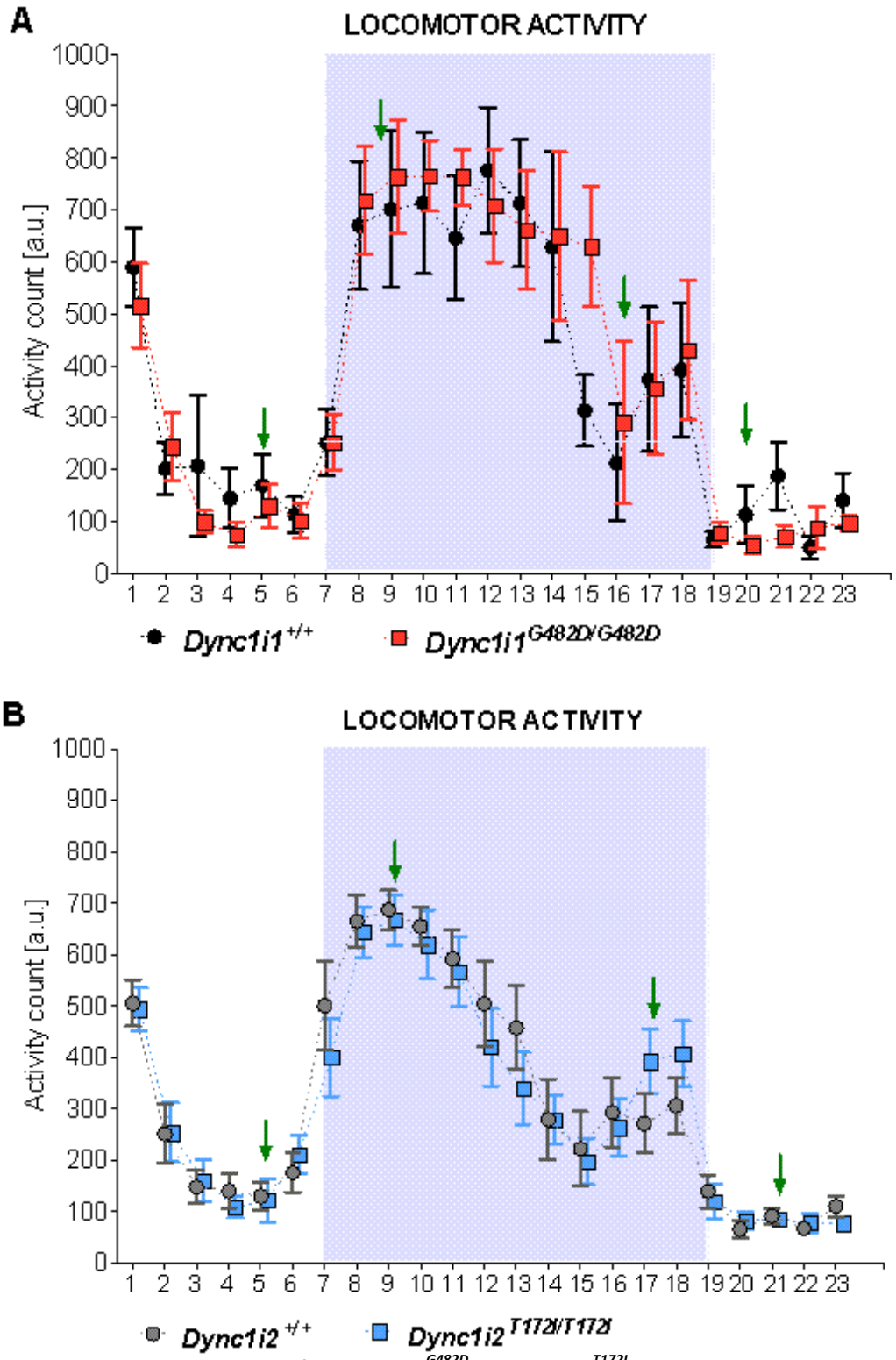

Figure 3.6. Circadian activity charts of the *Dync1i1*^{G482D} and *Dync1i2*^{T172I} mice

Data were collected for 23 hours period and locomotor activity of individual mice scored; a 12 hours long dark phase shaded (from 7 – 19); results plotted as means ± SEM (standard error of the mean); colours correspond to: wildtype *Dync1i1*$^{+/+}$ (black), homozygous *Dync1i1*$^{G482D/G482D}$ (red), wildtype *Dync1i2*$^{+/+}$ (grey), homozygous *Dync1i2*$^{T172I/T172I}$ (blue); representative time points shown in Table 3.7 marked with arrows (5, 9, 17, 21 hours), a.u. – arbitrary units

A. Mean locomotor activity of wildtype (*Dync1i1*$^{+/+}$) and homozygous (*Dync1i1*$^{G482D/G482D}$) females
B. Mean locomotor activity of wildtype (*Dync1i2*$^{+/+}$) and homozygous (*Dync1i2*$^{T172I/T172I}$) females

Burrowing has been defined as displacement of material from the burrow and piling it around the entrance to the burrow (Deacon, 2006b). A pattern of coordinated movements can be observed, as a mouse digs with forelimbs and pushes the material out of the burrow with its hind limbs. Mice have been shown to burrow spontaneously regardless of the material used, and the burrowing has been suggested to be a rewarding activity. During the test the amount of the material displaced in a given time is measured. The test is usually performed 3 hours before the dark cycle and an additional practical 'run' helps in decreasing variability as animals get used to a new object introduced to the home cage. The amount of displaced material from a burrow was analysed with non-parametric Mann-Whitney test due to a data structure (ceiling effect, described in Deacon, 2006b). Therefore, all the values are reported as median and an interquartile range (IQR, difference between 25^{th} and 75^{th} percentile). The results and statistics applied are summarized in Table 3.8.

A cohort of *Dync1i1*^{G482D} females was tested for burrowing ability at 20 months of age. The test was performed twice for 1 hour and an average from 2 measurements was used in statistical analysis. *Dync1i1*$^{G482D/G482D}$ females (n=10) displaced less material (91.2 g; 57.3 – 189.8) than wildtype *Dync1i1*$^{+/+}$ (n=10) littermates during the same period of time (178.7 g; 163.0 - 197.6) (p=0.2406) (Figure 3.7 A).

The *Dync1i2*^{T172I} mice were allowed to burrow for 3 hours and the task was performed once. There were no differences in the amount of material removed between wildtype *Dync1i2*$^{+/+}$ (n=14, 127.1 g; 44.4 - 198.9) and *Dync1i2*$^{T172I/T172I}$ mice (n=14, 114.4 g; 8.1 - 172.8) (p=0.4894). In addition, there was no practice run and the numerical measurements were highly scattered (Figure 3.7B). Interestingly, the *Dync1i2*^{T172I} mice displayed much slower rate of burrowing when compared with the *Dync1i1*^{G482D} cohort, which may be explained by their different origin.

Table 3.8. Performance of the *Dync1i1*^{G482D} and *Dync1i2*^{T172I} cohorts in species-specific tasks
Results are shown as median and IQR (interquartile range); on the left measurements performed, the results of Mann-Whitney test shaded; genotypes annotated as follows: wildtype (*Dync1i1*$^{+/+}$), homozygous *Dync1i1*^{G482D} (*Dync1i1*$^{G482D/G482D}$), wildtype (*Dync1i2*$^{+/+}$), homozygous *Dync1i2*^{T172I} (*Dync1i2*$^{T172I/T172I}$); n - number of animals tested; weight of displaced and left material in grams [g]

Measurement		*Dync1i1*$^{+/+}$ n=10	*Dync1i1*$^{G482D/G482D}$ n=10	*Dync1i2*$^{+/+}$ n=14	*Dync1i2*$^{T172I/T172I}$ n=14
Weight of material burrowed [g]		178.7 (163.0 -197.6)	91.2 (57.3 – 189.8)	127.1 (44.4 - 198.9)	114.4 (8.1 - 172.8)
		p=0.2406		p=0.4894	
Nest	Score (scale 1-5)	5.0 (4.4 – 5.0)	4.8 (4.5 – 5.0)	4.5 (4.0 – 5.0)	4.0 (3.4 – 4.5)
		p=0.6960		p=0.1249	
	Material left [g]	0.0 (0.0 – 0.2)	0.0 (0.0 – 0.0)	0.0 (0.1 – 0.4)	0.3 (0.3 – 0.8)
		p=0.5036		p=0.3027	

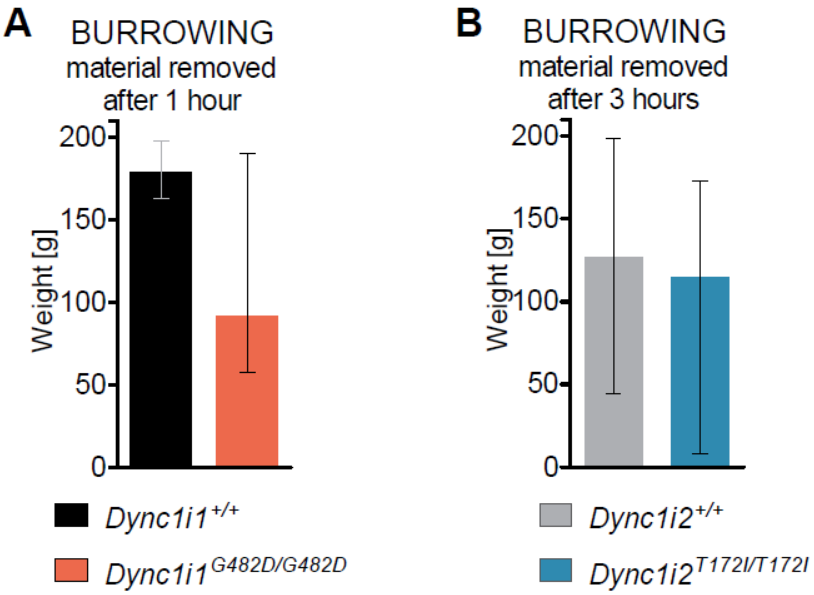

Figure 3.7. Burrowing of the *Dync1i1*^{G482D} and *Dync1i2*^{T172I} mouse lines
Results plotted as median and IQR (interquartile range), colours correspond to: wildtype *Dync1i1*$^{+/+}$ (black), homozygous *Dync1i1*$^{G482D/G482D}$ (red), wildtype *Dync1i2*$^{+/+}$ (grey), homozygous *Dync1i2*$^{T172I/T172I}$ (blue), weight of material displaced burrowing in grams [g], for *Dync1i1*$^{+/+}$ error bar marked in grey for a better visualisation

A. Median amount of material removed from a burrow by *Dync1i1*^{G482D} mice measured after 1 hour
B. Median amount of material removed from a burrow by *Dync1i2*^{T172I} mice measured after 3 hours

For a mouse an ability to build a nest is crucial, as it serves not only as a shelter but also as a way to conserve body temperature. Both males and females construct nests instinctively, thus nesting can be used in behavioural studies. On the other hand, the nesting is a complex behaviour which can be affected by many factors, e.g. hormonal balance. The standardised scoring protocol (in scale 1-5) with assigned illustrations of nests can be found in Deacon (2006a).

Nests built by 20 months old *Dync1i1*^{G482D} and *Dync1i2*^{T172I} mice were scored visually and by weighing the unshredded material (if present). Similarly to burrowing task, the majority of mice would build good nests (score 5) using all the material, thus the data were analysed with a non-parametric test (Mann-Whitney) and median values with an interquartile range were reported (Table 3.8).

Nearly all the nests build by the *Dync1i1*^{G482D} mice received high scores (above 4.5) and none was scored below 4.0. The comparison of nest quality of the wildtype *Dync1i1*$^{+/+}$ (n=10, 5.0; 4.4 – 5.0) and homozygous *Dync1i1*$^{G482D/G482D}$ (n=10, 4.8; 4.5 – 5.0) mice showed neither differences in nest scores (p=0.6960) nor in the amount of material left (p=0.5036) (Figure 3.8 A, B).

On the other hand, the nests built by the *Dync1i2*^{T172I} mice were scored lower than *Dync1i1*^{G482D}, with median 4.5 (4.0 - 5.0) for wildtype *Dync1i2*$^{+/+}$ (n=14) and 4.0 (3.4 – 4.5) for homozygous *Dync1i2*$^{T172I/T172I}$ (n=14) animals (Figure 3.8 A, B). Although the nests built by the *Dync1i2*$^{T172I/T172I}$ females were poorer the difference was within variation (p=0.1249). At the same time there was more unshredded material found in cages occupied by *Dync1i2*$^{T172I/T172I}$ (0.3 g; 0.0 – 0.8) than in cages where *Dync1i2*$^{+/+}$ mice were housed (0.0 g; 0.0 – 0.4) (p=0.3027).

In summary, mice from both cohorts were capable of building nests, which were often scored above 4.0. On the other hand the results obtained for the *Dync1i2*^{T172I} mice were highly variable thus affecting the final analysis (Figure 3.8 C). Therefore, it might be beneficial to test a bigger cohort of animals or perform the nest assessment several times.

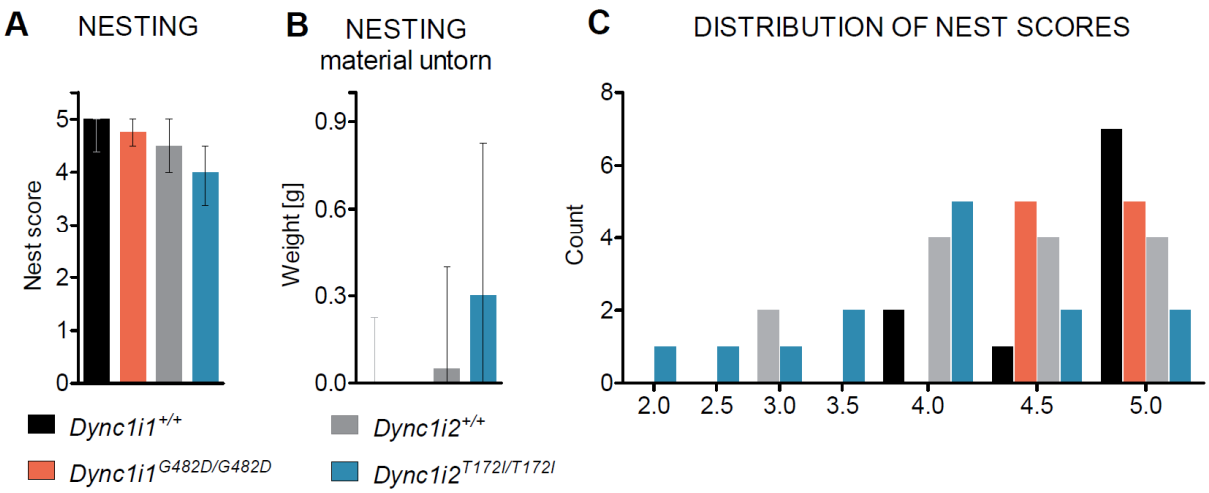

Figure 3.8. Nesting of the *Dync1i1*^{G482D} and *Dync1i2*^{T172I} mouse lines
Results plotted as median and IQR (interquartile range), colours correspond to: wildtype *Dync1i1*$^{+/+}$ (black), homozygous *Dync1i1*$^{G482D/G482D}$ (red), wildtype *Dync1i2*$^{+/+}$ (grey), homozygous *Dync1i2*$^{T172I/T172I}$ (blue), weight of material displaced (burrowing) or left untorn (nesting) in grams [g], for *Dync1i1*$^{+/+}$ error bar marked in grey for a better visualisation; combined legends for A-B

A. Median score of nests built by the *Dync1i1*^{G482D} and *Dync1i2*^{T172I} mice
B. Median amount of nesting material left untorn, in case of the *Dync1i1*$^{G482D/G482D}$ mice no material was found (median 0.0 g; 0.0 – 0.0)
C. Frequency distribution of scores quantifying the quality of nests in a scale 1 – 5, the *Dync1i2*^{T172I} mice displayed more variability than *Dync1i1*^{G482D}

3.4.4.4 Anxiety-like behaviour (emotionality tests)

Tests described as 'emotionality tests' quantify behaviour of an animal in situations when anxiety is induced. Those tasks are usually based on a mouse tendency to avoid bright light and open areas. On the other hand, animals can get accustomed to handling, which may affect the outcomes of anxiety tests (Deacon *et al.*, 2002). All the measurements were taken for 5 min (300 s) and treated as non-parametric data; the analysis was performed using Mann-Whitney test and results reported as median and interquartile range (IQR, difference between 25th and 75th percentile) (Deacon *et al.*, 2002).

Successive alleys are an emergence task, which consists of 4 distinct compartments which gradually change from closed black area (Alley 1) to an open white lane (Alley 4). During the test a mouse is placed in an Alley 1 and time spent in each compartment, latency to enter each alley, and number of entries into each of the alleys are measured. The summary with the results of statistical analysis is shown in Table 3.9.

The *Dync1i1*^{G482D} mice spent most of the time in the Alley 1 (starting compartment, the least anxiogenic) and none of them ventured behind Alley 2. Seven wildtype *Dync1i1*$^{+/+}$ (n=10) and 4 mutant *Dync1i1*$^{G482D/G482D}$ (n=10) mice stayed in the Alley 1; median times spent in the Alley 1 were thus 300.0 s (290.5 – 300.0) for *Dync1i1*$^{+/+}$ and 289.0 s (276.5 – 300.0) and did not differ (p=0.2465). The median latency time before entering Alley 2 was 300.0 s (198.8 – 300.0) in *Dync1i1*$^{+/+}$ and 210.0 s (157.0 – 300.0) in *Dync1i1*$^{G482D/G482D}$ (p=0.2640). The mutant *Dync1i1*$^{G482D/G482D}$ mice seemed to move sooner to a new compartment, but the result might reflect the fact that more wildtype *Dync1i1*$^{+/+}$ mice never left Alley 1 (Figure 3.9 A,B). Because mice 'shuttled' only between 2 compartments, they stayed for the rest of the testing period in Alley 2, with the median times measured for *Dync1i1*$^{+/+}$: 0.0 s (0.0 – 9.5) and 11.0 s (0.0 – 23.5) for *Dync1i1*$^{G482D/G482D}$. Number of entries into Alley 1 and 2 were the same and performance of the wildtype *Dync1i1*$^{+/+}$ (0.0; 0.0 – 1.2) did not vary from *Dync1i1*$^{G482D/G482D}$ mice (1.0; 0.0 – 2.0) (p=0.3369) (Figure 3.9 C, D).

The *Dync1i2*^{T172I} mice were tested in two batches, and their behaviour strongly differed during the test. There were 5 wildtype (*Dync1i2*$^{+/+}$) and 6 mutant (*Dync1i2*$^{T172I/T172I}$) mice in the second batch tested, and almost all of them (except for 2) never left Alley 1. Because that behaviour was not informative and increased the skewness of the data sets when analysed (e.g. skewness value calculated for 'Time in Alley 1' increased 100% in *Dync1i2*$^{+/+}$, and 28% in *Dync1i2*$^{T172I/T172I}$), those mice were not taken into account during statistical analysis. From the first batch all but 2 *Dync1i2*^{T172I} mice left Alley 1, only 3 wildtype *Dync1i2*$^{+/+}$ and 1 homozygous *Dync1i2*$^{T172I/T172I}$ females entered Alley 3, and 2 passed all the way and reached Alley 4. Because they were not representative, the results from Alley 3 and Alley 4 were not analysed.

Table 3.9. Performance of the *Dync1i1*^{G482D} and *Dync1i2*^{T172I} cohorts in the successive alleys
Results are shown as median and IQR (interquartile range); on the left measurements performed, the results of Mann-Whitney test shaded; genotypes annotated as follows: wildtype (*Dync1i1*$^{+/+}$), homozygous *Dync1i1*^{G482D} (*Dync1i1*$^{G482D/G482D}$), wildtype (*Dync1i2*$^{+/+}$), homozygous *Dync1i2*^{T172I} (*Dync1i2*$^{T172I/T172I}$); n - number of animals tested; s – in seconds, time measured

Measurement		*Dync1i1*$^{+/+}$ n=10	*Dync1i1*$^{G482D/G482D}$ n=10	*Dync1i2*$^{+/+}$ n=9	*Dync1i2*$^{T172I/T172I}$ n=8
Alley 1	Time [s]	300.0 (290.5 - 300.0)	289.0 (276.5 - 300.0)	283.0 (271.0 - 295.5)	282.5 (263.8 - 294.0)
		p=0.2465		p=0.9615	
Alley 2	Time [s]	0.0 (0.0 – 9.5)	11.0 (0.0 – 23.0)	17.0 (4.5 - 26.5)	17.5 (6.0 – 36.2)
		p=0.2465		p=0.6638	
	Latency to enter [s]	300.0 (198.8 –300.0)	210 (157 – 300)	105.0 (37.5 - 197.5)	111.0 (38.5 – 245.0)
		p=0.2640		p=1.0000	
	Number of entries	0.0 (0.0 – 1.2)	1.0 (0.0 – 2.0)	2.0 (1.0 – 4.0)	2.0 (1.0 – 3.0)
		p=0.3369		p=0.7310	

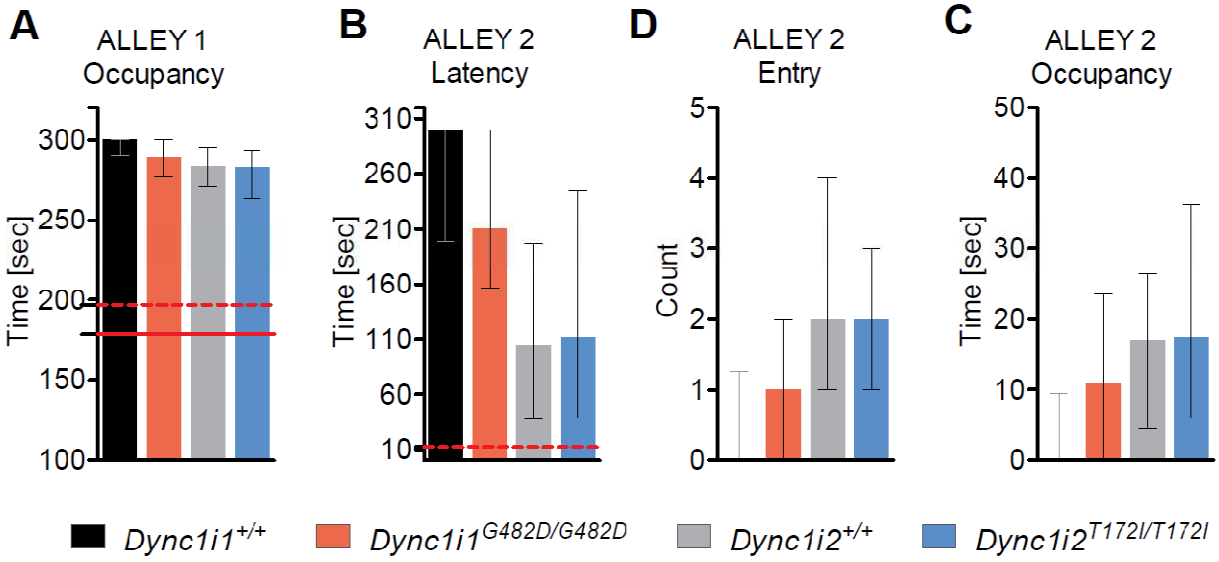

Figure 3.9. Performance of the *Dync1i1*^{G482D} and *Dync1i2*^{T172I} mouse lines in tests for anxiety-like behaviour
Results plotted as median and IQR (interquartile range), colours correspond to: wildtype *Dync1i1*$^{+/+}$ (black), homozygous *Dync1i1*$^{G482D/G482D}$ (red), wildtype *Dync1i2*$^{+/+}$ (grey), homozygous *Dync1i2*$^{T172I/T172I}$ (blue), time spent in each of compartments in seconds [sec]; because mice hardly entered Alleys 3 and 4 the results are shown only for Alleys 1 and 2; for *Dync1i1*$^{+/+}$ error bar marked in grey for a better visualisation; combined legends for A-B, C-D

A. Median time spent in the Alley 1, compared with results reported for a cohort of healthy C57BL/6J (dashed line) and C57BL/6J mice with lesions in hippocampus (straight line) adapted from Deacon and Rawlins (2005)
B. Median time before a mouse moved to Alley 2, compared with results reported for a cohort of healthy C57BL/6J (dashed line) mice
C. Median time mice spent in Alley 2
D. Median number of entries into Alley 2

There was no difference in the median time spent in Alley 1 (p=0.9615). Wildtype *Dync1i2*$^{+/+}$ females (n=9) stayed for 283.0 s (271.0 – 295.5) while *Dync1i2*$^{T172I/T172I}$ (n=8) stayed for 282.5 s (263.8 – 294.0) (Figure 3.9 A). Furthermore, the latency to enter a second compartment (Alley 2) was shorter by 100 s than in case of the *Dync1i1*^{G482D} mice, and nearly identical for both groups: *Dync1i2*$^{+/+}$ entered Alley 2 after 105.0 s (37.5 – 197.5), and *Dync1i2*$^{T172I/T172I}$ entered at 111.0 s (38.5 – 245.0) (p=1.00) (Figure 3.9 B). Once in the Alley 2 *Dync1i2*$^{+/+}$ mice stayed there for 17.0 s (4.5 – 26.5) and *Dync1i2*$^{T172I/T172I}$ mice for 17.5 s (6.0 - 36.3), which was not different (p=0.6638). The analysis of number of entries to Alley 2 did not show differences between both groups (p=0.7310), with a median number of entries: 2 (1 – 4) in case of the wildtype *Dync1i2*$^{+/+}$ mice and also 2 (1 – 3) for *Dync1i2*$^{T172I/T172I}$ (Figure 3.9 C, D).

The performance of the *Dync1i1*^{G482D} and *Dync1i2*^{T172I} mice was compared with reported behaviour of healthy C57BL/6J and matched C57BL/6J with induced lesions in hippocampus (Deacon *et al.*, 2002) (Figure 3.9 A, B). In general, both mutant cohorts were much slower in leaving the first compartment and stayed there much longer. This behaviour might be related with lower reactivity to a new situation, reduced exploration or much higher anxiety (also called emotionality).

Light/dark Box is another test based on innate aversiveness to brightly light places. The main scope is assessing the preference for dark, small places, but it is also helpful in observations of the exploration level and alertness (Deacon and Rawlins, 2005). In the version of the test performed here, animals were placed in the dark compartment. The behaviour was scored for 5 minutes, during which the latency to emerge, number of entries to the light areas, time spent in light and defecations were recorded. Although the test seems to be straightforward to perform, there are many factors which constitute for the final performance. The summary with results of statistical analysis is shown in Table 3.10.

There were no differences in the 'reaction' time, when a mouse emerged from the dark box, between wildtype *Dync1i1*$^{+/+}$ (n=10) and mutant *Dync1i1*$^{G482D/G482D}$ (n=10) littermates (p=0.7328). In addition, 4 mice (2 wildtype *Dync1i1*$^{+/+}$, 2 homozygous *Dync1i1*$^{G482D/G482D}$)

never left the dark compartment which is in agreement with the results obtained with the successive alleys. On average, *Dync1i1*$^{G482D/G482D}$ took slightly more time to exit the dark compartment (170.5 s; 65.8 - 273.8) than wildtype *Dync1i1*$^{+/+}$ mice (142.5 s; 58.8 - 236.3) (Figure 3.10 A). Furthermore, *Dync1i1*$^{G482D/G482D}$ mice stayed in the light compartment for as long as wildtype *Dync1i1*$^{+/+}$ (24.6 s; 6.8 - 40.6 and 24.4 s; 2.2 - 53.6, respectively, p=0.8495) (Figure 3.10 B), and crossed the compartments similar number of times (p=0.8486). Finally, the events of defecation, which are thought to reflect fear and anxiety, were also comparable (p=0.7808), with 1.0 (0.0 - 3.0) recorded for *Dync1i1*$^{+/+}$, and 1.0 (0.0 - 1.2) recorded for *Dync1i1*$^{G482D/G482D}$.

When the *Dync1i2*^{T172I} mice were tested their overall performance did not show differences between the wildtype *Dync1i2*$^{+/+}$ and mutant *Dync1i2*$^{T172I/T172I}$ mice, although they stayed longer in dark and avoided light to a bigger extent than *Dync1i1*^{G482D} mice. Mutant *Dync1i2*$^{T172I/T172I}$ females were slower to emerge from the dark (203.5 s; 129.0 - 300.0) than wildtype *Dync1i2*$^{+/+}$ mice (192.0 s; 34.0 - 242.0) (p=0.3440) (Figure 3.10 A). They also spent approximately 4.9 s (0.0 - 23.4) in the light chamber while wildtype *Dync1i2*$^{+/+}$ stayed for 10.0 s (5.8 - 38.8) (p=0.0894). That behaviour was also reflected in lower number of entries to the light chamber as recorded for *Dync1i2*$^{T172I/T172I}$ mice (1.0; 0.0 - 1.5) when compared with the wildtype *Dync1i2*$^{+/+}$ (1.0; 1.0 - 6.0) (p=0.0753) (Figure 3.10 B, C). However, that result might be affected by the fact, that 4 *Dync1i2*$^{T172I/T172I}$ females never left the dark box. Finally, the events of defecation did not indicate increased fear reaction and it was recorded only for 3 wildtype *Dync1i2*$^{+/+}$ and 5 *Dync1i2*$^{T172I/T172I}$ mice (p=0.5673) (Figure 3.10 D).

Interestingly, the *Dync1i2*^{T172I} cohort was slower than the *Dync1i1*^{G482D} mice to leave the dark, which is in the contrary to results obtained with the successive alleys. On the other hand, both cohorts tested (*Dync1i1*^{G482D} and *Dync1i2*^{T172I}) performed much worse than reported for C57BL/6J (Deacon and Rawlins, 2005). The discrepancy might be caused by many factors, e.g. age of mice tested, handling.

Table 3.10. Performance of the *Dync1i1*^{G482D} and *Dync1i2*^{T172I} cohorts in the light/dark box
Results are shown as median and IQR (interquartile range); on the left measurements performed, the results of Mann-Whitney test shaded; genotypes annotated as follows: wildtype (*Dync1i1*$^{+/+}$), homozygous *Dync1i1*^{G482D} (*Dync1i1*$^{G482D/G482D}$), wildtype (*Dync1i2*$^{+/+}$), homozygous *Dync1i2*^{T172I} (*Dync1i2*$^{T172I/T172I}$); n - number of animals tested; s – in seconds, time measured

Measurement	*Dync1i1*$^{+/+}$ n=10	*Dync1i1*$^{G482D/G482D}$ n=10	*Dync1i2*$^{+/+}$ n=13	*Dync1i2*$^{T172I/T172I}$ n=14
Latency to light [s]	142.5 (58.8 - 236.3)	170.5 (65.8 - 273.8)	192.0 (34.0 - 242.0)	203.5 (129.0 - 300.0)
	p=0.7328		p=0.3440	
Time in light [s]	24.4 (2.2 - 53.6)	24.6 (6.8 - 40.6)	10.0 (5.8 - 38.8)	4.9 (0.0 - 23.4)
	p=0.8495		p=0.0894	
Entries to light	3.0 (0.8 - 6.5)	2.5 (0.8 - 5.2)	1.0 (1.0 - 6.0)	1.0 (0.0 - 1.5)
	p=0.8486		p=0.0753	
Defecation	1.0 (0.0 - 3.0)	1.0 (0.0 - 1.2)	0.0 (0.0 - 0.5)	0.0 (0.0 - 1.2)
	p=0.7808		p=0.5673	

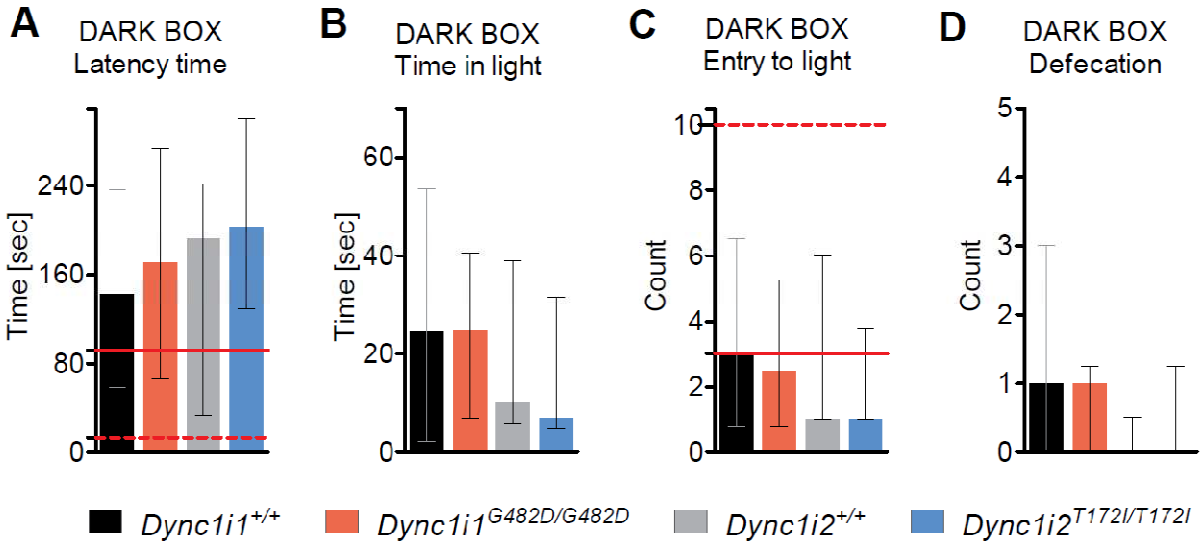

Figure 3.10. Performance of the *Dync1i1*^{G482D} and *Dync1i2*^{T172I} cohorts in the light/dark box
Results plotted as median and IQR (interquartile range), colours correspond to: wildtype *Dync1i1*$^{+/+}$ (black), homozygous *Dync1i1*$^{G482D/G482D}$ (red), wildtype *Dync1i2*$^{+/+}$ (grey), homozygous *Dync1i2*$^{T172I/T172I}$ (blue), time spent in each of compartments in seconds [sec]; values corresponding to C57BL/6J adapted from Deacon and Rawlins (2005) for *Dync1i1*$^{+/+}$ error bar marked in grey for a better visualisation; combined legends for A-B, C-D

A. Median time before a mouse moved from dark to light box, compared with results reported for a cohort of healthy C57BL/6J (dashed line) and C57BL/6J mice with lesions in hippocampus (straight line)
B. Median time a mouse spent in the light compartment
C. Median numbers of crosses between light/dark compartments, compared with results reported for a cohort of healthy C57BL/6J (dashed line) and C57BL/6J mice with lesions in hippocampus (straight line)
D. Median number of defecations observed

3.4.4.5 Spatial working memory

Assessing cognitive abilities of animals can be challenging, and usually certain domains are assessed, e.g. learning abilities or memory. In addition, the assessment of spatial memory in mice is often based on a natural tendency to explore and novelty-seeking. There are many tests designed to describe spatial memory, whether it is reference memory involving a reward, or spatial working memory based on exploration and novelty preference.

Spatial working memory was assessed using a T-maze. Mice preferentially explore new location over the familiar one, and in the case of the T-maze they choose a new arm instead of the familiar one. This kind of behaviour is also called spontaneous alternation: the animal remembers an arm it entered during a first run and chooses another one in the second run. Thus, a healthy mouse should obtain high percent of alternations (over 50%). Data collected during sessions are usually expressed as a percent of correct alternations ('the other arm'). In this case data were analysed as non-parametric data and all the values are presented as median and interquartile range (IQR).

Dync1i1^{G482D} mice were tested at the age of 15 months. Twelve runs were performed over 6 days and number of alternation was recorded. There were no differences between wildtype *Dync1i1*$^{+/+}$ (n=10) and homozygous *Dync1i1*$^{G482D/G482D}$ (n=10) females (p=0.2966), although mutant *Dync1i1*$^{G482D/G482D}$ mice had higher score of correct alternations (95.8%, 89.6 – 100.0) than wildtype *Dync1i1*$^{+/+}$ littermates (87.5%; 81.2 – 100.0) (Table 3.11, Figure 3.11 A).

Dync1i2^{T172I} mice were also tested at the age of 15 months, and 20 runs were performed over 14 days. As above, the results were calculated as percentage of correct alternations and analysed as non-parametric data. *Dync1i2*$^{T172I/T172I}$ mice (n=14) were found to alternate less than wildtype *Dync1i2*$^{+/+}$ littermates (n=14). While wildtype *Dync1i2*$^{+/+}$ females alternate correctly 90% (80.0 – 90.0) of runs, mutant *Dync1i2*$^{T172I/T172I}$ chose a new arm 82.5% (73.7 – 85.0) of all the runs (p=0.0174), which suggests an impairment in spatial working memory (Table 3.11, Figure 3.11 A).

Table 3.11. Performance of the *Dync1i1*^{G482D} and *Dync1i2*^{T172I} mice in T-maze
Results are shown as median and IQR (interquartile range); on the left number of runs performed, the results of Mann-Whitney test shaded; genotypes annotated as follows: wildtype *Dync1i1*$^{+/+}$, homozygous *Dync1i1*$^{G482D/G482D}$, wildtype *Dync1i2*$^{+/+}$, homozygous *Dync1i2*$^{T172I/T172I}$; n - number of animals tested; for **p<0.05 in bold**

T-maze	*Dync1i1*$^{+/+}$ n=10	*Dync1i1*$^{G482D/G482D}$ n=10	*Dync1i2*$^{+/+}$ n=14	*Dync1i2*$^{T172I/T172I}$ n=14
Number of runs	12	12	20	20
Percentage of correct alternations	87.5 (81.2 –100.0)	95.8 (89.6 –100.0)	90.0 (80.0 – 90.0)	82.5 (73.7 – 85.0)
	p=0.2966		**p=0.0174**	

In order to confirm the deficits in the spatial working memory the Dync1i2T172I mice were tested for novelty preference in Y-maze, which consisted of 3 identical arms. In contrast to the T-maze, there was a 2 min long training session when mice were allowed to explore 2 arms (called Start and Other). This sample run was followed by 2 min long test run, during which another arm was opened (Novel) and animal's behaviour was recorded. The preference for Novel arm over familiar Other arm of the maze was expressed by a discrimination ratio calculated for both number of entries and time spent in the Novel arm (Sanderson et al., 2009). Aditionally, the performance in the Y-maze is sensitive to deficits in spontaneous locomotor activity or exploratory motivation.

The data were presented as mean ± SEM (standard error of the mean), whereas the novelty discrimination ratios (NDR) for time and number of entries were calculated as below:

$$\mathrm{NDR}_{\mathrm{Time}} = \frac{Time_{Novel}}{Time_{Novel} + Time_{Other}} \quad (1), \text{ and} \quad NDR_{Entry} = \frac{Entry_{Novel}}{Entry_{Novel} + Entry_{Other}} \quad (2).$$

In addition, the ratios were compared to a hypothetical value 0.5 using one sample *t*-test; p> 0.05 indicated a chance performance and lack of preference.

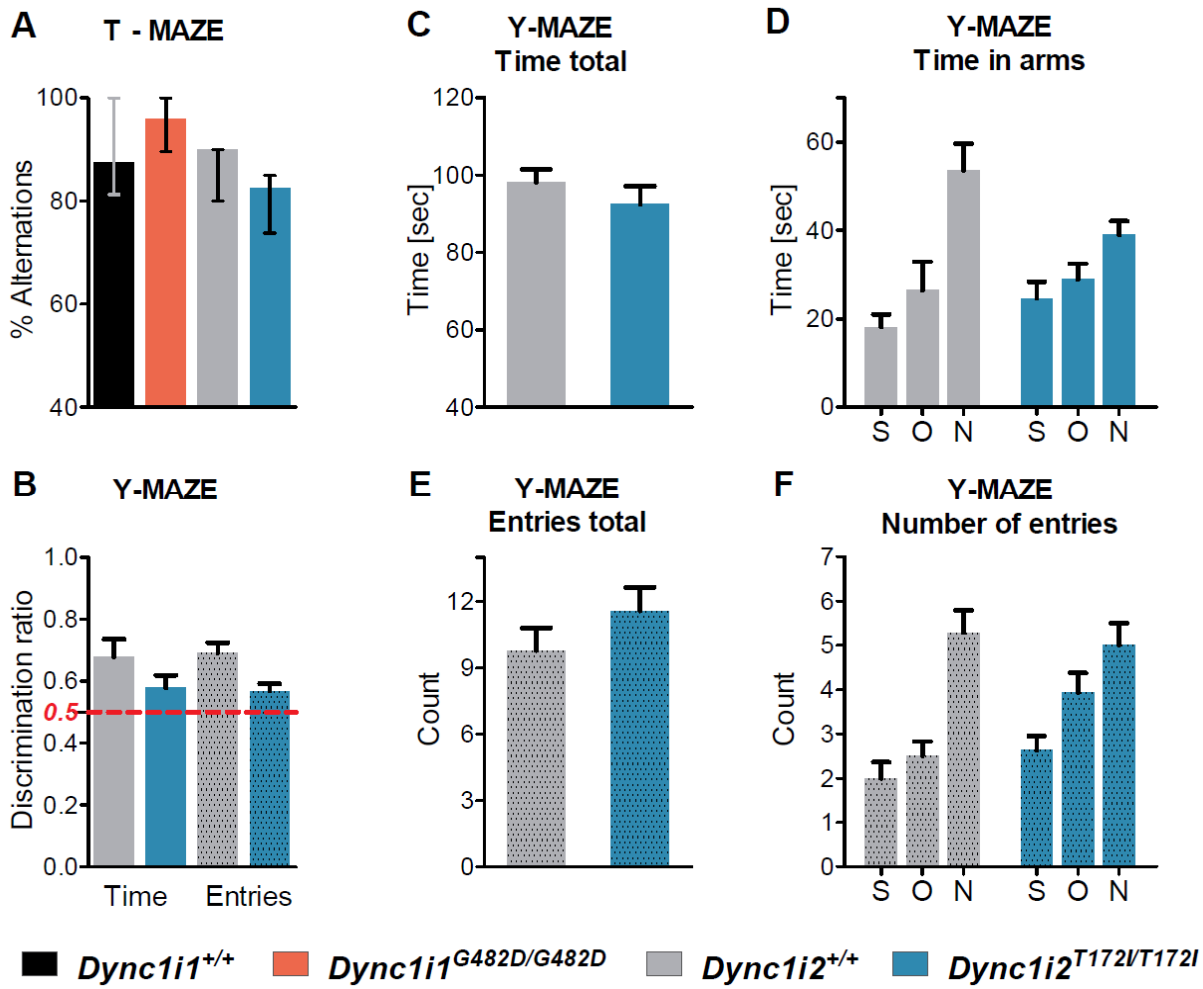

Figure 3.11. Performance of the *Dync1i1*^{G482D} and *Dync1i2*^{T172I} mice in tasks for working spatial memory
Results from Y-maze plotted as means ± SEM (standard error of a mean), the legend refers to all graphs and colours correspond to: wildtype *Dync1i1*$^{+/+}$ (black), homozygous *Dync1i1*$^{G482D/G482D}$ (red), wildtype *Dync1i2*$^{+/+}$ (grey), homozygous *Dync1i2*$^{T172I/T172I}$ (blue); sec – seconds, abbreviations used correspond to Start arm (S), Other arm (O), Novel arm (N)

A. Percentage of correct alternations in a T-maze plotted as median and IQR (interquartile range), for *Dync1i1*$^{+/+}$ error bar marked in grey for a better visualisation
B. Performance of the *Dync1i2*^{T172I} mice in Y-maze: value of discrimination ratio describing preference for a new location calculated for time (plain bars) and number of entries in arms (dotted bars); dashed line at Y=0.5 indicates chance performance
C. Total time of exploration calculated as a sum of times a mouse spent in any of the arms, total duration of the test: 2 min (120 s)
D. Total time of exploration split by arms mouse occupied for a given time
E. Total number of entries recorded during the test
F. Total number of entries split by the arms a mouse entered during the test

Both groups explored all 3 arm of the maze (**Start, Other, Novel**) for the same amount of time (p=0.3209), when *Dync1i2*$^{T172I/T172I}$ mice (n=14) spent 92.5 ± 4.6 s and wildtype *Dync1i2*$^{+/+}$ littermates 98.2 ± 3.3 s (Table 3.12). Comparison of times corresponding to distinct arms however, showed that homozygous *Dync1i2*$^{T172I/T172I}$ mice spent on average less time in the **Novel** arm (38.9 ± 3.1 s) than wildtype *Dync1i2*$^{+/+}$ (53.6 ± 6.0 s) (p=0.0426). Furthermore, both wildtype *Dync1i2*$^{+/+}$ and *Dync1i2*$^{T172I/T172I}$ occupied the **Other** (familiar) arm for the same time (p=0.7366), but homozygous *Dync1i2*$^{T172I/T172I}$ stayed longer in the **Start** arm (24.6 ± 3.8 s) than wildtype *Dync1i2*$^{+/+}$ animals (18.1 ± 2.8 s) (p=0.1796) (Figure 3.11 C, D). A time-dependent discrimination ratio for a **Novel** arm preference described the level of exploration of an unfamiliar area. The value calculated for wildtype *Dync1i2*$^{+/+}$ animals was 0.677 ± 0.057, the result different from value (0.5) expected for a random choice (t(13)=3.100, p=0.0085) (Figure 3.11 B). On the other hand, the ratio of novelty preference calculated for the *Dync1i2*$^{T172I/T172I}$ females was much lower (0.578 ± 0.041), and that result was very likely caused by random alternation and lack of preference (t(13)=1.920, p=0.0771). Likewise, the values of the discrimination ratio did not vary (p=0.1715) when wildtype *Dync1i2*$^{+/+}$ and homozygous *Dync1i2*$^{T172I/T172I}$ were compared.

In a similar manner the number of entries into each arm of the Y-maze was analysed, as it often reflects exploratory motivation of a mouse. There were no differences detected in the total number of entries (p=0.2380) and homozygous *Dync1i2*$^{T172I/T172I}$ mice (n=14) made on average more entries (11.6 ± 1.1) than wildtype *Dync1i2*$^{+/+}$ littermates (n=14, 9.8 ± 1.0) (Table 3.12). The comparison of entries into individual arms revealed that *Dync1i2*$^{T172I/T172I}$ mice entered **Other** (familiar) arm more often than wildtype *Dync1i2*$^{+/+}$, with 3.9 ± 0.4 entries recorded for *Dync1i2*$^{T172I/T172I}$ and 2.5 ± 0.3 entries for *Dync1i2*$^{+/+}$ (p=0.0164) (Figure 3.11 E, F). The difference may express a reduction in spontaneous alternation while exploration was not affected. Moreover, a trend could be observed when the mutant *Dync1i2*$^{T172I/T172I}$ animals preferentially entered the **Start** arm (*Dync1i2*$^{+/+}$: 2.0 ± 0.4 and *Dync1i2*$^{T172I/T172I}$: 2.6 ± 0.3, p=0.1884), while wildtype *Dync1i2*$^{+/+}$ females chose more often the **Novel** arm (*Dync1i2*$^{+/+}$: 5.3 ± 0.5 and *Dync1i2*$^{T172I/T172I}$: 5.0 ± 0.5, p=0.6924). Finally, the novelty discrimination ratio calculated for the number of entries was much higher in the group of wildtype *Dync1i2*$^{+/+}$ animals (0.691 ± 0.033) than

in mutant *Dync1i2*$^{T172I/T172I}$ (0.567 ± 0.024), which supported observations of reduced events of spontaneous alternation in homozygous *Dync1i2*$^{T172I/T172I}$ mice (p=0.0054). Although the value of NDR was strongly reduced in the *Dync1i2*$^{T172I/T172I}$ mice, it was not proven to be a result of random choices (one sample *t*-test, p=0.0164).

In conclusion, while no deficits in spatial working memory were observed in the *Dync1i1*^{G482D} mouse line, the *Dync1i2*^{T172I} females had slightly impaired performance in the spontaneous alternation task. Furthermore, reduction in exploration of a new area and repetitive returning to a familiar location suggest impairment in the working memory. A comparable performance was described in the *GluA1*$^{-/-}$ mice (Sanderson *et al.*, 2009), and it would be beneficial to investigate long-term and reference memory in the *Dync1i2*^{T172I} mice.

Table 3.12. Performance of the *Dync1i2*^{T172I} mice in the Y-maze
Results are shown as mean ± SEM (standard error of a mean); on the left parameter analysed; the results of unpaired t-test shaded; genotypes annotated as follows: wildtype *Dync1i2*$^{+/+}$, homozygous *Dync1i2*$^{T172I/T172I}$; n - number of animals tested, s – seconds, *(1), (2)* refer to equations used, reported two-tailed p values significant at p<0.05, * - unpaired *t*-test with Welch's correction for unequal variances whereas F(13,13)=3.620 and p=0.0275; for **p<0.05 in bold**

Observation		*Dync1i2*$^{+/+}$ (n=14)	*Dync1i2*$^{T172I/T172I}$ (n=14)	Statistics
Total exploration time [s]		98.2 ± 3.3	92.5 ± 4.6	p=0.3209
Time spent in arms [s]	**Start**	18.1 ± 2.8	24.6 ± 3.8	p=0.1796
	Other	26.5 ± 6.4	28.9 ± 3.5	p=0.7366
	Novel	53.6 ± 6.0	38.9 ± 3.1	**p=0.0426**
Total number of entries		9.8 ± 1.0	11.6 ± 1.1	p=0.2380
Number of entries in arms	**Start**	2.0 ± 0.4	2.6 ± 0.3	p=0.1884
	Other	2.5 ± 0.3	3.9 ± 0.4	**p=0.0164**
	Novel	5.3 ± 0.5	5.0 ± 0.5	p=0.6924
NDR_{Time} *(1)*		0.677 ± 0.057	0.578 ± 0.0409	p=0.1715
NDR_{Entry} *(2)*		0.691 ± 0.033	0.567 ± 0.0245	**p=0.0054**
Chance performance for NDR_{Time}=0.5		**p=0.0085**	p=0.0771	
Chance performance for NDR_{Entry}=0.5		**p < 0.0001**	**p=0.0164**	

3.4.5 Detailed gait analysis with CatWalk XT

An analysis of gait is usually performed together with locomotor tasks and it is helpful in detecting abnormalities in the animal's posture or difficulties during walking, which often accompany neurological deficits. The gait in the *Dync1i1*^{G482D} and *Dync1i2*^{T172I} mice was recorded and analysed using CatWalk XT, which is an automated system designed to capture paw prints during a free run. The system consists of an enclosed walkway on a glass plate that is illuminated from underneath and coupled with a high speed camera. An animal is let on a walkway and each footprint is recorded and classified. The images from the walking sequence are analysed and numerous parameters retrieved, e.g. width and length of an individual paw, relative print positions, sequence of footprints (Angeby-Moller *et al.*, 2008). The CatWalk XT has been applied in studies on neuropathic pain (Angeby-Moller *et al.*, 2008), effects of sciatic nerve injury (Eickholt *et al.*, 2007), ataxia associated with Refsum neuropathy (Ferdinandusse *et al.*, 2008), recovery from early chronic spinal cord injury after transplantation of human neural stem cells (Salazar *et al.*, 2010), and many other studies. An example of a run is presented in Figure 3.12, when footprints are visible as areas and right/left sides marked green/red, respectively.

The gait patterns were recorded for both mutant mouse lines (*Dync1i1*^{G482D} and *Dync1i2*^{T172I}) and several parameters were analysed in detail. Parameters were automatically calculated by the CatWalk XT software and for each mouse values from 4 successive runs were collected. Although it was possible to analyse data split into 4 sets corresponding to prints of all paws, means of front (left-right) and hind (left-right) paws prints, which were also computed, were chosen as raw data. By having done so, the reported bias towards higher values for one side than the other was avoided (Angeby-Moller *et al.*, 2008). Summing up, the gait of each mouse was described by comparing gait parameters of front and hind paws, which were defined by average of 4 runs. The means from 4 runs are therefore measurements referred to in following paragraphs.

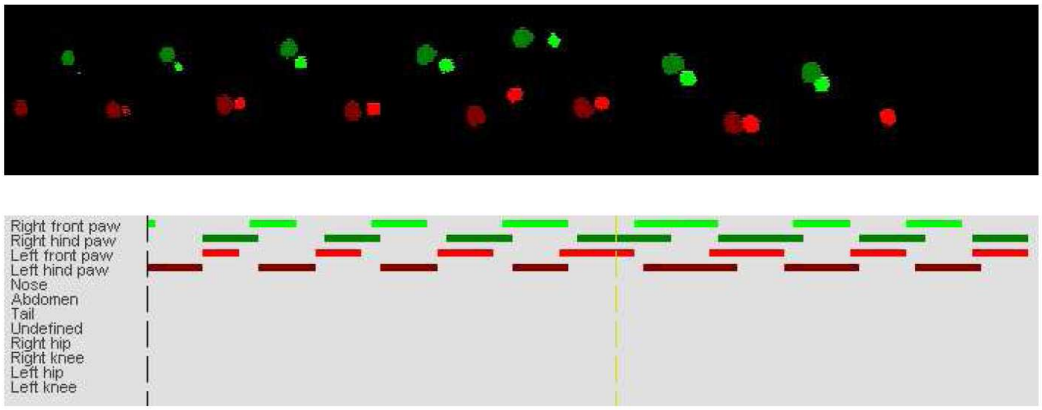

Figure 3.12. An example of a footprint pattern registered with CatWalk XT
Each paw is assigned in relation to an animal (left, right, front, hind) and after extracting background noise various parameters are measured. Picture kindly provided by Samantha Line

In order to detect even mild effects of mutations on the mouse phenotype, multiple parameters, which quantified many aspects of the gait, were analysed. Initially, parameter values for front and hind prints (raw data) were grouped and their means compared between wildtype (*Dync1i1*$^{+/+}$, *Dync1i2*$^{+/+}$) and mutant (*Dync1i1*$^{G482D/G482D}$, *Dync1i2*$^{T172I/T172I}$) animals. Unfortunately, statistical testing with two-way repeated-measures ANOVA probably lacked power and in some cases failed to give definite result within assumed 95% confidence intervals (Appendix 10.1). The difficulty might have resulted from the nature of measurements, because all the parameters were derived from objects (paw prints) identified automatically by the CatWalk software. Therefore, the quality of individual runs was also examined, and 3 runs from 3 mice were discarded (time of initial and maximum contact was above 3 s whereas average time was 0.8 s). In addition 'Print area' was used to calculate front to hind paws area ratio **(F/H)**, which served as a coefficient to control the quality of the raw data. The calculated values for area **(F/H)** were expected to be between 0.4 – 1.0 based on the assumption, that *(1)* front paws had smaller print area than hind paws (≤ 1), and *(2)* front paws were placed on the glass surface strongly enough to provide support during the walk. Proportional values for all the mice fitted in the boundaries described apart from 1 wildtype *Dync1i1*$^{+/+}$ (1.22) and 1 wildtype *Dync1i2*$^{+/+}$ (0.27), which were not considered during analyses. In the second round, parameters for prints of front and hind paws were tied in proportions and expressed as relative values whenever possible; this operation reduced variation within

the subjects and facilitated hypothesis testing. The scatter of data was estimated by comparing values of coefficient of variation (% CV, see analysis of print width and length).

The tested cohorts consisted of 10 wildtype *Dync1i1*$^{+/+}$, 10 homozygous *Dync1i1*$^{G482D/G482D}$, 9 wildtype *Dync1i2*$^{+/+}$, and 8 homozygous *Dync1i2*$^{T172I/T172I}$ females, however, after detailed analysis 1 wildtype *Dync1i1*$^{+/+}$ and 1 wildtype *Dync1i2*$^{+/+}$ were discarded. For simplicity, all the descriptions and detailed results can be found in Appendix 10.1, while and only parameters, which differed between wildtype (*Dync1i1*$^{+/+}$, *Dync1i2*$^{+/+}$) and homozygous (*Dync1i1*$^{G482D/G482D}$ or *Dync1i2*$^{T172I/T172I}$) females are discussed here in details. The results, unless stated otherwise, are shown as mean ± SEM (standard error of the mean). There were few gait parameters, for which only trends were observed with values of $p< 0.10$: p=0.0636 for 'Swing' and p=0.0852 for 'Print length' in the *Dync1i1*^{G482D} cohort; p=0.0735 for 'Maximum contact at' in the *Dync1i2*^{T172I} cohort. The gait parameters, which associated with a mutant phenotype, were regularity index, base of support, and swing speed.

Regularity index (%), which expresses number of steps in a sequence which are aligned with an established pattern relative to the total number of paw placements. The regularity is a fractional measure of inter-paw coordination and is often affected after a spinal cord injury. Theoretically, a healthy animal should reach 100%. Data were analysed using a non-parametric test (Mann-Whitney) and presented as median and interquartile range (IQR).

Interestingly, the median RI for the *Dync1i1*$^{G482D/G482D}$ mice (n=10; 100.0%; 99.00 - 100.0) was higher than median RI calculated for wildtype *Dync1i1*$^{+/+}$ females (n=9; 98.5%; 97.5 - 99.5) (p=0.0340) (Table 3.13).

The median step regularity of the *Dync1i2*$^{T172I/T172I}$ mice (n=8; 99.0%; 98.5 - 100.0) seemed to be slightly impaired when compared with wildtype *Dync1i2*$^{+/+}$ (n=8; 100.0%; 100.0 - 100.0) (p=0.0772) (Figure 3.13 A).

Base of support (BOS) is an average width between prints of front (left-right) or hind (left-right) paws, and it is often used as a measure of animal stability during walking. Furthermore, the BOS parameter has been shown to be sensitive to gait impairment caused by a trauma to the spinal cord (Hamers et al., 2001).

Since BOS values for front and hind paws did not vary, the ratio of BOS of front to hind paws - BOS (F/H) was calculated. The proportion (F/H) would reflect changes in the parameter for both pairs of paws and could be tested with unpaired *t*-test. That method proved to be sensitive enough, and differences in the paws placement were observed in the mutant *Dync1i1*$^{G482D/G482D}$ mice (n=10; 0.520 ± 0.026) when compared with wildtype *Dync1i1*$^{+/}$ littermates (n=9; 0.597 ± 0.019). The difference in the mean value of BOS (F/H) was an effect of simultaneous change in position of both sets of paws, with mean width of the front paws shorter by 0.9 mm, and the mean width of the hind paws longer by 1.0 mm (p=0.0289) when compared to the wildtype *Dync1i1*$^{+/+}$ littermates.

Table 3.13. Analysis of selected gait parameters of the *Dync1i1*^{G482D} and *Dync1i2*^{T172I} mice
Results are shown as mean ± SEM (standard error of a mean) or as medians and IQR (interquartile range); on the left parameter analysed; genotypes annotated as follows: wildtype *Dync1i1*$^{+/+}$, homozygous *Dync1i1*$^{G482D/G482D}$, wildtype *Dync1i2*$^{+/+}$, homozygous *Dync1i2*$^{T172I/T172I}$; n - number of animals tested, m/s – meters per second, **F/H** refers to ratio(s) obtained by division of values for **front** paws by **hind** paws, **WTH/LTH** corresponds to ratio(s) obtained by division of **width** by **length** of a print; results of statistical tests shaded, *- unpaired *t*-test with Welch's correction for unequal variances, F(7,7)=12.2700, F(DFn, DFd) is F ratio calculated for DFn: degrees of freedom for the numerator, DFd: degrees of freedom for the denumerator; reported two-tailed p values significant at p<0.05, bolded results of statistical tests where p<0.05

Parameter		*Dync1i1*$^{+/+}$ n=9	*Dync1i1*$^{G482D/G482D}$ n=10	*Dync1i2*$^{+/+}$ n=8	*Dync1i2*$^{T172I/T172I}$ n=8	*Statistics*
Regularity Index (%)		98.5 (97.5 - 99.5)	100 (99.0- 100)	100 (100- 100)	99.0 (98.5 - 100)	Mann-Whitney
		p=0.0340		p=0.0772		
Base of support F/H		0.597 ± 0.019	0.520 ± 0.026	0.512 ± 0.042	0.533 ± 0.012	Unpaired *t*-test
		p=0.0289		p=0.6389*		
WTH/LTH	**F**	1.006 ± 0.016	1.048 ± 0.012	1.005 ± 0.041	0.988 ± 0.031	Two-way RM ANOVA
	H	0.924 ± 0.016	0.991 ± 0.023	0.981 ± 0.015	0.977 ± 0.020	
		F(1,17)=8.0690, p=0.0113 Bonferroni post-test p<0.05 for H		F(1,14)=0.1331, p=0.7207		
Swing speed [m/s]	**F**	0.539 ± 0.060	0.402 ± 0.030	0.422 ± 0.027	0.428 ± 0.029	
	H	0.560 ± 0.041	0.436 ± 0.037	0.432 ± 0.025	0.463 ± 0.031	
		F(1,17)=5.1380, p=0.0367		F(1,14)=0.2321, p=0.6374		

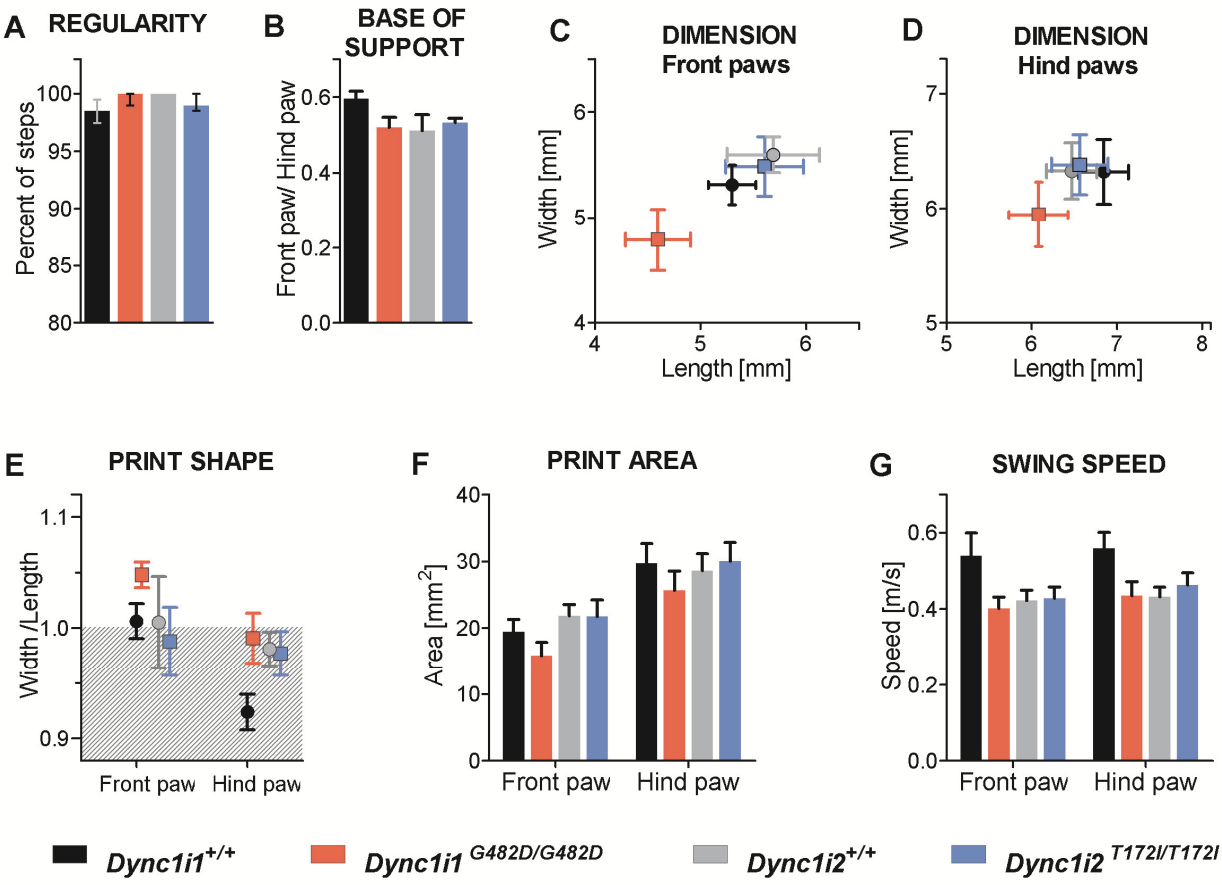

Figure 3.13. Representative parameters calculated during gait analysis on the CatWalk XT (next page)
Selected gait parameters plotted as means ± SEM (standard error of the mean), or median and IQR (interquartile range); a legend refers to all graphs below and colours correspond to: wildtype *Dync1i1*$^{+/+}$ (black), homozygous *Dync1i1*$^{G482D/G482D}$ (red), wildtype *Dync1i2*$^{+/+}$ (grey), homozygous *Dync1i2*$^{T172I/T172I}$ (blue); mm – millimetres, mm^2 – square millimetre, m/s – meter per second

A. Regularity index (RI, median and IQR) is a measure of inter-paw coordination, fraction of steps which were placed within a pattern, for *Dync1i1*$^{+/+}$ error bar marked in grey for a better visualisation
B. Base of support is a width between pairs of paws (front or hind), here expressed as a ratio of values for front to hind paws
C. Front paw print parameters plotted as coordinates, when X – print length, Y – print width
D. Hind paw print parameters plotted as coordinates, when X – print length, Y – print width
E. Print 'shape' as determined by WTH/LTH ratio, when Y=1 defines square print, Y<1 print longer than wide (area shaded)
F. Area of prints of front and hind paws, described in Appendix 10.1
G. Speed of swing of front and hind paws, expresses speed of paws during swing phase (when paws are not touching the glass walkway) relates the stride length to duration of the swing phase

The homozygous *Dync1i2*$^{T172I/T172I}$ (n=8) did not differ from wildtype *Dync1i2*$^{+/+}$ (n=8) in the values obtained for BOS (p=0.8588). Neither values of BOS (F/H) suggested abnormal gait (p=0.6389), even though the homozygous *Dync1i2*$^{T172I/T172I}$ showed a bit higher mean (0.533 ± 0.012) than wildtype *Dync1i2*$^{+/+}$ littermates (0.512 ± 0.042) (Figure 3.13 B).

Width and length [mm] of a paw print can be described as width and length of a rectangle containing a complete print, which depends on the spread and paw positioning on a surface. The measurements of print width and length were used to detect impairment in paw placement (Deumens *et al.*, 2007) and monitor recovery after sciatic nerve injury (Bozkurt *et al.*, 2008).

Initially the paw print parameters (width-length) were grouped and the walking pattern was analysed for front and hind paws separately. In general the trend was observed within the *Dync1i1*$^{G482D/G482D}$ mice suggesting differences in the shape of front and hind paws prints when compared with wildtype *Dync1i1*$^{+/+}$ mice (width: p=0.2296, length: p=0.0852). As mentioned before, scatter was estimated with % CV, which ranged from 8.6 % to 21.7 % in the data for front paws, and from 11.0 % to 18.0 % in the set of hind paws prints. On the other hand, by drawing both parameters in the proportion the number of data sets was reduced from 4 (width and length of front and hind paws) to 2 (front - hind paws). In addition, the variation within new parameters **(WTH/LTH)** in both cohorts did not exceed 11.6 % for front paws or 7.2 % for hind paws. Furthermore, both parameters (width-length) served as coordinates in a two-dimensional space thus a placement of each paw could be described as relative outcome of a toe spread (width), and the use of plantar surface of a paw (length) (Figure 3.14).

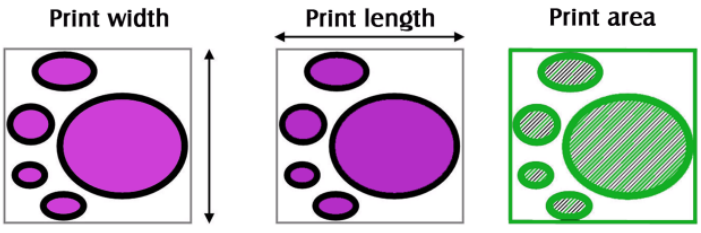

Figure 3.14. Schematic representation of relation between print parameters generated with CatWalk XT
A footprint is recorded for each paw when it is placed on the walkway; parameters described correspond to measurements taken during stand phase: print width [mm] (vertical arrow) and length [mm] (horizontal arrow) parameters reflect the foot placement and toe spread. Print area [mm^2] corresponds to the total surface, adapted from 'CatWalk XT 8.1 Reference Manual', Noldus Information Technology

Mutant *Dync1i1*$^{G482D/G482D}$ mice (n=10) tended to display smaller prints of front and hind paws than wildtype *Dync1i1*$^{+/+}$ littermates (n=9), in terms of both width/length and area (Figure 3.13 C, D, F; Appendix 10.1). However, mean **WTH/LH** ratios calculated for front (1.048 ± 0.012) and hind (0.991 ± 0.023) paws of *Dync1i1*$^{G482D/G482D}$ animals were bigger than the relative values calculated for front (1.006 ± 0.016) and hind (0.924 ± 0.016) paws of *Dync1i1*$^{+/+}$ (p=0.0113). The diversity resulted mostly from different parameters for hind paws prints (Bonferroni post-test p< 0.05) (Figure 3.13 E). The results suggested a subtle change in the placement of paws during walking observed in the homozygous *Dync1i1*$^{G482D/G482D}$ females, with an increase in print width corresponding to spread of toes or decrease in print length reflecting lifting a part of foot above the glass surface.

On the other hand there were no differences in relative print size between homozygous *Dync1i2*$^{T172I/T172I}$ (n=8) and wildtype *Dync1i2*$^{+/+}$ females (n=8) (p=0.7207), although prints recorded for front and hind paws of the *Dync1i2*$^{T172I/T172I}$ animals were slightly longer (WTH/LTH <1.0) than corresponding prints of wildtype *Dync1i2*$^{+/+}$ animals (Figure 3.13 E).

One of the parameters describing dynamic movement of paws is **swing speed**, which expresses the speed of paws during swing phase. It is calculated as ratio of **stride length [mm]** to time of **swing [s]** with $^{m}/_{s}$ as a unit, where stride is a distance between successive placements of the same paw, and swing describes the time, during which a paw is lifted and does not contact a glass plate.

The mean swing speed of front and hind paws recorded for the *Dync1i1*$^{G482D/G482D}$ females (n=10; 0.402 ± 0.030 $^{m}/_{s}$ and 0.436 ± 0.037 $^{m}/_{s}$, front and hind paws respectively) was smaller than in the wildtype *Dync1i1*$^{+/+}$ (0.539 ± 0.060 $^{m}/_{s,}$ and 0.560 ± 0.041 $^{m}/_{s}$) (p=0.0367). The swing speed is an outcome of many parameters, which affect the mouse gait; as mentioned before, the *Dync1i1*$^{G482D/G482D}$ females had smaller paws prints, which might result in shorter strides (e.g. *Dync1i1*$^{G482D/G482D}$ hind paws were placed on average every 50.4 ± 1.6 mm and 54.0 ± 2.4 mm in *Dync1i1*$^{+/+}$*)* and longer swing phase (e.g. hind paws lifted for 124.5 ± 7.3 ms in *Dync1i1*$^{G482D/G482D}$ and 106.2 ± 6.7 ms in *Dync1i1*$^{+/+}$).

Furthermore, *Dync1i2*$^{T172I/T172I}$ (n=8) and *Dync1i2*$^{+/+}$ (n=8) mice did not vary in the swing speed (p=0.6374), however, their performance was very similar to mean values observed for the *Dync1i1*$^{G482D/G482D}$ females (0.432 ± 0.025 $^{m}/_{s}$, and 0.463 ± 0.031 $^{m}/_{s}$ for *Dync1i2*$^{+/+}$ and *Dync1i2*$^{T172I/T172I}$ hind paws respectively) (Figure 3.13 G).

The parameters discussed above suggest differences in the locomotor performance caused by the *Dync1i1*^{G482D} mutation, when positioning of paws and speed of paws placement seem to be affected the most. The deficit, however, was limited only to few parameters, and it is likely to be associated with a mild phenotype. On the other hand, the *Dync1i2*$^{T172I/T172I}$ females did not vary from wildtype *Dync1i2*$^{+/+}$ littermates in any of the parameters analysed. Furthermore, there were no differences in the weight within animals from the same cohort; although *Dync1i2*^{T172I} mice were slightly heavier than *Dync1i1*^{G482D} females (see section 3.4.4.2). In addition, in some cases dissimilarities were noted between cohorts of the wildtype (*Dync1i1*$^{+/+}$ and *Dync1i2*$^{+/+}$) females, which were likely to be caused by the variation in the genetic background.

CatWalk XT was initially developed to study gait impairment in rats (Hamers *et al.*, 2001) but it has been successfully adapted to mouse. Thanks to automated data collection and multiparametric analysis the accuracy and sensitivity of measurements are greatly improved when compared with a traditional method of ink and paper. On the other hand, there are many factors known to affect the measurements and interpretation of results, including weight of animals and speed of movement. Therefore, some researchers train animals to move fluently before the recorded runs (Bozkurt *et al.*, 2008). Moreover, high variation was observed within measurements recorded for the *Dync1i1*^{G482D} and *Dync1i2*^{T172I} mice, therefore raw data were checked before final analysis.

3.4.6 Histological analysis of brains of the *Dync1i2*$^{T172I/T172I}$ mice

Saggital sections of brains isolated from 6 months old wildtype *Dync1i2*$^{+/+}$ and homozygous *Dync1i2*$^{T172I/T172I}$ females were stained and their morphology assessed, with focus on hippocampal formation and cerebellum, where dynein intermediate chain 2 was found to be expressed at high levels (Allen Mouse Brain Atlas, ©2009 by the Allen Institute for Brain Science, http://mouse.brain-map.org) (Figure 3.15). Apart from general staining with H&E, specific antibodies against glial fibrillary acidic protein (GFAP) and calbindin (CALB1) were used, which expression is often affected in neurological deficits. In general, on the anatomical level no differences were found between brain structures of the aged wildtype *Dync1i2*$^{+/+}$ and homozygous *Dync1i2*$^{T172I/T172I}$ females (Figure 3.16 and Figure 3.17).

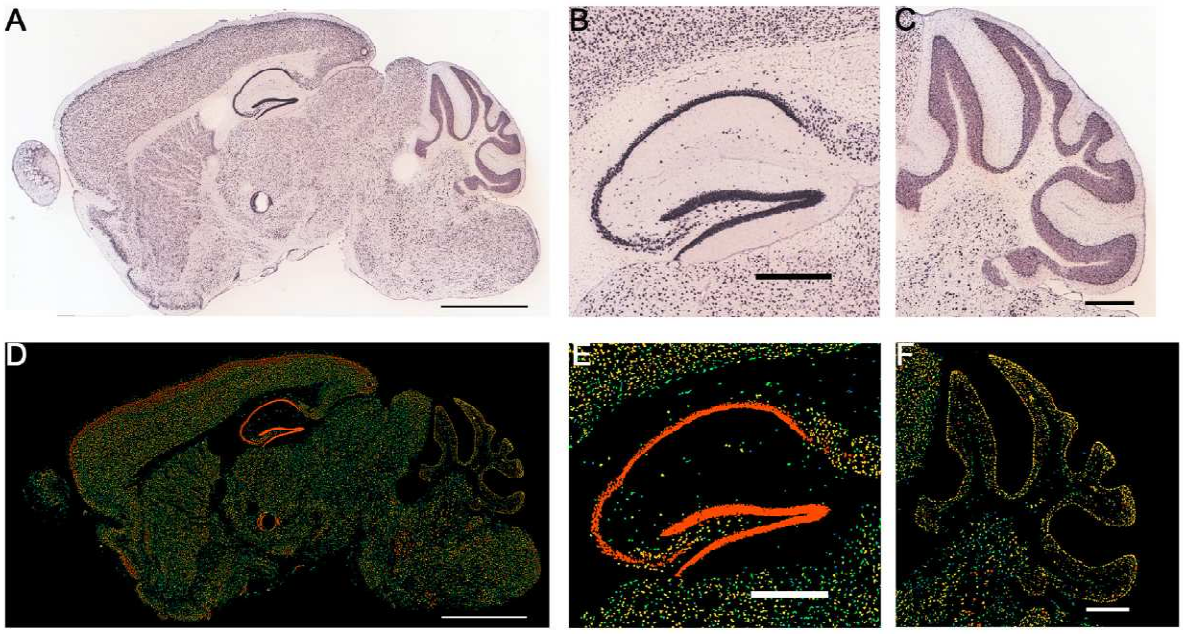

Figure 3.15. Expression patterns of cytoplasmic dynein subunits in mouse brain
In situ-hybridisation with probes detecting *Dync1i2* adapted from Allen Mouse Brain Atlas (©2009 by the Allen Institute for Brain Science, http://mouse.brain-map.org) showing expression pattern (top) and relative abundance where red corresponds to high and blue to low signal (bottom)
A., D. whole brain, scale bar 2.0 mm
B., E. hippocampus, scale bar 500 µm
C., F. cerebellum, scale bar 500 µm

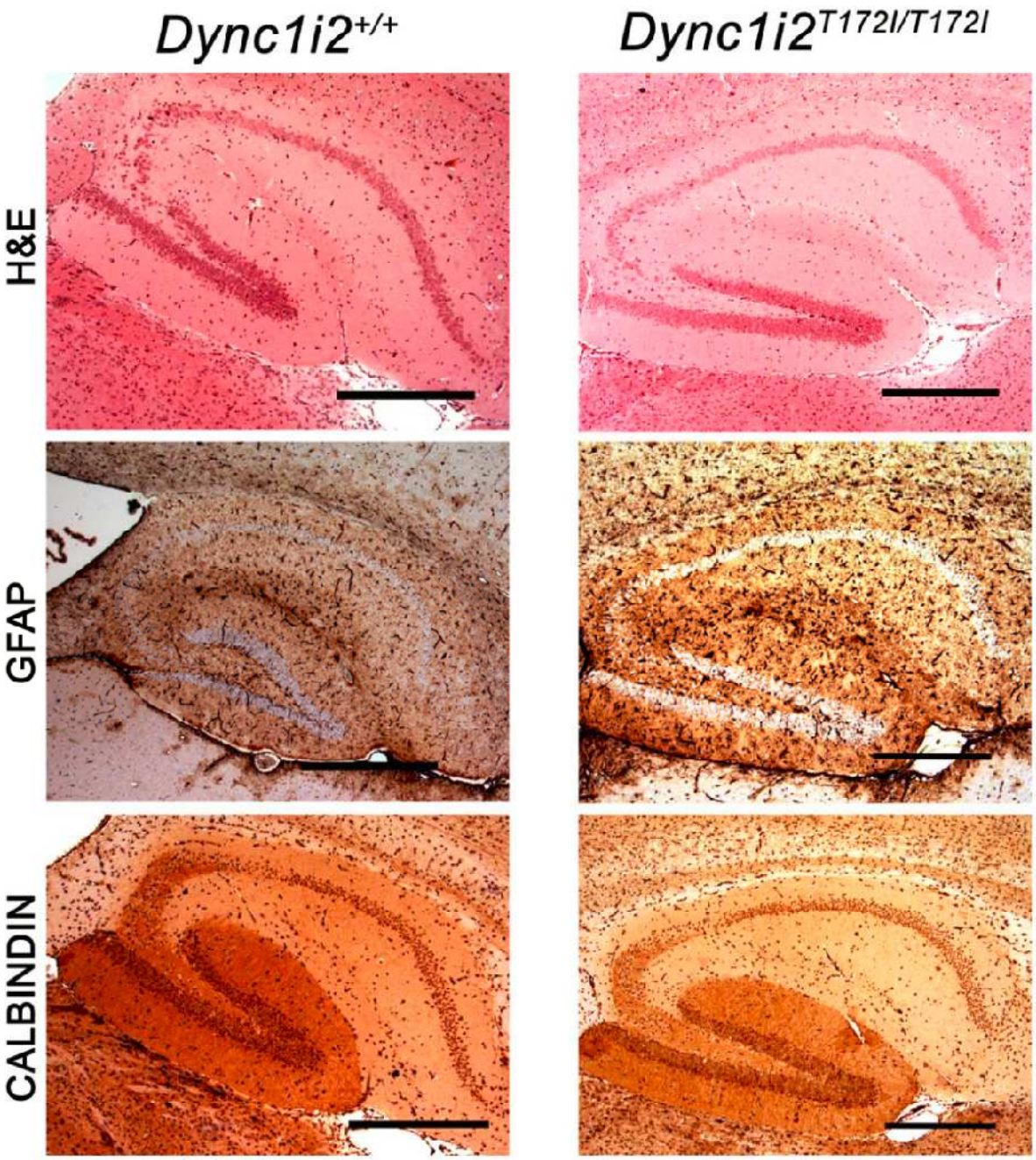

Figure 3.16. Representative pictures of hippocampi isolated from *Dync1i2*^{T172I} mice
Brain sections of wildtype *Dync1i2*^{T172I} and homozygous *Dync1i2*$^{T172I/T172I}$ mice were stained with heamatioxylin and eosin (H&E), antibodies against glial fibrillary protein (GFAP), and calbindin; scale bar 500 µm

Figure 3.17 Representative pictures of cerebella isolated from *Dync1i2*^{T172I} mice (next page)
Brain sections of wildtype *Dync1i2*^{T172I} and homozygous *Dync1i2*$^{T172I/T172I}$ mice were stained with heamatioxylin and eosin (H&E), antibodies against glial fibrillary protein (GFAP), and calbindin; scale bar 500 µm

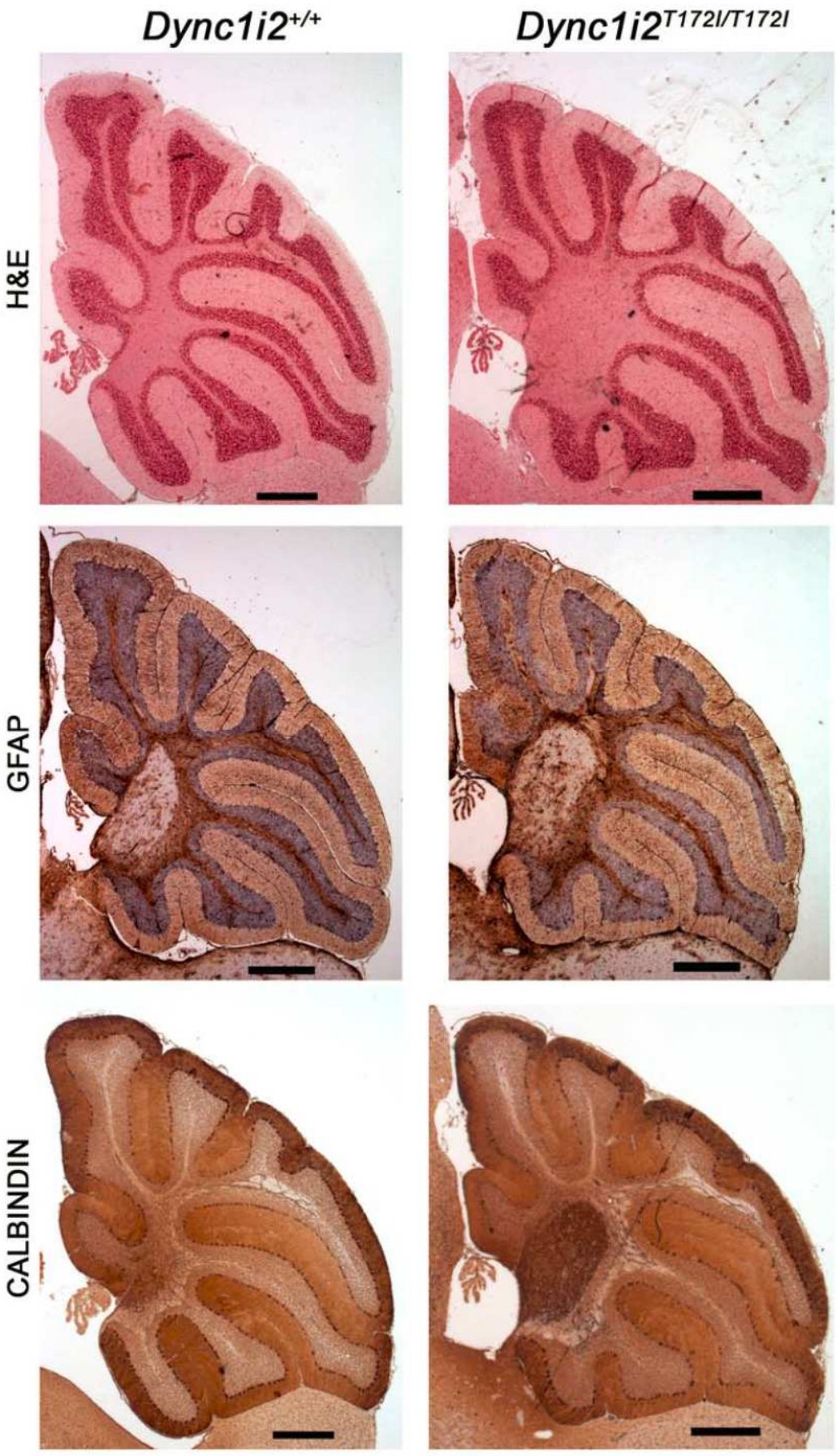
Dync1i2+/+
Dync1i2T172I/T172I
H&E
GFAP
CALBINDIN

3.5 Discussion

In Chapter 3 we describe the origin of 2 novel mouse mutants carrying ENU-induced point mutations in the cytoplasmic dynein intermediate chains 1 and 2 and the analysis of their phenotype. Detailed behavioural test were also carried out, after carefully considering the breadth of possible mutant phenotype and time constrains. The mutations identified: *Dync1i1*^{G482D} and *Dync1i2*^{T172I} are placed in different domains of the intermediate chains, which were predicted to participate in interactions between different subunits of the cytoplasmic dynein complex.

Both mutant mouse lines were established on the C57BL/6J genetic background and homozygous *Dync1i1*$^{G482D/G482D}$ and *Dync1i2*$^{T172I/T172I}$ animals were viable, therefore their phenotype was tested in relation to wildtype littermates (*Dync1i1*$^{+/+}$ and *Dync1i2*$^{+/+}$). While no breeding data of the *Dync1i1*^{G482D} line were available, the *Dync1i2*^{T172I} mutation did not affect an allele transmission, *Dync1i2*$^{T172I/T172I}$ mice were fertile and showed slightly longer survival (section 3.4.2). In addition, the presence of both mutated alleles (*Dync1i1*^{G482D} and *Dync1i2*^{T172I}) did not affect an embryo development at least till E14.5 (section 3.4.3).

The phenotypes arising from mutations are discussed in sections 3.5.1 and 3.5.2, and behavioural traits which were not affected are summarised below. Both mouse lines had normal motor functions (see *Dync1i1*^{G482D} mice discussed in details), consumed the same amounts of food, water, and glucose solution maintaining very similar weight. Behaviour typical for rodents was not affected, as assessed by measuring locomotor activity, burrowing and nesting skills. When anxiety-like behaviour was tested mice did not perform very well (did not leave apparatus), thus small differences might have been missed. Finally, while performance of the *Dync1i1*^{G482D} mice on the spatial working memory task was normal, the spatial working memory was impaired in the *Dync1i2*^{T172I} mice (Table 3.14).

Table 3.14. Summary of behavioural phenotypes of the *Dync1i1*^{G482D} and *Dync1i2*^{T172I} mouse lines
Results of tasks performed presented based on the results of statistical tests, where **n.s**. corresponds to lack of significant differences for p>0.05; trends were noted if p<0.1; NRD – novelty discrimination ratio; genotypes correspond to homozygous mutant *Dync1i1*$^{G482D/G482D}$ or *Dync1i2*$^{T172I/T172I}$ animals; N/A – not applicable

Behaviour/task		*Dync1i1*^{G482D}	*Dync1i2*^{T172I}
Locomotion (section 3.4.4.1)			
Accelerating rotarod		n.s.	n.s.
Multiple static rods	Orient	n.s. (*Dync1i1*$^{G482D/G482D}$ turned faster on rod 1)	n.s.
	Traverse	n.s.	n.s.
Wheel running	Distance	*Dync1i1*$^{G482D/G482D}$ tended to run less	n.s.
	Average speed	*Dync1i1*$^{G482D/G482D}$ tended to run slower	n.s.
	Maximum speed	n.s.	*Dync1i2*$^{T172I/T172I}$ tended to run slower
Metabolic functions (section 3.4.4.2)			
Animal weight		n.s.	n.s.
Food consumption		n.s.	n.s.
Water consumption		n.s.	n.s.
Glucose consumption (7.5%)		n.s.	n.s.
Species specific behaviour (section 3.4.4.3)			
Circadian activity		n.s.	n.s.
Burrowing		n.s.	n.s.
Nesting		n.s.	n.s.
Anxiety-like behaviour (section 3.4.4.4)			
Successive alleys	Time in alley 1	n.s.	n.s.
	Time in alley 2	n.s.	n.s.
	Number of entries to alley 2	n.s.	n.s.
Light/dark box	Latency to emerge from dark	n.s.	n.s.
	Time spent in light	n.s.	*Dync1i2*$^{T172I/T172I}$ tended to spend less time
	Number of entries to light compartment	n.s.	*Dync1i2*$^{T172I/T172I}$ tended to make fewer entries

Table 3.14. Continued

Behaviour/task		*Dync1i1*^{G482D}	*Dync1i2*^{T172I}
Spatial woking memory (short-term habituation) (section 3.4.4.5)			
T-maze (number of correct alternations)		n.s.	*Dync1i2*$^{T172I/T172I}$ made fewer alternation
Y-maze	Exploration time	N/A	n.s.
	Time spent in novel arm	N/A	*Dync1i2*$^{T172I/T172I}$ spent less time
	Time spent in other (familiar) arm	N/A	n.s.
	NRD_{Time}	N/A	n.s.
	Total number of entries	N/A	n.s.
	Number of entries to novel arm	N/A	n.s.
	Number of entries to other (familiar) arm	N/A	*Dync1i2*$^{T172I/T172I}$ made more entries
	NRD_{Entry}	N/A	*Dync1i2*$^{T172I/T172I}$ showed lower values
Gait (section 3.4.5)			
Regularity index		*Dync1i1*$^{G482D/G482D}$ showed increase	n.s.
Base of support (front/hind paws)		*Dync1i1*$^{G482D/G482D}$ showed decrease	n.s.
Foot print (widht/length)		*Dync1i1*$^{G482D/G482D}$ showed increase	n.s.
Swing speed		*Dync1i1*$^{G482D/G482D}$ showed decrease	n.s.

Several of the tasks described in the chapter showed, that both cohorts were diverse despite having been bred with a well known inbred mouse strain (C57BL/6J). All mice were housed and tested in the same environment, but they were established and bred with C57BL/6J in two places (MRC Harwell and MRC Prion Unit). Furthermore, the *Dync1i1*^{G482D} were at N4 and *Dync1i2*^{T172I} at N5 when all the tasks described were performed, therefore the genetic background was the most likely factor responsible for variation observed between wildtype *Dync1i1*$^{+/+}$ and *Dync1i2*$^{+/+}$.

3.5.1 Mutant phenotype caused by the *Dync1i1*^{G482D} mutation

Mutant animals, homozygous for the new allele (*Dync1i1*$^{G482D/G482D}$) were compared with littermates carrying the wildtype version of the gene (*Dync1i1*$^{+/+}$). However small, there were differences observed in gait, namely increase in step regularity, paws placement and decrease in speed of paws movement. Furthermore, homozygous *Dync1i1*$^{G482D/G482D}$ females oriented faster than wildtype *Dync1i1*$^{+/+}$ on the widest static rod (p=0.0319), and all but one *Dync1i1*$^{G482D/G482D}$ females shredded all the material used for nest while two *Dync1i1*$^{+/+}$ animals left twice as much nest-let untorn. Although the observations were not conclusive, an increase in paw coordination in the *Dync1i1*$^{G482D/G482D}$ animals would explain faster orientation on the rod and more effective shredding. Building a nest involves use of fore paws to pull material apart and break it down (Upchurch and Schallert, 1983).

In addition, performance of the mutant *Dync1i1*$^{G482D/G482D}$ mice on the running wheel was worse than *Dync1i1*$^{+/+}$ littermates, regarding both average speed (p=0.0618) and distance run (p=0.0665). Because the results obtained on rotarod were comparable for both *Dync1i1*$^{+/+}$ and *Dync1i1*$^{G482D/G482D}$ mice, fatigue was not the factor affecting the wheel running. On the other hand, wheel running could also reflect the ability to learn motor skills, and the steady increase in running speed was often used as a learning index. A similar reduction in running was reported for a mutant *Foxp2*$^{R552H/+}$ mouse line, which apart from impaired motor learning skills, displayed also deficits in synaptic plasticity. Interestingly though, neither *Foxp2*$^{R552H/+}$ nor *Dync1i1*$^{G482D/G482D}$ mutant mice differed from wildtype animals when anxiety and working memory were tested (Groszer *et al.*, 2008).

Gait is often affected by impairment or damage to the central nervous system. Solberg *et al.* (2006) carried out a comprehensive quantitative analysis of various parameters across 4 modes of locomotion, showing that defects of overground walking could be detected with high accuracy by assessing body height, base of support, stride length, paw position, front hind paws coordination, and pattern of footfalls. Furthermore, animal's gait depended on a nature of injury or manipulation, and distinct parameters also differed accordingly. The examples of gait parameters assessed in various conditions using the

CatWalk XT system are given for comparison in Table 3.15. The gait of the *Dync1i1*$^{G482D/G482D}$ females might share characteristics with a model of neuropathy and sciatic nerve injury. On the other hand, the increase in the paw width in relation to paw length (WTH/LTH) seemed to be unique feature of the mutant *Dync1i1*^{G482D} mice. In a model of the sciatic nerve injury the increase in the print length is accompanied by decrease in the spread of toes due to denervation of foot muscles (Deumens *et al.*, 2007).

Table 3.15. Summary of changes in gait parameters recorded with the CatWalk XT
Three rodent models presenting different neurological deficits were compared in relation to the *Dync1i1*^{G482D} mice, on the left selected gait parameters, in bold features similar to the *Dync1i1*^{G482D} mouse line, in case of sciatic nerve injury 2 publications are referred and distinguished by underline; arrows indicate direction of change (↓ decrease or ↑ increase), paws taken into account marked as F – front paws, H – hind paws, F/H – ratio of front to hind paws, HL/HR – ratio of left to right hind paw, arbitrary annotation used to measure effects of an unilateral injury, WTH/LTH – ratio of width to length of a print, n. s. – effect not significant, in brackets arrows indicate direction of a trend observed

Deficit and reference	*Dync1i1*^{G482D}	**Neuropathy** induced by phytanic acid (Refsum disease) Ferdinandusse *et al.*, (2008)	**Neurotmesis** (sciatic nerve resection) or <u>sciatic nerve crush</u> Bozkurt *et al.*, (2008) Deumens *et al.*, (2007)	**Neuropathic pain** in induced monoarthritis Angeby-Moller *et al.*, (2008)
Model used	Mouse	*Phyh*$^{-/-}$ mouse	Adult rat	Adult rat
Regularity	**↑**		**n.s.** **<u>n.s</u>**	**↓**
BOS	**↓ (F/H)** **↓ (H) ↑ (F)**	**↓ (H), F n.s.**	**↓ (H)**	
Stride length	n.s.		n.s.	
Print area	n.s. (↓)	↓ (F, H)	↓ (HL/HR) <u>↓ (HL/HR)</u>	↓ (H)
Print width	**n.s. (↓)** **↑ WTH/LTH**	**↓ (H)**	**↓ (HL/HR)** **<u>↓ (HL/HR)</u>**	
Print length	n.s. (↓)		↓ (HL/HR) <u>↓ (HL/HR)</u>	
Swing	**n.s. (↑)**		**↓ (HL/HR)** **<u>↑ (HL/HR)</u>**	
Stand	n.s.	n.s.	↓ (HL/HR) <u>↓ (HL/HR)</u>	↓ (H)
Swing speed	**↓**		**↓ (HL/HR)**	
Duty cycle	n.s (↓)		↓ (HL/HR)	

3.5.2 Defects in the short-term memory in the *Dync1i2*$^{T172I/T172I}$ mice

There are several types of memory distinguished in the behavioural studies, and often the same apparatus is used with various setups, depending on a method of data collection and analysis different behaviours are described. Therefore, a phenotype displayed by the *Dync1i2*^{T172I} mutant mice was compared with a mouse model, which had a similar performance under the same conditions. The *Dync1i2*^{T172I} mice were tested in the novelty preference task with 2 min habituation in the Y-maze, the results were recorded and analysed as described in Sanderson *et al.*, 2009. The comparison of two parameters (time spent and arm entries) showed that mutant *Dync1i2*$^{T172I/T172I}$ females performed in a very similar fashion as *GluA1*$^{-/-}$ mice, which supports the notion of an impaired working (short-term) memory. Moreover, this outcome was not replicated in mice with lesioned hippocampal formation (Sanderson *et al.*, 2009). The deficits in the *GluA1*$^{-/-}$ mice were specifically restricted to working memory, whereas long-term memory was enhanced and learning crucial for spatial reference memory intact, thus evaluation of the *Dync1i2*$^{T172I/T172I}$ mice in relevant task would be priority.

The discrepancy in the nomenclature should also be noted, as spontaneous alternation in rodents does not model perfectly human working memory; therefore, Sanderson and Bannerman, (2010) suggested a term of short-term habituation to spatial stimuli.

3.5.3 Future directions

Two new mutant mouse lines carrying single point mutations in the cytoplasmic dynein intermediate chains, *Dync1i1*^{G482D} and *Dync1i2*^{T172I} are a valuable resource and extend the knowledge of the cytoplasmic dynein complex. Both mutations cause distinct phenotypes when present in the homozygous state, with *Dync1i1*$^{G482D/G482D}$ affecting gait and possibly causing mild neuropathy and *Dync1i2*$^{T172I/T172I}$ impairing working spatial memory. Both phenotypes are specific to these lines and were not described in any of the known mouse lines with mutations in other subunits of the cytoplasmic dynein (see section 1.5.1). Nonetheless, in all the mutants characterised so far the mutations cause various neuronal

deficits, thus supporting notion of the importance of the cytoplasmic dynein complex in functions of neurons.

Because the mutant phenotypes were mild, there were few traits which would require more detailed analysis, including more mice, mixed sex, or cohorts of mice at different age. Likewise, The performance of the *Dync1i1*$^{G482D/G482D}$ mice on a running wheel suggested a decrease in the motor skills which might be related to the learning ability. On the other hand, data obtained during gait analysis point towards deficits in the peripheral nerves or distinct coordination. Therefore, more detailed tasks evaluating learning, precise paw movement (e.g. grasping, (Kieran *et al.*, 2005; Tucci *et al.*, 2007) or physiological measurements of nerve conductance would be required.

As far as the homozygous *Dync1i2*$^{T172I/T172I}$ mice were concerned, it would be crucial to assess the functions of reference and long-term memory. Furthermore, brains isolated from mutant *Dync1i2*$^{T172I/T172I}$ animals were structurally normal; the functional analysis of hippocampal region and neuronal plasticity might be helpful in dissecting the roles of cytoplasmic dynein in formation of memory. Recently, electrophysiology was combined with fMRI in a study of working memory deficits related to neurofibromin resulting in a model of increased inhibition of a circuits in medial prefrontal cortex (mPFC) (Shilyansky *et al.*, 2010). Furthermore, although time consuming, the long term observation of survival of bigger (over 20 per genotype) cohorts would bring definite answers as to the impact of the *Dync1i2*^{T172I} mutation on the longevity of a mouse.

Introduction of additional mutant alleles by crossing different lines often results in progeny displaying modified phenotype or completely new features, as in case of the *Dync1h1*^{Loa} mice (Banks et al., 2009; Kieran et al., 2005). Therefore, another step would be characterisation of double homozygous *Dync1i1*$^{G482D/G482D}$ *Dync1i2*$^{T172I/T172I}$ mice, as so far we only know that the presence of both alleles does not cause developmental deficits at least till midgestation (section 3.4.3).

So far several mutant alleles of mouse cytoplasmic dynein 1 intermediate chains (*Dync1i1*, *Dync1i2*) have been deposited in the International Mouse Strain Resource database (IMSR, v.2.45, http://www.findmouse.org). The majority of mutations have arisen in a gene trapping or targeted mutagenesis experiments and causes disruption of a gene structure (null allele); those are available as embryonic stem (ES) cell lines. The ES cell lines carrying null alleles of *Dync1i1* have been generated by the NIH Knock-Out Mouse Project (KOMP, CSD30098) while conditional knock-out alleles of the *Dync1i2* have been created by European Conditional Mouse Mutagenesis Program (EUCOMM, ID 31464) at the Wellcome Trust Sanger Institute, UK. As for today, the transmission of a targeted mutation in the *Dync1i2* gene to a germ line and the mutant genotype of the progeny have been confirmed, yet a phenotype of mutant animals needs to be assessed. More details can be found at the International Knock-out Mouse Consortium website (http://www.knockoutmouse.org). All those line will further our understanding in the functions of the cytoplasmic dynein intermediate chains.

4. Insight into effects of single point mutations in the cytoplasmic dynein intermediate chains *Dync1i1*^{G482D} and *Dync1i2*^{T172I} using cellular models

4.1 Characteristics of mouse embryonic fibroblast cell lines

Fibroblasts are heterogeneous population of cells present in stroma of all organs, although their features are not well defined. In adult mammals fibroblasts produce extracellular matrix (EMC), thus providing mechanical support and a framework for organs. Furthermore, they can produce cytokines in response to tissue damage (Flavell *et al.*, 2008). The functional heterogeneity may reflect different cellular populations (primary mesenchyme, local epithelial mesenchyme, bone marrow precursors) from which fibroblasts are thought to originate. Usually, fibroblasts were characterised as terminally differentiated cells, adherent to plastic, which displayed contact inhibition, and generate EMC. In addition, the cellular markers associated with fibroblasts included vimentin (VIM), α-smooth muscle α-actin (α-SMA), collagen I (COL1A1) (Alt *et al.*, 2011). However recently, the usefulness of these diagnostics was questioned, because for example commonly used human skin-derived fibroblasts (hSDFs) displayed the same cellular markers and differentiation potential as adipose tissue-derived stem cells (hASCs) (Alt *et al.*, 2011).

Mouse embryonic fibroblasts (MEFs) are isolated from ventral tissues of a whole embryo between E12.5 – E14.5 days of age, and they are used to study genetic alteration, cell differentiation, or as a feeder layer for embryonic stem cells (ESC). MEFs are primary cells, which display signs of cellular senescence, which limits the 'life-span' to 10-20 passages (vom Brocke J. *et al.*, 2006). This feature, however, results from oxidative stress in culturing conditions (~ 20% of oxygen) and the process of senescence can be withheld when fibroblasts are kept in atmosphere with low (3%) oxygen levels. Nonetheless, if kept in culture, MEFs immortalise spontaneously due to genetic alterations, which resemble transformations seen in tumours, with the majority of genetic aberrations located in known suppressor genes (e.g. p53/p19^{ARF}) (Odell *et al.*, 2010). The immortalisation often follows a period of limited growth, and increase in proliferation indicates the outgrowth of transformed clones.

The first stable MEF lines were derived from spontaneously mutated clones, and this feature was reflected in cell properties, which differed depending on the conditions employed (Todaro and Green, 1963). The immortalised Swiss/3T3 MEF line displayed contact inhibition and inability to form tumours when transplanted into a mouse, in spite of bearing chromosomal rearrangements and hypotetraploidity.

MEFs were used to study cytoskeletal rearrangements and signalling pathways active during wound healing. In migrating cells necdin (NDN) initiated polarisation of cytoskeleton via cell division cycle 42 (CDC42) mediated phosphorylation of myosin light chain (MLC) (Bush and Wevrick, 2010), while protein phosphatase 1, regulatory (inhibitor) subunit 15A (PPP1R15A) was shown to regulate both translation via eIF2α, and migration by inhibiting expression of non-muscle myosin heavy chain 2A (MYH9) (Tanaka *et al.*, 2010). Furthermore, MEFs were used as a support for embryonic myoblasts, increasing their attachment and differentiation in cardiac cells (Pfannkuche *et al.*, 2010).

Embryonic fibroblasts originate from mesenchymal cells and specific tissue lineages can be derived in the presence of morphogenetic factors. S-phase kinase-associated protein 2 (SKP2) was shown to be a component in the adipocyte differentiation pathway (Okada *et al.*, 2009), adipogenesis was also induced by treatment with a bone morphogenetic protein 2 (BMP-2) (Sun *et al.*, 2009). In addition, depending on the BMP-2 concentrations MEFs were transformed in chondrocytes via up regulation of SRY-box containing gene 9 (SOX9) transcription (Pan *et al.*, 2008). Adipocitic and osteoblastic potentials of MEFs were found to be modified by Krüppel-like factor 7 (KLF7) (Caiazzo *et al.*, 2010). Moreover, MEFs can be reprogrammed into pluripotent stem cells (iPSC), with features of stem cells on both, transcriptional and epigenetic levels. Examples of proteins involved in the reversal include an orphan nuclear steroid hormone receptor β (ESRRB) acting with transcription factors (POU5F1 and SOX2) (Feng *et al.*, 2009), or human mitochondrial ribosomal protein S18-2 (MRPS18-2) (Kashuba *et al.*, 2009).

4.2 Roles of the cytoplasmic dynein complex in retrograde vesicular transport

The intra-cellular trafficking is one of the basic properties of a cell regardless of the organism or a cell type. Retrograde transport often refers to the dynein dependent movement of a vesicular compartment, which consists of endosomes, Golgi network, and endoplasmic reticulum (ER). A general mechanism involves internalisation of a cargo (receptor, proteins) at the plasma membrane and formation of early endosomes (EE). Endosomes are transported to perinuclear endocytic recycling compartment (ERC), where cargo is sorted from receptors (Stenmark, 2009). During the sorting, receptors and cargoes are directed to subsequent compartments, whose functions are well determined: recycling endosomes move receptors back to the plasma membrane (e.g. transferrin receptor, TfnR), late endosomes (LE) fuse with lysosomes and cargoes are degraded after fusion with lysosomes or phagosome (e.g. EGF receptor, EGFR), or endosomes can enter trans-Golgi network (TGN). In addition many enzymes and structural proteins are shuffled from ER back to the Golgi complex (Johannes and Popoff, 2008 and references therein).

Each step on the route is strictly regulated and often involves several protein complexes interacting in a well defined manner. All the events are controlled by RAB GTPases, whose presence identifies a membrane compartment and they are actively involved in vesicle budding, fusion, recruitment of effectors and motility (Stenmark, 2009). There are over 60 different RAB GTPases known in the human genome, and the GTP hydrolysis causes conformational change, which is necessary for docking at the membrane. Many of RAB GTPases have been characterised, including RAB5, which initiates vesicle budding and early endosomes formation. During maturation to late endosomes RAB5 is replaced with RAB7, which directs vesicles to degradation. On the other hand, RAB4 and RAB11 are found in the compartment of fast and slow recycling endosomes (Chen *et al.*, 2008). The dynein complex does not only move early endosomes towards the Golgi complex as it also promotes receptor sorting, membrane fusion and maturation to late endosomes (Driskell *et al.*, 2007). In addition, cytoplasmic dynein was found to interact with sorting nexin-4 (SNX4) and WW, C2 and coiled-coil domain containing protein 1 (WWC1/KIBRA) (Traer *et al.*, 2007). Discrete endocytic compartments are associated with cytoplasmic dynein,

which is recruited to vesicles by RAB GTPases and their accessory complexes, however the mechanisms of its recruitment and detailed interactions are not always known (Hutagalung and Novick, 2011).

In parallel with characterisation of mutant mouse lines, we assessed effects of the single point mutations in various subunits of the cytoplasmic dynein complex on the retrograde trafficking in MEFs.

4.2.1 Assembly and positioning of Golgi apparatus

The Golgi complex lies next to the MTOC, and is an organelle with both distinct functions and spatial organisation. It forms ribbon made of interconnected stacks of membranes with well defined polarity (*cis, trans*) maintained by many protein complexes. However, strict boundaries between endoplasmic reticulum (ER) and Golgi complex are hard to define (Hehnly and Stamnes, 2007). A general route starts in ER where proteins are synthesised and are packed in vesicles at ER exit sites (ERES), which then fuse with tubular ER-Golgi intermediate compartment (ERGIC) and are sorted. Translocation through the Golgi cisterns (from c*is*- to *trans*-) is associated with modifications, sorting and packing in secretory vesicles (Wilson *et al.*, 2010).

In unpolarised mammalian cells Golgi ribbon is located in the vicinity of centrosomes, where it closely associates with microtubules (MTs) and a matrix of actin filaments. Furthermore, additional MTs are nucleated in the region of the *cis*-network, where γ-tubulin ring complex (γ-TuRC) interacts with A-kinase anchor protein 9 (AKAP9) and golgin A2 (GOLGA2). Consequently, the Golgi apparatus is surrounded by actin and MTs based motor complexes, which along with trafficking vesicles to and from the Golgi network, also maintain its organisation. Therefore, any disturbance in motor function affects the structure or positioning of the Golgi apparatus. Cytoplasmic dynein complex 1 (DYNC1) was shown to associate preferably with the peripheral membranes of the network (ERGIC and the intermediate part of the Golgi apparatus) and it cycles between ER and Golgi membranes (Roghi and Allan, 1999). Moreover, cytoplasmic dynein 2 heavy chain 1

(DYNC2H1) was also found associated with Golgi membranes in cells devoid of cilia (Vaisberg *et al.*, 1996).

4.2.2 Overview of the epidermal growth factor (EGF) uptake, trafficking, and degradation

Epidermal growth factor (EGF) belongs to a well characterised family of peptides, which mediate cell survival, proliferation, and differentiation (Sorkin and Duex, 2010). The EGF binding to its receptor (EGFR) initiates both signal transduction and endocytosis leading to lysosomal degradation, however this chapter focuses on endosomal trafficking.

In the presence of EGF, the monomeric receptors dimerise and autophosphorylate, which results in fast internalisation of the EGF-EGFR complex within 10 min (Schmidt-Glenewinkel *et al.*, 2009). The endosomes undergo temporal and spatial evolution during which number of vesicles and their size increase reaching its maximum 30 min after stimulation. During this phase EGF is found in early endosomes, which are transported by cytoplasmic dynein towards the perinuclear area (Rink *et al.*, 2005). The sorting step is crucial in the EGF-EGFR trafficking, and in normal conditions the ligand-receptor complexes are directed to multivesicular bodies (MVB), which fuse with lysosomes, thus degrading both ligand and its receptor (Traer *et al.*, 2007). Approximately 60 min after stimulation mature MVBs could be easily identified, which coincided with on going lysosomal degradation of the EGF (50% degraded) (Futter *et al.*, 1996). One of the long term-effects of the EGF on the epithelial cells was stimulation of locomotion and changes in cell morphology due to cytoskeleton remodelling (Torok *et al.*, 1996). Furthermore, increased motility was associated with induction of expression of the cytoplasmic dyneins observed 10 hours after the EGF treatment.

4.2.3 *Salmonella enterica* ser. Typhimurium as an alternative model to study endocytosis

A eukaryotic cell with its complex processes makes a desirable environment for many pathogens, which are known to take over cellular machinery. Apart from viruses (mentioned in section 1.3), there are many pathogenic bacteria, which manipulate cellular machinery in an intricate manner; therefore pathogens can be used as a tool to study cellular responses. Bacteria responsible for intestinal and systemic infections are Gram-negative *Salmonella enterica,* which infect a variety of animals but can also survive in the environment (Ramsden *et al.*, 2007a). There are several serovars characterised; except for serovar Typhi, all of them cause localised intestinal infections (Spano and Galan, 2008).

Out of those, serovar Typhimurium (referred later on as *Salmonella* typhimurium) is often used to study molecular mechanisms of infection. Once bacteria cross a plasma membrane, they exploit the endocytic pathway to create an intracellular compartment, in which *Salmonella* typhimurium replicate (Ramsden *et al.*, 2007a). Many cell types are susceptible to the bacteria, and *in vivo Salmonella* are usually found in macrophages, dendritic cells, gut epithelium (enterocytes), and fibroblasts (Garcia-del *et al.*, 2008). Moreover, both an entry mode and replication efficiency of intracellular *Salmonella* typhimurium, are cell specific: only macrophages are capable of active phagocytosis, bacteria replicate easily in cytoplasm of epithelial cells, whereas cytoplasm of macrophages and fibroblasts is not permissive for replication (Beuzon *et al.*, 2002).

The genome of *Salmonella* typhimurium contains 2 clusters of genes thought to be responsible for virulence (Ramsden *et al.*, 2007b). Their products are secreted by bacteria and interact with host proteins, thus modifying the cellular environment. Proteins coded by *Salmonella* pathogenicity island 1 and 2 (SPI-1, SPI-2) form type III secretion systems (T3SS), which are activated and deposited in host membrane during invasion and intracellular phase respectively. As mentioned before, only macrophages actively uptake *Salmonella* typhimurium, therefore bacteria evolved diverse mechanisms of entry into non-phagocytic cells (Aiastui *et al.*, 2010). Invasion of epithelial cells (HeLa) requires activity of the SPI-1 T3SS, which induces membrane ruffling and formation of filopodia due

to activation of Rho GTPases and actin rearrangement. The F-actin meshwork surrounds newly internalised bacteria, due to *SteC* kinase activity, which was found to mimic Raf-1 signalling (Poh *et al.*, 2008). However, during invasion of fibroblasts additional mechanisms are employed, which while independent of SPI-1, require actin and microtubule cytoskeleton. Furthermore, activity of both phosphatidylinositol 3-kinase (PIK3) and mitogen-activated protein kinase kinase 1 (MAP2K1) is necessary while activation of Rho GTPase family kinases depends on a cell line (Aiastui *et al.*, 2010).

A switch in expression from SPI-1 to SPI-2 T3SS marks the intracellular phase, during which wildtype *Salmonella* typhimurium use the endocytic pathway to move and replicate in a vesicular compartment. The effectors present on the membranes of *Salmonella* containing vesicles (SCV) actively control all the steps by direct interactions with eukaryotic complexes (Ramsden *et al.*, 2007a). The SCV undergo maturation, which is marked by proteins associated with early (EEA1, TfnR, RAB5, RAB11) and then late (LAMP-1, -2, RAB7) endosomes (Guignot *et al.*, 2004). At the same time the recruitment of the kinesin-1 and cytoplasmic dynein enables retrograde transport along MTs (Boucrot *et al.*, 2005). The molecular motors are engaged by bacterial effectors interacting with endsomal complexes (kinesin-1 through SifA - PLEKHM2, cytoplasmic dynein by RAB7 – RILP). Furthermore, the kinesin-1 and cytoplasmic dynein, by pulling membranes along MTs, form a network of tubular *Salmonella* induced filaments (Sifs) (Mota *et al.*, 2009). The final destination of *Salmonella* typhimurium in epithelial cells (HeLa) is a perinuclear region containing Golgi apparatus, where bacteria replicate and form tight clusters, although positioning of microcolony is not essential for replication (Ramsden *et al.*, 2007b). The *Salmonella* microcolonies are relatively immobile once they reach the Golgi stacks; this feature is dependent on SPI-2 and suggests an active tethering to the eukaryotic membranes (Ramsden *et al.*, 2007b). In addition, the activity of SPI-2 effectors disrupts vesicular transport from *trans*-Golgi to the plasma membrane (Kuhle *et al.*, 2006) and bacteria were found to modify a secretory pathway by interacting with secretory carrier-associated membrane proteins (SCAMP 2 and 3) (Mota *et al.*, 2009). Furthermore, after incorporation in the membranes around *Salmonella* typhimurium, SCAMP3 is actively sorted from Sifs containing endosomal markers and moved to the separate tubular compartment (Sits, as

Salmonella-induced SCAMP3 tubules). The exact function of the process is not known, although it might be a mechanism to acquire nutrients and membranes.

The importance of the membrane surrounding each cell of *Salmonella* typhimurium may be reflected by the number of effectors involved in spatial and temporal maintenance of the SCV. Bacteria, which loose the membranes are killed when released to cytosol in macrophages (Beuzon *et al.*, 2002). In the case of epithelial cells, damaged SCV are labelled with LC3 and directed to autophagosomes (Birmingham and Brumell, 2006). The role of SifA, one of SPI2-T3SS, has been studied thanks to the *SifA*$^{-}$ mutant strain, which poses a distinct phenotype (Beuzon *et al.*, 2000). Membrane dynamics of the *SifA*$^{-}$ strain are strongly impaired and bacteria loose the SCV membranes. Furthermore, these strains seldom can be observed in vicinity of the Golgi complex (Ramsden *et al.*, 2007b).

In some cases *Salmonella* typhimurium stays in a state of latency in fibroblasts, which causes asymptomatic persistent infections. Although intracellular growth is restricted in fibroblasts, prolonged residence results in establishment of small colony variants (Cano *et al.*, 2003). The bacteria isolated are genetically stable variants selected for survival in specific conditions. These mutations fall mostly within genes involved in metabolic pathways, and are associated with anaerobic respiration, decreased virulence yet increase in intracellular persistence.

Finally, there are few examples showing complex responses of the host cells to the invading bacteria. George *et al.* (2005) suggested, that increased levels of interferon (IFN) in response to *Salmonella* typhimurium infection induced the expression and alternative splicing of mouse *Adar1*. The role of RNA editing by ADAR1 was also implicated in viral growth after IFN stimulation (Li *et al.*, 2010). Furthermore, bacterial infections have an impact on surrounding tissues, and often result in inflammatory reaction. Likewise, *Salmonella* was implicated as an arthritogenic agent acting via infected rat synovial fibroblasts (Zhang *et al.*, 2004). Infection caused increase in expression of tumor necrosis factor ligand (TNFSF11), which formed a complex with the tumor necrosis factor receptor (TNFRSF11A), thus inducing osteoclast differentiation and bone resorption.

4.3 Project overview

Trafficking of membranous organelles was investigated using as a model MEFs lines, which were isolated from wildtype and mutant animals (*Dync1i1*^{G482D}, *Dync1i2*^{T172I}, and *Dync1h1*^{Loa}). The cellular localisation of the dynein complex was examined along with dynamics of the Golgi complex, endosomal degradation and trafficking.

4.4 Results

This chapter presents results of various assays employed to investigate the effects of mutations in subunits of the cytoplasmic dynein on membrane trafficking. The mouse lines, from which cells were rederived were *Loa,* carrying a mutation in the heavy chain (*Dync1h1*^{Loa}), newly characterised animals with mutation in the intermediate chain 2 (*Dync1i2*^{T172I}), and cells isolated from embryos carrying double homozygous mutant alleles of the intermediate chains 1 and 2 (*Dync1i1*^{G482D} *Dync1i2*^{T172I}). In all cases MEF lines were compared with wildtype 'littermate' lines. In all experiments described the same cell lines, derived from animals carrying wildtype and mutant alleles of the cytoplasmic dynein subunits were used.

4.4.1 Colocalisation of the cytoplasmic dynein complexes with microtubules in wildtype (*Dync1i1*$^{+/+}$ *Dync1i2*$^{+/+}$) and homozygous (*Dync1i1*$^{G482D/G482D}$ *Dync1i2*$^{T172I/T172I}$) mouse embryonic fibroblasts

4.4.1.1 Remarks on quantification and statistical approach

Fluorescence based microscopy provides great tools for visualisation of intracellular structures and processes. Along with a qualitative description the quantitative analysis is possible, although it has many limitations, determined by optical resolution, physical properties of fluorochromes, method of acquisition etc., which are discussed in detail in Bolte and Cordelieres, 2006. One of the frequently quantified features is colocalisation of intensities of different markers, which represents physical overlap of cellular components. Recently, a term 'protein – protein proximity' was suggested as a replacement for 'colocalisation', as because of limited resolution it is simply impossible to locate interacting proteins directly (except for FRET, which is not discussed) (Wu *et al.*, 2010). Several quantitative methods have been proposed, however they are often based on assumptions which are rarely fulfilled by biological samples. The intensity correlation coefficient based (ICCB) analysis employs a statistical approach to calculate parameters, which express an overlap of pixel intensities from 2 sources (Bolte and Cordelieres, 2006). Because all the pixels in the picture are taken into account (global statistics), the results are affected by many factors (e.g. noise, background, uneven intensities), some of which can be reduced by applying intensity thresholds. Therefore, object based analysis has been proposed, when the level of colocalisation is calculated only in the area defined by objects of interest. Because methods restricted to a certain region of interest (ROI) are not free from bias caused by a chance distribution, additional steps are required (Fletcher *et al.*, 2010). Simulations of sets of images with randomly distributed intensities have been shown to accurately estimate levels of chance colocalisation, which then can be applied to accurately estimate statistical significance of results observed in biological samples. Furthermore, image manipulations, which remove noise and subtract non-specific or out of focus intensities (median filtering, image restoration/deconvolution) were shown to greatly increase signal-to-noise ratio thus improve accuracy of subsequent colocalisation

(Landmann and Marbet, 2004). A multi-step protocol, which employs an improved image cross-correlation spectroscopy (ICCS) approach, has been recently proposed by Wu *et al.*, (2010). The output value corresponding to the fraction of colocalised fluorescent molecules was described as protein-protein proximity index (PPI). When compared with other popular methods, estimations obtained with PPI were more accurate and less sensitive to intrinsic heterogeneity.

4.4.1.2 Analysis of cytoplasmic dynein complex associated with microtubules in MEFs

The colocalisation module provided with the Volocity software (Perkin Elmer) is based on a method described by Mander, yet improved due to applying additional thresholding, which corrected bias caused by non-specific background (Barlow *et al.*, 2010). Although Mander's method is sensitive to noise and no spatial exploration is possible, it gives reliable estimates of colocalisation when sets of pictures are compared. The algorithm reports thresholded Pearson's correlation coefficient (PCC), Mander's coefficients for both channels (M_X, M_Y), and voxel ratio Ch.X/Ch.Y (referred as pixel ratio as all the images were taken only in XY plane). Values of PCC range from -1.0 to 1.0 and refer to a linear relationship between intensities of 2 channels within the set thresholds. M_X and M_Y described fractions of pixels from each channel (X or Y), which colocalised with the other channel (Y or X) in relation to total intensities of pixels in channel X or Y. Colocalisation coefficients (e.g. M_X) ranged between 0.0 and 1.0, when 0 indicated that none of the signal within threshold in channel X existed as colocalised with the channel Y. These coefficients were suggested to be useful in evaluating proportions of colocalised signals (Bolte and Cordelieres, 2006). Finally, values of pixel ratio X/Y referred to the ratio of number of pixels in channel X to number of pixels in channel Y, which were within threshold.

Localisation of the cytoplasmic dynein complex in relation to the microtubules (MTs) was examined in mouse embryonic fibroblasts carrying wildtype (*Dync1i1*$^{+/+}$ *Dync1i2*$^{+/+}$, n=3) and homozygous mutant alleles of the cytoplasmic dynein intermediate chains 1 and 2 (*Dync1i1*$^{G482D/G482D}$ *Dync1i2*$^{T172I/T172I}$, n=3). Cells were fixed, α-tubulin and dynein

intermediate chains (1 and 2) labelled as described in section 2.6.8. In order to obtain accurate images, Plan-Apochromat 63x/1.4 Oil DIC objective was used with twice magnified (2x zoom) field of view, so that the size of imaged area was 73.1 μm^2. Digital images were recorded in 12-bit mode, processed by removing noise (fine median filter) and defining ROI based on cell outline. Colocalisation of signal intensities was calculated for microtubules in channel X (annotated with MTs) and dynein intermediate chains in channel Y (annotated with IC74). Upper and lower intensity thresholds were set for each channel: 100 – 4090 for MTs signal and 800 – 4090 for IC74 signal.

An objective with high magnification was used, and most of the pictures contained only a portion of a cell, where bundles of microtubules were clearly visible. On the other hand, the cytoplasmic dynein complex was not distributed evenly throughout the cell, and the signal corresponding to the intermediate chains was often enhanced in the perinuclear area. Therefore, in order to control for possible differences caused by cell topology, values of ratio MTs/IC74 were used as a criterion to annotate cell images to bins: bin 1 (ratio: 1 - 2), bin 2 (ratio: 2 – 4), and bin 3 (ratio: 4 – 5) (Figure 4.1). Within bins, colocalisation parameters (PCC, M_{MTs}, and M_{IC74}) calculated for each image were compared for effect of genotype on distribution of the cytoplasmic dynein complex.

Distribution of the cytoplasmic dynein complex was assessed in untreated MEF cell lines, which were derived from wildtype *Dync1i1*$^{+/+}$ *Dync1i2*$^{+/+}$ (n=3) and double homozygous *Dync1i1*$^{G482D/G482D}$ *Dync1i2*$^{T172I/T172I}$ (n=3) embryos. Twenty pictures of each cell line analysed by calculating colocalisation parameters as described. Bins distinguished corresponded to amount of MTs staining relative to IC74 signal, and most images were located in Bin 2 while only few were annotated to Bin 3 (Table 10.2, Appendix 10.2, Figure 4.2A). Results are summarised in Table 4.1.

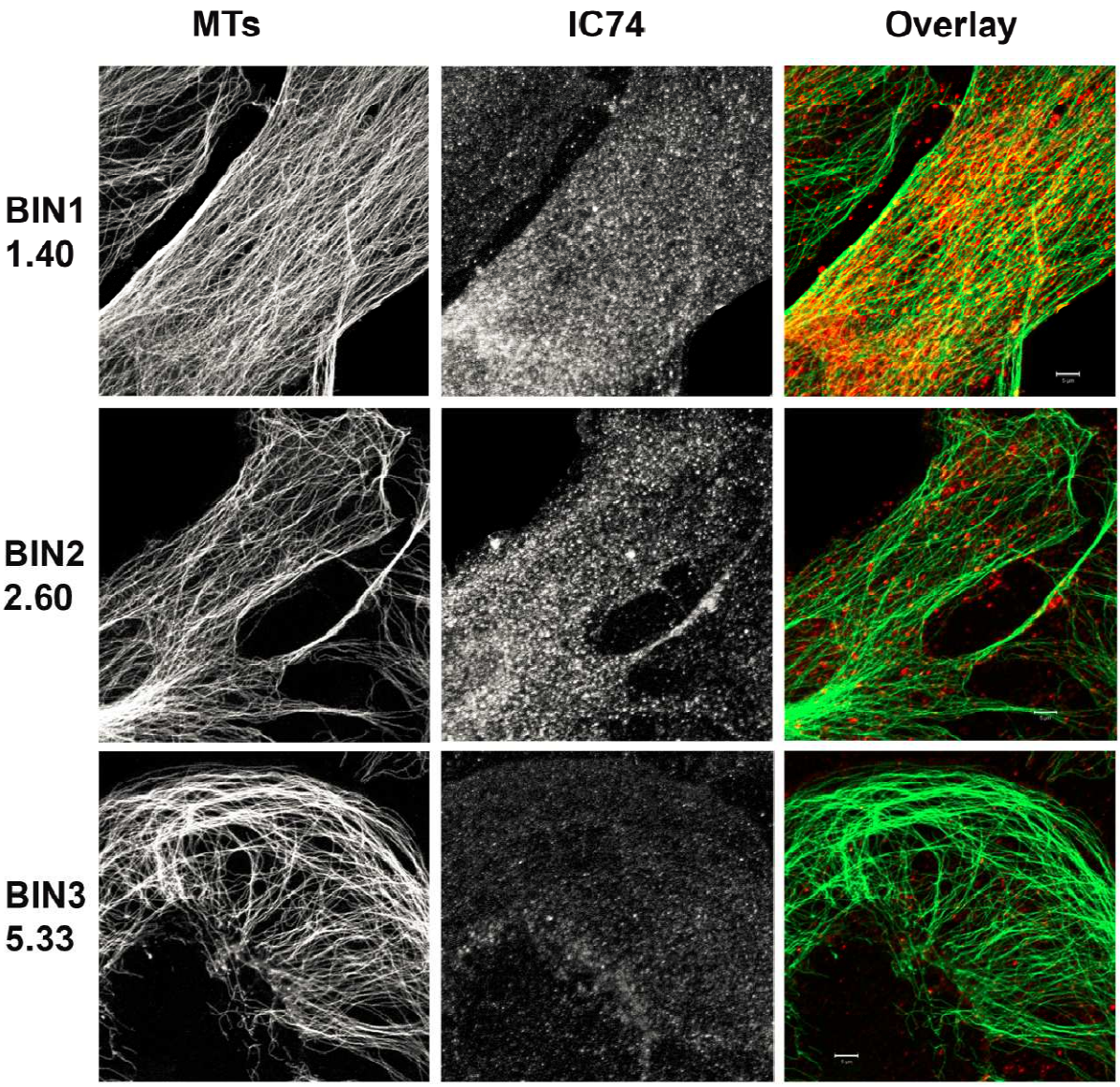

Figure 4.1. Representative pictures of wildtype (*Dync1i1*$^{+/+}$ *Dync1i2*$^{+/+}$) MEFs and the annotation to 3 bins
Intracellular structures were stained with antibodies against α–tubulin (MTs, green) and cytoplasmic dynein intermediate chains (IC74, red); cells were annotated to bins (1-3) based on the thresholded value of pixel ratio of MTs/IC74 as shown for each picture sequence; scatter plots correspond to pixels colocalised in each channel; nuclei were not labelled and only their outlines are visible; scale bar 5µm

Table 4.1. Summary of analysis of colocalisation of MTs and dynein intermediate chains
Colocalisation of microtubules and cytoplasmic dynein complex presented based on the results of statistical tests, where **n.s**. corresponds to lack of significant differences for p>0.05; trends were noted if p<0.1; for cells annotated to distinct bins values of each parameter were compared between wildtype *Dync1i1*$^{+/+}$*Dync1i2*$^{+/+}$ and double homozygous *Dync1i1*$^{G482D/G482D}$ *Dync1i2*$^{T172I/T172I}$ cell lines; detailed analysis is presented in Appendix 10.2

Parameter	Bin 1	Bin 2	Bin 3
Pearson's colocalisation coefficient (PCC)	n.s.	n.s.	n.s.
Mander's colocali-sation coefficient MT intensities (M_{MTs})	n.s.	*Dync1i1*$^{G482D/G482D}$*Dync1i2*$^{T172I/T172I}$ tended to show lower values	n.s.
Mander's colocalisation coefficient IC74 intensities (M_{IC74})	n.s.	n.s.	n.s.

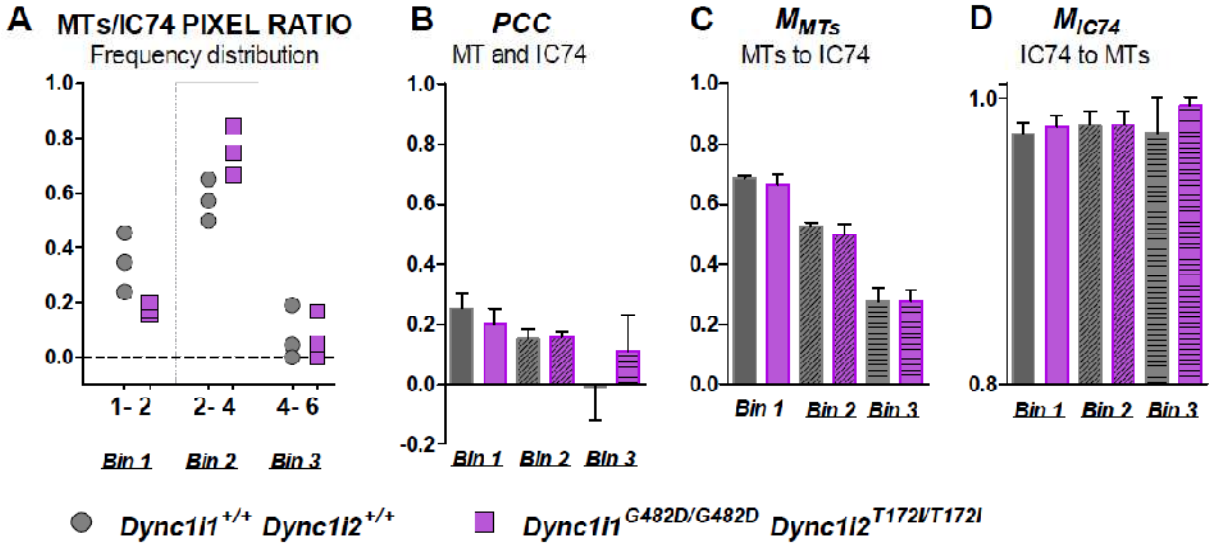

Figure 4.2. Analysis of colocalisation parameters calculated for MTs and cytoplasmic dynein intermediate chains
Parameters calculated for 3 bins represented as mean±standard deviation (SD); legend refers to all graphs and colours correspond to wildtype *Dync1i1*$^{+/+}$ *Dync1i2*$^{+/+}$ (grey), double homozygous *Dync1i1*$^{G482D/G482D}$ *Dync1i2*$^{T172I/T172I}$ (violet) cell lines; each bin marked with distinct pattern

A. Distribution of images to 3 bins based on the MTs/IC74 pixel ratio, points represent average value from each cell line
B. Values of Pearson's colocalisation coefficient (PCC) calculated for images in each bin
C. Values of Mander's coefficient (M_{MTs}) corresponding to fraction of MTs colocalising with cytoplasmic dynein intermediate chains
D. Values of Mander's coefficient (M_{IC74}) corresponding to fraction of the dynein complexes colocalising with MTs

Pearson's colocalisation coefficient (PCC) did not differ between wildtype and mutant cells (p=0.2876, p=0.8011, p=0.1768) (Figure 4.2B). However, calculations of PCC employed all the pixels within the ROI, therefore Mander's coefficients were also compared, so that proportions of both signals could be related. Values of M_{MTs} corresponded to fraction of MTs signal associated with staining for the dynein intermediate chains and were slightly lower in the mutant *Dync1i1*$^{G482D/G482D}$ *Dync1i2*$^{T172I/T172I}$ fibroblasts when compared with wildtype *Dync1i1*$^{+/+}$ *Dync1i2*$^{+/+}$ cells (Figure 4.2C); the distinction was the biggest in case of images annotated to the second bin (p=0.0737). Furthermore, the M_{MTs} decreased within subsequent bins relative to the increase in MTs signal and MTs/IC74 pixel ratio. On the other hand, the M_{IC74} displayed fairly constant values, which indicated colocalisation of over 95% of the intermediate chains with MTs (Figure 4.2D). Nonetheless, there were no differences observed between wildtype *Dync1i1*$^{+/+}$ *Dync1i2*$^{+/+}$ and homozygous *Dync1i1*$^{G482D/G482D}$ *Dync1i2*$^{T172I/T172I}$ fibroblasts.

In conclusion, single point mutations in both cytoplasmic dynein intermediate chains (*Dync1i1*^{G482D} and *Dync1i2*^{T172I}) affected neither the distribution of the dynein complex nor it association with microtubules within cells examined.

4.4.2 Reassembly of the Golgi complex after nocodazole treatment of MEFs isolated from wildtype (*Dync1i1*$^{+/+}$ *Dync1i2*$^{+/+}$) and double homozygous (*Dync1i1*$^{G482D/G482D}$ *Dync1i2*$^{T172I/T172I}$) embryos

Disruption of microtubule cytoskeleton causes dramatic changes in structure of the Golgi apparatus, which locates at periphery in a form of small stacks (Cole *et al.*, 1996). The 'mini'-Golgi were found to reorganise near the ER exit sites as functional complexes. When MTs repolymerise, the Golgi apparatus is reassembled around microtubule organising centre (MTOC) thanks to the dynein driven transport (Roghi and Allan, 1999). Therefore, the activity of the cytoplasmic dynein can be assessed by monitoring the process of the reassembly of the Golgi stacks after MTs disruption. The Golgi reassembly was assayed in MEFs as described in 2.6.3. Briefly, cells were treated with nocodazole and fixed at 0, 20, and 50 min after nocodazole washout. The overall morphology of the complex was assessed by scoring cells untreated and fixed after 0, and 50 min; whereas detailed image analysis was performed for cells untreated, and fixed at 0, 20, and 50 min.

4.4.2.1 Analysis of morphology of the Golgi complex

Wildtype *Dync1i1*$^{+/+}$ *Dync1i2*$^{+/+}$ and double homozygous *Dync1i1*$^{G482D/G482D}$ *Dync1i2*$^{T172I/T172I}$ cells were examined for Golgi complex morphology at different time points after nocodazole washout. Two experiments were performed and in each at least 300 cells were scored blindly to genotype and experiment for the appearance of the Golgi labelling. There were 3 types distinguished, corresponding to perinuclear complex (reticular or compact), and fragmented within a cytosol (Figure 4.3). In all wildtype (*Dync1i1*$^{+/+}$ *Dync1i2*$^{+/+}$, n=3) and double homozygous (*Dync1i1*$^{G482D/G482D}$ *Dync1i2*$^{T172I/T172I}$, n=3) cell lines, fractions of cells with the distinct morphology were compared across different conditions. The detailed analysis can be found in Appendix 10.3 and Table 10.3, while the results are summarised in Table 4.2, all the values correspond to mean±standard deviation (SD).

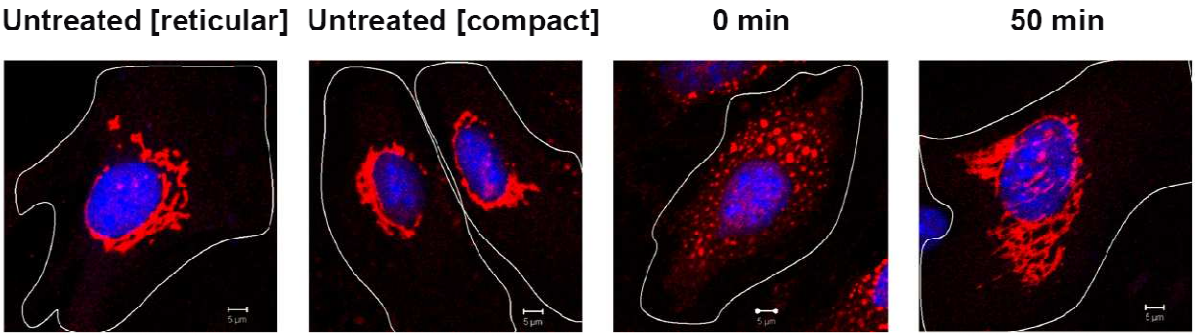

Figure 4.3. Representative pictures of wildtype (*Dync1i1*$^{+/+}$ *Dync1i2*$^{+/+}$) MEFs showing various morphologies of the Golgi complex

Intracellular structures were stained with antibodies against Golgi protein (giantin, red) and chromatin (DAPI, blue); cell boundaries outlined; distinct morphology was visible in untreated or incubated in the presence of nocodazole (0 min) cells; at 50 min majority of the Golgi membranes was reassembled around a nucleus; 5 µm scale bar.

Time point '0 min' corresponded to cells observed in the presence of nocodazole, which prevented polymerisation of microtubules (MTs). In all cells examined the Golgi membranes, visualised by labelling of giantin, were found as small fragments throughout the cell body (Figure 4.3). Therefore, the results obtained at this time point were not discussed in detail.

The 'reticular' structure was scored when interlaced Golgi stacks could be distinguished as ribbons located in the perinuclear area. The fraction of untreated wildtype *Dync1i1*$^{+/+}$ *Dync1i2*$^{+/+}$ cells with a reticular structure was 0.503±0.068, whereas the proportion was slightly smaller in the untreated double homozygous *Dync1i1*$^{G482D/G482D}$ *Dync1i2*$^{T172I/T172I}$ fibroblasts: 0.416±0.095 (Table 10.3). The opposite trend was observed in cells, in which MTs were allowed to repolymerise for 50 min, during which 0.379±0.026 of wildtype *Dync1i1*$^{+/+}$ *Dync1i2*$^{+/+}$ and 0.405±0.051 of mutant *Dync1i1*$^{G482D/G482D}$ *Dync1i2*$^{T172I/T172I}$ fibroblasts displayed the reticular network of Golgi complex. While no difference was found between MEFs (p=0.3732 for untreated, p=0.5767 at 50 min), fewer wildtype cells reassembled the Golgi stack to the levels observed in the untreated fibroblasts (p=0.0355) (Table 4.2, Figure 4.4A).

Cells annotated to the 'compact' category displayed a perinuclear labelling of the Golgi apparatus with tight stacks, where tubules were not well defined (Figure 4.3). In the population of the untreated wildtype *Dync1i1*$^{+/+}$ *Dync1i2*$^{+/+}$ MEFs 0.412±0.057 of cells were scored as having the compact structure, while in the double homozygous *Dync1i1*$^{G482D/G482D}$ *Dync1i2*$^{T172I/T172I}$ cells the fraction was 0.504±0.107 (Table 10.3). After disruption and MTs repolymerisation for 50 min the fractions were lower in both groups, with 0.363±0.028 of wildtype *Dync1i1*$^{+/+}$ *Dync1i2*$^{+/+}$ and 0.364±0.072 of mutant *Dync1i1*$^{G482D/G482D}$ *Dync1i2*$^{T172I/T172I}$ fibroblasts showing compact Golgi stacks (Figure 4.4B). The mutant allele did not affect the formation of the compact stacks neither in the untreated cells (p=0.3866) nor after nocodazole washout (p=0.9898). However, at 50 min fibroblasts carrying double mutant allele (*Dync1i1*$^{G482D/G482D}$*Dync1i2*$^{T172I/T172I}$) failed to reach the same proportion of the compact Golgi as the untreated cells (p=0.0219) (Table 4.2, Figure 4.4B).

Finally, a 'fragmented' morphology corresponded to the giantin-positive membranes dispersed in the cytosol or in a form of discontinuous tubular structures. It also reflected the capacity of cytoplasmic dynein complex to transport Golgi membranes towards the MTOC. While in the untreated cells only small numbers of fibroblasts were observed to have fragmented Golgi apparatus (0.086±0.011 of the wildtype *Dync1i1*$^{+/+}$*Dync1i2*$^{+/+}$, and 0.080±0.036 of mutant *Dync1i1*$^{G482D/G482D}$*Dync1i2*$^{T172I/T172I}$ MEFs), the disruption of the MTs increased the proportions to 0.257±0.006 and 0.231±0.022 of wildtype *Dync1i1*$^{+/+}$ *Dync1i2*$^{+/+}$ and mutant *Dync1i1*$^{G482D/G482D}$*Dync1i2*$^{T172I/T172I}$ MEFs respectively (Table 10.3). Nonetheless, the results were not different in any of conditions described (p=0.7412 for untreated and p=0.2338 at 50 min) (Figure 4.4C).

Table 4.2. Summary of analysis of Golgi apparatus reassembly after nocodazole treatment
Results of analysis of Golgi complex morphologies presented based on the results of statistical tests, where **n.s**. corresponds to lack of significant differences for p>0.05; trends were noted if p<0.1; for cells annotated to distinct bins values of each parameter were compared between wildtype *Dync1i1*$^{+/+}$*Dync1i2*$^{+/+}$ and double homozygous *Dync1i1*$^{G482D/G482D}$ *Dync1i2*$^{T172I/T172I}$ cell lines; detailed analysis is presented in Appendix 10.3.

Morphology/ time point	**Reticular**	**Compact**	**Fragmented**
Untreated	n.s.	n.s.	n.s.
0 min	-	-	-
50 min	n.s.	n.s.	n.s.
Reassembly after 50min to the level of untreated cells	*Dync1i1*$^{+/+}$ *Dync1i2*$^{+/+}$ cells did not reassemble (p=0.0355)	*Dync1i1*$^{G482D/G482D}$ *Dync1i2*$^{T172I/T172I}$ cells did not reassemble (p=0.0219)	n.s.

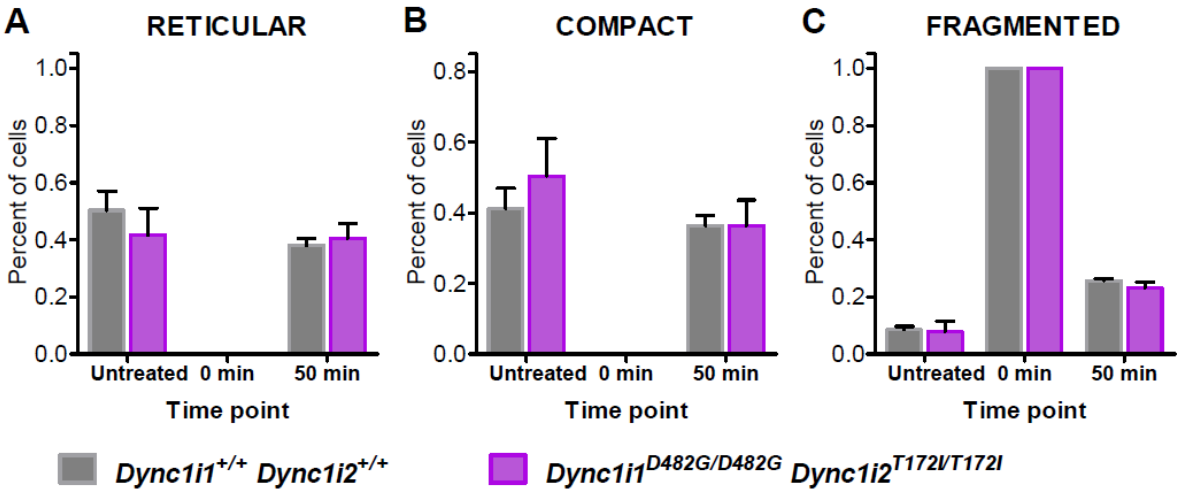

Figure 4.4. Analysis of Golgi apparatus morphology in untreated and fibroblasts treated with nocodazole
Fractions of cells with annotated to different classes represented as mean±SD; legend refers to all graphs and colours correspond to wildtype *Dync1i1*$^{+/+}$ *Dync1i2*$^{+/+}$ (grey), double homozygous *Dync1i1*$^{G482D/G482D}$ *Dync1i2*$^{T172I/T172I}$ (violet) cell lines; 0 min and 50 min refer to time after nocodazole washout, when Golgi apparatus was observed

A. Fraction of MEFs with Golgi showing perinuclear localisation and reticular morphology
B. Fraction of MEFs with Golgi showing perinuclear localisation and compact morphology
C. Fraction of MEFs with Golgi fragmented (often dispersed in the cytosol)

4.4.2.2 *Image based analysis of the Golgi complex in wildtype (Dync1i1$^{+/+}$ Dync1i2$^{+/+}$) and double homozygous (Dync1i1$^{G482D/G482D}$ Dync1i2$^{T172I/T172I}$) MEFs*

In addition, a detailed analysis of the Golgi structure at different time points was performed by comparing high resolution images of individual cells. The pictures were taken and analysed as described in sections 2.7.2 and 2.7.3. From each condition (0 min, 20 min, and 50 min, and untreated) at least 5 pictures of each cell line were taken, thus over 15 pictures of wildtype *Dync1i1$^{+/+}$Dync1i2$^{+/+}$* (n=3) and double homozygous *Dync1i1$^{G482D/G482D}$Dync1i2$^{T172I/T172I}$* (n=3) fibroblasts were analysed. For each cell image performed analysis was based on identification of objects positive for giantin labelling, for which a set of parameters was automatically calculated by the software (Cell Profiler). The parameters compared included: ratio of Golgi stacks number to their total area, form factor, eccentricity, and perimeter (in pixels). For each cell a mean value of a parameter was recorded and those were averaged giving a mean from a cell line. Due to high variation between cell lines, means from each time point were normalised to mean values recorded for untreated cells. The final relative values were analysed using paired *t*-test (the genotype effect at different time points), repeated measures one-way ANOVA (the time point effect on results obtained) followed by Dunnett's multiple comparison test (results for each time point tested against results for untreated cells). In all analyses two-tailed p-values were reported, statistically significant for $p<0.05$. The detailed analysis can be found in Appendix 10.3 and Table 10.4, while the results are summarised in Table 4.3.

Number of objects related to their area was used as a way to describe a global structure of the Golgi complex in a similar manner as described in section 4.4.2.1. Although the values were arbitrary, it increased for cells with fragmented Golgi membranes. At 0 min in all fibroblasts examined, Golgi complex was dispersed throughout the cytosol in a form of small fragments. The mean normalised values ranged 2.533 – 3.275 in the wildtype *Dync1i1$^{+/+}$Dync1i2$^{+/+}$* (n=3) and 2.406 - 3.125 in the double homozygous *Dync1i1$^{G482D/G482D}$ Dync1i2$^{T172I/T172I}$* (n=3) fibroblasts (p=0.4681) (Table 10.4). By 20 min the normalised ratio decreased approximately by half, while by 50 min mean values were comparable with untreated cells (for which normalised values were 1), which corresponded either to fewer

stacks observed or increase in the measured area due to membrane rearrangements. At both time points the double homozygous *Dync1i1*$^{G482D/G482D}$ *Dync1i2*$^{T172I/T172I}$ fibroblasts showed lower mean ratio (1.163 - 1.432 at 20 min, 0.848 - 1.169 at 50 min) than wildtype *Dync1i1*$^{+/+}$ *Dync1i2*$^{+/+}$ cells (1.280 - 1.522 at 20 min, 0.953 - 1.319 at 50 min) (Figure 4.5A). The difference observed at 20 min (p=0.0063) and 50 min (p=0.0183) might reflect faster reassembly of the Golgi membranes in the double homozygous *Dync1i1*$^{G482D/G482D}$ *Dync1i2*$^{T172I/T172I}$ MEFs. Finally, untreated cells did not vary when the raw values of the ratio were tested (p=0.1420).

The effect of time on the observed values were also tested and compared to the 'untreated' cells in order to evaluate the kinetics of the process of Golgi reassembly. There were differences observed within both wildtype *Dync1i1*$^{+/+}$*Dync1i2*$^{+/+}$ (p=0.0003) and double homozygous *Dync1i1*$^{G482D/G482D}$ *Dync1i2*$^{T172I/T172I}$ (p=0.0002) fibroblasts. However, in both groups only values recorded at '0 min' were different from the 'untreated' cells ($p<0.001$), and this result confirmed the visual observations of complete fragmentation and dispersal of Golgi membranes. Furthermore, because the normalised values of the ratio did not vary at any other time point, these results suggested that 20 min after the nocodazole washout the Golgi complex membranes were already reassembled to a level comparable with the untreated cells.

On the other hand, within both genotypes the form factor varied depending on the time point, which likely reflected dynamics of the Golgi reassembly. In the wildtype *Dync1i1*$^{+/+}$*Dync1i2*$^{+/+}$ cells (p=0.0288), the shape of the Golgi membranes was affected the most at 0 min ($p< 0.05$), whereas 20 min and 50 min after the nocodazole washout the normalised values of form factor were comparable with untreated cells. Similar results were obtained for double homozygous *Dync1i1*$^{G482D/G482D}$ *Dync1i2*$^{T172I/T172I}$ MEFs (p=0.0072), and only at 0 min the form factor varied from the values recorded for the untreated cells ($p<0.05$) (Figure 4.5B).

Another shape parameter that was taken into account was object eccentricity and its mean values were calculated for each cell and cell line. The eccentricity of the ellipse that had the same second-moments as the object identified was defined as the ratio of the distance between the foci of the ellipse and its major axis length. The values ranged from 0 to 1, where the eccentricity of circular objects was 0 and 1 characterised a line segment.

Table 4.3. Summary of the image based analysis of shape parameters of Golgi complex membranes
Results of analysis of Golgi complex shape parameters presented based on the results of statistical tests, where **n.s**. corresponds to lack of significant differences for $p>0.05$; trends were noted if $p<0.1$; for cells annotated to distinct bins values of each parameter were compared between wildtype *Dync1i1*$^{+/+}$*Dync1i2*$^{+/+}$ and double homozygous *Dync1i1*$^{G482D/G482D}$*Dync1i2*$^{T172I/T172I}$ cell lines; detailed analysis is presented in Appendix 10.3.

Parameter/ time point	0 min	20 min	50 min	Untreated
Ratio number/ area	n.s.	*Dync1i1*$^{G482D/G482D}$ *Dync1i2*$^{T172I/T172I}$ showed lower normalised values	*Dync1i1*$^{G482D/G482D}$ *Dync1i2*$^{T172I/T172I}$ showed lower normalised values	n.s.
Form factor	n.s.	n.s.	n.s.	n.s.
Eccentricity	*Dync1i1*$^{G482D/G482D}$ *Dync1i2*$^{T172I/T172I}$ tended to have higher normalised valued	*Dync1i1*$^{G482D/G482D}$ *Dync1i2*$^{T172I/T172I}$ tended to have higher normalised valued	*Dync1i1*$^{G482D/G482D}$ *Dync1i2*$^{T172I/T172I}$ tended to have higher normalised valued	*Dync1i1*$^{G482D/G482D}$ *Dync1i2*$^{T172I/T172I}$ showed lower values
***Log* of perimeter [a.u.]**	n.s.	n.s.	n.s.	n.s.

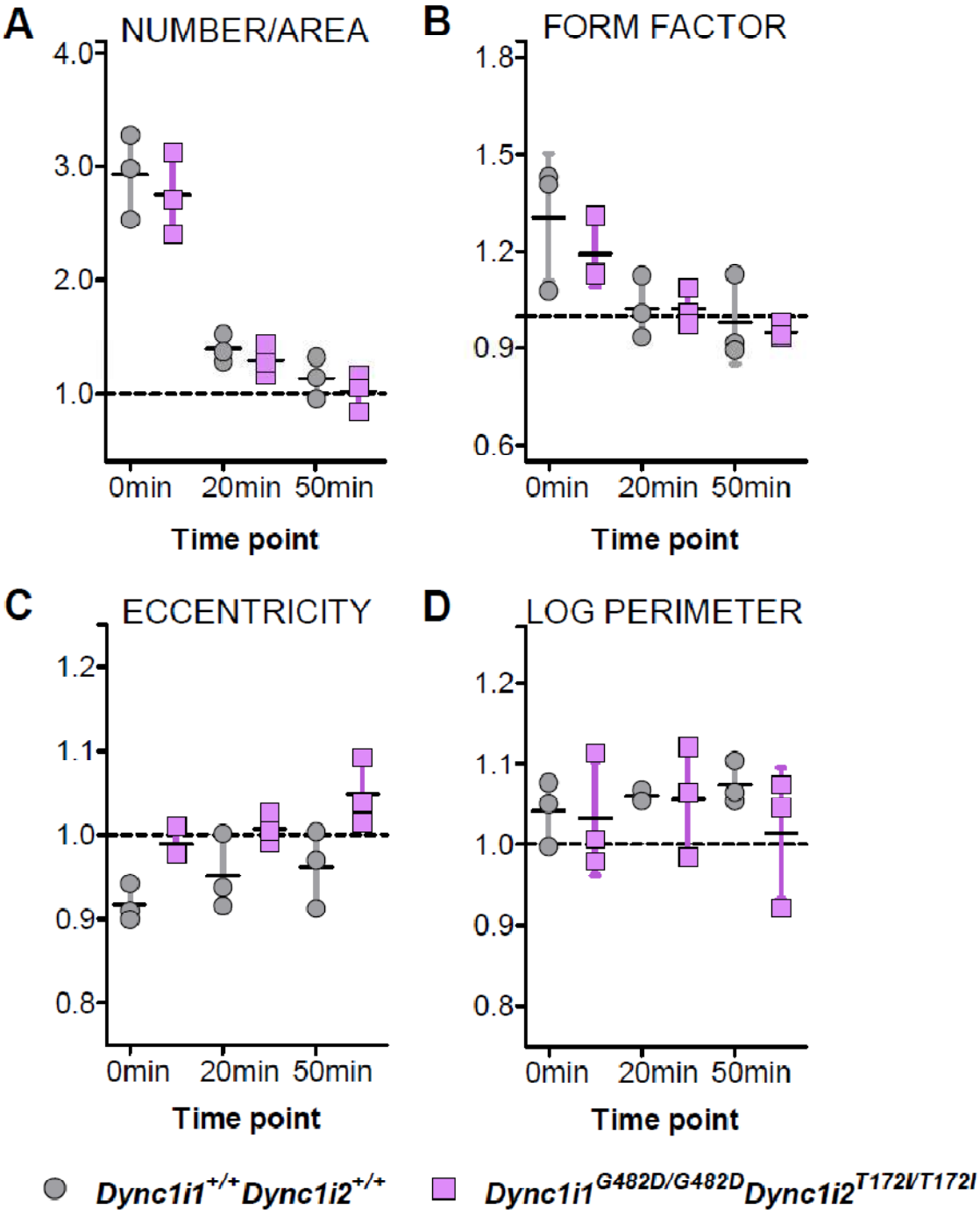

Figure 4.5. Analysis of shape parameters of the Golgi complex in the wildtype (*Dync1i1*$^{+/+}$ *Dync1i2*$^{+/+}$) and double homozygous (*Dync1i1*$^{G482D/G482D}$*Dync1i2*$^{T172I/T172I}$) fibroblasts treated with nocodazole

Results obtained for individual cell lines (aligned dots) represented together with a mean (horizontal line) and standard deviation; legend refers to all graphs and colours correspond to wildtype *Dync1i1*$^{+/+}$ *Dync1i2*$^{+/+}$ (grey) and double homozygous *Dync1i1*$^{G482D/G482D}$*Dync1i2*$^{T172I/T172I}$ (violet) MEFs; 0min, 20min, and 50min refer to time after nocodazole washout, when Golgi apparatus was analysed; for each time point and cell line mean values were normalised to mean values recorded for the untreated cells, here marked with dashed line at Y=1

A. Mean values of number of particles to total area ratio
B. Mean values of a form factor as a measure of shape
C. Mean values of eccentricity as a measure of shape
D. Mean values of total perimeter of objects identified transformed using function: *Y=log(Y)*

In case of the Golgi membranes, fragmented stacks (0 min) showed the lowest eccentricity values, which then increased during the time course. At all time points there was a trend observed in the double homozygous *Dync1i1*$^{G482D/G482D}$ *Dync1i2*$^{T172I/T172I}$ fibroblasts towards higher normalised mean eccentricity values when compared with the wildtype *Dync1i1*$^{+/+}$*Dync1i2*$^{+/+}$ cells (at 0 min p=0.0648, at 20 min p=0.0684, and at 50 min p=0.0837) (Table 10.3, Table 4.3). In contrast, the untreated wildtype *Dync1i1*$^{+/+}$*Dync1i2*$^{+/+}$ cells displayed higher values of the mean eccentricity (0.749 - 0.782) than double homozygous *Dync1i1*$^{G482D/G482D}$ *Dync1i2*$^{T172I/T172I}$ fibroblasts (0.727 - 0.741) (p=0.0325). Furthermore, during the time course the normalised mean eccentricity values varied only in the wildtype *Dync1i1*$^{+/+}$ *Dync1i2*$^{+/+}$ MEFs (p=0.0380) and the differences were noted for cells examined at 0 min ($p< 0.05$). On the contrary, the normalised mean eccentricity of the double homozygous *Dync1i1*$^{G482D/G482D}$*Dync1i2*$^{T172I/T172I}$ cells was comparable with values observed in the untreated cells at all time points examined (p=0.0819) (Figure 4.5C).

The summed perimeter of all objects identified as Golgi membranes was also analysed, however data displayed high variability and a broad range of values. Therefore, they were transformed using a function: $f(x) = logY$, and *log(perimeter)* values were used in subsequent analyses. Overall, there were no differences observed between wildtype *Dync1i1*$^{+/+}$ *Dync1i2*$^{+/+}$ and double homozygous *Dync1i1*$^{G482D/G482D}$ *Dync1i2*$^{T172I/T172I}$ fibroblasts at any of the time points examined (Table 4.3). Moreover, at 20 min and 50 min normalised mean values of *log(perimeter)* were higher than untreated wildtype *Dync1i1*$^{+/+}$ *Dync1i2*$^{+/+}$ MEFs (p=0.0311). On the other hand, the values recorded for double homozygous *Dync1i1*$^{G482D/G482D}$ *Dync1i2*$^{T172I/T172I}$ cell lines did not vary at any of the time points examined (p=0.6522) (Figure 4.5D).

In this chapter the effects of point mutations in the cytoplasmic dynein intermediate chain 1 (*Dync1i1*^{G482D}) and chain 2 (*Dync1i2*^{T172I}) were investigated using a Golgi complex reassembly assay. Various features of Golgi-associated membranes were observed at different time points during microtubule repolymerisation after nocodazole treatment. As a model primary MEF lines were used, which were isolated from animals carrying either both wildtype alleles (*Dync1i1*$^{+/+}$ *Dync1i2*$^{+/+}$) or both mutant alleles (as double homozygotes, *Dync1i1*$^{G482D/G482D}$ *Dync1i2*$^{T172I/T172I}$) of the cytoplasmic dynein intermediate chains 1 and 2. The process of Golgi reassembly at certain time points was analysed using different approaches: qualitative scoring of global structure of Golgi membranes (section 4.4.2.1), and quantitative image-based analysis of shape parameters (section 2.7.3).

One of the advantages of the qualitative scoring was a big number of cells analysed in a short time. Cells were scored at 0min and 50min by classifyng cells depending on Golgi morphology and there were no differences observed between wildtype *Dync1i1*$^{+/+}$*Dync1i2*$^{+/+}$ and double homozygous *Dync1i1*$^{G482D/G482D}$ *Dync1i2*$^{T172I/T172I}$ cells. It should be noted though, that while this method was used to characterise effects of disruption of genes (Bechler *et al.*, 2010), it might lack sensitivity in case of mild phenotypes.

Therefore, quantitative analysis of high-resolution images was also performed. Although the method applied consisted of several steps, it was automated and few parameters describing individual stacks were retrieved. Parameters taken into account were the ratio of number to total area, form factor, eccentricity, and total perimeter, however, the values object perimeter were very variable thus posing difficulties in analysis and interpretation. On the other hand, number to area ratio, form factor, and eccentricity gave consistent results, showing differences in Golgi structure and shape only early after nocodazole wash out (up to 20 min) in the wildtype *Dync1i1*$^{+/+}$ *Dync1i2*$^{+/+}$ fibroblasts. The changes observed likely corresponded to early events of fusion of small fragments (number to area ratio values descreased) and reshaping of membranes from circular to more elongated structures (form factor descreased, eccentricity increased). However it should be noted, that changes in both number and area of Golgi membranes contributed

to the the ratio values, therefore the interpretation was not straightforward. MEFs homozygous for mutations in both cytoplasmic dynein intermediate chains 1 and 2 (*Dync1i1*$^{G482D/G482D}$ *Dync1i2*$^{T172I/T172I}$) displayed lower values of the number to area ratios during the time course (20 min, 50 min) than wildtype *Dync1i1*$^{+/+}$ *Dync1i2*$^{+/+}$ cells. Furthermore, while relative values of form factor were comparable with the wildtype *Dync1i1*$^{+/+}$ *Dync1i2*$^{+/+}$ at all time points examined, the mean eccentricity of the Golgi complex in untreated cells was lower, yet during the time course the eccentricity tended to be slightly higher in the double homozygous *Dync1i1*$^{G482D/G482D}$ *Dync1i2*$^{T172I/T172I}$ cells.

In conclusion, while mutations in the intermediate chains 1 and 2 (*Dync1i1*^{G482D}, *Dync1i2*^{T172I}) did not affect global structure of the Golgi complex or kinetics of its reassembly, detailed quantitative analysis revealed subtle differences in distribution of Golgi membranes and their shape parameters.

4.4.3 Time course of EGF uptake in wildtype *(Dync1i2$^{+/+}$)* and homozygous *(Dync1i2$^{T172I/T172I}$)* embryonic fibroblasts

As mentioned, there are many distinct events, which contribute to EGF endocytosis. During translocation to a perinuclear region early endosomes mature to late endosomes, in processes which involve changes in number and size (Rink *et al.*, 2005). As EGF trafficking is tightly controlled, the endosome dynamics was shown to reflect changes in the endocytosis, and number of endosomes, area, and distance from nucleus were recently used in a quantitative high-throughput screen of EGF and TfR endocytosis (Collinet *et al.*, 2010).

Endosomal motility was investigated using fluorescently labelled EGF in MEFs isolated from wildtype *Dync1i2$^{+/+}$* (n=2) and homozygous *Dync1i2$^{T172I/T172I}$* (n=2) embryos. Cells were observed at different time points after EGF stimulation: 0 min, 15 min, 30 min, 45 min, and 60 min (Figure 4.6). Images of individual cells obtained from 2 experiments were analysed and parameters describing EGF-positive (EGF$^{+/ve}$) endosomes were calculated: the rate of translocation, endosome number and area. It should be also noted, that EGF gets internalised in a complex with the EGF receptors, and the amount of EGF observed depends on the number of receptors present in the plasma membrane. Consequently, during the analysis the total number of vesicles was normalised relatively to the cytoplasm area (Collinet *et al.,* 2010). Because values of parameters obtained deviated from Gaussian distribution, raw data were transformed using: $f(x) = logY$ and *log* values were used in all the analysis performed. Details of labelling, time course, and analysis can be found in sections 2.6.4 and 2.7.3 respectively.

Figure 4.6. Representative pictures of wildtype (*Dync1i2$^{+/+}$*) MEFs showing retrograde movement of EGF$^{+/ve}$ endosomes (next page)

Intracellular structures were stained with antibodies against α-tubulin protein (grey) and chromatin (DAPI, blue); distinct position of endosomes loaded with fluorescently labelled EGF (red) was observed during the time course; panel below each picture correspond to image of EGF only; yellow pseudocoloring present in case of overlapping intensities from EGF and α-tubulin; images not in scale

A. MEF imaged 0 min after EGF stimulation
B. MEF imaged 15 min after EGF stimulation
C. MEF imaged 30 min after EGF stimulation
D. MEF imaged 45 min after EGF stimulation
E. MEF imaged 60 min after EGF stimulation

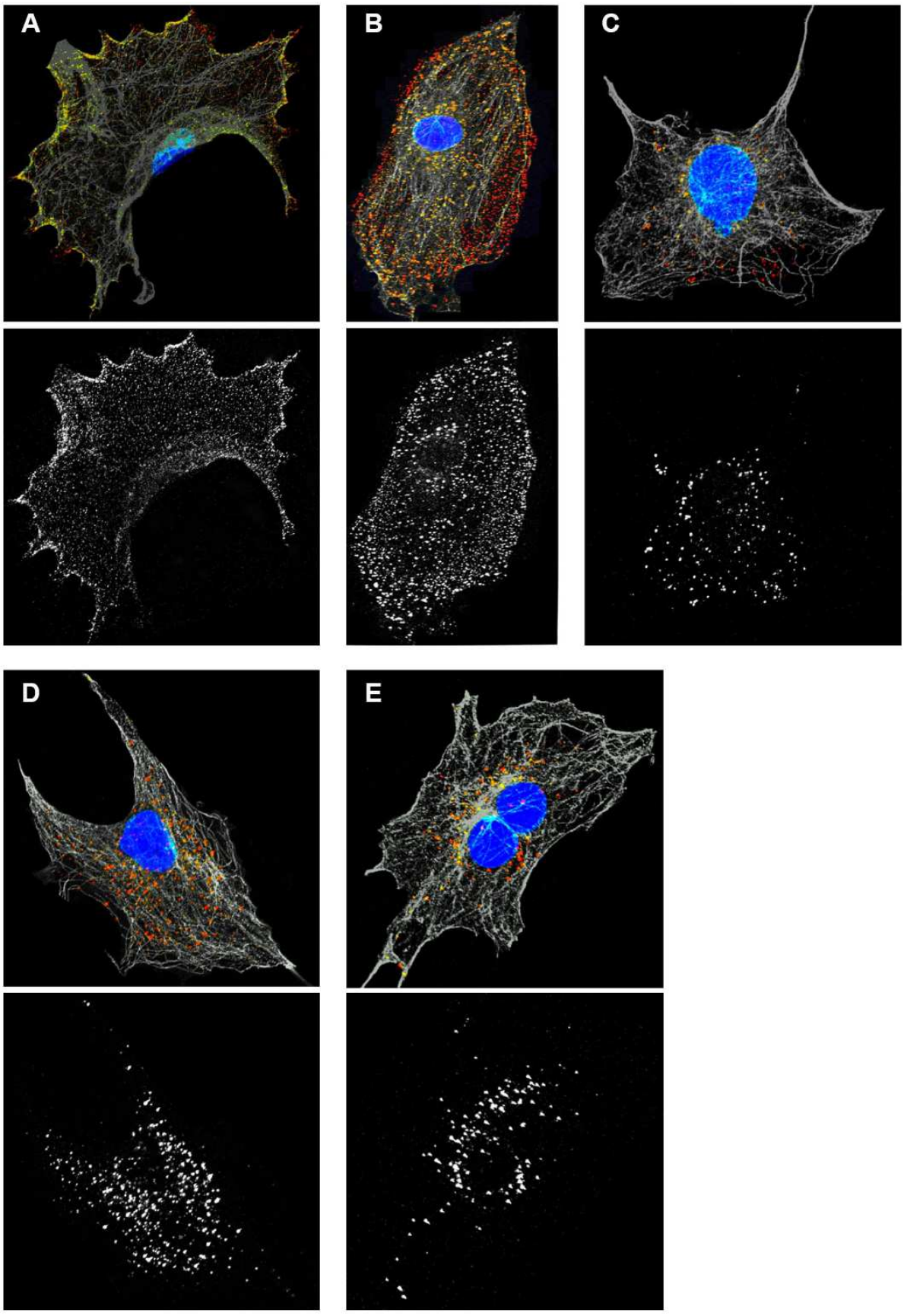
A
B
C
D
E

4.4.3.1 Analysis of endosomal transport

MEFs are a highly heterogeneous population in terms of both shape and size; therefore an indirect approach was used in order to quantify the rate of movement from cell periphery to perinuclear area. In images of each cell (at least 20 per time point) numbers of identified vesicles were recorded for both the area of whole cell and perinuclear area. For each cell the perinuclear ring had a width of a nuclear radius. Finally, a ratio of perinuclear to total number of endosomes was calculated, with values raging from 0 in case of EGF bound at the plasma membrane, to 1 when all the $EGF^{+/ve}$ vesicles were found in the perinuclear area. Ratios were analysed twice: *(1)* by comparing means normalised to time point '0 min' and *(2)* by fitting an exponential model (one-phase association) (Motulsky and Christopoulos, 2004).

The ratio of perinuclear to total number of vesicles was used as a measure of a transport towards the nucleus, and it increased during the time course reaching over 0.5 (50% of vesicles translocated) or 3 times when relative means were compared after 60 min of stimulation with EGF (Table 4.4). It should be noted, that variability within results likely reflected different efficiency of transport within fibroblasts. Furthermore, due to small sample size only relative means were tested statistically (two-way ANOVA). There were no differences found in the efficiency of transport at the time points examined (p=0.0979), although homozygous *Dync1i2*$^{T172I/T172I}$ (n=2) cells showed a trend towards slower movement than wildtype *Dync1i2*$^{+/+}$ (n=2) fibroblasts (at 60 min: 2.743 and 3.698, 4.766 and 2.925 respectively) (Figure 4.7A).

Table 4.4. Image based analysis of retrograde transport of EGF$^{+/ve}$ endosomes

Digital images were taken and analysed at different time points after stimulation with EGF; for each cell line mean values were normalised to values recorded for the untreated cells *(in italics)*, while raw data are shown as mean±standard deviation (SD); genotypes annotated as follows: wildtype (*Dync1i2*$^{+/+}$), homozygous (*Dync1i2*$^{T172I/T172I}$); result of two-way ANOVA and reported two-tailed p-values shaded grey, n - number of cell lines derived from animals

Time point		***Dync1i2*$^{+/+}$ n=2**		***Dync1i2*$^{T172I/T172I}$ n=2**	
Number of cells	0 min	19	14	16	18
	15 min	29	19	29	18
	30 min	30	26	33	24
	45 min	31	20	35	20
	60 min	28	21	23	28
Ratio perinuclear / total	0 min	0.124±0.122 *1.0*	0.175±0.116 *1.0*	0.208±0.190 *1.0*	0.149±0.171 *1.0*
	15 min	0.343±0.162 *2.758*	0.251±0.096 *1.438*	0.249±0.182 *1.197*	0.247±0.109 *1.662*
	30 min	0.413±0.198 *3.321*	0.479±0.188 *2.740*	0.419±0.176 *2.016*	0.373±0.132 *2.505*
	45 min	0.534±0.152 *4.293*	0.510±0.200 *2.917*	0.551±0.199 *2.650*	0.477±0.159 *3.201*
	60 min	0.593±0.193 *4.766*	0.511±0.199 *2.925*	0.571±0.205 *2.743*	0.551±0.184 *3.698*
		Two-way ANOVA, F(1,10)=3.333, p=0.0979			

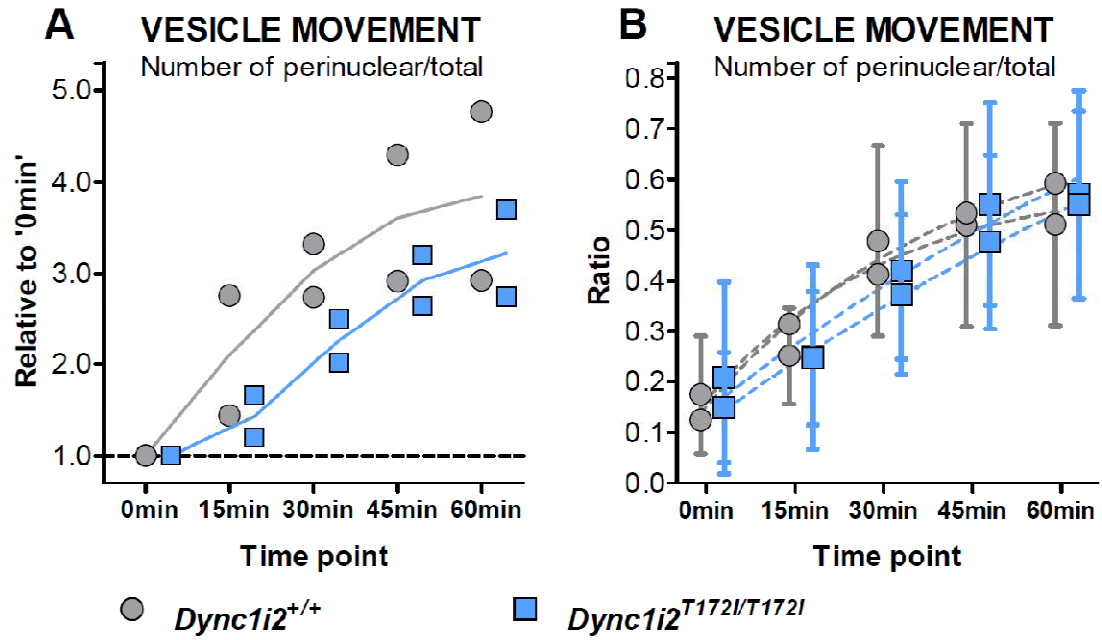

Figure 4.7. Analysis of movement of the EGF$^{+/ve}$ endosomes in the wildtype (*Dync1i2*$^{+/+}$) and homozygous (*Dync1i2*$^{T172I/T172I}$) fibroblasts observed at different time points after EGF stimulation

Increase in perinuclear/total number ratio represented as means of individual cell lines (aligned dots) in a function of time; legend refers to all graphs and colours correspond to wildtype *Dync1i2*$^{+/+}$ (grey) and homozygous *Dync1i2*$^{T172I/T172I}$ (blue) MEFs

A. Mean values of ratio normalised to mean values recorded at 0 min (marked with dashed line at Y=1)
B. Mean values of ratio shown as mean ± SD with fitted exponential model (dash lines)

In addition the time course data were analysed using non-linear regression. Although a simple model only describing retrograde transport could not be found, an exponential equation was used to calculate parameters of folate receptor recycling (Chen *et al.*, 2008). Values of ratio were fitted in GraphPad using one-phase association model:

$$Y = Y_0 + (Plateau - Y_0) * (1 - exp^{-K*x}),$$

where Y_0 was the Y value at time 0 min, *Plateau* was the *Y* value at infinite times (constrain to <1.0 or not), and *K* was the rate constant expressed in min^{-1}. Initially, the *Plateau* was restricted to a maximum of 1, relevant to all of the vesicles in the perinuclear area. The data recorded for wildtype *Dync1i2*$^{+/+}$ cells was fitted with the exponential model. This was not possible for the set of data for homozygous *Dync1i2*$^{T172I/T172I}$ MEFs ('Hit constraint') (Table 4.5). This result might suggest some other than exponential kinetics for the transport observed in the homozygous *Dync1i2*$^{T172I/T172I}$ cells (Figure 4.7B). When the constraint was lifted allowing for the best fit to the data, the values of $Plateau$ calculated for both sets from homozygous *Dync1i2*$^{T172I/T172I}$ (n=2) cells were comparable (1.315 ± 1.496, 1.367 ± 1.675), although above 1.0, thus biologically irrelevant. It should also be noted that the values of the rate constant (K) calculated for wildtype *Dync1i2*$^{+/+}$ (n=2) cells were much higher (0.02435 ± 0.01137, 0.03212 ± 0.01654) than observed in the homozygous *Dync1i2*$^{T172I/T172I}$ (n=2) fibroblasts (0.00795 ± 0.01313, 0.00684 ± 0.01150). Nonetheless, all of the parameters were had high standard deviations, likely due to high variability within the data sets.

In summary, the rate of retrograde transport was expressed as fraction of endosomes identified in the perinuclear area calculated for each cell at different time points. The comparison of mean values normalised to '0 min' showed no differences between wildtype *Dync1i2*$^{+/+}$ and homozygous *Dync1i2*$^{T172I/T172I}$ MEFs in the retrograde transport over the period of 60 min. An alternative approach to data analysis was also employed and the data from the time course were fitted to an exponential model in order to calculate parameters describing the kinetics of the transport. Given the calculations performed, the conclusion of different kinetics of the transport observed in the homozygous *Dync1i2*$^{T172I/T172I}$ cells could be drawn, as the data could not be described with the exponential model. At the same time, an equation for Boltzmann sigmoidal

seemed to be more suitable (data not shown). Unfortunately, further interpretation of numerical values was hindered by the big spread of values and a more sophisticated mathematical analysis would be required.

Table 4.5. Parameters of the exponential model

Values of ratio of perinuclear to total number of vesicles were analysed using exponential model (one-phase association) according to equation: $Y = Y_0 + (Plateau - Y_0) * (1 - exp^{-K*x})$, where Y_0 - Y value at time 0 min, *Plateau* - *Y* value at infinite times (constrain to <1.0 or not), *K* - the rate constant [min^{-1}]; best fit values of parameters shown as mean±standard deviation (SD); genotypes annotated as follows: wildtype (*Dync1i2*$^{+/+}$), homozygous (*Dync1i2*$^{T172I/T172I}$); R^2 - correlation factor square, corresponds to goodness of fit; n - number of cell lines derived from animals

Parameter		***Dync1i2*$^{+/+}$ n=2**		***Dync1i2*$^{T172I/T172I}$ n=2**	
Constraints		*Plateau < 1.0*		*Plateau < 1.0 [Hit constraint]*	
Best fit values	Y_0	0.129 ± 0.036	0.148 ± 0.045	0.162 ± 0.045	0.137 ± 0.035
	Plateau	0.794 ± 0.199	0.604 ± 0.104	~1.000	~1.000
	K [min^{-1}]	0.02007 ± 0.02435	0.03212 ± 0.03212	0.01212 ± 0.00795	0.01080 ± 0.00684
	R²	**0.4732**	**0.3512**	**0.3389**	**0.4698**
Absolute sum of squares		3.542	2.961	4.906	2.562
Constraints		None		None	
Best fit values	Y_0	0.136 ± 0.038	0.148 ± 0.045	0.169 ± 0.044	0.143 ± 0.035
	Plateau	0.726 ± 0.143	0.604 ± 0.104	1.315 ± 1.496	1.367 ± 1.675
	K [min^{-1}]	0.02435 ± 0.01137	0.03212 ± 0.01654	0.00795 ± 0.01313	0.00684 ± 0.01150
	R^2	**0.4379**	**0.3512**	**0.3396**	**0.4704**
Absolute sum of squares		3.882	2.961	4.901	2.559

4.4.3.2 Analysis of endosomal dynamics

The parameters of endosomes were analysed at 0min, 15min, 30min, 45min, and 60min. Pictures of individual cells were analysed as before and values calculated included ratio of total number of endosomes to cytoplasm area (multiplied by 1000 for facilitate visualisation), number and total area of vesicles in the perinuclear area (nuclear radius marked the width of a ring around a nucleus), and Pearson correlation between number and area. All the data were transformed ($f(x) = logY$) before final analysis. The detailed analysis can be found in Appendix 10.4 and Table 10.5, while the results are summarised in Table 4.6.

The ratio of endosome number to cytoplasm area described changes in the $EGF^{+/ve}$ vesicles and would decrease with time due to fusion during sorting and maturation. The values obtained during the time course showed a mild increase with a maximum at 30 min and constant decrease till 60 min after the EGF stimulation. Because EGF was not degraded within the first 30 min (Driskell *et al.*, 2007), the fluctuation observed might reflect maturation of early endosomes involving fusion-fission of vesicles (Rink *et al.*, 2005). Subsequent decrease might then be due to formation of late endosomes in the perinuclear area. The comparison of number/cytosol area ratio at different time points did not show differences between wildtype *Dync1i2*$^{+/+}$ (n=2) and homozygous *Dync1i2*$^{T172I/T172I}$ (n=2) fibroblasts (Table 10.5), although 60 min after the EGF uptake homozygous *Dync1i2*$^{T172I/T172I}$ cells tended to have more endosomes than wildtype *Dync1i2*$^{+/+}$ MEFs (p=0.0774). Furthermore, the number/area ratio calculated for the wildtype *Dync1i2*$^{+/+}$ cells decreased at constant rate (test for linear trend, p=0.0362), while it was not linear when homozygous *Dync1i2*$^{T172I/T172I}$ cells were analysed (p=0.0811) (Figure 4.8A,B).

The mean endosomal content of the EGF was shown to remain constant and to be tightly regulated through changes in number and total load of endosomes (Collinet *et al.*, 2010). Therefore, these two parameters were also analysed in relation to both time point and to each other. In order to normalise the differences in the cell area only endosomes identified in the perinuclear area were taken into account. Following this design, the number of vesicles was an outcome of both retrograde transport (increase with time), and

endosomal maturation and fusion, as late endosomes clustered in the perinuclear area (decrease). At the same time, the total area, corresponding to the total amount of internalised EGF, was affected by both transport (accumulation of endosomes) and EGF degradation (decrease in fluorescent signal).

The number of perinuclear endosomes first increased from 0 min to 30 min, which likely reflected the translocation of endosomes. Following that, the values decreased, which would correspond to fusion of vesicles. The wild type *Dync1i2*$^{+/+}$ (n=2) and homozygous *Dync1i2*$^{T172I/T172I}$ (n=2) fibroblasts did not vary when the number of EGF$^{+/ve}$ endosomes was compared at any of the time points (Table 10.5, Table 4.6). However, at 15 min and 45 min homozygous *Dync1i2*$^{T172I/T172I}$ MEFs displayed trends towards lower (p=0.0811) and higher (p=0.0503) numbers of endosomes when related to cell lines isolated from wildtype *Dync1i2*$^{+/+}$ animals. These results might correspond to both slightly slower transport (at 15 min) and impaired membrane fusion (at 45 min) (Figure 4.8C,D).

Table 4.6. Summary of the image based analysis of number and area of EGF$^{+/ve}$ endosomes
Parameters of the endosomes presented based on the results of statistical tests, where n.s. corresponds to lack of significant differences for p>0.05; trends were noted if p<0.1; for each parameter values obtained at different timepoints were compared between wildtype *Dync1i2*$^{+/+}$ and homozygous *Dync1i2*$^{T172I/T172I}$ cell lines; detailed analysis is presented in Appendix 10.4

Parameter/ time point	Number of endosomes/ cytosol area	Perinuclear endosomes - NUMBER	Perinuclear endosomes - AREA
0 min	n.s.	n.s.	n.s.
15 min	n.s.	*Dync1i2*$^{T172I/T172I}$ tended to have lower values	n.s.
30 min	n.s.	n.s.	*Dync1i2*$^{T172I/T172I}$ tended to have lower values
45 min	n.s.		*Dync1i2*$^{T172I/T172I}$ showed higher values
60 min	*Dync1i2*$^{T172I/T172I}$ tended to have higher values	n.s.	n.s.

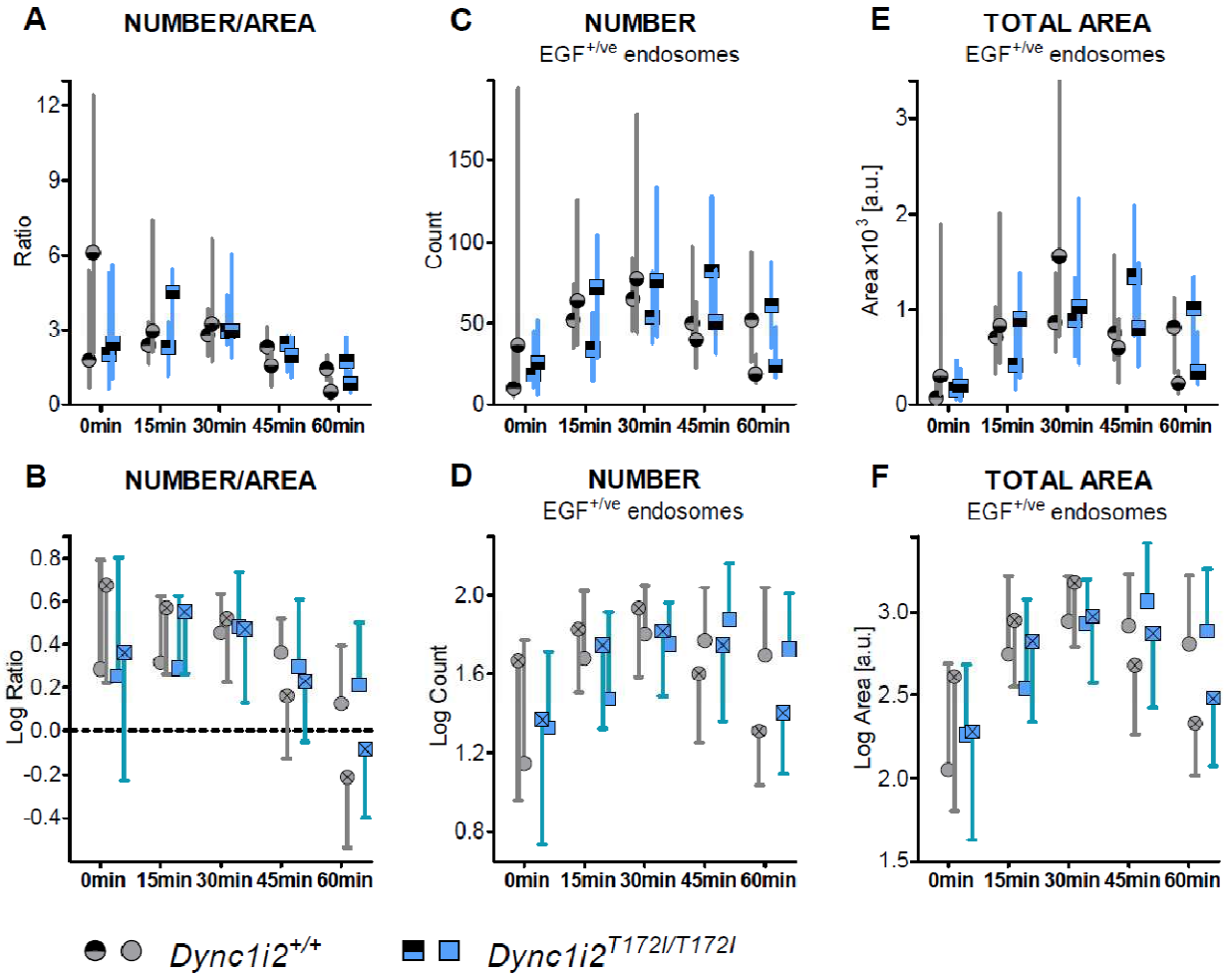

Figure 4.8. Analysis of parameters of the EGF$^{+/ve}$ endosomes in the wildtype (*Dync1i2*$^{+/+}$) and homozygous (*Dync1i2*$^{T172I/T172I}$) fibroblasts observed at different time points after EGF stimulation

Raw data collected for individual cell lines represented as median and interquatrile range (IQR) (two-tone symbols) while *log* transformed values shown as mean ± standard deviation (SD), for easier visualisation SD bars extended in 1 direction only; legend refers to all graphs and colours correspond to wildtype *Dync1i2*$^{+/+}$ (grey) and homozygous *Dync1i2*$^{T172I/T172I}$ (blue) MEFs; time points marked on the X-axis refer to time after EGF stimulation, a.u. – arbitrary units; patterns of symbols correspond to paired cell lines

A.B. Median/mean values of ratio of number of endosomes to cytosol area (x 1000)

C.D. Median/mean values of number of endosomes identified in the perinuclear area

E.F. Median/mean values of total area of perinuclear endosomes, corresponding to amount of the EGF

The changes of the total area of the endosomes in the perinuclear area in relation to time showed more prominent effect of retrograde transport, as the total area increased almost 10-fold within 30 min due to accumulation of the $EGF^{+/ve}$ vesicles. The values then decreased slightly reflecting lysosomal degradation and approximately 50% of the EGF was reported to be degraded by 60 min after stimulation (Ren et al., 2008). The initial flow of the EGF observed at 0 min and 15 min did not vary when wildtype *Dync1i2*$^{+/+}$ (n=2) and homozygous *Dync1i2*$^{T172I/T172I}$ (n=2) fibroblasts were compared (p=0.7048, p=0.1047 respectively) (Table 10.5, Table 4.6). However, total area of the perinuclear endosomes observed in the homozygous *Dync1i2*$^{T172I/T172I}$ cells tended to be slightly lower at 30 min (p=0.0817), while it was higher at 45 min (p=0.0246). This result might be explained by delay in the retrograde transport affecting other processes, e.g. sorting (Figure 4.8E,F). There were no differences by 60 min (p=0.1418), suggesting that the rate of EGF degradation at this time points was comparable between cell lines. Nonetheless, a delay in the initiation of lysosomal degradation would explain the differences observed at 45 min. In addition, the values of total area calculated for homozygous *Dync1i2*$^{T172I/T172I}$ MEFs increased in a linear fashion (0min – 30min, p=0.0329), which was not observed in the wildtype *Dync1i2*$^{+/+}$ cells.

Various parameters of the endosomal machinery are often functionally linked and their dependency can be statistically expressed as a correlation. A high positive correlation between the number of endosomes and total internal cargo was suggested to be a way to control the distribution of intracellular EGF (Collinet *et al.*, 2010).

For perinuclear endosomes observed at various time points Pearson correlation coefficients were calculated between their number and their total area (Table 10.5). In all data sets the values of coefficient were above 0.85 showing a very high positive correlation (Figure 4.9).

The dynamics of $EGF^{+/ve}$ endosomes is a combination of different processes often acting simultaneously over certain time, therefore different parameters were analysed in order to investigate effects of a point mutation in the cytoplasmic dynein intermediate chain 2 (*Dync1i2*^{T172I}). A maturation from early to late endosomes, which was known to involve

receptor sorting and fusion of vesicles, was assessed by comparing parameters describing number of vesicles. Furthermore, total area of vesicles corresponded to changes in the amount of internalised EGF. By limiting analysis to endosomes in the perinuclear area, the component of the transport was also included, as distance from the nucleus was shown to strongly influence other parameters (Collinet *et al.*, 2010).

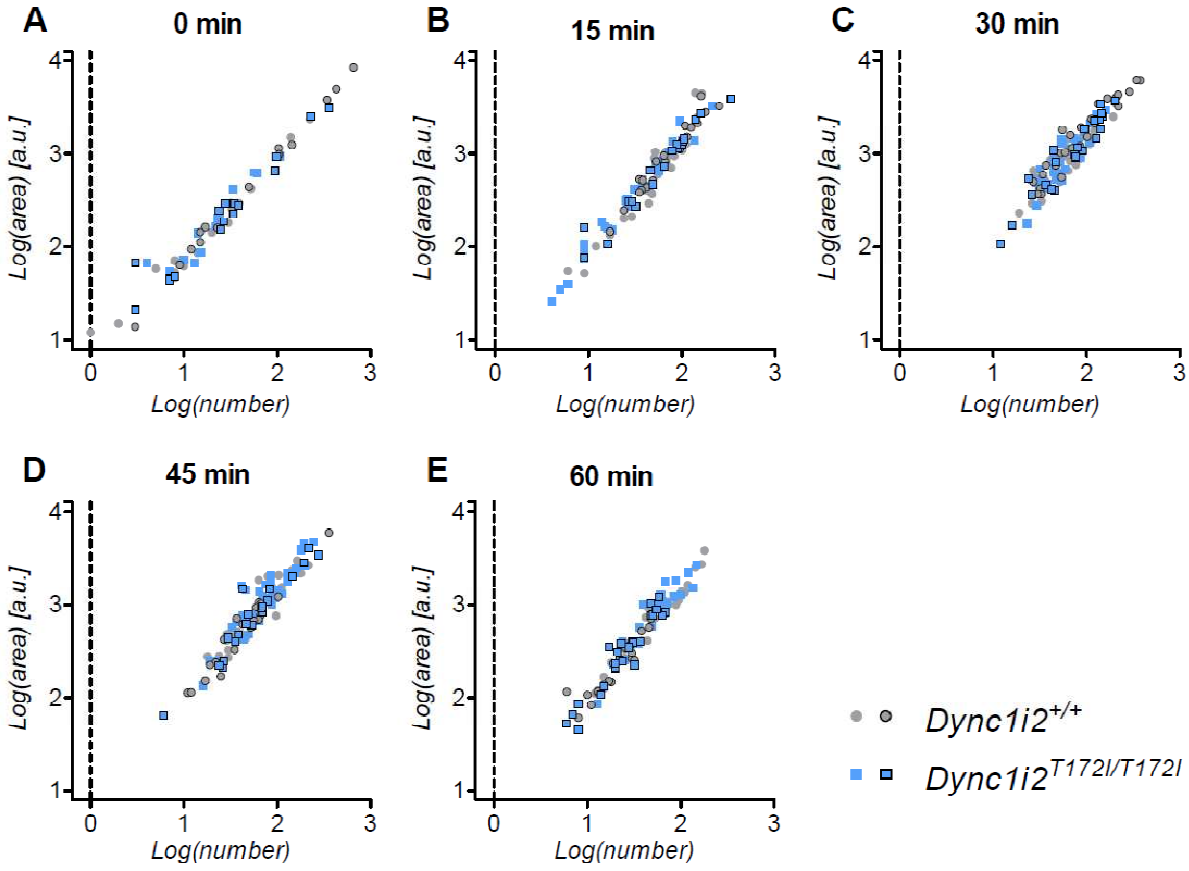

Figure 4.9. Correlation between parameters of the EGF$^{+/ve}$ endosomes in the wildtype (*Dync1i2*$^{+/+}$) and homozygous (*Dync1i2*$^{T172I/T172I}$) fibroblasts observed at different time points after EGF stimulation

Number and total area recorded for endosomes in the perinuclear area represented as scatter graphs, *log* transformed values are plotted as dots corresponding to individual cells; shape of 'clouds' typical for positive correlation; legend refers to all graphs and colours correspond to wildtype *Dync1i2*$^{+/+}$ (grey) and homozygous *Dync1i2*$^{T172I/T172I}$ (blue) MEFs; a.u. – arbitrary units; patterns of symbols correspond to paired cell lines

A. Correlation between number and total area examined at 0 min
B. Correlation between number and total area examined at 15 min
C. Correlation between number and total area examined at 30 min
D. Correlation between number and total area examined at 45 min
E. Correlation between number and total area examined at 60 min

Fibroblasts isolated from homozygous *Dync1i2*$^{T172I/T172I}$ embryos varied at different time points depending on the parameter analysed, which suggested kinetic differences in the dynein function affecting the EGF endocytosis. Total number of vesicles observed in the wildtype *Dync1i2*$^{+/+}$ cells decreased steadily during the time course, whereas in homozygous *Dync1i2*$^{T172I/T172I}$ MEFs the values were higher 60 min after EGF stimulation thus deviating from linear trend. This observation suggested delay in the endosomal fusion which might be related to transport. Furthermore, when perinuclear area was analysed, homozygous *Dync1i2*$^{T172I/T172I}$ cells tended to have fewer EGF$^{+/ve}$ endosomes at 15 min but more at 45 min than wildtype *Dync1i2*$^{+/+}$ at the same time points. Although the results were affected by variation thus inconclusive, they might indicate delayed accumulation of endosomes in the perinuclear area (at 15 min), which would relate to deficits in maturation and fusion of vesicles (at 45 min).

4.4.4 Infection with *Salmonella enterica* ser. Typhimurium

Salmonella typhimurium was used as a model to investigate whether point mutations in the subunits of cytoplasmic dynein (*Dync1i1*^{G482D}, *Dync1i2*^{T172I}, *Dync1h1*^{Loa}) affect membrane dynamics or replication of intracellular bacteria.

4.4.4.1 Multiplicity of infection (m.o.i.) adjusted for MEFs

The efficiency of invasion strongly depends on properties of host cell (section 4.2.3), and the invasion assay was performed in order to adjust the amount of *Salmonella* typhimurium, expressed as multiplicity of infections (m.o.i.), used to infect MEFs.

The efficiency of invasion of wildtype (WT) and *SifA*$^{-}$ *Salmonella* was tested using wildtype *Dync1h1*$^{+/+}$ MEFs seeded at 2x10^{4} cells/ml per coverslips. The bacteria were in an exponential growth phase and used when OD_{600} measured against pure LB medium ranged 1.9 – 2.0. A series of aliquots was prepared by mixing 1.0 µl, 2.0 µl, 3.0 µl, 5.0 µl, and 7.0 µl bacteria with 1 ml EBSS used per each coverslip. The invasion proceeded for 15 min, and MEFs were fixed and stained.

Coverslips were examined with fluorescent microscopy, as bacteria expressed green fluorescent protein (GFP). Ideally, each fibroblast should be invaded only by 1 bacterium, so that efficiency of bacterial replication could be estimated. Adding 1.0 µl of *Salmonella* typhimurium suspension (WT and *SifA*$^{-}$, m.o.i. 1:1000) resulted in expected single invasions; however number of infected MEFs was very low, and it increased when 2.0 µl of *Salmonella* typhimurium culture were used. In case of m.o.i. higher than 1:350 (above 3.0 µl bacterial culture per well) the multiple invasions were observed. In final experiments MEFs were infected with bacterial culture at m.o.i. 1:400 (2.5 µl bacteria per well).

4.4.4.2 Phenotypes of the bacterial microcolonies observed in the wildtype and homozygous (Dync1i1$^{G482D/G482D}$Dync1i2$^{T172I/T172I}$, and Dync1h1$^{Loa/Loa}$) cell lines

The invasion of MEFs isolated from mouse lines carrying point mutations in subunits of the cytoplasmic dynein complex was carried out as described in section 2.6.5. Fibroblasts were fixed after 8 hours post infection (p.i.), and labelled with antibodies against LAMP-1 (late endosomes, SCV) and GM130 (Golgi complex). Because secondary antibodies used against GM130 were conjugated with far red dye (Alexa Fluor 647), the Golgi complex was not taken into account during analysis performed. There were 6 cell lines used in both experiments, each was derived from individual embryos. MEFs isolated from embryos carrying wildtype or mutant alleles were selected to come from the same litter in order to limit possible variation. The cell lines included: one of wildtype *Dync1i1*$^{+/+}$ *Dync1i2*$^{+/+}$ and double homozygous *Dync1i1*$^{G482D/G482D}$ *Dync1i2*$^{T172I/T172I}$, two of wildtype *Dync1h1*$^{+/+}$ and homozygous *Dync1h1*$^{Loa/Loa}$. It should be noted that due to time constraints only 1 experiment with each cell line was performed. From the statistical point of view, embryos should be treated as 'independent' subjects. Therefore, cell lines derived from embryos with mutations in the intermediate chains (*Dync1i1*^{G482D} *Dync1i2*^{T172I}) were not tested statistically (n=1), cell lines with mutation in the *Dync1h1*^{Loa} were tested for n=2 with tests for categorical data (Fisher's exact test, Chi-squared); results presented as mean (tables) or mean ± standard deviation (SD, figures). All MEF lines were seeded at the same concentration and passage. For MEFs infected with WT *Salmonella* typhimurium phenotypes of micro colony (split into 4 bins), approximate number of bacteria, and

association with LAMP-1 positive (annotated as LAMP-$1^{+/ve}$) compartment were noted. Furthermore, for each fibroblast infected with the *SifA*$^{-}$ mutant, features of LAMP-$1^{+/ve}$ compartment were recorded along with number of bacteria. From each condition 120 cells were scored blindly. The efficiency of 8 hour long infection with WT strain of *Salmonella* typhimurium was scored by 3 categorical parameters, which described the position and speed of replication of bacteria in each fibroblast. Those included: *(1)* position of bacteria in regards to nucleus (*perinuclear* or *periphery*), *(2)* ability to form micro colony (*clustered* or *scattered*), *(3)* and presence of *fewer* or *more* than 20 bacteria per fibroblast (Figure 4.10). The phenotypes of *Salmonella* typhimurium were allocated to 8 categories and few approaches to testing were taken by analysing parameters individually or in pairs. Detailed analysis is presented in Appendix 10.5 and Table 10.6.

While infection progresses in epithelial cells, wildtype (WT) *Salmonella* typhimurium form clustered micro colonies, which locate close to the Golgi complex and nucleus. The bacteria replicate in SCVs and a replication rate depends on a cell type: at 10 hours p.i. there were 20 bacteria observed in HeLa cells on average (Guignot *et al*., 2004), while at 8 hours p.i. 90% MEFs contained fewer than 10 bacteria (Radtke *et al.*, 2007). In all of cell lines examined, over 70% *Salmonella* micro colonies contained fewer than 20 bacteria. Furthermore, colonies with increased proliferation (>20) were evenly distributed in 4 bins, ranging from 4.2% to 5.8% for *Dync1i1*^{G482D} *Dync1i2*^{T172I} cell lines (10% in one case), and from 3.3% to 7.9% in *Dync1h1*^{Loa} cell lines. The contribution of this parameter was small (Figure 4.11).

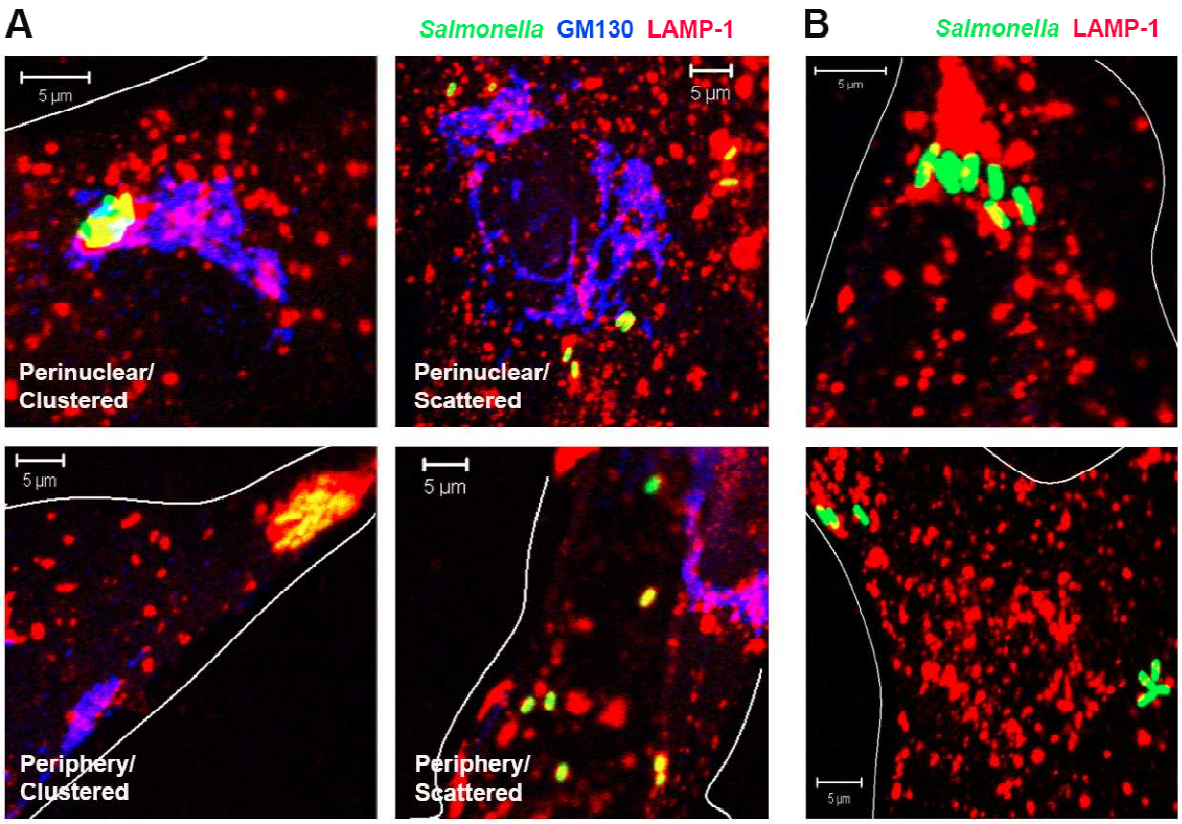

Figure 4.10. Representative pictures of wildtype MEFs showing intracellular *Salmonella* typhimurium (WT, *SifA*$^-$)

Images showing various distribution of intracellular bacteria 8 hours after infection; bacteria (green), late endosomal compartment labelled with anti-LAMP-1 antibodies (red), additionally Golgi complex stained with anti-GM130 (blue), bacteria in LAMP-1 enriched SCV are pseudocolored yellow; host cell boundaries marked with white line; scale bar 5µm

A. Wildtype (WT) *Salmonella* categorised based on their position (perinuclear or periphery) and morphology) (clustered in micro colony or scattered)
B. *SifA*$^-$ *Salmonella* mutant showing lack of colocalisation with LAMP-1 compartment due to disruption of the SCV membrane

The infection with wildtype *Salmonella* typhimurium was performed with only 1 wildtype *Dync1i1*$^{+/+}$*Dync1i2*$^{+/+}$ and 1 double homozygous *Dync1i1*$^{G482D/G482D}$*Dync1i2*$^{T172I/T172I}$ cell line, therefore the results obtained were not conclusive. The comparison of distributions in 8 categories suggested, that bacteria were observed more often in a perinuclear area as clustered micro colonies in the double homozygous *Dync1i1*$^{G482D/G482D}$*Dync1i2*$^{T172I/T172I}$ cells (0.417) than in the wildtype MEFs (0.300) (Table 10.6, Table 4.7). Moreover, bacteria were annotated to other categories in small fractions of the mutant *Dync1i1*$^{G482D/G482D}$ *Dync1i2*$^{T172I/T172I}$ cells (0.108, 0.100, 0.108) (Figure 4.11A); while within infected wildtype *Dync1i1*$^{+/+}$ *Dync1i2*$^{+/+}$ cells more micro colonies were observed in the cell periphery (0.225) (Figure 4.11A). The comparison of fractional distributions calculated for individual or grouped parameters indicated a trend towards increase in the intracellular *Salmonella* observed in perinuclear area of the double homozygous *Dync1i1*$^{G482D/G482D}$ *Dync1i2*$^{T172I/T172I}$ (0.675, 0.467 and 0.208, 0.525 and 0.150; Figure 4.12A,D,F) when related to wildtype *Dync1i1*$^{+/+}$ *Dync1i2*$^{+/+}$ fibroblasts (0.525, 0.350 and 0.175, 0.433 and 0.092; Figure 4.12A,D,F respectively).

The course of *Salmonella* typhimurium infection of the *Dync1h1*$^{Loa/Loa}$ fibroblasts did not differ from wildtype *Dync1h1*$^{+/+}$ cells (Table 10.6, Table 4.7). In the cells homozygous for *Dync1h1*^{Loa} allele higher proportions of scattered and clustered bacterial colonies were observed at the cell periphery (0.246, 0.208 respectively) than in wildtype *Dync1h1*$^{+/+}$ cells (0.196, 0.146) (Figure 4.11B). Furthermore, *Dync1h1*$^{Loa/Loa}$ cells displayed a proportional decrease in the number of perinuclear clustered micro colonies (0.225) when compared with wildtype *Dync1h1*$^{+/+}$ lines (0.288) (Figure 4.11B). When individual parameters were analysed, in the *Dync1h1*$^{Loa/Loa}$ cells more *Salmonella* typhimurium localised at the periphery (0.575) than in the wildtype *Dync1i1*$^{+/+}$ *Dync1i2*$^{+/+}$ MEFs (0.483, p=0.1958) (Figure 4.12A). Furthermore, the trend was more pronounced when both, position and number of bacteria were taken into account (p=0.0877). In the homozygous *Dync1h1*$^{Loa/Loa}$ cells WT *Salmonella* were observed more often in small number at the cell periphery (0.454) than at the nucleus (0.342) (Figure 4.12F). At the same time, in the wildtype *Dync1h1*$^{+/+}$ cells bacteria were observed more frequently in the perinuclear area (0.442) than at the periphery (0.342) (Figure 4.12F).

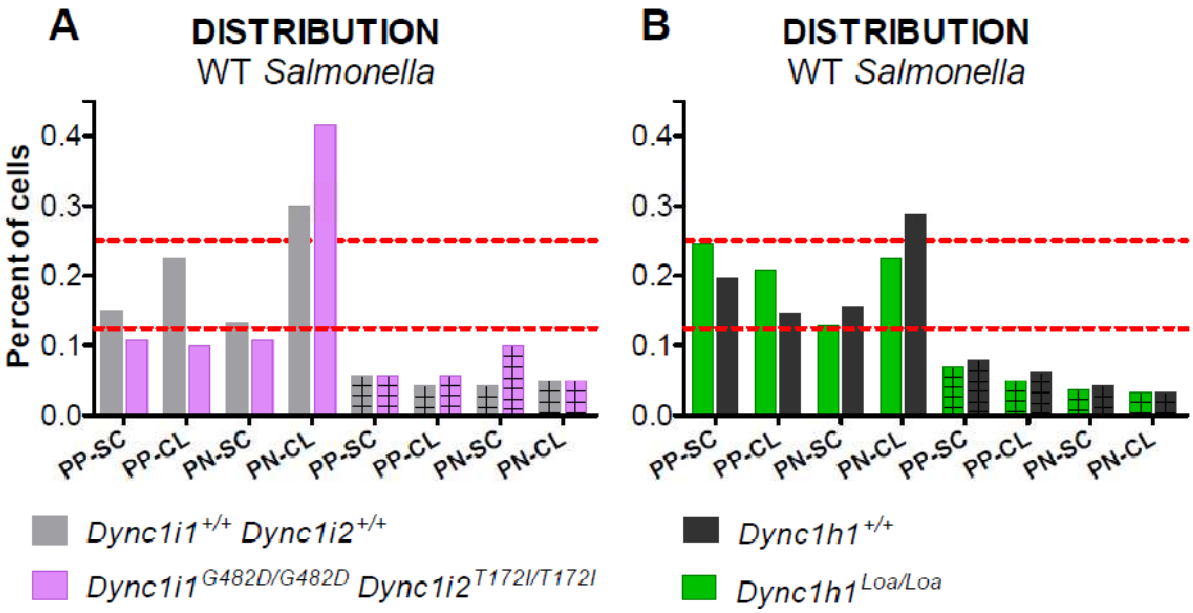

Figure 4.11. Distribution of colony features observed in MEFs infected with wildtype (WT) *Salmonella* typhimurium

Frequency distribution plotted as fraction of total; colours correspond to wildtype *Dync1i1*$^{+/+}$ *Dync1i2*$^{+/+}$ (light grey), double homozygous *Dync1i1*$^{G482D/G482D}$ *Dync1i2*$^{T172I/T172I}$ (pink), wildtype *Dync1h1*$^{+/+}$ (dark grey), homozygous *Dync1h1*$^{Loa/Loa}$) (green); cells with increased bacterial proliferation (>20) marked with cross-hatched bars (PP-SC to PN-CL); Y-axis title refers to both graphs and dashed lines at Y=1.25 and Y=2.50 indicate the chance distribution; abbreviations used annotate: PP-SC – periphery scattered, PP-CL – periphery clustered, PN-SC – perinuclear scattered, PN-CL – perinuclear clustered

A. Distribution of *Salmonella* micro colonies in MEFs derived from *Dync1i1*^{G482D} *Dync1i2*^{T172I} embryos
B. Distribution of *Salmonella* micro colonies in cells derived from *Dync1h1*^{Loa} embryos

Table 4.7. Summary of analysis of the distribution of micro colony features observed in MEFs infected with wildtype *Salmonella* typhimurium

Results of analysis of intracellular bacteria presented based on the results of statistical tests, where **n.s**. corresponds to lack of significant differences for p>0.05; trends were noted if p<0.1; distinct micro colony features were compared between wildtype *Dync1h1*$^{+/+}$ and homozygous *Dync1h1*$^{Loa/Loa}$ cell lines; detailed analysis is presented in Appendix 10.5.

Category	*Position (1)* Perinuclear or periphery	*Microcolony (2)* Scattered or clustered	*Number (3)* < 20 or > 20
Position (1)	n.s. (Figure 4.12A)	-	-
Microcolony (2)	n.s. (Figure 4.12D)	n.s. (Figure 4.12B)	n.s. (Figure 4.12E)
Number (3)	*Dync1h1*$^{Loa/Loa}$ tended to show differences in distribution of bacteria (Figure 4.12F)	-	n.s. (Figure 4.12C)

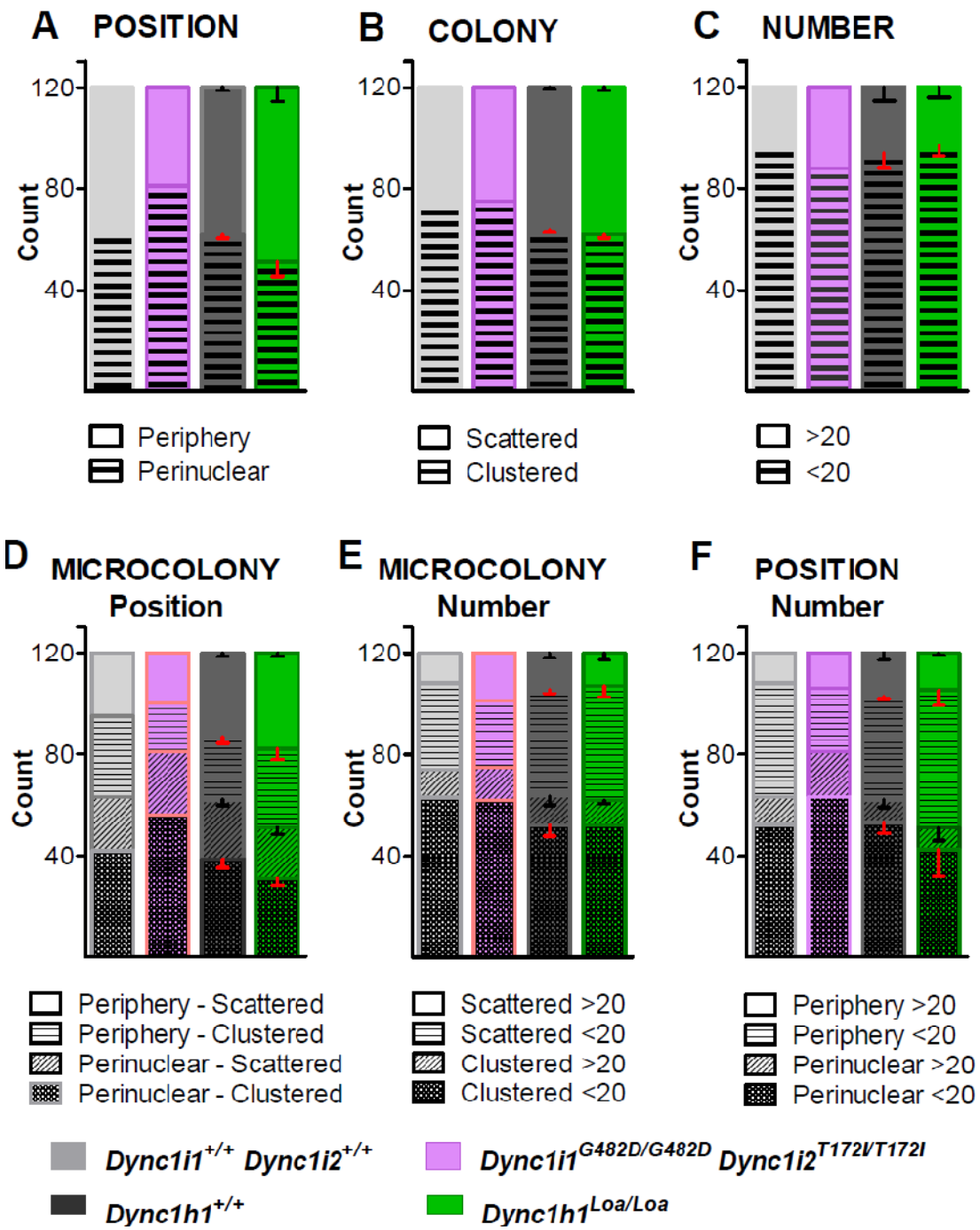

Figure 4.12. Analysis of selected micro colony features observed in MEFs infected with wildtype (WT) *Salmonella* typhimurium

Results for distinct categories were grouped depending on parameter(s) compared; the legend refers to all graphs and colours correspond to wildtype *Dync1i1*$^{+/+}$ *Dync1i2*$^{+/+}$ (light grey), double homozygous *Dync1i1*$^{G482D/G482D}$ *Dync1i2*$^{T172I/T172I}$ (violet), wildtype *Dync1h1*$^{+/+}$ (dark grey), homozygous *Dync1h1*$^{Loa/Loa}$) (green) cell lines; each category marked with distinct pattern; on Y-axis plotted number of infected cells from each line (120); due to small sample size (n=2) MEFs carrying *Dync1h1*^{Loa} allele represented as mean ± SD

A, B, C – comparison of individual parameters, where numbers were grouped relative to (A) position of *Salmonella* within a host cell, (B) formation of micro colony, (C) and number of bacteria above/below a value

D, E, F – results compared in relation to 2 parameters, (D) position and micro colony appearance, (E) micro colony and numbers of bacteria, (F) and position and number of bacteria

In conclusion, the single point mutations in the subunits of the cytoplasmic dynein complex (intermediate or heavy chains) did not affect progression of intracellular infection with *Salmonella* typhimurium, and the bacteria were found mostly in small clusters in the perinuclear area of the host cells. Bacterial micro colonies were scored by 3 parameters, however the parameter describing an assembled micro colony *(clustered* or *scattered)* was nearly equal in all groups examined (Figure 4.12B); the most likely it was irrelevant in the assay performed. On the other hand, at 8 hours p.i. the intracellular position and number of bacteria in fibroblasts displayed a level of correlation. In the cell lines derived from the *Dync1i1*^{G482D} *Dync1i2*^{T172I} embryos, the mutant allele was associated with the increase in the frequencies of small (<20) perinuclear micro colonies and more numerous colonies (both, at the periphery and around nucleus) (Figure 4.12F). This shift in position was reflected by the decrease in fraction of small peripheral colonies. Furthermore, the contrary effects were observed in the *Dync1h1*^{Loa} fibroblasts, and homozygous *Dync1h1*$^{Loa/Loa}$ cells displayed more small peripheral micro colonies, whereas the frequencies of *Salmonella* in the remaining categories decreased (Figure 4.12F). Finally, results obtained for the wildtype cell lines (*Dync1i1*$^{+/+}$ *Dync1i2*$^{+/+}$ and *Dync1h1*$^{+/+}$) were comparable, thus not affected by the genetic background.

4.4.4.3 Progression of the infection with the Salmonella typhimurium SifA^{-} mutant strain

The *SifA*$^{-}$ mutant strain, which looses the SCV membranes early after infection, proved useful in investigating membrane dynamics. The compartment, in which *Salmonella enetrica* replicate, is decorated with many proteins, yet markers associated with late endosomes are usually the most prominent. Therefore, MEFs were infected with WT and *SifA*$^{-}$ *Salmonella* typhimurium and at 8 hours p.i. stability of bacterial vacuoles was investigated by following the distribution of LAMP-1 (Lysosomal-associated membrane protein 1). The data were collected from 120 cells (from each genotype and strain used) and recorded as a number of bacteria, which colocalised with LAMP-1 staining; they are represented as a fraction of *Salmonella* found in LAMP-1$^{+/ve}$ compartment (Figure 4.10B).

In all MEF lines infected with WT *Salmonella* over 95% of internalised bacteria were surrounded by structures which labelled with LAMP-1, whereas less than 10% in case of infection with *SifA*$^{-}$ strain (Table 10.7, Table 4.8). Furthermore, there were no differences between cell lines infected with either of strains: WT *Salmonella* was observed in association with LAMP-1 in 0.991 and 0.990 of wildtype *Dync1i1*$^{+/+}$ *Dync1i2*$^{+/+}$ and double homozygous *Dync1i1*$^{G482D/G482D}$ *Dync1i2*$^{T172I/T172I}$ cells respectively, whereas the fractions were 0.989 and 0.986 in case of wildtype *Dync1h1*$^{+/+}$ and *Dync1h1*$^{Loa/Loa}$ cells respectively (Figure 4.13A). On the other hand, nearly all the *SifA*$^{-}$ mutant bacteria lost the LAMP-1$^{+/ve}$ membrane, except for: 0.075 and 0.109 of bacteria in the *Dync1i1*$^{+/+}$*Dync1i2*$^{+/+}$ cells and *Dync1i1*$^{G482D/G482D}$*Dync1i2*$^{T172I/T172I}$ MEFs, together with 0.078 and 0.091 of bacteria invading *Dync1h1*$^{+/+}$ and *Dync1h1*$^{Loa/Loa}$ respectively (Figure 4.13B).

Table 4.8. Summary of membrane dynamics observed in MEFs infected with wildtype (WT) and *SifA*$^{-}$ *Salmonella* typhimurium

Membrane dynamics presented based on the results of statistical tests, where **n.s**. corresponds to lack of significant differences for p>0.05; for each bacterial strain values obtained for each observation were compared between wildtype *Dync1h1*$^{+/+}$ and homozygous *Dync1h1*$^{Loa/Loa}$ cell lines; detailed analysis is presented in Appendix 10.5.

Phenotype observed	WT *Salmonella*	*SifA*$^{-}$ *Salmonella*
Salmonella in LAMP -1$^{+/ve}$ compartment	n.s.	n.s.
MEFs with *Salmonella* in 2 compartments	n.s.	n.s.
Salmonella with lost /retained LAMP -1$^{+/ve}$ membranes	n.s.	n.s.

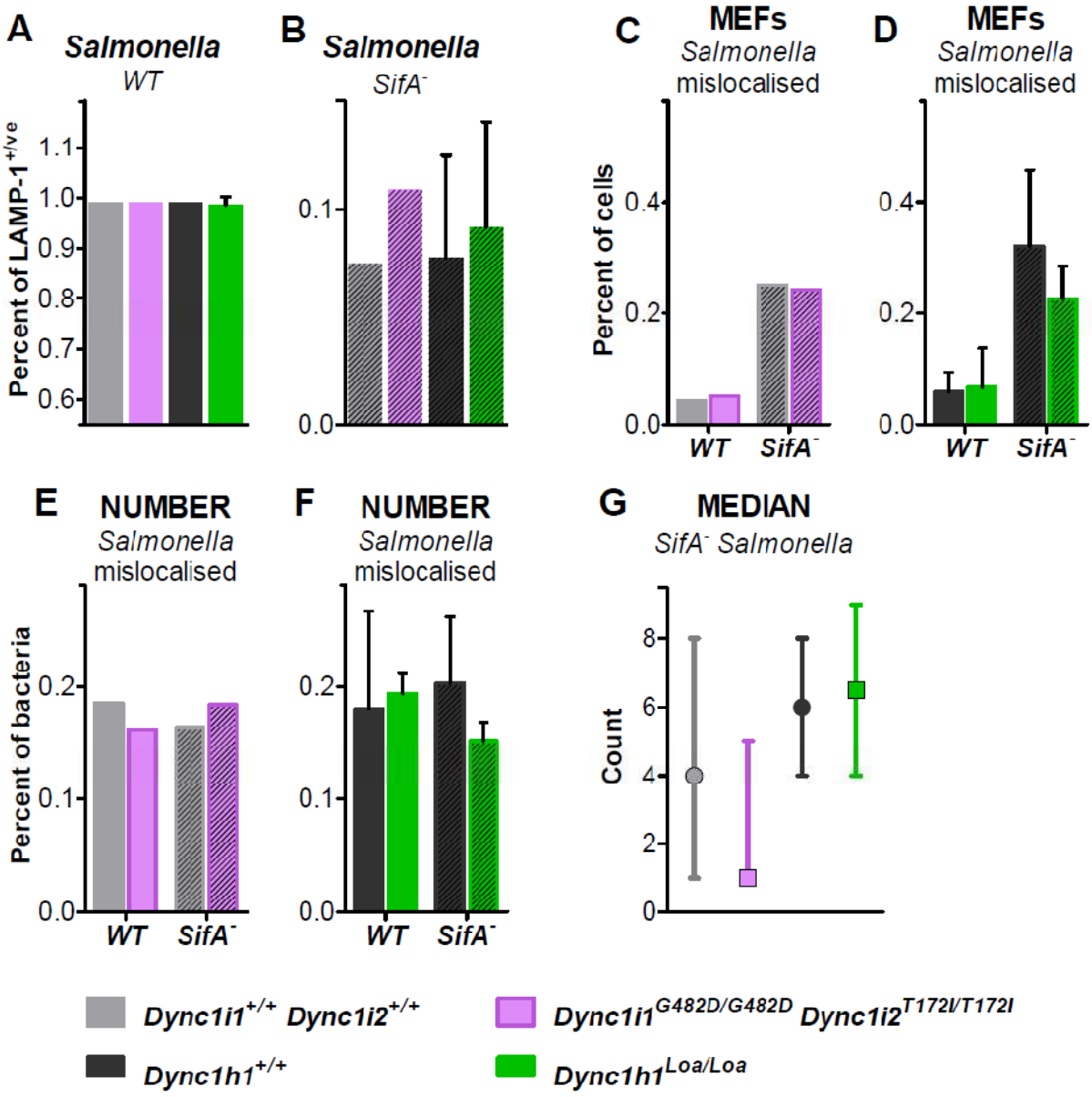

Figure 4.13. Comparison of the LAMP-1$^{+/ve}$ compartment in MEFs infected with wildtype (WT) and *SifA*$^{-}$ *Salmonella* typhimurium

Results for various features describing bacteria in relation to LAMP-1$^{+/ve}$ compartment; the legend refers to all graphs and colours correspond to wildtype *Dync1i1*$^{+/+}$ *Dync1i2*$^{+/+}$ (light grey), double homozygous *Dync1i1*$^{G482D/G482D}$ *Dync1i2*$^{T172I/T172I}$ (pink), wildtype *Dync1h1*$^{+/+}$ (dark grey), homozygous *Dync1h1*$^{Loa/Loa}$) (green) cell lines; bars corresponding to *SifA*$^{-}$ strain striped; on Y-axis plotted fraction of *Salmonella*, due to small sample size (n=2) MEFs carrying *Dync1h1*^{Loa} allele represented as mean ± standard deviation (SD); number from pooled observations shown as median and interquartile range (IQR)

A. Fraction of total WT *Salmonella,* which colocalised with LAMP-1 staining
B. Fraction of total *SifA*$^{-}$ *Salmonella*, which was retained in the LAMP-1$^{+/ve}$ membranes
C, D. Fraction of MEFs examined in each group (120 cells), which showed misplaced WT and *SifA*$^{-}$ bacteria
E, F. Fraction of WT and *SifA*$^{-}$ *Salmonella*, which was mis-localised in cells shown in C and D (only bacteria present in MEFs mentioned were taken into account)
G. Number of *SifA*$^{-}$ *Salmonella* observed in MEFs at 8 hours p.i.

Eukaryotic cells are known to interact with *Salmonella,* and there are few cellular mechanisms described which participate in preserving stable membranes around SCVs (Radtke et al., 2007). Therefore, the cellular input in membrane stability was expressed as number of fibroblasts, in which bacteria were observed in 2 compartments and number of mis-localised bacteria. WT *Salmonella* typhimurium was observed in LAMP-$1^{+/ve}$ compartment in nearly all fibroblasts examined (Table 4.8). Values were comparable between wildtype *Dync1i1*$^{+/+}$ *Dync1i2*$^{+/+}$ and homozygous *Dync1i1*$^{G482D/G482D}$ *Dync1i2*$^{T172I/T172I}$ cells, as 5 (0.042) and 6 (0.051) fibroblasts were found to have *Salmonella* in the cytosol (Figure 4.13C). Similar frequencies were noted for wildtype *Dync1h1*$^{+/+}$ (0.058) and homozygous *Dync1h1*$^{Loa/Loa}$ (0.066) cells (Figure 4.13D). It should be pointed though, that results were not informative due to big spread of raw values recorded for both, wildtype *Dync1h1*$^{+/+}$ (10 and 4) and homozygous *Dync1h1*$^{Loa/Loa}$ (13 and 2) cells. Misplaced bacteria in those cells were then counted and cytosolic WT *Salmonella* represented 0.186 and 0.161 of bacteria observed in *Dync1i1*$^{+/+}$ *Dync1i2*$^{+/+}$ and *Dync1i1*$^{G482D/G482D}$ *Dync1i2*$^{T172I/T172I}$ respectively (Figure 4.13E). Closer analysis of *Dync1h1*^{Loa} fibroblasts did not show differences (p=0.8459), and frequencies were comparable to values obtained for the *Dync1i1*^{G482D} *Dync1i2*^{T172I} line, where 0.194 (in *Dync1h1*$^{Loa/Loa}$) and 0.180 (in *Dync1h1*$^{+/+}$) of examined bacteria were misplaced from the LAMP-$1^{+/ve}$ compartment (Figure 4.13F).

Similar analysis was performed for MEFs infected with *SifA*$^{-}$ strain, but results were fairly uniform in all cell lines. Furthermore, the fraction of mutant bacteria, which retains LAMP-$1^{+/ve}$ membrane was suggested to represent defective trafficking of cellular components, thus not relevant (Beuzon *et al.*, 2002). Overall, between 0.242 and 0.321 of MEFs examined displayed *Salmonella* associated with the LAMP-$1^{+/ve}$ membranes (Table 10.7, Table 4.8). Within individual fibroblasts, *SifA*$^{-}$ bacteria which retained SCVs comprised 0.164 (in *Dync1i1*$^{+/+}$ *Dync1i2*$^{+/+}$), 0.184 (in *Dync1i1*$^{G482D/G482D}$ *Dync1i2*$^{T172I/T172I}$), 0.203 (in *Dync1h1*$^{+/+}$), and 0.151 (in *Dync1h1*$^{Loa/Loa}$) of all the bacteria counted (Figure 4.13E, F). Finally, numbers of mutant *Salmonella* present in MEFs at 8 hours p.i. were noted as a measure of replication rate. Regardless of genotype WT *Salmonella* were found in colonies containing over 20 bacteria in 20% of fibroblasts, whereas the bacteria from *SifA*$^{-}$ strain

were seldom observed in numbers higher than 20 (90th percentile was from 4.5 to 8.7 *Salmonella* per MEF). Furthermore, in both mutant cell lines (*Dync1i1*$^{G482D/G482D}$*Dync1i2*$^{T172I/T172I}$, *Dync1h1*$^{Loa/Loa}$) fewer bacteria were observed (median 1.0 and 6.0 respectively) than in corresponding wildtype cells (median 4.0 and 7.0 respectively) (Table 10.7, Figure 4.13G). Results were not tested for statistical significance due to a small sample size.

In summary, there were no differences in dynamics of LAMP-1$^{+/ve}$ membranes when cell lines carrying alleles of cytoplasmic dynein intermediate (*Dync1i1*^{G482D} *Dync1i2*^{T172I}) and heavy (*Dync1h1*^{Loa}) chains. Nonetheless, the mutant *SifA*$^{-}$ strain seemed to replicate slower in double homozygous *Dync1i1*$^{G482D/G482D}$ *Dync1i2*$^{T172I/T172I}$ cells, as expressed by number of bacteria observed 8 hours p.i.

4.5 Discussion

4.5.1 Mutations in the cytoplasmic dynein intermediate chains 1 and 2 (*Dync1i1*^{G482D}, *Dync1i2*^{T172I}) affect membrane dynamics during reassembly of the Golgi apparatus

Pericentriolar localisation of the Golgi complex depends on a constant flow of membranes and proteins mediated by microtubule associated motors. Stacks of membranes are also kept in tight clusters by Golgi tethering proteins (Vinke *et al.*, 2011), and different phenotypes of the Golgi complex can be observed by interfering with either tethering or membrane transport. The disruption of tethering proteins results in a network of tubules and vesicular structures often localised in the perinuclear region (Lam *et al.*, 2010). This morphology of the Golgi complex was observed during mitosis (Persico *et al.*, 2009), or after cleavage of GRASP65 after caspase-3 activation (Lane *et al.*, 2002). Furthermore, similar phenotype was caused by depletion of NDE1 and NDEL1, suggesting their role in maintaining Golgi structure. On the other hand, when retrograde transport is impaired, the Golgi complex becomes dispersed through the cytosol, as all the material diffuses towards ER and ERES. The most pronounced effect was observed after disruption of MTs (Cole *et al.*, 1996), or the dynein-dynactin complex (Roghi and Allan, 1999). Moreover, the

Golgi complex is highly dynamic and a perturbation of the membrane transport driven by the cytoplasmic dynein complex was shown to affect the structural integrity of the Golgi apparatus. The fragmentation of stacks was reported after depletion of various subunits of the cytoplasmic dynein (Palmer *et al.*, 2009), known interacting complexes, like LIS1 (Lam *et al.*, 2010), or dephoshorylation of the dynein intermediate chains (Vaughan, 2005). On the other hand, up regulation of RAB11-FIP3 resulted in Golgi scattering due to sequestration of the DYNC1LI1 (Horgan *et al.*, 2010a), while cells over-expressing any of LIS1, NDE1, or NDEL1 displayed Golgi stacks more compact than wildtype cells (Lam *et al.*, 2010). Partial decrease in the levels of intact dynein complex resulted an intermediate morphology of the Golgi consisting of reduced ribbon accompanied by small peripheral structures (Lam *et al.*, 2010). Huntingtin was also shown to participate in positioning of the Golgi, however its lack does not cause complete scatter but Golgi membranes formed tubules which extended in the cytosol (Caviston *et al.*, 2007).

Although the involvement of many complexes in the dynein mediated movement is well known, its mechanism and regulation are still not well described. Therefore, in this work we used a cell model carrying point mutations in the subunits of the cytoplasmic dynein complex (*Dync1i1*^{G482D}*, Dync1i2*^{T172I}) in order to investigate their effect on Golgi membrane dynamics during reassembly. Once scattered, individual Golgi fragments coalesce via tubules into a ribbon and are transported towards MTOC in a dynein dependent movement (Bechler *et al.*, 2010). Here, we observed these processes in the wildtype *Dync1i1*$^{+/+}$ *Dync1i2*$^{+/+}$ MEFs as the changes in the number of fragments and their shape during 20 min after nocodazole wash out. Although the homozygous mutations in the intermediate chains 1 and 2 (*Dync1i1*$^{G482D/G482D}$ *Dync1i2*$^{T172I/T172I}$) did not cause severe impairment in Golgi structure, the rate of its reassembly was slightly higher than in wildtype *Dync1i1*$^{+/+}$ *Dync1i2*$^{+/+}$ fibroblasts. In addition, values of mean eccentricity of Golgi stacks in the double homozygous cells were lower and did not vary during the reassembly. These results might suggest quicker fusion of membranes and different dynamics and tubulation of the Golgi membranes observed in the cells carrying two single point mutations (*Dync1i1*^{G482D}, *Dync1i2*^{T172I}). There are 2 other mouse lines carrying point mutations in the subunits of the dynein complex, which on the cellular level have been

shown to affect Golgi reassembly. The mutation in the cytoplasmic dynein heavy chain 1 (*Dync1h1*^{Loa}) caused defects in coalescence of dispersed stacks, which were described as increased number of Golgi fragments at 20 min after nocodazole washout in the homozygous *Dync1h1*$^{Loa/Loa}$ cells (Hafezparast *et al.*, 2003). Furthermore, mutation in the light intermediate chain 1 (*Dync1li1*^{N235Y}) was shown to affect the rate of the Golgi reassembly, as the values of number to area ratio were higher than in untreated *Dync1li1*$^{N235Y/N235Y}$ cells as late as 50 min (Banks *et al.*, 2011). However, no differences in the interactions between DLIC1 and RAB11-FIP3 were observed in the homozygous *Dync1li1*$^{N235Y/N235Y}$ fibroblasts (M.W. McCaffrey, personal communication).

4.5.2 Point mutations in the subunit of cytoplasmic dynein selectively influence the vesicular transport in the embryonic fibroblasts

4.5.2.1 EGF trafficking

Molecular motors were shown to take part in all the steps of the endosomal pathway, and the role of the dynein-dynactin complex in endosome movement is well documented, however, the exact role of its subunits in the domain of time is not well described. Apart from triggering a long range movement of endosomes, the cytoplasmic dynein complex was shown to actively participate in maturation of early endosomes and receptor sorting (Driskell *et al.*, 2007). Disruption of the dynein complex delayed the procession from early endosomes to endocytic recycling compartment (ERC) (Traer *et al.*, 2007), and reduced size distribution of endosomes observed and their movement (Driskell *et al.*, 2007). Furthermore, cells with depleted dynein failed to establish a perinuclear ERC, although kinetics of endosomal processes (sorting, TfnR recycling, EGFR degradation) were not affected (Caviston et al., 2007). Also RAB7 was suggested to retain dynein complex on the vesicles with folate receptor (FR), therefore keeping them in the ERC and preventing their recycling to plasma membrane (Chen *et al.*, 2008). A multiparametric screen for genes involved in the EGF trafficking also identified dynein heavy chain (DYNC1H1) and light chain RP3 (DYNLT3) (Collinet et al., 2010). It should be noted, however, that the majority of observations was recorded after complete disruption of the dynein complex or depletion of its components. Here, we describe the analysis of EGF endocytosis in the

presence of point mutation in the cytoplasmic dynein intermediate chain 2 (*Dync1i2*^{T172I}). Small differences were identified at different time points affecting discrete parameters of the endosomal pathway. The fact that they were defined temporally and spatially suggests a specific role of the DYNC1I2 in the processes of maturation or membrane dynamics in the perinuclear area. Recently, another mouse line with point mutation in the dynein light chain 1 (DYNC1LI1) was reported, and homozygous *Dync1li1*$^{N235Y/N235Y}$ fibroblasts displayed increase in the number of EGF$^{+/ve}$ endosomes 20 min and 40 min after the stimulation (Banks *et al.*, 2011).

4.5.2.2 Membrane dynamics in cells infected with Salmonella typhimurium

The involvement of the cytoplasmic dynein complex in the course of intracellular phase of infection has been well documented in HeLa cells, and lack of retrograde transport impaired both formation of vacuoles and bacterial replication (Guignot *et al.*, 2004). Several groups reported that cytoplasmic dynein is recruited to SCVs by interactions of P150^{Glued} with RAB7-RILP complex (Marsman *et al.*, 2004). Retrograde transport is initiated by activation of RAB7, and within 2 hours p.i. majority of bacteria can be found in the perinuclear region (Abrahams *et al.*, 2006). Furthermore, disruption of the cytoplasmic dynein by over expression of P50/DYNAMITIN or truncated RILP caused dispersion of bacteria or redistribution of colonies towards cell periphery (Abrahams *et al.*, 2006; Harrison *et al.*, 2004). *Salmonella* micro colonies were also shown to sequester the dynein complex around SCVs; however the timescale and mechanism of this interaction remain controversial. On the contrary, although lysosomal compartment was redistributed to the periphery, the association of *Salmonella* typhimurium with LAMP-1 and their perinuclear positioning were unaffected despite disruption of the dynein-dynactin interactions (Guignot *et al.*, 2004). Furthermore, detailed analysis of discrete movements of individual bacteria showed, that the movement along MTs was bidirectional and variable in terms of velocity, which suggested recruitment with both, kinesin-1 and dynein (Beuzon *et al.*, 2000). In addition, the activity of the cytoplasmic dynein was also implicated in bacterial replication, although both, decrease (Marsman *et al.*, 2004) and increase (Abrahams *et al.*, 2006) in number of bacteria were reported in effect.

In this chapter the localisation of *Salmonella* micro colonies and number of bacteria in the different MEF lines carrying mutations in the subunits of the cytoplasmic dynein were examined 8 hours p.i. There were no differences observed neither in the replication nor fraction of bacteria in the perinuclear region in any of the mutant in dynein subunits cell lines, and usually over 50% of WT *Salmonella* were found in perinuclear micro colonies. On the contrary, between 70% to 80% of HeLa cells were reported to have micro colonies located close to the Golgi complex from 4 hours after infection (Ramsden *et al.*, 2007a). Furthermore, a slight increase (9.2%) in the frequency of small (<20) perinuclear colonies was observed in the double homozygous *Dync1i1*$^{G482D/G482D}$ *Dync1i2*$^{T172I/T172I}$ cells when compared with wildtype *Dync1i1*$^{+/+}$ *Dync1i2*$^{+/+}$. On the other hand, the fraction of mutant *Dync1h1*$^{Loa/Loa}$ MEFs with the perinuclear micro colonies was smaller by 8.8% than in the wildtype cells.

The membrane dynamics of the SCVs assembled by WT and *SifA*$^{-}$ *Salmonella* was also investigated by comparing the association of both strains with the LAMP-1$^{+/ve}$ compartment. WT *Salmonella* were reported to maintain the SCV membrane intact during the infection, and in fibroblasts 97.1% of intracellular bacteria were surrounded by LAMP-1$^{+/ve}$ membranes 8 hours p.i. (Radtke *et al.*, 2007). On the contrary, the *SifA*$^{-}$ strain loses the SCV membrane and replicates in the cytoplasm. In HeLa cells this process starts approximately 6 hours p.i., and results in translocation of over 95% of bacteria to the cytosol (Beuzon *et al.*, 2002). Furthermore, the disruption of dynein-dynactin complex resulted in 60% of *SifA*$^{-}$ bacteria remaining in SCVs 8 hours p.i. Finally, fibroblasts inhibit replication of intracellular *Salmonella* (Martinez-Moya *et al.*, 1998), and levels of the intracellular nitric oxide (NO) were often elevated in response to infection (Garcia, 2001). This reaction is especially effective when bacteria are found in the cytosol, and the replication rate of the *SifA*$^{-}$ strain in mouse fibroblasts was reduced to 10% of replication of WT *Salmonella* (Beuzon *et al.*, 2002).

This analysis of MEFs with mutation in cytoplasmic dynein (*Dync1h1*^{Loa}, *Dync1i1*^{G482D} *Dync1i2*^{T172I}) and infected with WT and *SifA*$^{-}$ *Salmonella* did not show impairment in membrane trafficking, although the total number of mutant bacteria was lower than values recorded for MEFs infected with WT *Salmonella*. Furthermore, the median number of intracellular bacteria tended to be lower in both mutant (*Dync1i1*$^{G482D/G482D}$ *Dync1i2*$^{T172I/T172I}$ and *Dync1h1*$^{Loa/Loa}$) cell lines.

Although in some cases results were inconclusive, it should be noted, that most of the work cited above was performed using HeLa cells as a model system. However, the role of cell type in pathogen-host interactions is a crucial factor, e.g. formation of Sifs in fibroblasts was shown to be reduced, while in HeLa cells a tubular network of SCVs membranous extensions is a common phenomenon (Martinez-Moya *et al.*, 1998). Therefore, comparisons might not be informative, and it would be beneficial to observe the progression of the bacterial infection in our fibroblast with measurements taken at few time points or employ quantitative methods to evaluate *Salmonella* proliferation within MEFs. Nonetheless, wildtype and mutant strains of *Salmonella* typhimurium present a very good tool to study endocytic pathway and its perturbations.

5. Cytoplasmic dynein complex and the formation of stress granules

5.1 Introduction

Stress granules (SG) have recently gained increased attention as a universal mechanism controlling RNA metabolism and translation; however their function, structure, or dynamics are still not well understood. There are many classes of RNA containing granules and they have been well described elsewhere (Anderson and Kedersha, 2009; Buchan and Parker, 2009).

5.1.1 Cellular stress and stress response pathways

Stress granules are non-membranous cytoplasmic foci ranging in size from 0.1 to 2.0 μm, composed of non-translating messenger ribonucleoproteins (mRNPs) that rapidly aggregate in cells exposed to environmental conditions (Anderson and Kedersha, 2009). Many stresses act via decreasing stability of proteins (e.g. heat shock), which triggers mechanisms dealing with structurally changed molecules (e.g. unfolded protein response (UPR), activation of chaperones and proteosomes) (Ron and Walter, 2007). In many cases, the stress-induced phosphorylation of the translation initiation factor eIF2α (EIF2A) triggers stress granule assembly by preventing or delaying translational initiation. Arsenite (SA) is known to induce oxidative stress via: mimicking of phosphate, oxidation of proteins, depletion of antioxidants (Ventura-Lima *et al.*, 2011). The imbalance in oxidative stress is a specific signal, which activates eukaryotic translation initiation factor 2α kinase 1 (EIF2AK1) resulting in EIF2A phosphorylation (McEwen *et al.,* 2005). Thapsigargin (TG) is a compound which inhibits an activity of ATPase Ca^{2+} pump 3 (ATP2A3) resulting in release of Ca^{2+} from ER stores and indirectly contributes to ER stress. The Ca^{2+} imbalance between cytosol and ER cisterns activates eukaryotic translation initiation factor 2α kinase 2 (EIF2AK2/PKR) (Prostko *et al.*, 1995), while ER stress triggers phosphorylation of eukaryotic translation initiation factor 2α kinase 3 (EIF2AK3/PERK) (Harding et al., 1999). The EIF2A is a common substrate for both kinases, and its modification initiates the assembly of stress granules.

5.1.2 Components of stress granules

SG are primarily composed of the stalled 48S complexes containing bound mRNAs derived from disassembling polysomes (Anderson and Kedersha, 2009). These contain poly(A)+ RNA bound to early initiation factors (such as EIF4E, EIF3, EIF4A, EIFG) and small, but not large, ribosomal subunits. In addition to these core components, SG contain an eclectic assembly of proteins that vary with cell type and with the nature and duration of the stress involved. RNA-binding proteins, transcription factors, RNA helicases, nucleases, kinases and signalling molecules have been reported to accumulate in SG. In some cases, recruitment of signalling proteins into stress granules influences cell survival. More recently, stress granules have been shown to contain the Argonaute complex, microRNAs, a number of mRNA-editing enzymes, and proteins required for transposon activity (Detzer *et al.*, 2011).

5.1.3 Role of the cytoplasmic dynein complex in the assembly of stress granules

The biophysical studies of SG assembly suggested an active mechanism driving RNA and proteins in the organised foci, and their kinetics could not be explained by diffusion (Chernov *et al.*, 2009). One possibility involved an action of microtubules, as microtubule-depolymerising drugs such as nocodazole inhibit SG formation, although smaller SG generally still form (Buchan and Parker, 2009). Recently, MT-associated motors have been observed in proximity to the SG and targeted depletion of the dynein heavy chain (DYNC1H1) strongly reduced the formation of cytosolic granules (Loschi *et al.*, 2009). Furthermore, dynein inhibition or knockdown also increases protease sensitivity of TIA-1 aggregates, providing additional evidence for a role in stress granule stability (Tsai *et al.*, 2009).

5.2 Project overview

Formation of SG was investigated using as a model MEF lines, which were isolated from wildtype and mutant animals (*Dync1i1*^{G482D}, *Dync1i2*^{T172I}, and *Dync1h1*^{Loa}). The cellular response to stress was examined along with detailed analysis of SG in individual cells.

5.3 Results

Cells were derived from mouse lines carrying double homozygous mutant alleles of the intermediate chains 1 and 2 (*Dync1i1*^{G482D} *Dync1i2*^{T172I}) and *Loa,* carrying mutation in the heavy chain (*Dync1h1*^{Loa}). In all cases MEF lines were compared with wildtype 'littermate' lines. Cellular stress was induced with sodium arsenite (SA, oxidative stress) and thapsigargin (TG, Ca^{2+} release and ER stress) and the phosphorylation of a eukaryotic translation initiation factor 2α (EIF2A) examined in response. Two well characterised markers: GTPase activating protein (SH3 domain) binding protein 1 (G3BP) and TIA1 cytotoxic granule-associated RNA binding protein-like 1 (TIAL1) were used in order to visualise SG, and details of the treatment, analysis, and protein analysis were described in sections 2.6.6, 2.6.8, 2.7.1, and 2.5.4 respectively. Briefly, cells were incubated in medium containing 200 µM SA for 45 min, or 1 µM thapsigargin for 1 hour. The specificity of induced granules was assessed by additional treatment with 50 µg/ml emetine, which inhibits formation of SG (Kedersha and Anderson, 2007).

5.3.1 Induction of stress granules in the wildtype and homozygous (*Dync1i1*$^{G482D/G482D}$ *Dync1i2*$^{T172I/T172I}$, and *Dync1h1*$^{Loa/Loa}$) MEFs

Wildtype *Dync1i1*$^{+/+}$ *Dync1i2*$^{+/+}$ (n=3), double homozygous *Dync1i1*$^{G482D/G482D}$ *Dync1i2*$^{T172I/T172I}$ (n=3), wildtype *Dync1h1*$^{+/+}$ (n=3), and homozygous *Dync1h1*$^{Loa/Loa}$ (n=3) MEFs were examined for formation of SG. There were 3 experiments performed with each cell line and cells were scored for the presence of G3BP and TIAL1 positive structures. In all the cell untreated and incubated with emetine no granules were observed (over 200 cells examined from each experiment), which confirms the specificity of an assay. Results are represented as mean ± standard deviation (SD).

5.3.1.1 Phosphorylation of EIF2A

A state of cellular stress was examined in each cell line by assessing phosphorylation of the EIF2A, as both sodium arsenite (SA) and thapsigargin (TG) activate kinases specific for serine at a position 51. MEFs were treated as described in section 2.6.6 and cell lysates probed with antibodies specific for phosphorylated EIF2A at serine 51 (sections 2.5.2, 2.5.3, and 2.5.4). From each sample 10 μg of total protein were loaded, as a positive control antibodies against β-actin (44 kDa) were used.

An increase in signal of phosphorylated EIF2A (36 kDa) was observed in both wildtype *Dync1i1*$^{+/+}$ *Dync1i2*$^{+/+}$ and double homozygous *Dync1i1*$^{G482D/G482D}$ *Dync1i2*$^{T172I/T172I}$ fibroblasts after treatment with SA or TG (Figure 5.1). In all samples additional bands were observed which likely correspond to unspecific detection. Furthermore, even untreated cells showed low immunoreactivity against phosphorylated EIF2A, which might reflect a state of oxidative stress typical for MEFs cultured in the atmospheric levels of oxygen (discussed in section 4.1).

Similar pattern was observed for protein extracts from wildtype *Dync1h1*$^{+/+}$ and homozygous *Dync1h1*$^{Loa/Loa}$ MEFs probed with antibodies against phosphorylated EIF2A (Figure 5.2). Treatment with either sodium arsenite (SA) or thapsigargin (TG) resulted in increased phosphorylation of the EIF2A when compared with the untreated cells.

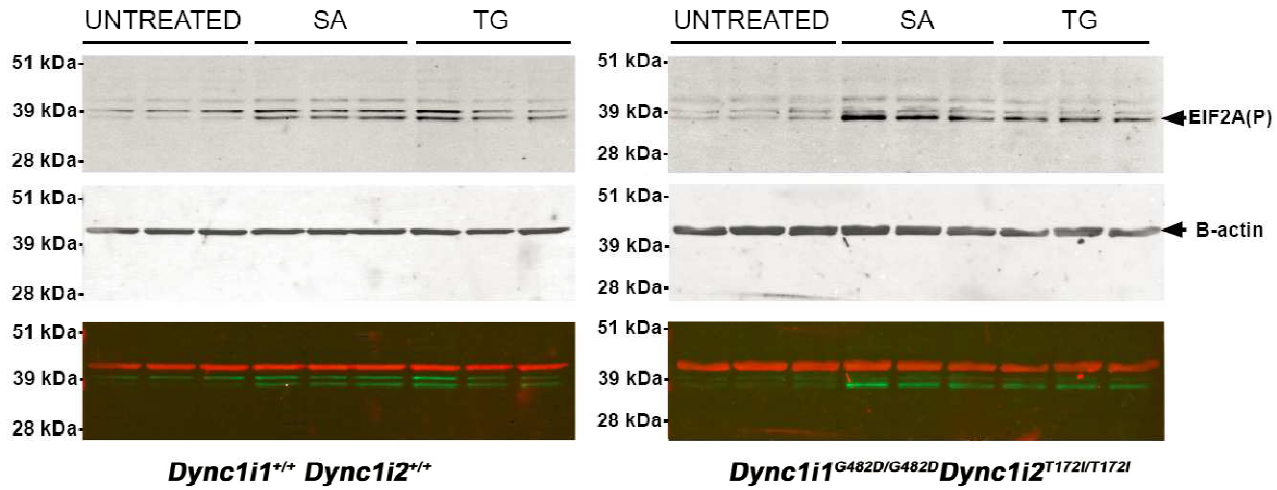

Figure 5.1. Immunodetection of phosphorylated EIF2A in the wildtype *Dync1i1*$^{+/+}$ *Dync1i2*$^{+/+}$ and double homozygous *Dync1i1*$^{G482D/G482D}$ *Dync1i2*$^{T172I/T172I}$ fibroblasts

Protein lysates from fibroblasts (3 cell lines) treated with sodium arsenite (SA, 200μM, 45min) or thapsigargin (TG, 1μM, 1hour) were separated (Bis-Tris NuPAGE), transferred on membranes (PVDF) and probed against phospho-EIF2A (arrow at 36 kDa, green channel) and β-actin (arrow at 44kDa, red channel); greyscale images show immunodetection of individual antigens while bottom image shows a 'dual channel' detection using Licor IR-Dye secondary antibodies; also visible unspecific bands detected by antibody aginst EIF2A(P)

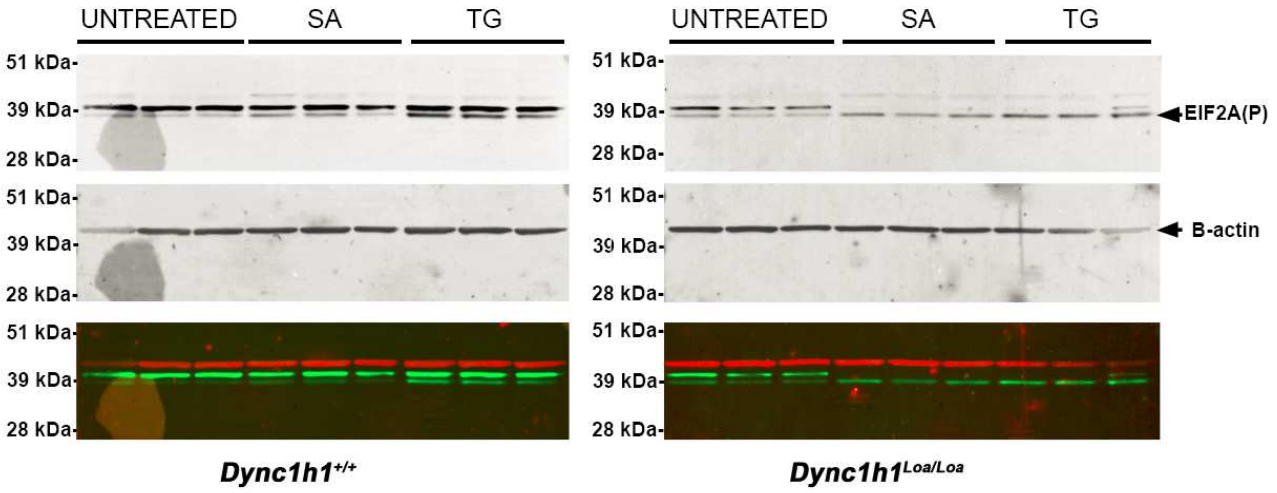

Figure 5.2. Immunodetection of phosphorylated EIF2A in the wildtype *Dync1h1*$^{+/+}$ and homozygous *Dync1h1*$^{Loa/Loa}$ fibroblasts

Protein lysates from fibroblasts (3 cell lines) treated with sodium arsenite (SA, 200μM, 45min) or thapsigargin (TG, 1μM, 1hour) were separated (Bis-Tris NuPAGE), transferred on membranes (PVDF) and probed against phospho-EIF2A (arrow at 36 kDa, green channel) and β-actin (arrow at 44kDa, red channel); greyscale images show immunodetection of individual antigens while bottom image shows a 'dual channel' detection using Licor IR-Dye secondary antibodies; also visible unspecific bands detected by antibody aginst EIF2A(P)

5.3.1.2 *Sodium arsenite treatment*

All cell lines examined displayed cytosolic foci positive for both G3BP and TIAL1 in response to SA treatment, which were present in approximately 30% of cells. There were no differences between cells isolated from the mutant intermediate chain 1 and 2 (*Dync1i1*^{G482D} *Dync1i2*^{T172I}) lines (p=0.3389), although double homozygous *Dync1i1*$^{G482D/G482D}$*Dync1i2*$^{T172I/T172I}$ (n=3) fibroblasts showed a slightly higher fraction of stressed cells (0.240 ± 0.044) than corresponding wildtype *Dync1i1*$^{+/+}$ *Dync1i2*$^{+/+}$ (n=3) lines (0.199 ± 0.015) (Table 5.1).

Cytosolic stress granules were also observed in the *Dync1h1*^{Loa} cell lines, and an average fraction of cells displaying G3BP$^{+/ve}$ structures was higher than in the *Dync1i1*$^{+/+}$ *Dync1i2*$^{+/+}$ MEFs (Figure 5.3). The fraction of stressed cells was higher in the homozygous *Dync1h1*$^{Loa/Loa}$ (n=3, 0.339 ± 0.032) cells than in the wildtype *Dync1h1*$^{+/+}$ (n=3, 0.288 ± 0.019) (p=0.0767) (Table 5.1). These results suggested that the presence of mutation in the cytoplasmic dynein heavy chain 1 (*Dync1h1*^{Loa}) might interact with the signalling pathways triggering stress response, however it did not affect the overall susceptibility of fibroblasts to stress.

Table 5.1. Analysis of stress granule formation after sodium arsenite (SA) treatment
Results obtained in 3 experiments were pooled and shown as total numbers of cells scored**,** fractions of G3BP$^{+/ve}$ cells recorded for each cell line, and mean ± standard deviation (SD); genotypes annotated as follows: wildtype (*Dync1i1*$^{+/+}$*Dync1i2*$^{+/+}$) double homozygous (*Dync1i1*$^{G482D/G482D}$ *Dync1i2*$^{T172I/T172I}$), wildtype (*Dync1h1*$^{+/+}$), homozygous (*Dync1h1*$^{Loa/Loa}$); results of statistical analysis and reported two-tailed p-values shaded grey; n - number of cell lines derived from animals

Observation	***Dync1i1*$^{+/+}$ *Dync1i2*$^{+/+}$ n=3**			***Dync1i1*$^{G482D/G482D}$ *Dync1i2*$^{T172I/T172I}$ n=3**		
Number of cells	1828	1278	1202	1179	1799	1188
G3BP$^{+/ve}$	0.216	0.187	0.195	0.209	0.291	0.221
	0.199 ± 0.015			0.240 ± 0.044		
	Paired *t*-test, p=0.3389					
Observation	***Dync1h1*$^{+/+}$ n=3**			***Dync1h1*$^{Loa/Loa}$ n=3**		
Number of cells	753	574	740	509	953	825
G3BP$^{+/ve}$	0.291	0.305	0.268	0.371	0.337	0.308
	0.288 ± 0.019			0.339 ± 0.032		
	Paired *t*-test, p=0.0767					

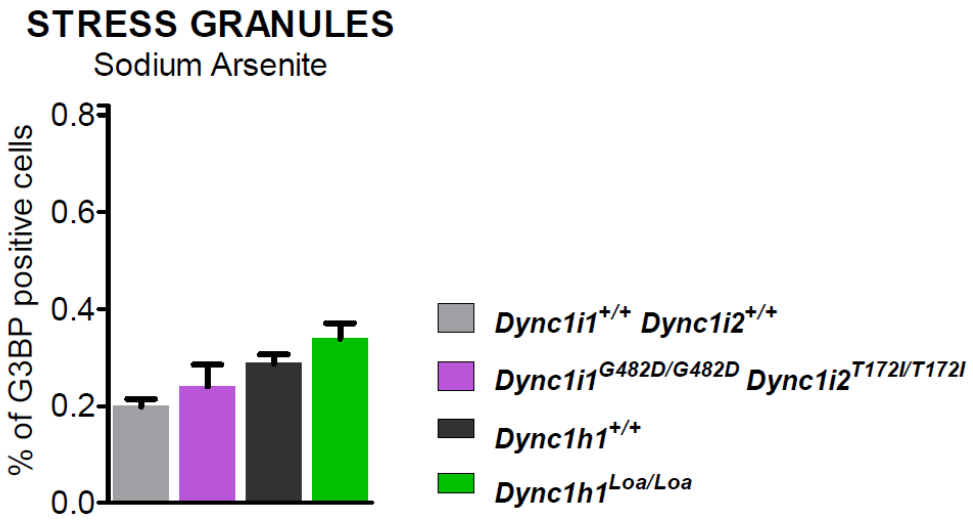

Figure 5.3. Analysis of stress granule formation after sodium arsenite (SA) treatment
Fractions of cells with G3BP$^{+/ve}$ cytosolic structures represented as mean ± standard deviation (SD); legend colours refer to wildtype *Dync1i1*$^{+/+}$ *Dync1i2*$^{+/+}$ (grey), double homozygous *Dync1i1*$^{G482D/G482D}$ *Dync1i2*$^{T172I/T172I}$ (violet), wildtype *Dync1h1*$^{+/+}$ (dark grey), homozygous *Dync1h1*$^{Loa/Loa}$ (green) cell lines

5.3.1.3 Thapsigargin treatment

Treatment with thapsigargin (TG) also triggered formation of SG, yet in twice as many cells as after sodium arsenite. This might be due to a dual action of TG: Ca^{2+} influx from endoplasmic reticulum (ER) activates a eukaryotic translation initiation factor 2-alpha kinase2 (EIF2AK2/PKR) (Prostko *et al.*, 1995), whereas Ca^{2+} imbalance causes ER stress and activation of a eukaryotic translation initiation factor 2-alpha kinase 3 (EIF2AK3/PERK) (Harding et al., 1999). Both kinases phosphorylate EIF2A thus triggering the assembly of stress granules.

Analysis of the *Dync1i1*^{G482D}*Dync1i2*^{T172I} fibroblasts treated with TG indicated towards an increased formation of the SG in the double mutant cells, which was in agreement with results obtained for SA treated MEFs. Over half of the double homozygous *Dync1i1*$^{G482D/G482D}$ *Dync1i2*$^{T172I/T172I}$ (n=3) cells examined displayed G3BP$^{+/ve}$ foci (0.512 ± 0.028), while the fraction of wildtype *Dync1i1*$^{+/+}$ *Dync1i2*$^{+/+}$ (n=3) MEFs was slightly lower (0.427 ± 0.055) (Table 5.2). However, this observation was not significant (p=0.1345) (Figure 5.4).

Table 5.2. Analysis of stress granule formation after thapsigargin (TG) treatment
Results obtained in 3 experiments were pooled and shown as total numbers of cells scored, fractions of G3BP$^{+/ve}$ cells recorded for each cell line, and mean ± standard deviation (SD); genotypes annotated as follows: wildtype (*Dync1i1*$^{+/+}$ *Dync1i2*$^{+/+}$) double homozygous (*Dync1i1*$^{G482D/G482D}$ *Dync1i2*$^{T172I/T172I}$), wildtype (*Dync1h1*$^{+/+}$), homozygous (*Dync1h1*$^{Loa/Loa}$); results of statistical analysis and reported two-tailed p-values shaded grey and for **p<0.05 in bold**; n - number of cell lines derived from animals

Observation	***Dync1i1*$^{+/+}$ *Dync1i2*$^{+/+}$ n=3**			***Dync1i1*$^{G482D/G482D}$ *Dync1i2*$^{T172I/T172I}$ n=3**		
Number of cells	1957	1419	1494	2582	2149	1683
G3BP$^{+/ve}$	0.398	0.393	0.490	0.483	0.538	0.515
	0.427 ± 0.055			0.512 ± 0.028		
	Paired *t*-test, p=0.1345					
Observation	***Dync1h1*$^{+/+}$ n=3**			***Dync1h1*$^{Loa/Loa}$ n=3**		
Number of cells	1116	1000	918	888	796	854
G3BP$^{+/ve}$	0.601	0.581	0.662	0.664	0.695	0.787
	0.615 ± 0.042			0.715 ± 0.064		
	Paired *t*-test, **p=0.0337**					

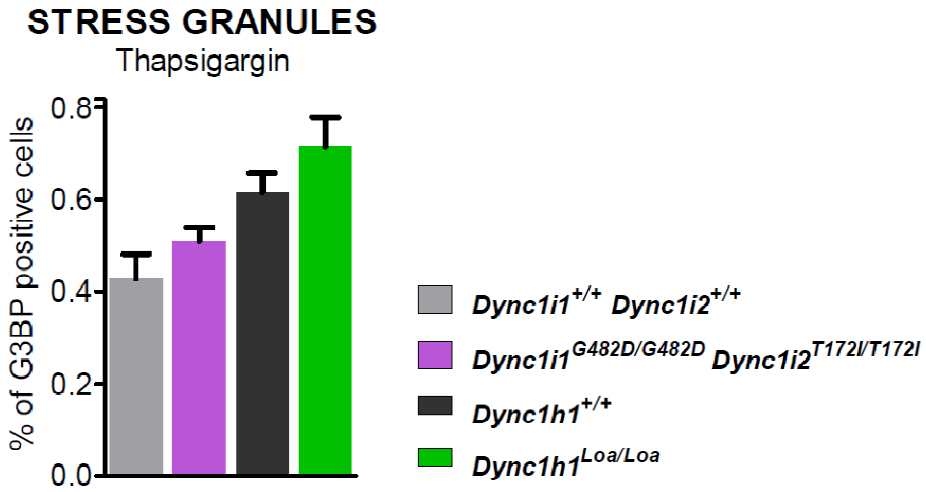

Figure 5.4. Analysis of stress granule formation after thapsigargin (TG) treatment
Fractions of cells with G3BP$^{+/ve}$ cytosolic structures represented as mean ± standard deviation (SD); legend colours refer to wildtype *Dync1i1*$^{+/+}$ *Dync1i2*$^{+/+}$ (grey), double homozygous *Dync1i1*$^{G482D/G482D}$ *Dync1i2*$^{T172I/T172I}$ (violet), wildtype *Dync1h1*$^{+/+}$ (dark grey), homozygous *Dync1h1*$^{Loa/Loa}$ (green) cell lines

On the other hand, TG induced the stress granules in relatively higher fraction of homozygous *Dync1h1*$^{Loa/Loa}$ (n=3) MEFs (0.715 ± 0.064) than in the wildtype *Dync1h1*$^{+/+}$ cells (0.615 ± 0.042) (p=0.0337) (Table 5.2). The effect of thapsigargin was more pronounced than in case of arsenite, which might reflect the induction of stress response mediated through activation of different signalling pathways.

In conclusion, the stress granules were successfully induced in mouse embryonic fibroblasts using different agents (SA, TG), which triggered different signalling pathways. In conditions used effects after the thapsigargin (TG) treatment were more pronounced than in case of the arsenite (SA), which might correspond to activation of more effective pathways or more specific cellular response to stress. Furthermore, treatment with SA for longer time (e.g. 1 hour) of with higher concentrations (e.g. 500 μM) often resulted in cell death (data not shown), therefore thapsigargin seems to be a better choice to induce SG formation in fibroblasts.

The formation of the SG triggered by applying stressors was investigated in the cell lines carrying mutant alleles in the cytoplasmic dynein intermediate chains 1 and 2 (*Dync1i1*^{G482D} *Dync1i2*^{T172I}) and cytoplasmic dynein heavy chain 1 (*Dync1h1*^{Loa}). The mutations in the intermediate chains 1 and 2 did not affect the observed response and the fractions of cells with G3BP$^{+/ve}$ structures were comparable. On the other hand, in the presence of a homozygous *Dync1h1*^{Loa} mutation more cells were observed to assemble SG when treated with thapsigargin.

It should also be noted, that differences observed between the cell lines (*Dync1i1*^{G482D} *Dync1i2*^{T172I} and *Dync1h1*^{Loa}*)* are likely to be caused by different genetic background, as many genes are known to be involved in the stress response. While *Dync1h1*^{Loa} mice were congenic C57BL6/J, *Dync1i1*^{G482D} *Dync1i2*^{T172I} animals were N4 generation backcrossed onto the C57BL6/J inbred strain.

5.3.2 Image-based analysis of stress granules in the wildtype and homozygous (*Dync1i1*$^{G482D/G482D}$ *Dync1i2*$^{T172I/T172I}$, and *Dync1h1*$^{Loa/Loa}$) MEFs

Disruption of dynein function was reported to affect not only the assembly of stress granules but also their size distribution (Loschi *et al.*, 2009). Furthermore, in the presence of mutant TARDBP (TPD43) granules assembled were bigger but less numerous (Dewey *et al.*, 2011). Therefore, a detailed analysis of the stress granules was performed by comparing high resolution images of individual cells. The pictures were taken and analysed as described in sections 2.7.2 and 2.7.3. From each condition (sodium arsenite, thapsigargin) at least 20 pictures of each cell line were taken from 2 experiments, thus over 40 pictures of wildtype *Dync1i1*$^{+/+}$*Dync1i2*$^{+/+}$ (n=3), double homozygous *Dync1i1*$^{G482D/G482D}$ *Dync1i2*$^{T172I/T172I}$ (n=3), wildtype *Dync1h1*$^{+/+}$ (n=3), and homozygous *Dync1h1*$^{Loa/Loa}$ (n=3) fibroblasts were taken (Figure 5.5). The number and total area of G3BP$^{+/ve}$ objects were recorded for individual cells. Because values obtained for each cell line did not have Gaussian distribution, raw data were transformed ($f(x) = logY$) prior to statistical analysis. All the parameter were analysed with two-way ANOVA. Detailed analysis can be found in Appendix 10.7 and Table 10.8 while results are summarised in Table 5.3.

Figure 5.5. Representative pictures of wildtype (*Dync1i1*$^{+/+}$*Dync1i2*$^{+/+}$) MEFs showing stress granules (next page)

Intracellular structures were stained with antibodies against G3BP protein (grey), TIAL1 protein (red) and chromatin (DAPI, blue); distinct foci were visible after treatment with sodium arsenite (SA, 200 µM for 45 min) or thapsigargin (TG, 1 µM, 1 hour) whereas in untreated cells only TIAL1 was visible in the nucleus, in the presence of emetine (Em, 50 µg/ml, 1 hour) stress granules were dissolved and G3BP remained only in small puncta; images from separate channels shown in greyscale yellow pseudocoloring present in case of overlapping intensities; not in scale

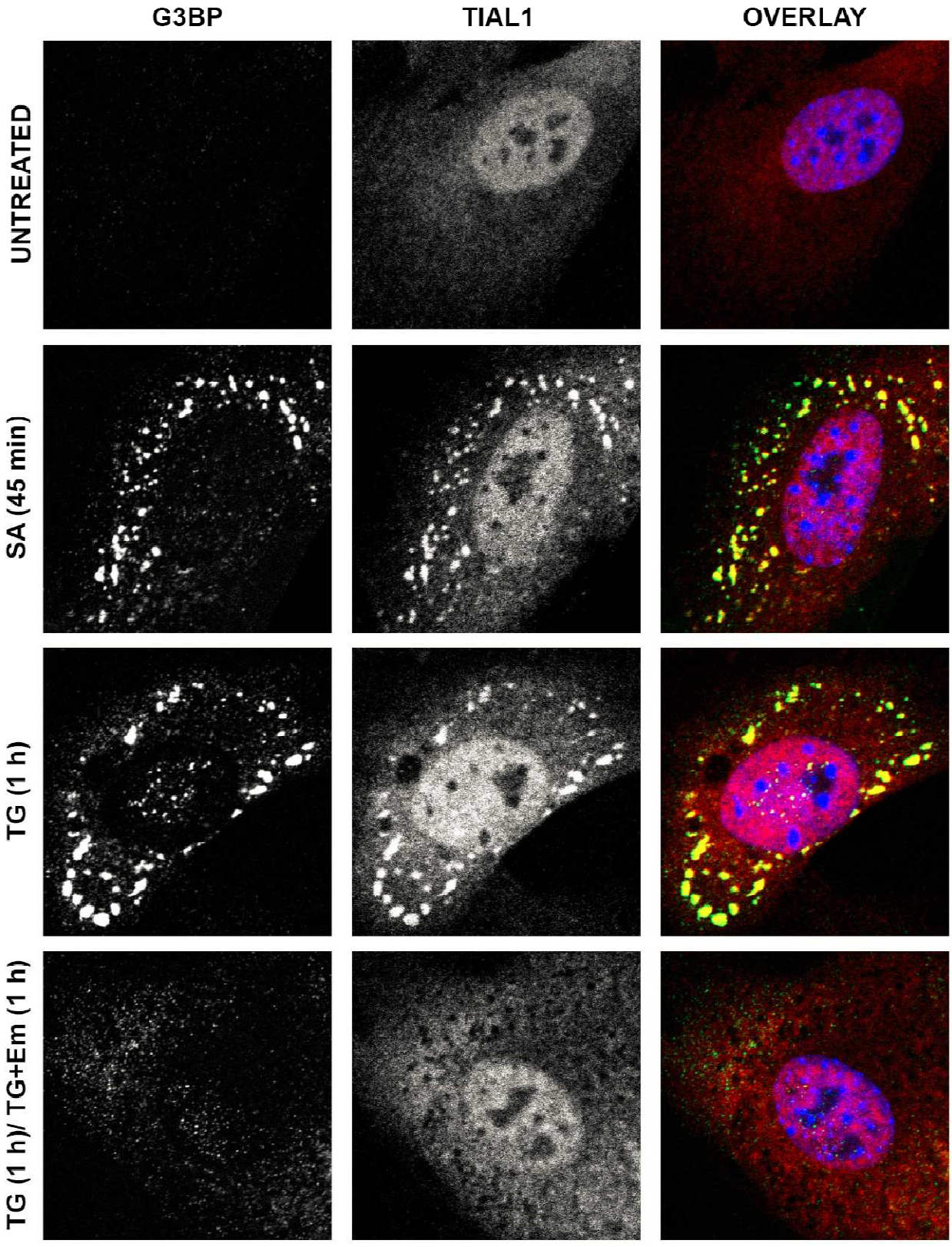
G3BP
TIAL1
OVERLAY
UNTREATED
SA (45 min)
TG (1 h)
TG (1 h)/ TG+Em (1 h)

5.3.2.1 Sodium arsenite treatment

Number of G3BP$^{+/ve}$ foci varied between cells ranging from 20 to 150. Although it was much higher than often reported (e.g. 5 – 10 in HEK293 cell, Dewey *et al.*, 2011), it might originate as a characteristic of MEFs and automated analysis, when objects above threshold intensity and size were counted as stress granules. After treatment with arsenite the median number of SG in the wildtype *Dync1i1*$^{+/+}$ *Dync1i2*$^{+/+}$ (n=3) cells ranged from 39 – 49, while double homozygous *Dync1i1*$^{G482D/G482D}$ *Dync1i2*$^{T172I/T172I}$ (n=3) had median from 42 – 50 (Table 10.8, Figure 5.6A). The summed area of the G3BP$^{+/ve}$ foci was measured in pixels and median values were in the range of 9308 – 10010 in the wildtype *Dync1i1*$^{+/+}$ *Dync1i2*$^{+/+}$ and 8516 – 11291 in the double homozygous *Dync1i1*$^{G482D/G482D}$ *Dync1i2*$^{T172I/T172I}$ fibroblasts (Figure 5.6B). These cells varied neither when number (p=0.4929) nor the total area of stress granules was analysed (p=0.8517) (Table 5.3).

Cell lines derived from *Dync1h1*^{Loa} animals showed slightly higher numbers than corresponding *Dync1i1*^{G482D}*Dync1i2*^{T172I} lines, which is in agreement with observed higher fraction of cells, which assembled stress granules. Furthermore, there were on average 13 more granules observed in the homozygous *Dync1h1*$^{Loa/Loa}$ (n=3) cells than in the wildtype *Dync1h1*$^{+/+}$ (n=3), with medians ranging 49 – 57 and 62 – 64 in the wildtype *Dync1h1*$^{+/+}$ and homozygous *Dync1h1*$^{Loa/Loa}$ MEFs respectively (p< 0.0001) (Table 5.3). Total area of the G3BP$^{+/ve}$ foci was also higher in the homozygous *Dync1h1*$^{Loa/Loa}$ cells (14519 – 16211) than in the corresponding wildtype *Dync1h1*$^{+/+}$ lines (11796 – 16556) (p=0.0006) (Figure 5.6.B). Because mutual increase in the number and total area of the granules bore a similarity to the EGF$^{+/ve}$ endosomes (4.4.3.2), the Pearson correlation coefficients were calculated for the data obtained for the *Dync1h1*^{Loa} lines (Figure 5.6C). The high values of the coefficients (above 0.90) suggested a strong link between number and area, which might correspond to structural and functional characteristics of the stress granules.

Table 5.3. Summary of analysis of stress granules in individual cells after sodium arsenite (SA) treatment
Parameters of cytoplasmic SG presented based on the results of statistical tests, where **n.s**. corresponds to lack of significant differences for p>0.05; trends were noted if p<0.1; for different cell lines (*Dync1i1*^{G482D} *Dync1i2*^{T172I}, *Dync1h1*^{Loa}) values of each parameter were compared between wildtype and homozygous MEFs; detailed analysis is presented in Appendix 10.6.

Parameter	*Dync1i1*^{G482D} *Dync1i2*^{T172I}	*Dync1h1*^{Loa}
Number of G3BP$^{+/ve}$ foci	n.s.	*Dync1h1*$^{Loa/Loa}$ cells formed more SG (p<0.0001)
Total area of G3BP$^{+/ve}$ foci	n.s.	*Dync1h1*$^{Loa/Loa}$ cells had higher area (p=0.0006)

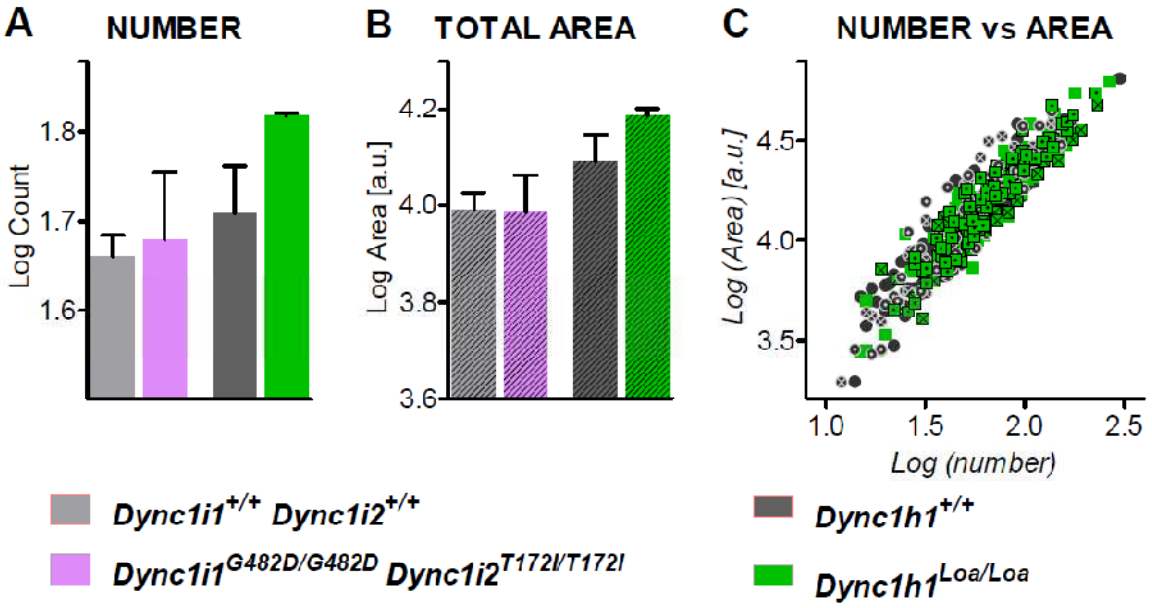

Figure 5.6. Analysis of parameters of the G3BP$^{+/ve}$ granules in the fibroblasts observed after sodium arsenite treatment
Data recorded as mean ± standard deviation (SD) of *log* transformed values; legend refers to all graphs and colours correspond to wildtype *Dync1i1*$^{+/+}$ *Dync1i2*$^{+/+}$ (grey), double homozygous *Dync1i1*$^{G482D/G482D}$ *Dync1i2*$^{T172I/T172I}$ (violet), wildtype *Dync1h1*$^{+/+}$ (dark grey), and homozygous *Dync1h1*$^{Loa/Loa}$ (green) MEFs; a.u. – arbitrary units

A. Mean values of *log* transformed number of stress granules
B. Mean values of *log* transformed total area of stress granules
C. Correlation between number and area of stress granules in the *Dync1h1*^{Loa} cells; *log* transformed values are plotted as dots corresponding to individual cells; shape of 'clouds' typical for positive correlation

5.3.2.2 Thapsigargin treatment

The detailed analysis of stress granules induced by thapsigargin (TG) was performed in the same way as in the case of arsenite treated MEFs. There were no differences observed between wildtype *Dync1i1*$^{+/+}$ *Dync1i2*$^{+/+}$ and double homozygous *Dync1i1*$^{G482D/G482D}$ *Dync1i2*$^{T172I/T172I}$ fibroblasts neither in the number of granules (p=0.9487) nor their total area (p=0.5599) (Table 10.9). Median number of G3BP$^{+/ve}$ foci indentified in the wildtype *Dync1i1*$^{+/+}$ *Dync1i2*$^{+/+}$ cells was 40 – 50 with the median total area ranging 8462 – 11659 (Figure 5.7A,B). These values were comparable with the parameters of stress granules induced with the sodium arsenite (p=0.8717 for 'number', p=0.9280 for 'area'). Likewise, in the double homozygous *Dync1i1*$^{G482D/G482D}$*Dync1i2*$^{T172I/T172I}$ MEFs median 39 – 52 granules were observed with the total area ranging 8988 – 10386. These parameters were not different from the values calculated for the cells treated with arsenite (p=0.6261 for 'number', p=0.6433 for 'area') (Table 5.4). It should be noted however, that results were often affected by differences between cell lines.

The features of thapsigargin (TG) induced granules in the wildtype *Dync1h1*$^{+/+}$ and homozygous *Dync1h1*$^{Loa/Loa}$ fibroblasts did not differ, which suggest different mechanism of granule assembly (Table 5.4). Although the homozygous *Dync1h1*$^{Loa/Loa}$ (n=3) cells tended to form more G3BP$^{+/ve}$ foci than wildtype *Dync1h1*$^{+/+}$ cells (median 48 – 61, and 46 – 64, respectively) (p=0.0948), the results were likely inconclusive due to high variation within cell lines (p=0.0006, not shown) (Table 10.9). Furthermore, total area was also comparable (p=0.5197), with median ranging 10903 – 12342 for the wildtype *Dync1h1*$^{+/+}$ and 10523 – 15156 for the homozygous *Dync1h1*$^{Loa/Loa}$ fibroblasts (Figure 5.7AB). As before, both number and granule area were well correlated with correlation coefficients above 0.89 (Figure 5.7C). Parameters of the TG induced granules did not differ from SA induced in the wildtype *Dync1h1*$^{+/+}$ cells (p=0.5622 for 'number', p=0.1247 for 'area'), but vary within homozygous MEFs (p=0.0004 for 'number', p=< 0.0001 for 'area').

The performed analysis of stress granules formed in the individual cells suggested differences in the distinct features of granules induced with different agents. While there were no effects observed in the cells carrying mutations in the dynein intermediate chains 1 and 2 (*Dync1i1*^{G482D} *Dync1i2*^{T172I}), the presence of mutation in the dynein heavy chain (*Dync1h1*^{Loa}) caused increase in the number and total area of the stress granules in cells treated with sodium arsenite but not with thapsigargin.

Table 5.4. Analysis of stress granule formation after thapsigargin (TG) treatment
Parameters of cytoplasmic SG presented based on the results of statistical tests, where **n.s**. corresponds to lack of significant differences for p>0.05; trends were noted if p<0.1; for different cell lines (*Dync1i1*^{G482D} *Dync1i2*^{T172I}, *Dync1h1*^{Loa}) values of each parameter were compared between wildtype and homozygous MEFs; detailed analysis is presented in Appendix 10.6.

Parameter	*Dync1i1*^{G482D} *Dync1i2*^{T172I}	*Dync1h1*^{Loa}
Number of G3BP$^{+/ve}$ foci	n.s.	*Dync1h1*$^{Loa/Loa}$ cells tended to form more SG (p=0.0948)
Total area of G3BP$^{+/ve}$ foci	n.s.	n.s.

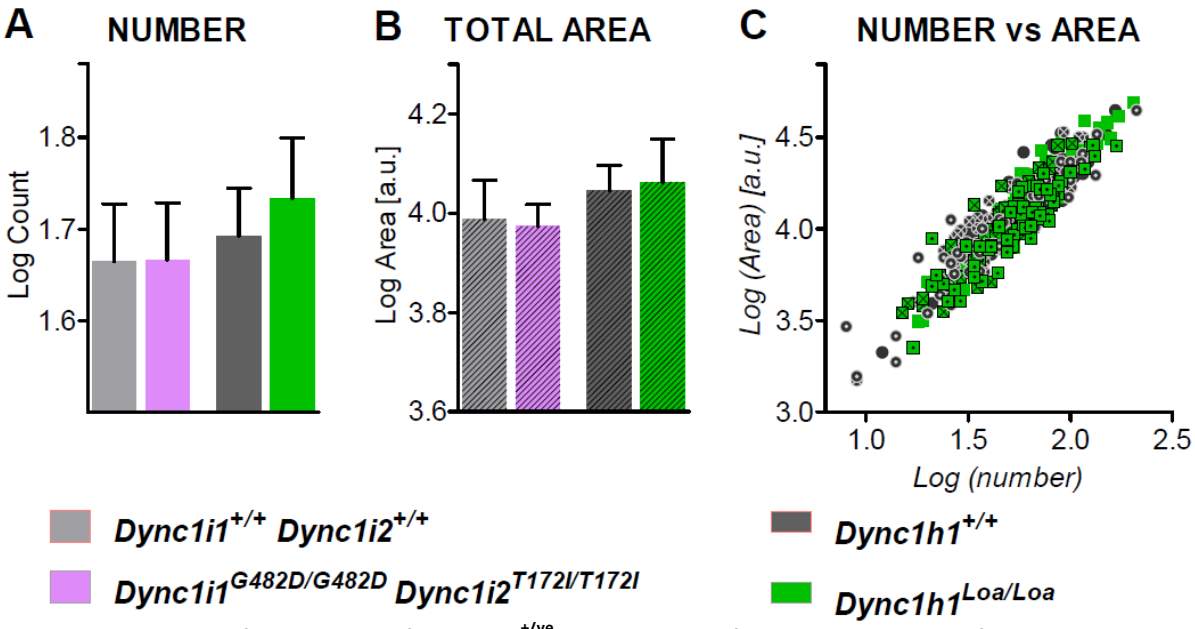

Figure 5.7. Analysis of parameters of the G3BP$^{+/ve}$ granules in the fibroblasts observed after thapsigargin treatment
Data recorded for represented as mean ± standard deviation (SD) of *log* transformed values; legend refers to all graphs and colours correspond to wildtype *Dync1i1*$^{+/+}$*Dync1i2*$^{+/+}$ (grey), double homozygous *Dync1i1*$^{G482D/G482D}$*Dync1i2*$^{T172I/T172I}$ (violet), wildtype *Dync1h1*$^{+/+}$ (dark grey), and homozygous *Dync1h1*$^{Loa/Loa}$ (green) MEFs; a.u. – arbitrary units

A. Mean values of *log* transformed number of stress granules
B. Mean values of *log* transformed total area of stress granules
C. Correlation between number and area of stress granules in the *Dync1h1*^{Loa} cells; *log* transformed values are plotted as dots corresponding to individual cells; shape of 'clouds' typical for positive correlation

5.4 Discussion

Although the mechanisms and regulation of the formation of stress granules have not been described, microtubule associated molecular motors, dynein and kinesin were shown to play an important role in this process (Loschi *et al.*, 2009). Depletion of the dynein heavy chain (DYNC1H1) resulted in decrease in fraction of cells positive for SG markers, while granules assembled tended to be smaller. Similar phenotypes were observed after disruption of MT cytoskeleton. Interestingly, the results presented in this chapter suggest a distinct role of the DYNC1H1 in the response to various stresses.

When homozygous *Dync1h1*$^{Loa/Loa}$ cells were treated with sodium arsenite, the level of cells with SG was comparable with response observed in the wildtype *Dync1h1*$^{+/+}$ cells. However, individual cells carrying mutant *Dync1h1*^{Loa} allele displayed more foci, which summed area was also higher. On the other hand, thapsigargin triggered more pronounced response in the homozygous *Dync1h1*$^{Loa/Loa}$ MEFs, which formed SG comparable in number and area with the structures observed in the wildtype *Dync1h1*$^{+/+}$ cells. While seemingly contradicting, these results suggest specific effects of the *Loa* mutation in the stress response. It can be hypothesised, that treatment with a potent agent, like thapsigargin, resulted in a strong response, which might feature different nucleation dynamics. Furthermore, the components of the SG are known to vary depending on the stress applied (Kedersha and Anderson, 2007), thus treatment with arsenite might promote specific interactions between mutant dynein heavy chain and yet-to-be-described protein. It should also be noted, that mean area of stress granules was found to be constant, which might be one of the mechanisms regulating the processes involved in cellular stress. Because response to stress is cell-specific, it would be beneficial to investigate the formation of SG in other cell types or in live animals.

6. Investigation of the expression pattern of the cytoplasmic dynein intermediate chains in mouse

6.1 Transcriptional regulation

In recent years the vertebrate proteome has been outshone by the transcriptome and its complexity, as only a relatively small portion of the genome is transcribed into protein coding mRNAs. Although many classes of RNAs are described, what happens behind a nuclear envelope still awaits to be discovered. So far, over 10 different species of non-coding RNAs have been described, including short (sRNA), intronic (ncRNA), micro RNA (miRNA) (Carninci, 2010). Majority of the non-coding RNA is essential for gene expression and it participates in transcription initiation, splicing of exons, RNA editing, silencing, and many more processes. Long intronic transcripts were shown to be tissue specific (Louro *et al.*, 2009), and hypothesised to be a scaffold for various proteins thus initiating an assembly of RNP complexes (Hogg and Collins, 2008). Furthermore, distinct RNP complexes were observed during stress, which suggested their function in adaptation to environmental conditions.

Splicing of transcribed pre- mRNA is catalysed by spliceosomes, which so far are the biggest known nuclear complexes (Valadkhan and Jaladat, 2010). A core of every spliceosome consists of highly conserved small nuclear RNAs (snRNA), which were suggested to evolve from class II self splicing introns. Linear pre-mRNA is formed by sequential exons and introns, and their boundaries are recognised by the molecular machinery. A basic splicing mechanism involves 5 snRNAs (U1, U2, U4, U5 and U6) in the protein complexes, which recognise intron splicing sites via base pairing (U1, and U2AF) (Li *et al.*, 2007). This step is thought to initiate an assembly of the spliceosome, recruitment of the U4–U5–U6 tri-snRNP, and intermolecular rearrangement resulting in detaching of the U1 and U4. Final reactions involve ligation of exons and excision of introns and a form of closed lariat. Apart from the core catalytic subunits, there are over 150 different components known to form spliceosome in human cells (Valadkhan and Jaladat, 2010).

6.1.1 Alternative splicing and its evolution

Alternative splicing can be defined as differential selection of splice sites in precursor mRNA, which creates another level of regulation of gene expression. Recent studies showed that over 90% percent of human genes are alternatively spliced (Wang *et al.*, 2008). A few modes of alternative splicing have been distinguished in vertebrates (Keren *et al.*, 2010). Exon skipping is the most common event and it is thought to have the biggest impact on the translated protein. Furthermore, constitutive exons can have alternative splice sites (3' and 5' defined in regards to an intron), or alternative promoters and alternative polyadenylation sites are also observed. The activity of intragenic promoters was also found to be regulated by their methylation in a tissue specific manner (Maunakea *et al.*, 2010).

Vertebrate genes generally consist of short exons and usually much longer introns. The distinct gene architecture influences alternative splicing where exons surrounded by long introns are more likely to be excluded (Roy *et al.*, 2008). Moreover, nucleosomes were suggested to actively participate in splicing. Nucleosomes were found associated with sequences enriched in CG pairs, but not with pseudoexons (Keren *et al.*, 2010). During transcription, an RNA polymerase II (RNAPII) is paused by a nucleosome, which might facilitate interactions between complexes. In addition, histone methylation was shown to be lower within alternative exons (Kolasinska-Zwierz *et al.*, 2009).

Comparative analysis of alternative splicing brings discoveries not only about gene regulation, but also about evolution of whole genomes and their diversification. Many genes were found to have not only conserved sequences, but also their splicing pattern (Xing and Lee, 2006). The most conserved pattern of splicing was found in brain, while the testis and cancerous cells had the most diverged when human and mouse genomes were analysed (Kan *et al.*, 2005). Furthermore, exon-intron boundaries of alternative exons, which contain splice signals, were also highly similar (Sugnet *et al.*, 2004). These findings suggest an evolutionary pressure, which often correlates with protein function. Likewise, genes expressed in brain often coded proteins involved in signalling pathways, and the levels of transcripts were also correlated between species (Kan *et al.*, 2005).

6.1.2 New exons and tissue specific alternative splicing

Apart from exons expressed in a constitutive manner, alternative splicing can diverge and there are many examples of exons or patterns specific to a lineage or a species. Several mechanisms describing emergence or loss of exons have been proposed based on analysis of large datasets (Keren *et al.*, 2010). Distinct protein domains are often coded by distinct exons, which support a hypothesis of intronic recombination. Furthermore, tandem duplications of an exon within the same gene (exon shuffling) were also observed, which was correlated with their mutual exclusion during splicing (Alekseyenko *et al.*, 2007).

Another mechanism, which often results in creation of a new or species specific splicing pattern, assumes exonification of intronic sequence. Alternative exons were found to originate from transposable elements (e.g. *Alu*), RNA editing, or random mutations (Keren *et al.*, 2010). While *Alu* elements are found only in primate genomes (Modrek and Lee, 2003), mutations changing splice sites are a more common phenomenon. The new isoforms are often expressed at low levels or restricted to a tissue or cell type. Furthermore, the cellular mechanisms degrade any aberrant transcript, thus imposing pressure towards maintaining open reading frame (ORF) of the mRNA (Resch *et al.*, 2004).

Tissue specific splicing is a well described phenomenon resulting from interactions between *cis*- and *trans*- acting elements. Sequence motifs within introns or exons *(cis-)* are recognised by RNA binding proteins *(trans-)*, which in turn promote or suppress splicing in the region (Tao and Sampath, 2010). Consequently, alternative splicing is controlled by regulation of the expression of various components involved in the splicing machinery, both spatially or temporally. A prominent example is a glucocortycoid receptor (GR), which can be found as 13 different isoforms (Turner *et al.*, 2010). Recently a new isoform of transducing-like enhancer of split 4 (TLE-4) has been described, which is expressed only in testis thanks to alternative splicing activated by germ cell specific nuclear factors (hnRNP G-T, RBMY) (Liu *et al.*, 2009).

6.2 Bioinformatics tools useful in the analysis of the alternative splicing

The completion of sequencing of many genomes enables insight into not only their functions but also their evolution. The advances in comparative genomics shed light on the evolutionary patterns and events taking places in closely related or distant species (Calarco *et al.*, 2007). An *in silico* analysis of alternative splicing can be based on the comparison of expressed sequence tags (ESTs), which are available in many genome assemblies. When abundant in sequences, the ESTs databases often contain sequencing artefacts or underrepresented regions (Modrek and Lee, 2003). EST databases (e.g. http://genome.uscs.edu) contain single read sequences approximately 500bp long, which correspond to RNAs isolated from a sample, transcribed into cDNA, and cloned into a vector prior to sequencing. In addition, a retrieval of 5' or 3' ends can be increased by 'capturing' relevant regions via chemical modifications (Kimura *et al.*, 2006). In the following paragraph different tools useful in the analysis performed are briefly summarised.

UCSC Genome Browser

The UCSC Genome Browser was developed and is maintained by the Genome Bioinformatics Group within the Centre for Biomolecular Science and Engineering (CBSE) at the University of California Santa Cruz (UCSC) (Kent *et al.*, 2002). It contains the reference sequence and working draft assemblies for a large collection of genomes and provides a portal to the Encyclopaedia of DNA Elements (ENCODE) project. The 2011 update contains assemblies of 53 genomes (19 mammals, 10 vertebrates, 3 deuterostomes, 13 insects, 6 nematotes, 2 'other') with extensive comparative genomics tools (Fujita *et al.*, 2011; Raney *et al.*, 2011).

UCSC Genes

UCSC Genes, is a gene prediction track generated at UCSC; it is based on data from RefSeq, GenBank, CCDS (Consensus Coding DNA Sequences) and UniProt (Fujita *et al.*, 2011). Furthermore, RefSeq and mRNA tracks, which display aligned sequences from all organisms in GenBank, are updated nightly, and EST tracks are updated weekly.

Target Scan

TargetScan 5.1 (Friedman *et al.*, 2009) predicts biological targets of miRNAs by searching for the presence of conserved 8-mer and 7-mer sites that match the seed region of each miRNA (Lewis *et al.*, 2005). In mammals, predictions are ranked based on the predicted efficacy of targeting as calculated using the context scores of the sites (Grimson *et al.*, 2007). Conserved targeting has also been detected within open reading frames (ORFs).

6.3 Project overview

This work aiming to establish the splicing pattern of the cytoplasmic dynein intermediate chains 1 and 2 *(Dync1i1, Dync1i2)* in mouse has been published in Kuta A. et al, (2010) Mouse cytoplasmic dynein intermediate chains: identification of new isoforms, alternative splicing and tissue distribution of transcripts, PLoS.One 5(7): e11682. In addition, expression levels of subunits of the cytoplasmic dynein complex were examined in neural tissues isolated from wildtype *Dync1i2*$^{+/+}$ and homozygous *Dync1i2*$^{T172I/T172I}$ mice. Finally, antibodies specific to the *Dync1i2* were successfully raised and tested using cellular extracts.

6.4 Results

The pattern of alternative splicing was examined on the level of mRNA isolated from different mouse tissues (C57BL6/J strain). Initially, full length cDNA of the intermediate chains 1 and 2 was cloned and inserts sequenced in order to detect possible splice variants. Subsequently, a detailed assay was carried out confirming the presence of distinct isoforms. The nomenclature of isoforms described follows the annotations as in (Kuta *et al.*, 2010). Briefly, 6 transcripts of the *Dync1i1* were found only in neural tissue (annotated in relation to rat isoforms *Dync1i1.A, Dync1i1.B, Dync1i1.D, Dync1i1.E, Dync1i1.C*, *Dync1i1.F*), while isoform *Dync1i1.C* was also present in ovaries and testes. Extracts from brains and spinal cords were also enriched in multiple isoforms of the *Dync1i2* (*Dync1i2.D, Dync1i2.E, Dync1i2.A, Dync1i2.B, Dync1i2.C*) and the only transcript detected in all the somatic tissues examined corresponded to isoform *Dync1i2.C*. In addition, transcript *Dync1i2.F* was found only during analysis of cloned cDNAs.

6.4.1 Investigating the alternative splicing of the mouse *Dync1i1* and *Dync1i2* genes

A PCR-based approach allowed detection of transcripts of the intermediate chains 1 and 2, which were not published before. Furthermore, results of semi-quantitative analysis suggest subtle differences in the abundance of distinct isoforms depending on region examined.

6.4.1.1 Cloning of splice variants and detailed survey of the splicing pattern of Dync1i1 and Dync1i2 genes in mouse tissues

A set of tissues was harvested from adult C57BL6/J mice (male and female): brain, spinal cord, ovary, testis, spleen, lungs, kidney, heart, intestine, muscle, liver (section 2.1.4.1). Total RNA was extracted as described in section 2.2. The RNA was transcribed into cDNA (section 2.3.3) and full length transcripts of the *Dync1i1* and *Dync1i2* (exon 1a, 1b) amplified using primers complementary to known sequences (UCSC, Uc009awn.1, Uc008kah.1, Uc008kak.1 respectively) (section 2.3.4). The resulting products were sequenced, and when multiple sequences for all individual products were obtained cloning was undertaken (section 2.4). Based on results of the cloning analysis, a survey of set of tissues was performed, aiming to detect all isoforms.

As a result of the alternative splicing six isoforms of mouse *Dync1i1* gene were detected arising from combinatorial use of three 3' alternative splice sites (AS) in exon 4 and transcripts with exon 5 included or skipped. All of them were exclusively present in neural tissues and one (*Dync1i1.C*) was also expressed in gonads (Table 6.1). The transcripts *Dync1i1.E* and *Dync1i1.F* are new isoforms described during the study. An exon 5 (60bp) was present in the isoforms *Dync1i1.A*, *Dync1i1.B*, and *Dync1i1.D*, whereas it was skipped in transcripts *Dync1i1.C, Dync1i1.E,* and *Dync1i1.F.* Importantly, none of the splicing events resulted in a change of ORF, and isoforms differed by short polypeptides (in exon 4 AS1 – AS2 spans 17amino acids, AS2 – AS3 spans 11 amino acids, exon 5 spans 20 amino acids) (Figure 6.1). Furthermore, all the splicing events were restricted within exons 4 and 5.

Table 6.1. Isoforms of dynein intermediate chain 1 *(Dync1i1)*

The isoforms were annotated with correspondence to previously used notation in rat; number of exons, amino acids shown, exon 4 refers to a splice site in the exon 4 used; isoforms detected in neural tissue only shaded, * new transcript described

Isoform	UCSC and/or *ENSEMBL* accession number for 'reference sequence' for each isoform	Exons	Exon 4	Number of amino acids
Dync1i1.A	*ENSMUST00000115555*	1 to 17	AS1	645
Dync1i1.B	uc009awn.1/*ENSMUST00000115559*	1 to 17	AS2	628
Dync1i1.D	*ENSMUST00000115556*	1 to 17	AS3	617
Dync1i1.E	**GU992206***	**1 to 4, 6 to 17**	**AS1**	**625**
Dync1i1.C	*ENSMUST00000115554*	1 to 4, 6 to 17	AS2	608
Dync1i1.F	**GU992207***	**1 to 4, 6 to 17**	**AS3**	**597**

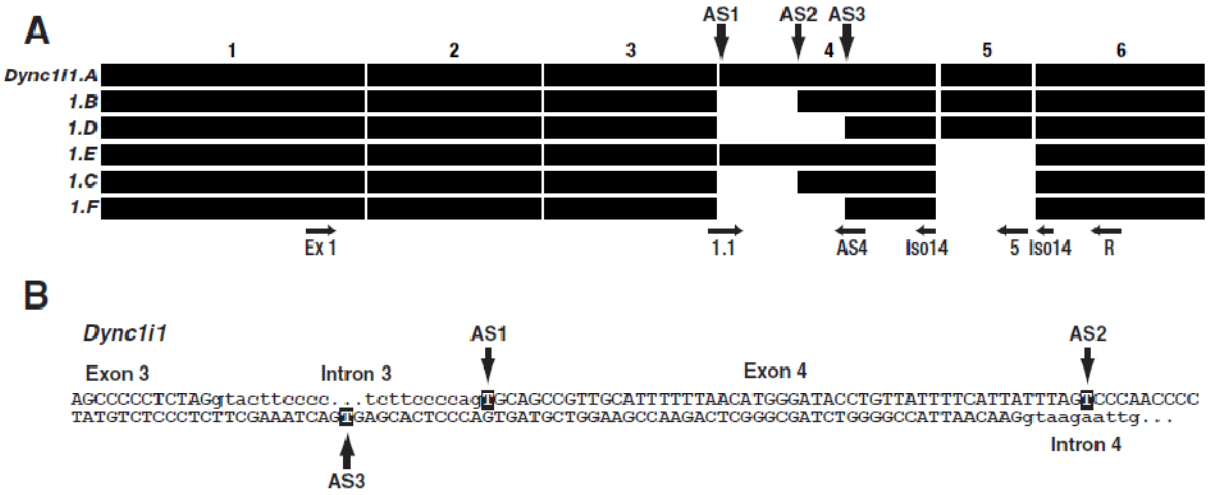

Figure 6.1. Splicing pattern of mouse dynein intermediate chain 1 gene

A. Summary of alternative splicing in *Dync1i1*, showing splice variants *Dync1i1.A* to *Dync1i1.F,* and the first 6 exons (numbered 1, 2, 3, 4, 5, 6); primer binding sites used for isoform specific RT-PCRs are as indicated (Appendix 10.12.4); AS1, 2 and 3 refer to the alternative splice sites in exon 4; exons are drawn to scale

B. Alternative splice sites in *Dync1i1* exon 4; the nucleotide in bold is the first base pair of the exon; bases in lower case are intronic, bases in upper case are exonic

Adapted from Kuta A. et al, (2010) Mouse cytoplasmic dynein intermediate chains: identification of new isoforms, alternative splicing and tissue distribution of transcripts, PLoS.One 5(7): e11682

In contrast to *Dync1i1,* the *Dync1i2* gene possessed an additional first exon, thus two sets of transcripts containing different first exons were expressed suggesting the presence of 2 active promoters. These non-coding exons, annotated 1a, 1b, did not overlap and were mutually exclusive. Because start codon 'AUG' was located in the second exon, the use of the first exon did not affect the protein sequence. The analysis was performed for both exons, and 11 transcripts coding 6 different proteins were detected (Table 6.2). As in the case of *Dync1i1*, all the transcripts were present only in neural tissues, while *Dync1i2.C (exon 1a/1b)* was the only variant ubiquitously expressed in all the tissues examined. Out of those, sequences of 3 new isoforms were obtained. The isoforms annotated as *Dync1i2.D* and *Dync1i2.E* contained a new exon located within intron 3 of mouse (Figure 6.2). This additional exon was annotated as 3b and was 51bp long or 36 bp long when additional AS was used. Additional isoform *Dync1i2.F* was represented only by one clone and could not be detected during the PCR based survey. Although its expression seemed unclear, it could be translated into a complete polypeptide showing the splicing pattern similar to *Dync1i1.F.* Furthermore, exons 4 and 6 were alternatively spliced 'cassette exons', both present in variants *Dync1i2.D (exon 1a/1b), Dync1i2.E (exon 1a/1b),* and *Dync1i2.A (exon 1a/1b).* While transcripts *Dync1i2.B (exon 1a/1b)* lacked exons 3b and 4, isoform *Dync1i2.F (exon 1a)* was found to have exons 3b and 6 omitted. The shortest variant was coded by *Dync1i2.C (exon 1a/1b),* and it contained only constitutive exons. The alternative exons observed in the *Dync1i2* transcripts did not change the open reading frame, and coded short peptides (exon 3b spans 17 amino acids, exon 4 spans 6 amino acids, exon 6 spans 20 amino acids).

Table 6.2. Isoforms of dynein intermediate chain 2 *(Dync1i2)*

The isoforms were annotated with correspondence to previously used notation in rat;, number of exons, amino acids shown, exon 3b refers to a splice site in the exon 3b used; isoforms detected in neural tissue only shaded; * new transcript described

Isoform	UCSC and/or *ENSEMBL* accession number for 'reference sequence' for each isoform	Exons	Exon 3b	Number of amino acids
Dync1i2.D	**GU992208***	**1a to 18**	**AS1**	**655**
Dync1i2.E	**GU992209***	**1a to 18**	**AS2**	**650**
Dync1i2.A	ENSMUST00000112140	1a to3, 4 to 18		638
Dync1i2.B	uc008kah.1/ ENSMUST00000112142	1a to 3, 5 to 18		632
Dync1i2.F	**GU992210***	**1a to 3, 4 to 5, 7 to 18**		**618**
Dync1i2.C	uc008kai.1/ ENSMUST00000112138	1a to 3, 5, 7 to 18		612
Dync1i2.D	**GU992211***	**1b to 18**	**AS1**	**655**
Dync1i2.E	**GU992212***	**1b to 18**	**AS2**	**650**
Dync1i2.A	ENSMUST00000112144	1b to3, 4 to 18		638
Dync1i2.B	ENSMUST00000100028	1b to 3, 5 to 18		632
Dync1i2.C	uc008kak.1/ ENSMUST00000081710	1b to 3, 5, 7 to 18		612

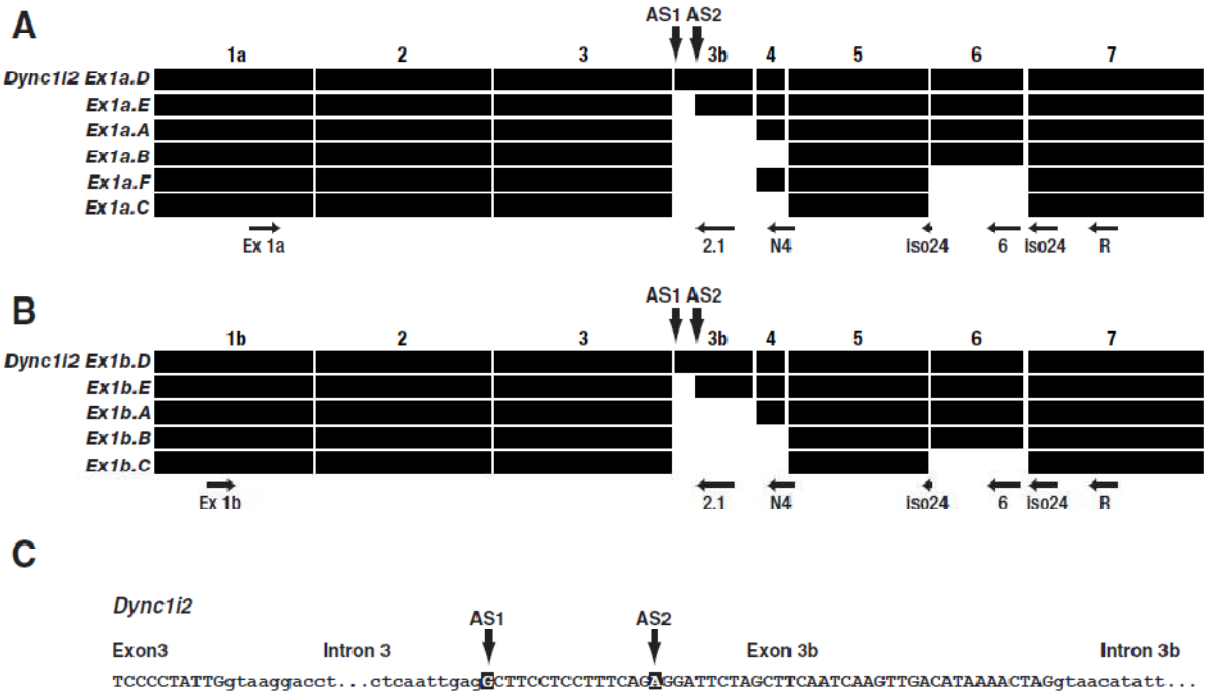

Figure 6.2. Splicing pattern of mouse dynein intermediate chain 2 gene *(Dync1i2)*

A. Summary of alternative splicing in *Dync1i2* with exon 1a; the first seven exons (numbered 1a, 2, 3, 3b, 4, 5, 6, 7), primer binding sites used for isoform specific RT-PCRs are indicated (Appendix 10.12.4); exons are drawn to scale

B. Summary of alternative splicing in *Dync1i2* with exon 1b, variant *Dync1i2.F* was not detected

C. Alternative splice sites in *Dync1i2* exon 3b, the nucleotide in bold is the first base pair of the exon, bases in lower case are intronic, bases in upper case are exonic

Adapted from Kuta A. et al., (2010) 'Mouse cytoplasmic dynein intermediate chains: identification of new isoforms, alternative splicing and tissue distribution of transcripts', PLoS.One 5(7): e11682

6.4.1.2 Capillary electrophoresis of FAM-conjugated PCR products of Dync1i1 and Dync1i2 genes

The use of a fluorescence-based method, which has the advantage of being semi-quantitative and could be multiplexed in one reaction, allowed us to estimate the levels of expression of different isoforms of mouse intermediate chains 1 and 2 (Charbonnier *et al.*, 2000). Capillary gel electrophoresis with laser induced fluorescence (CGE-LIF) provided high efficiency separation of nucleic acids up to a single base resolution by combining polyacrylamide in capillaries as medium and fluorescence based detection for better resolution. The results were produced in a form of chromatogram thus options for analysis and quantitation similar to those in high pressure liquid chromatography (HPLC) could be applied (Altria, 1996). Quantitation of the amount of nucleic acids can be achieved by relative or absolute estimates via applying external or internal standardisation. When an internal standard of a known concentration is analysed together with a sample an absolute concentration of PCR product can be determined by comparing the peak heights of a sample and standard on a CGE chromatogram (Lu *et al.*, 1994). In addition, a ratio of a target DNA peak area to the peak area of added DNA internal standard gives an estimate of the relative amount of DNA in the sample (Richards M.P., 2005). When quantitative internal standards are not available, the standard can derive from amplification of genes that remain at constant levels in the sample (Richards M.P., 2005) or by integrating the area of all peaks of interests and adding them to give a total normalised area of electropherogram and calculating a ratio (Altria, 1996). Furthermore, when low copy number products are quantified a competitive PCR gives the most accurate means for quantification.

Splice isoforms of mouse *Dync1i* genes were analysed using CGE – LIF; in this case reverse primers (DIC1_R rev, DIC2_R rev, section 10.12.4) were conjugated with 5-carboxyfluorescein (5-FAM) and reactions run as described with cDNAs isolated from 4 C57BL6/J mice (section 2.3.4). Chromatograms recorded contained sets of peaks separated by their sizes with the accuracy to one bp. By comparison of expected sizes of amplified isoforms with peak positions on a chromatogram, five isoforms of each gene were annotated. Relative amounts were calculated as fraction of peak area to the total

area of peaks identified and individual isoforms compared between samples. Detailed analysis can be found in Appendix 10.7 and Table 10.10, while the summary is presented in Table 6.3.

There were 5 isoforms of the *Dync1i1* annotated except for *Dync1i1.E*, likely due to very low abundance. Likewise, there were samples, in which the contribution of transcripts annotated as *Dync1i1.A* and *Dync1i1.F* to the total peak area was below 2%. In these cases the low abundant transcripts were not included in the statistical analysis. Samples from adult brain and spinal cord varied in fractions of isoforms *Dync1i1.A* (p=0.0314), *Dync1i1.D* (p=0.0068), and *Dync1i1.C* (p=0.0337) (Table 6.3, Figure 6.3A). On the other hand, in the samples from embryonic brain and spinal cord (collected at E17.5) there were differences in the amounts of 4 isoforms (*Dync1i1.B, Dync1i1.D, Dync1i1.C,* and *Dync1i1.E)* while *Dync1i1.A* was not detected (Figure 6.3B). Furthermore, samples isolated from various regions of an adult brain also displayed region specificity in the relative abundance of signal corresponding to distinct *Dync1i1* transcripts (Figure 6.3C). When compared to results obtained for hippocampus, differences were observed in olfactory bulbs (transcripts *Dync1i1.B, Dync1i1.D, Dync1i1.C, Dync1i1.F),* cerebellum (transcripts *Dync1i1.C, Dync1i1.F),* and brain stem (transcripts *Dync1i1.D, Dync1i1.C, Dync1i1.F).*

Chromatograms of PCR products with primers specific for the *Dync1i2* showed in most cases peaks corresponding to 3 major isoforms annotated as *Dync1i2.A, Dync1i2.B,* and *Dync1i2.C.* If additional fluorescent signals matching the products of isoforms *Dync1i2.E* and *Dync1i2.F* were detected, their levels were below 1% and not included in further comparisons. Similar distribution was also observed in the PCR based analysis. In majority of samples the relative amounts were comparable when the use of the first exon (*exon 1a* or *1b*) was examined (Table 6.3). In the adult brain and spinal cord, different levels of *Dync1i2.A (exon 1a/1b)* and *Dync1i2.C (exon 1a/1b)* were observed (Figure 6.3D,G), and a similar pattern was found in the embryonic tissues (Figure 6.3E,H). Moreover, the brain regions varied when transcripts *Dync1i2.A (exon 1a/1b)*, *Dync1i2.B (exon 1a/1b)*, and *Dync1i2.C (exon 1b)* were compared. Relative to the hippocampus, different levels of isoforms were found in all the other regions: cortical (*Dync1i2.B exon 1a*), olfactory

(*Dync1i2.A exon 1a/1b, Dync1i2.B exon 1a/1b*), cerebellar (*Dync1i2.A exon 1b, Dync1i2.C exon 1b*), and in the brain stem (*Dync1i2.A exon 1a/1b, Dync1i2.B exon 1a/1b, Dync1i2.C exon 1b*) (Figure 6.3I).

Table 6.3. Summary of relative abundance of individual isoforms of *Dync1i1* and *Dync1i2* (exon 1a, exon 1b) in mouse neural tissues

Relative abundance of splice isoforms of the cytoplasmic dynein chains 1 and 2 presented as a 'heat map' when values were classified and color coded (blue for low and red for high levels); isoforms *Dync1i1.E*, and *Dync1i2.D* were not observed due to low sensitivity of the assay; marked transcripts detected at levels below 2%; n.d. – not detected; detailed analysis is presented in Appendix 10.7

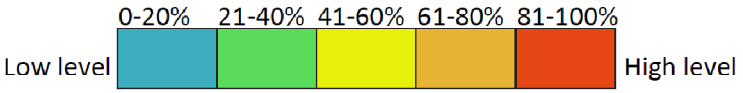

Tissue/ Isoform	*Dync1i1*					*Dync1i2 exon 1a*					*Dync1i2 exon 1b*				
	1.A	***1.B***	***1.D***	***1.C***	***1.F***	***2.E***	***2.A***	***2.B***	***2.F***	***2.C***	***2.E***	***2.A***	***2.B***	***2.F***	***2.C***
Brain	<2%					n.d.			n.d.		n.d.			<2%	
Spinal cord						n.d.			n.d.		n.d.			n.d.	
Embryonic brain	n.d.					<2%			n.d.		<2%			n.d.	
Embryonic sp. cord	n.d.				<2%	<2%			n.d.		n.d.			n.d.	
Cortex	<2%					<2%			<2%		n.d.			n.d.	
Hippocampus	<2%					n.d.			<2%		n.d.			<2%	
Olfactory bulbs	<2%					<2%			n.d.		<2%			n.d.	
Cerebellum					<2%	<2%			n.d.		n.d.			n.d.	
Brain stem					<2%	n.d.			<2%		n.d.			<2%	

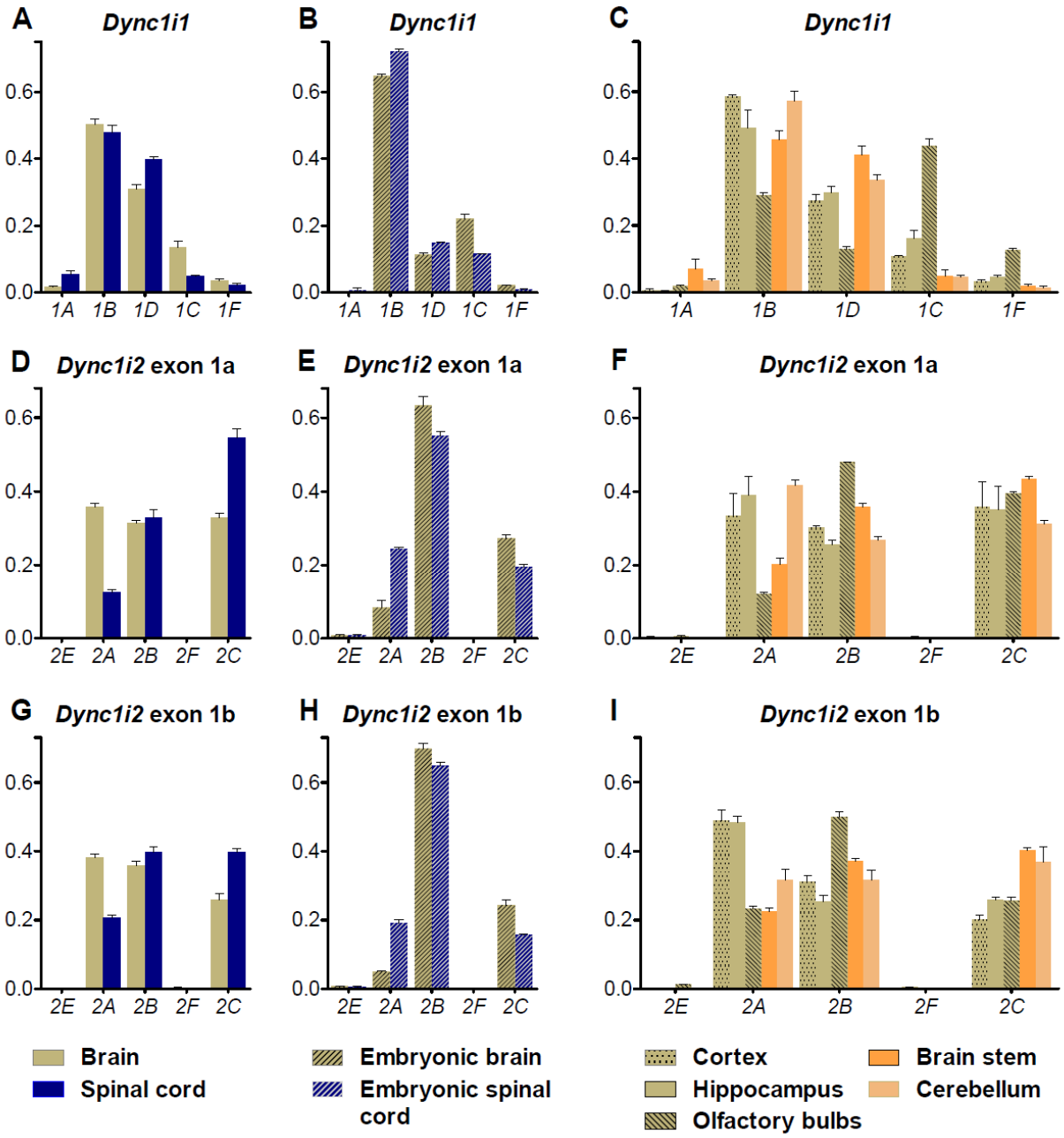

Figure 6.3. Distribution of isoforms of *Dync1i1* and *Dync1i2* (exon 1a, exon 1b) in mouse neural tissues
Relative amounts of distinct isoforms shown as fractions of total signal and plotted as mean ± standard error (SEM); results obtained for transcripts of each gene were grouped and compared between adult brain and adult spinal cord (A,D,G), embryonic brain and embryonic spinal cord (B,E,H), and different regions of adult brain (C,F,I); isoforms *Dync1i1.E* and *Dync1i2.D* were not detected in this assay

A, B, C. Comparison of relative abundance of the *Dync1i1* isoforms

D, E, F. Comparison of relative abundance of the *Dync1i2* isoforms containing exon 1a

G, H, I. Comparison of relative abundance of the *Dync1i2* isoforms containing exon 1b

6.4.2 The expression of subunits of the cytoplasmic dynein complex in neural tissues isolated from wildtype (*Dync1i2*$^{+/+}$) and homozygous (*Dync1i2*$^{T172I/T172I}$) mice

Analysis of expression levels of different subunits was performed by Dr G. Banks. Briefly, total RNA was extracted from 12 week old wildtype *Dync1i2*$^{+/+}$ (n=3) and homozygous *Dync1i2*$^{T172I/T172I}$ (n=3) mice and cDNA synthesised (section 2.3.3). Levels of transcripts were examined using real-time PCR and relative quantification performed by calculating the ratio between the amounts of a target gene (dynein subunits) and a control gene (β-actin). Calculations were based on the values of threshold cycle (C_T), which was number of cycle, when a fluorescence increased above a set threshold. Firstly, C_T values of β-actin were subtracted from values recorded for a dynein gene (ΔC_T). The ΔC_T values recorded for wildtype *Dync1i2*$^{+/+}$ mice (n=3) were averaged and used as 'calibrating' value when calculating $\Delta\Delta C_T$ ($\Delta\Delta C_T = \Delta C_T$ 'calibrating' - ΔC_T sample). Finally, normalised expression levels of dynein subunits were calculated as $2^{-\Delta\Delta CT}$. Detailed description of the quantitative real-time PCR can be found in Qiagen handbook (Critical Factors for Successful Real-Time PCR). Each sample was run in triplicate and values averaged before analysis.

Pairs of primers were designed to detect different subunits and isoforms of components of the cytoplasmic dynein complex: dynein intermediate chain 1 (*Dync1i1,* 6 isoforms), dynein intermediate chain 2 (*Dync1i2*, 6 isoforms), dynein light intermediate chain 1 (*Dync1li1*), dynein light chains Tctex-1 (*Dynlt1*), RP3 (*Dynlt3*), light chains LC8 (*Dynll1, Dynll2*). Relative levels of expression of each gene were examined in samples isolated from adult brain cortex, hippocampus, and adult spinal cord. Unfortunately, we did not obtain results for rare isoforms of the intermediate chains 1 and 2 (*Dync1i1.E, Dync1i1.F, Dync1i2.D, Dync1i2.E, Dync1i2.F*), likely due to lack of sensitivity of the assay undertaken. All the results are presented as mean ± standard error (SEM) and values of normalised expression ($2^{-\Delta\Delta CT}$) were analysed using *t*-test. Detailed analysis can be found in Appendix 10.7 and Table 10.11, results are summarised in Table 6.4.

On overall, there were no major differences in the levels of RNA between wildtype *Dync1i2*$^{+/+}$ (n=3) and homozygous *Dync1i2*$^{T172I/T172I}$ (n=3) mice, although mutant mice displayed fluctuations within the same amplicon but between different tissue. Furthermore, although all mice were from one litter, high variation between samples isolated from individual animals was observed. There were 4 isoforms of the *Dync1i1* analysed (*Dync1i1.A, Dync1i1.B, Dync1i1.D,* and *Dync1i1.C*), and the levels of their expression were comparable in all tissue samples examined. Likewise, *Dync1i2* was represented by 3 isoforms (*Dync1i2.A, Dync1i2.B, Dync1i2.C*), which did not vary between wildtype *Dync1i2*$^{+/+}$ and homozygous *Dync1i2*$^{T172I/T172I}$ mice (Table 6.4, Figure 6.4). However, the expression of *Dync1i2.A* in adult spinal cord tended to be elevated by 40% in the homozygous *Dync1i2*$^{T172I/T172I}$ animals (p=0.0852). Furthermore, relative levels of light chain *Rp3 (Dynlt3)* but not *Tctex 1 (Dynlt1*) in the spinal cord were higher in homozygous *Dync1i2*$^{T172I/T172I}$ mice (1.392±0.079) than in the wildtype *Dync1i2*$^{+/+}$ animals (1.009±0.090) (p=0.0329). Interestingly, mutation in the intermediate chain 2 affected the expression of another gene coding for dynein light chain *LC8-2 (Dynll2)* but not *LC8-1 (Dynll1).* Homozygous *Dync1i2*$^{T172I/T172I}$ animals showed decrease in the levels of *Dynll2* in samples isolated from hippocampus (0.801±0.060; p=0.0491), while values tended to be higher in the spinal cord (1.828±0.168; p=0.0823). Normalised expression recorded in samples from wildtype *Dync1i2*$^{+/+}$ littermates was 1.002±0.040 and 1.072±0.282 respectively (Table 10.11).

In conclusion, subtle differences between wildtype *Dync1i2*$^{+/+}$ and homozygous *Dync1i2*$^{T172I/T172I}$ mice were observed in the expression levels of 2 genes encoding dynein light chains (*Dynlt3, Dynll2*). Interestingly, only specific regions of the nervous system were affected, including hippocampus and spinal cord. The mutation *Dync1i2*^{T172I} was mapped to a light chain binding domain (DYNLL) (Nyarko and Barbar, 2011). Although effects of mutation on the conformation of the intermediate chain are not known, we can hypothesise that it might affect interactions between subunits in the complex. If that was the case, this observation would suggest an existence of regulatory mechanism reacting to structural features of the complex.

Table 6.4. Summary of quantitative analysis of expression levels of dynein subunits in wildtype *Dync1i2*$^{+/+}$ and homozygous *Dync1i2*$^{T172I/T172I}$ mice (next page)

Expression levels of different subunits of the cytoplasmic dynein complex presented based on the results of statistical tests, where **n.s**. corresponds to lack of significant differences for p>0.05; trends were noted if p<0.1; for samples isolated from different brain parts the expression levels of genes examined were compared between wildtype *Dync1i2*$^{+/+}$ and homozygous *Dync1i2*$^{T172I/T172I}$ animals; isoforms of intermediate chains: *Dync1i1.E*, *Dync1i1.F, Dync1i2.D, Dync1i2.E,* and *Dync1i2.F* were not observed due to low sensitivity of the assay; genotypes correspond to wildtype *Dync1i2*$^{+/+}$ and homozygous *Dync1i2*$^{T172I/T172I}$ animals; *Dync1li1* – dynein light intermediate chain1, *Dynlt1, Dynlt3* – dynein light chains Tc-tex1, RP3, *Dynll1, Dynll2* – dynein light chains LC8-1 and 2; detailed analysis is presented in Appendix 10.27

Gene	Cortex	Hippocampus	Spinal cord
Dync1i1.A	n.s.	n.s.	n.s.
Dync1i1.B	n.s.	n.s.	n.s.
Dync1i1.D	n.s.	n.s.	n.s.
Dync1i1.C	n.s.	n.s.	n.s.
Dync1i2.A	n.s.	n.s.	*Dync1i2*$^{T172I/T172I}$ tended to show higher level
Dync1i2.B	n.s.	n.s.	n.s.
Dync1i2.C	n.s.	n.s.	n.s.
Dync1li1	n.s.	n.s.	n.s.
Dynlt1	n.s.	n.s.	n.s.
Dynlt3	n.s.	n.s.	*Dync1i2*$^{T172I/T172I}$ showed higher level (p=0.0329)
Dynll1	n.s.	n.s.	n.s.
Dynll2	n.s.	*Dync1i2*$^{T172I/T172I}$ showed lower level (p=0.0491)	*Dync1i2*$^{T172I/T172I}$ tended to show higher level

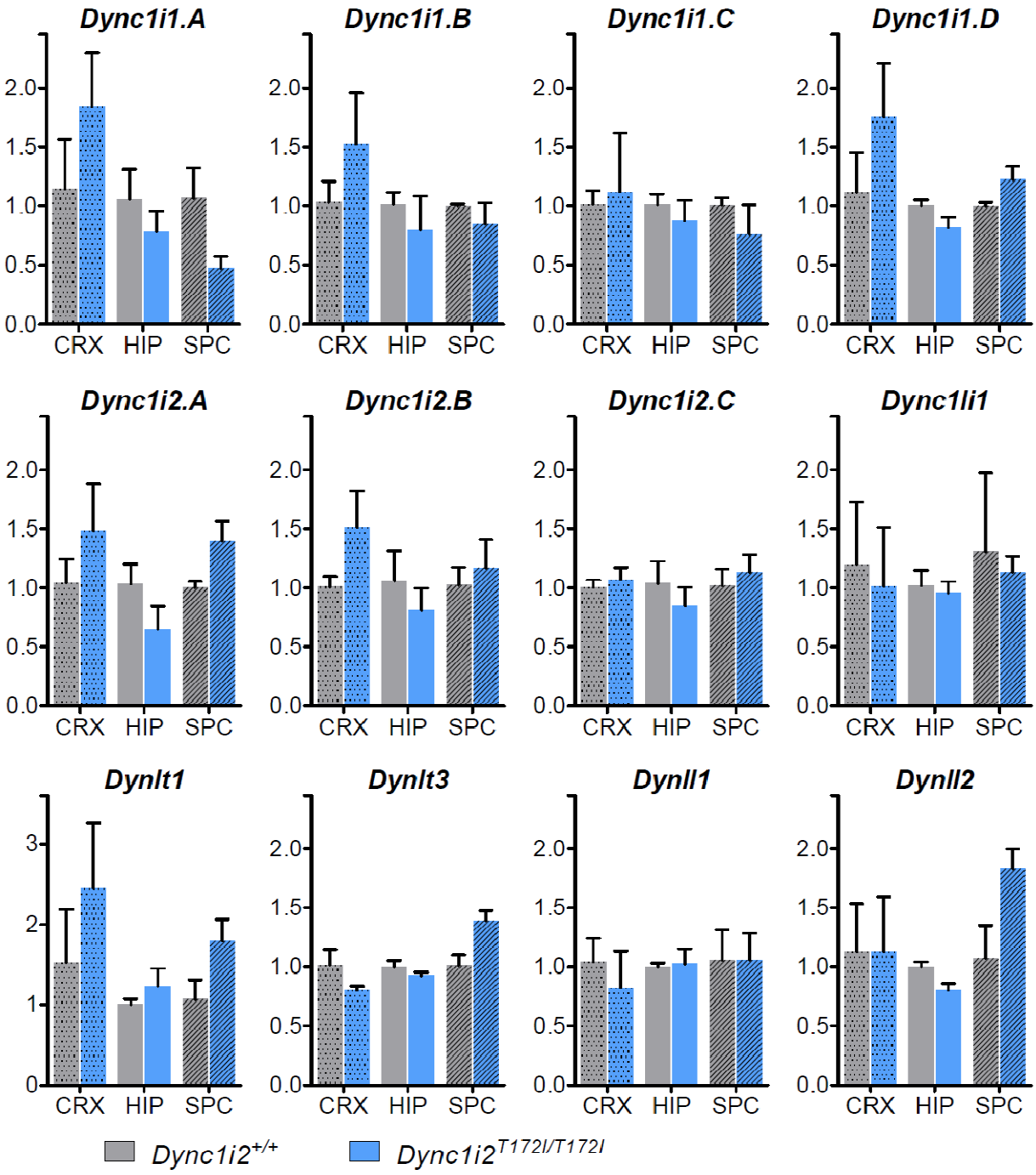

Figure 6.4.Quantitative analysis of expression levels of dynein subunits in wildtype *Dync1i2*$^{+/+}$ and homozygous *Dync1i2*$^{T172I/T172I}$ mice

Results of normalised expression levels ($2^{-\Delta\Delta CT}$) shown as mean ± standard error (SEM); real-time PCRs were run using primers designed to detect 1 population of cDNAs (Appendix 10.12.5) and subunits detected shown; isoforms of intermediate chains: *Dync1i1.E*, *Dync1i1.F, Dync1i2.D, Dync1i2.E,* and *Dync1i2.F* were not observed due to low sensitivity of the assay; genotypes correspond to wildtype *Dync1i2*$^{+/+}$ and homozygous *Dync1i2*$^{T172I/T172I}$ animals; *Dync1li1* – dynein light intermediate chain1, *Dynlt1* – dynein light chain Tc-tex1, *Dynlt3* – dynein light chain RP3, *Dynll1* – dynein light chain LC8-1*, Dynll2* – dynein light chain LC8-2; samples used were from adult brain cortex (CRX), hippocampus (HIP), and spinal cord (SPC)

6.4.3 Antibodies specific to mouse DYNC1I2 protein

Protein sequences of the dynein intermediate chains 1 and 2 (DYNC1I1, DYNC1I2) share 73% of identity and 85% similarity (DYNC1I1.A vs. DYNC1I2.D calculated with BLOSUM62 matrix, BioEdit) and antibodies available commercially react to both peptides. Recently, we successfully raised antibodies recognising DYNC1I1 (Banks *et al.*, 2011) and here we report antibodies binding specifically to the DYNC1I2.

6.4.3.1 Epitope design

Rabbit polyclonal anti-dynein intermediate chain 2 antibodies were generated by BioGenes GmbH (Berlin, Germany). Two peptide immunogens were selected, coupled to *Limulus polyphemus* hemocyanin (LPH, horseshoe crab hemocyanin), and injected into 2 rabbits each. Antisera were purified and affinity purified antibodies tested.

Epitope sequences were chosen to be the most divergent from the DYNC1I1: (1) GLTTDSPIEDSSFN corresponding to 68 – 81 amino acids, and (2) EEEKTLKKDEENDS corresponding to 182 – 195 amino acids of isoform DYNC1I2.E (D6Q0F6, UniProtKB) (Figure 6.5). Because antiserum isolated from rabbit immunised with peptide 2 (4257) failed initial test, 3 remaining affinity purified antibodies from 2 batches were tested using western blotting. Protein lysates from whole brain (section 2.5.1) and HEK293T cells expressing GFP-tagged isoforms of intermediate chains 1 and 2 (sections 2.5.2 and 2.6.7) were run on gels and probed with raised antibodies, and monoclonal IC74 (Millipore). There were 3 isoforms of the intermediate chain 1 (DYNC1I1.B, DYNC1I1.D, DYNC1I1.C) and 2 isoforms of the intermediate chain2 (DYNC1I2.B, DYNC1I2.C) expressed in the HEK293T cells.

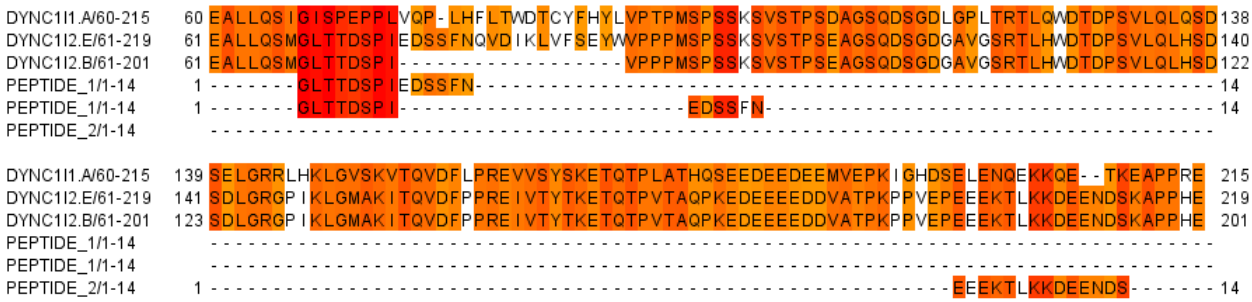

Figure 6.5. Alignment of sequences of peptides used with mouse DYNC1I1.A and DYNC1I2.B
Sequences shaded based on their similarity (JalView 2.6, BLOSUM62 matrix); although short sequences were designed based on sequence of DYNC1I2.E, they were tested against cell lysates transfected with isoforms *Dync1i2.B* and *Dync1i2.C*

6.4.3.2 Antibody testing using western blotting

Antibodies were affinity purified from antisera isolated from 3 rabbits annotated as 4258 (immunised with peptide 2), 4259 and 4260 (immunised with peptide 1). Membranes were incubated simultaneously with antibodies against DYNC1I2, IC74, β-actin. All the antibodies (4258, 4259, 4260) detected GFP-DYNC1I2 chimaeric protein only but not GFP-DYNC1I1 (Figure 6.6, Figure 6.7, Figure 6.8). However, a signal was weak when protein lysate from mouse brain was probed with antisera 4259 and 4260. Furthermore, antibody 4258 detected human DYNC1I2 in the protein lysates extracted from HEK293T cells.

In summary, we were successful in raising antibodies reacting with DYNC1I2 only, however further optimisation of blotting conditions would be required.

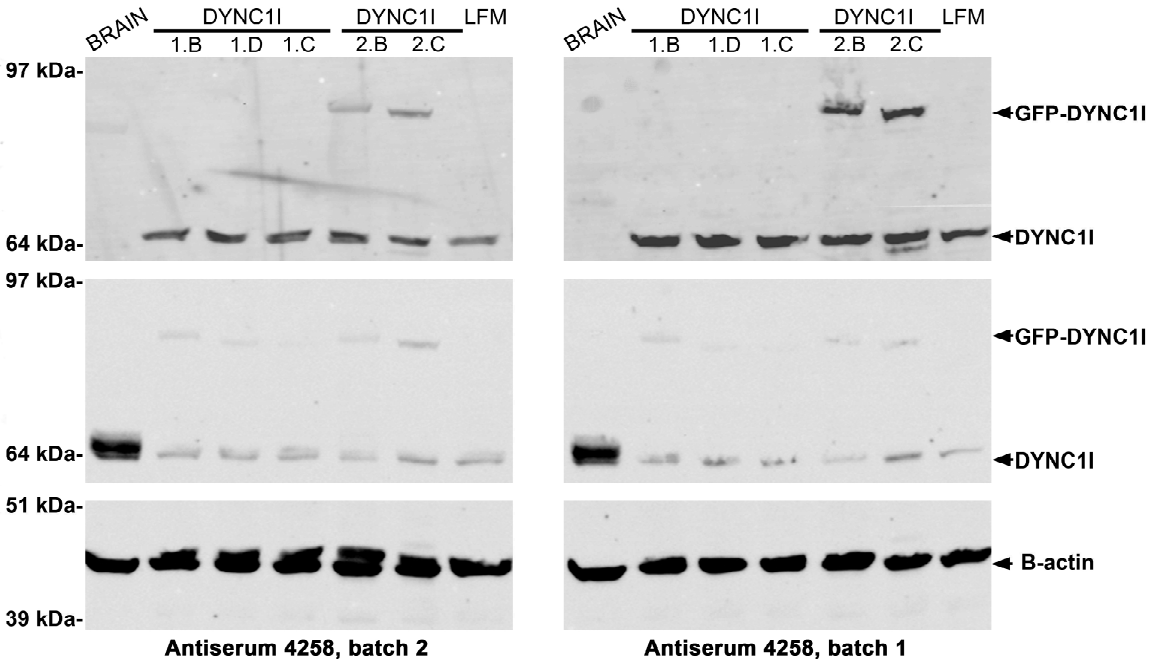

Figure 6.6. Western blots probed with antibodies raised against DYNC1I2 (peptide 2, rabbit 4258)
Lanes correspond to protein lysates from: whole mouse brain, HEK293T cells transfected with GFP-tagged DYNC1I1.B, DYNC1I1.D, DYNC1I1.C, DYNC1I2.B, DYNC1I2.C, and lipofectamine only (LFM); membranes were incubated with antibodies reactive to DYNC1I2 (upper panel), IC74 (middle panel), β-actin (lower panel); bands correspond to DYNC1I2 – GFP chimearic (100 kDa), unmodified DYNC1I (74 kDa), and β-actin (44 kDa); antisera 4258 reacted with DYNC1I2 – GFP and human DYNC1I from cell lysed but did not detect mouse DYNC1I from brain lysate; IC74 gave strong signal only in the brain lysate

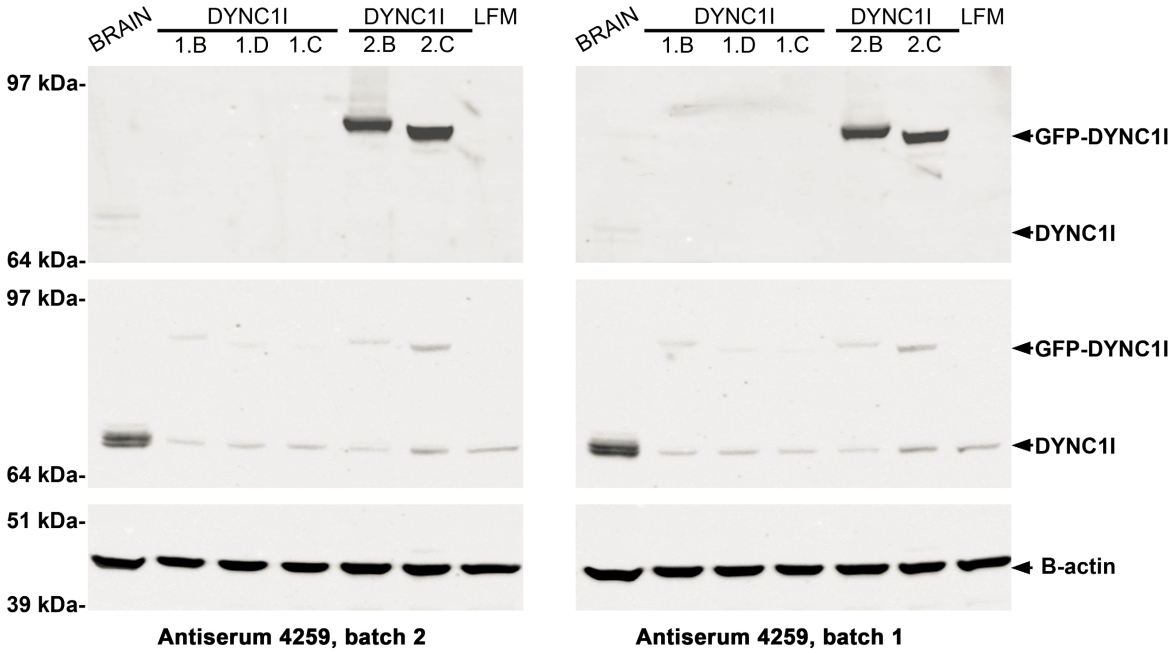

Figure 6.7. Western blots probed with antibodies raised against DYNC1I2 (peptide 1, rabbit 4259)
Lanes correspond to protein lysates from: whole mouse brain, HEK293T cells transfected with GFP-tagged DYNC1I1.B, DYNC1I1.D, DYNC1I1.C, DYNC1I2.B, DYNC1I2.C, and lipofectamine only (LFM); membranes were incubated with antibodies reactive to DYNC1I2 (upper panel), IC74 (middle panel), β-actin (lower panel); bands correspond to DYNC1I2 – GFP chimearic (100 kDa), unmodified DYNC1I (74 kDa), and β-actin (44 kDa); antisera 4259 reacted with DYNC1I2 – GFP and weakly with mouse DYNC1I from brain lysate; IC74 gave strong signal in the brain lysate

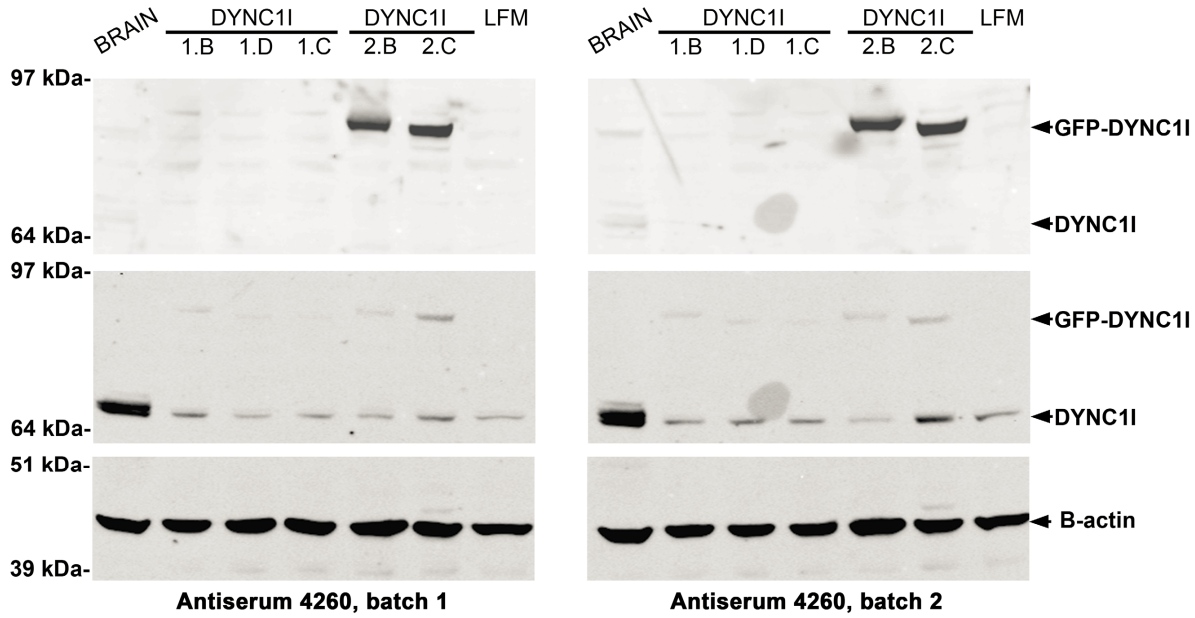

Figure 6.8. Western blots probed with antibodies raised against DYNC1I2 (peptide 1, rabbit 4260)
Lanes correspond to protein lysates from: whole mouse brain, HEK293T cells transfected with GFP-tagged DYNC1I1.B, DYNC1I1.D, DYNC1I1.C, DYNC1I2.B, DYNC1I2.C, and lipofectamine only (LFM); membranes were incubated with antibodies reactive to DYNC1I2 (upper panel), IC74 (middle panel), β-actin (lower panel); bands correspond to DYNC1I2 – GFP chimearic (100 kDa), unmodified DYNC1I (74 kDa), and β-actin (44 kDa); antisera 4260 reacted with DYNC1I2 – GFP and weakly with mouse DYNC1I from brain lysate; IC74 gave strong signal in the brain lysate

6.5 Discussion

The examination of different splice variants of cytoplasmic dynein intermediate chain 1 and 2 *(Dync1i1 and Dync1i2)* resulted in establishing of alternative splicing pattern in mouse tissues. In addition, new isoforms were detected, thus increasing the complexity of the dynein complex. Alternative splicing was observed within corresponding regions of both genes, which suggests conservation of the pattern. During processing of the *Dync1i1* transcript three 3' alternative splice sites in exon 4 can be used, and exon 5 serves as cassette exon, thus 6 different isoforms are produced. In the case of *Dync1i2* three cassette exons were detected, annotated as 3b, 4, and 6, and 5 variants were confirmed. Although coding sequences of both genes are highly similar (83%), the region of alternative splicing is the most variable. On the protein level, isoforms differ in the N-termini, which are thought to be site of interactions with adaptor complexes (Figure 6.9).

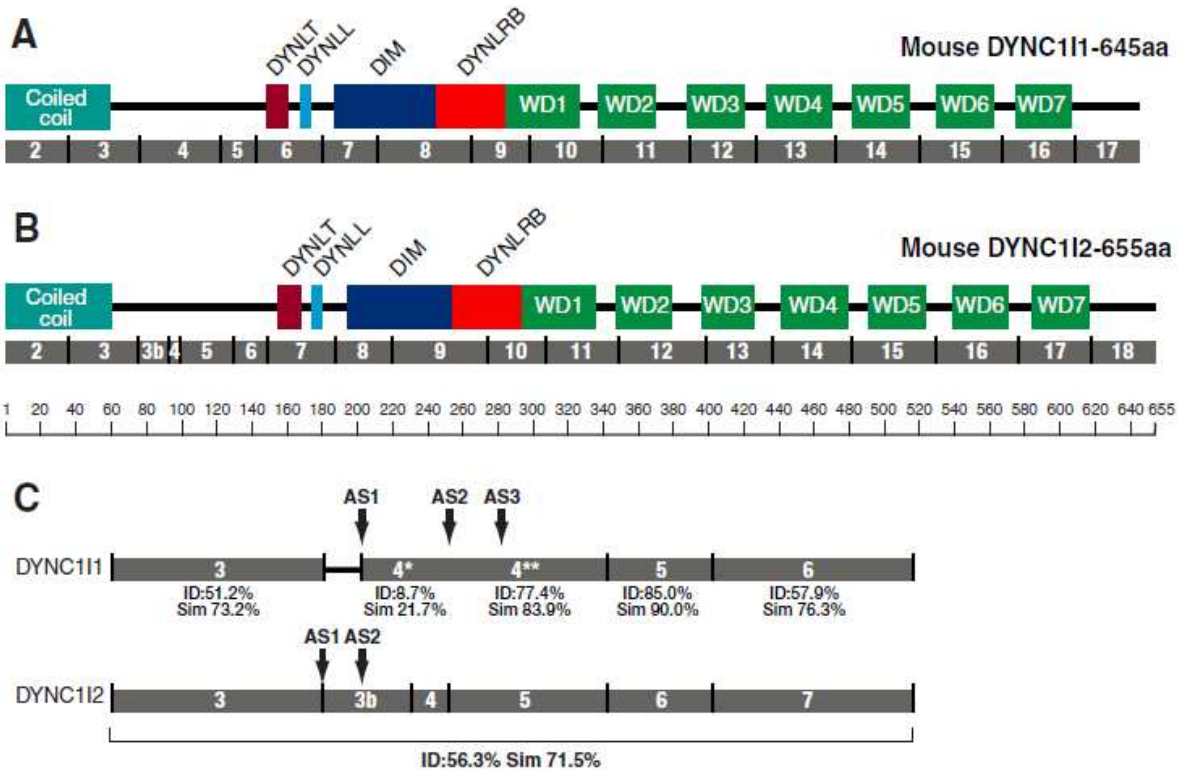

Figure 6.9. Exon – protein domain relationship for dynein intermediate chain genes

Protein domains marked as blocks, numbered exons marked in grey, the coiled coil region where protein interactions occur is shown as is DYNLT – binding region of Tc-Tex dynein light chains, DYNLL –binding region of LC8 dynein light chains, DIM – intermediate chain dimerisation domain, DYNLRB – binding domain of Roadblock dynein light chains; seven WD40 repeats marked in green

A. Mouse DYNC1I1 isoform 1.A (645 amino acids).
B. Mouse DYNC1I2 isoform 2.D (655 amino acids) including exons 1 to 3 and new exon 3b; exon 4 to 18
C. Schematic alignment of DYNC1I1 and DYNC1I2 protein sequences coded by exons 3 to 6 of *Dync1i1* and exons 3 to 7 of *Dync1i2* genes; alternative splice sites in *Dync1i1* exon 4 (AS1, AS2, AS3) and *Dync1i2* exon 3b (AS1, AS2) are marked; the percent of identity (ID) and similarity (Sim) between segments of protein sequences coded by specific exons were compared using AliSubSimP; protein sequence of DYNC1I1 exon 4 was compared as two segments marked with asterix: 4* from AS1 to AS2 and 4** from AS2 to the end of exon 4

6.5.1 *In silico* analysis of mechanism of alternative splicing observed in *Dync1i1* and *Dync1i2* genes

There are several features known that define alternatively spliced exons. Apart from conservation of exon/intron boundary sequences, the strength of alternative splice sites can be statistically assessed. (Koren *et al.*, 2007) proposed the mechanism, in which constitutive exons accumulate mutations which create new splice site competing with the constitutive site. Likewise, constitutive splice sites were found to have stronger splice signals than alternative ones. Furthermore, as minor and new isoforms are known to have different *cis*- acting splicing signals, the strength of splice sites in the *Dync1i1* and *Dync1i2* genes was assessed using 'Splice Site Score Calculation' (http://rulai.cshl.edu /new_alt_exon_db2/HTML/score.html). The comparison was performed for constitutive and alternatively spliced exons. Each splice site had a score calculated based on its sequence: for 3'AS site the maximum score was 14.2 with mean 7.9 for a constitutive exon; for 5' AS site the maximum score was 12.6 with mean 8.1 for a consecutive exon. Intronic sequences used were genomic sequences of mouse *Dync1i1* and *Dync1i2* deposited in the Ensembl (built NCBIM37) (ENSMUST00000115555 and ENSMUST00000112140/ENSMUST00000112144 respectively).

There were 3 exons of mouse *Dync1i1* examined, which are known to be consecutive (exon 4), alternative cassette (exon 5), and containing alternative 3' splice site (exon 4) (Table 6.5). The scores for both splice sites in exon 3 (2.1 and 4.9) were higher than scores recorded for exon 5 (0.4 and 3.2), thus confirming bioinformatics data of alternative exons showing weaker splice sites. Furthermore, 5' splice site in exon 4 was scored as very strong (11.3) when alternative 3' slice sites had lower scores (AS1 – 7.9, AS2 – 3.0, and AS3 – 0.5). These results were in agreement with observed imbalance in the strength of splice sites observed for exons with one site alternatively spliced (Koren *et al.*, 2007). Based on the values, isoforms with AS1 in exon 4 *(Dync1i1.A, Dync1i1.E*) would be the major isoforms. However, in mouse tissues isoform *Dync1i1.B*, in which AS2 is used, was observed to be the most abundant.

The splicing pattern of the mouse *Dync1i2* gene involved alternative use of a first exon and 3 additional cassette exons (3b, 4, and 6) (Table 6.5). The 5' splice site in the exon 1a was much stronger (12.6) than splice site in the exon 1b (2.7). Furthermore, both constitutive exons examined (3 and 5) showed high scores for the 5' (7.8, 8.7 respectively) but not for the 3' splice sites (-0.5, 3.0 respectively). Although exon 4 is a cassette exon found in minor isoforms *(Dync1i2.D, Dync1i2.E, Dync1i2.A),* its splice sites were scored higher than corresponding sites in the exon 3. On the other hand, exon 6 was characterised by weak splice sites when related to exon 5. Finally, a new exon 3b, which was found at a low level and likely represents a minor variant, had splice sites scored lower than adjoining exons 3 and 4, but higher than exon 6. Based on the scores, exon 4 should be included more preferentially than exon 3, which is not the case.

The analysis performed did not reflect completely the preference towards exon inclusion, which we observed in mouse tissues. This result suggests that the 'strength' of the splice site sequence is not sufficient to determine the pattern of the alternative splicing.

Table 6.5. Summary of scores of 3' and 5' splice sites
Values of scores calculated using 'Splice Site Score Calculation' for constitutive and alternative (shaded) exons of mouse *Dync1i1* and *Dync1i2* genes; sequences of intron/exon boundaries and numbers of exons retrieved from Ensembl (built NCBIM37), where sequence ENSMUST00000115555 referred to *Dync1i1* exons, sequence ENSMUST00000112140 referred to *Dync1i2 (exon 1a)*, and ENSMUST00000112144 referred to *Dync1i2 (exon 1b)*; exonic sequence in upper case, intronic in lower, in case of exon 1a/1b the 3' sites were not defined thus omitted; in brackets shown mean values for 3' (7.9) and 5' (8.1) splice sites of constitutive exons, values higher than mean in bold; maximum scores were: 14.2 for 3' splice site and 12.6 for 5' splice site

Dync1i1					***Dync1i2***				
Exon	**3' Splice site (7.9)**		**5' splice site (8.1)**		**Exon**	**3' Splice site (7.9)**		**5' splice site (8.1)**	
	intron/EXON	Score	EXON/intron	Score		intron/EXON	Score	EXON/intron	Score
					1a	-	-	AAG gtaagt	12.6
					1b	-	-	CAG gtcggt	2.7
3	caaatcttttag G	2.1	TAG gtactt	4.9	3	ttaaaattttag A	- 0.5	TTG gtaagg	7.8
					3b AS1	ttctcaattgag G	- 2.9	TAG gtaaca	6.2
					3b AS2	tcctcctttcag A	11.3		
4 AS1	gctcttccccag T	7.9			4	ctgtacgttcag T	3.1	GGG gtaagg	8.0
4 AS2	ttcattatttag T	3.0	AAG gtaaga	11.3	5	ttcattatttag T	3.0	TAG gtatgt	8.7
4 AS3	cttcgaaatcag T	0.5							
5	ctgcacgattag G	0.4	TTG gtatat	3.2	6	acaaccatttag G	- 0.6	GGG gtattg	1.7

6.5.2 Comparison of the expression pattern of the cytoplasmic dynein intermediate chains 1 and 2 across species

As databases are frequently updated, the summary presented aimed to revise available information. In order to retrieve the most accurate sequences few assumptions were made, and only full length transcripts containing first exon (exon 1 in *Dync1i1*, exons 1a, 1b in *Dync1i2*) present in the majority of transcripts were taken into account. The transcripts retrieved displayed splicing events within exons 3 to 7 and could be translated into full length DYNC1I proteins.

6.5.2.1 Comparison of the human, rat, and mouse Dync1i1 splicing pattern

The alternative splicing of the *Dync1i1* gene was fairly uniform when human, mouse, and rat sequences were compared (Table 6.6). There were 5 variants present in the human assemblies, which corresponded to mouse variants *Dync1i1.A, Dync1i1.B, Dync1i1.D, Dync1i1.E,* and *Dync1i1C.* In the rat genome assembly only 4 isoforms were found, likely due to fewer sequences available. Those isoforms corresponded to mouse *Dync1i1.A, Dync1i1.B, Dync1i1.E,* and *Dync1i1C.*

Table 6.6. Comparison of the *Dync1i1* splice variants in human, mouse, and rat

The sequences of various isoforms were retrieved from available genome assemblies, and annotated according to the UCSC Genome Browser and Ensembl release 62 *(in italics);* mouse isoforms annotated as in Kuta *et al.*, 2010; non-curated sequences present in EST databases underlined

Feature	Human (GRCh37/hg19)	Mouse (NCBI37/mm9)	Rat (Baylor 3.4/rn4)
Position (UCSC)	Chr7 q21.3 95,401,818-95,727,735	Chr6 qA1 5,675,812-5,978,039	Chr4 q13 30,496,410 – 30,809,621
Length [bp]	325,918	302,228	313,212
Trans-cripts and peptides	uc003uoc.3/ *ENST00000324972* 645 aa	Dync1i1.A/ *ENSMUST00000115555* 645 aa	*ENSRNOT00000013184* 643 aa
	uc003uod.3/ *ENST00000447467* 628 aa	Dync1i1.B/ *ENSMUST00000115559* 628 aa	CB703089, CB747457
	DA392898	Dync1i1.D/ *ENSMUST00000115556* 617 aa	
	uc003uoe.3/ *ENST00000437599* 625 aa	Dync1i1.E 625 aa	CB712052
	uc003uob.2/ *ENST00000359388* 608 aa	Dync1i1.C/ *ENSMUST00000115554* 608 aa	CB616735, CB713291
		Dync1i1.F 597 aa	

6.5.2.2 Comparison of the human, rat, and mouse Dync1i2 gene

In contrast to *Dync1i1*, the expression pattern of *Dync1i2* was more complicated, including 2 alternative first exons and isoforms there are potentially species specific. Because the start codon is located in exon 2, the transcription of two independent first exons may reflect an existence of additional regulation. There were 3 major isoforms found in all assemblies, and in mouse annotated as *Dync1i2.A, Dync1i2.B* and *Dync1i2.C*. In mouse tissues isoform *Dync1i2.C* was present in somatic tissues, thus it was sufficient for housekeeping functions of the dynein complex (Table 6.7).

The new exon identified in mouse transcripts was annotated as 3b and was located within intron 3. The variant annotated as *Dync1i2.D* (exon1a/1b) was 51 bp long, which resulted in insertion of 17 amino acids. The use of an alternative 3' splice site created a 36 bp long exon 3b and resulted in the additional transcript annotated *Dync1i2.E* (exon 1a/1b). Both splice variants were detected in mouse neural tissues and as they maintained the open reading frame, they might represent rare transcripts. The multiple alignment of the mouse intron 3 containing new exon generated by 'multiz' (UCSC/Penn State Bioinformatics tool) alignment of vertebrate species with the mouse genome showed high conservation only with rat genomic sequence. However, this region was reported to match a sequence of a long terminal repeat (LTR) on the complement strand (RepeatMasker). The sequence was annotated as Mammalian apparent LTR-retrotransposons (MaLR) class MTC (Smit, 1993). MaLR are super family of elements consisting only from the LTR sequence, and MTC are a group found only in rodents, for example in mouse multifinger gene mKr2 cDNA, 3' UTR, and in 3' flanking regions of the mouse serum amyloid A-1 *(Saa1)* and mouse serum amyloid A-2 *(Saa2)* genes. The repeat elements were reported to contribute to protein sequences, the functionality of a new transcript is not easy to predict (Piriyapongsa *et al.*, 2007).

The assembly of human sequences also contained transcripts, whose splicing pattern was not observed in mouse or rat. Transcripts annotated as ENST00000410079 and ENST00000358002 contained longer exon 5 by 54 bp but lacked exons 4 and 6. This

additional isoform had ORF maintained and when translated, the DYNC1I2 would be 630 amino acids long (Table 6.7).

Table 6.7. Comparison of the *Dync1i2* splice variants in human, mouse, and rat
The sequences of various isoforms were retrieved from available genome assemblies, and annotated according to the UCSC Genome Browser and Ensembl release 62 *(in italics);* mouse isoforms annotated as in Kuta *et al.*, 2010; non-curated sequences present in EST databases underlined; in brackets first exon used; * - no longer present in the UCSC

Feature	Human (GRCh37/hg19)	Mouse (NCBI37/mm9)	Rat (Baylor 3.4/rn4)
Position (UCSC)	Chr2 172,543,982-172,604,919	Chr2 71,050,070-71,101,351	Chr3 53,480,918-53,533,222
Length [bp]	60,938	51,282	52,305
Trans-cripts and peptides	(1a) uc002uha.1/ *ENST00000397119* 638 aa	(1a) Dync1i2.A *ENSMUST00000112140* 638 aa	(1a) CB784025 638 aa
	(1b) uc002uhe.1/ *ENST00000409773* 638 aa	(1b) Dync1i2.A *ENSMUST00000112144* 638 aa	(1b) *ENSRNOT00000067729* 638 aa
	(1a) *ENST00000263811* 632 aa	(1a) Dync1i2.B uc008kah.1 /*ENSMUST00000112142* 632 aa	(1a) CF977964 632 aa
	(1b) *ENST00000409317* 632 aa	(1b) Dync1i2.B *ENSMUST00000100028* 632 aa	(1b) *ENSRNOT00000047243* 632 aa
	(1a) uc002uhb.1/ *ENST00000340296* 612 aa	(1a) Dync1i2.C uc008kai.1/ *ENSMUST00000112138* 612 aa	(1a) CK365527, EV774963, FM056664 612 aa
	(1b) uc002uhf.1/ *ENST00000409197* 612 aa	(1b) Dync1i2.C uc008kak.1 /*ENSMUST00000081710* 612 aa	(1b) *ENSRNOT00000013400* 612 aa
Species specific/ minor isoforms	(1a) uc010zds.1*/ *ENST00000410079* 630 aa	Dync1i2.D (1a) GU992208/ (1b) GU992211 655 aa	
	(1b) uc010zdt.1*/ *ENST00000358002* 630 aa	Dync1i2.E (1a) GU992209/ (1b) GU992212 650 aa	
		(1b) *ENSMUST00000112136* 637 aa	
	uc002uhc.2/ *ENST00000508530* 611 aa	(1a) *ENSMUST00000112139* 611 aa	

Another variation in the splicing pattern of the *Dync1i2* gene was selective choice of the 3' splice site within exon 18, which resulted in deletion of a glutamine residue (Q). This pattern was found common, with approximately 50% of alternative 3' splice sites being exactly 3 bp apart (known as the NAGNAG motif) (Koren *et al.*, 2007). This seemingly erroneous isoforms were recently found within transcripts of a cardiac voltage-gated sodium channel ($Na_v1.5$ Na) as fully functional (Schroeter *et al.*, 2010).

In conclusion, the alternative splicing of the dynein intermediate chains 1 and 2 displays high similarity within mammals, which may correspond to distinct functions of the dynein complex. Furthermore, the *Drosophila sp.* orthologous gene, *Dcic* was also shown to be alternatively spliced resulting in the presence of 10 isoforms (Nurminsky *et al.*, 1998). Interestingly, the splicing events were mapped to the region containing three small 'variable' exons located between exon 4 and exon 5, and the use of two splice acceptors preceding exon 1.

7. General discussion

In this work two novel mouse lines carrying single point mutations in the cytoplasmic dynein intermediate chains 1 *(Dync1i1)* and 2 *(Dync1i2)* were presented. During the screen of archive of the ENU mutagenised DNA we identified single point mutations in the dynein intermediate chains 1 and 2, which resulted in a substitution of glycine at the position 482 with aspartic acid (*Dync1i1*^{G482D}) and threonine 172 with isoleucine respectively. Mutant mouse lines were rederived and homozygous *Dync1i1*$^{G482D/G482D}$ and *Dync1i2*$^{T172I/T172I}$ mice and cell lines were tested for a variety of phenotypes.

7.1 Characterisation of mouse line mutant in the cytoplasmic dynein intermediate chain 1 (*Dync1i1*^{G482D})

The homozygous mutant *Dync1i1*$^{G482D/G482D}$ allele did not cause behavioural deficits. Nonetheless, detailed analysis of gait revealed differences in paw placement, speed of movement, and weight bearing. Furthermore, homozygous *Dync1i1*$^{G482D/G482D}$ animals tended to perform worse on the running wheel than wildtype *Dync1i1*$^{+/+}$ littermates. Deficits in the toe spread and swing speed are often observed after denervation of foot muscles (Deumens *et al.*, 2007), while shift in the base of support between front and hind paws was similar to reported for the homozygous *Dync1li1*$^{N235Y/N235Y}$ mice (Banks *et al.*, 2011). Disruption of the interactions between dynein and dynactin in motor neurons resulted in neurodegeneration and denervation of muscles, and in live animals those changes were reflected by decrease of stride length and endurance on a treadmill (LaMonte *et al.*, 2002). These characteristics might suggest mild neuropathy or denervation of sensory neurons. On the other hand, there are many factors influencing an animal's performance when tested on the running wheel. Voluntary running induces neurogenesis of hippocampal neurons in adult mice thus improving memory (Brandt *et al.*, 2010), it was shown to reduce the serotonin-mediated stress response (Rozeske *et al.*, 2011), and have antidepressive effects via increase in the expression of brain derived growth factor (BDNF) (Sartori *et al.*, 2011). However, the beneficial effects were alleviated in a mouse model of Huntington's disease (Potter *et al.*, 2010). Taken together, the interpretation of decrease in running is not straightforward and it might reflect

impairment occurring within different systems, for example abnormalities of NMJs are common for mice expressing mutant DCTN1/P150^{Glued} (Chevalier-Larsen *et al.*, 2008), while improper synaptic organisation affects learning and acquisition of motor skills (Groszer *et al.*, 2008). Finally, a single nucleotide polymorphism (SNP) in the intron of the *DYNC1I1* gene was found associated with peripheral sensory neuropathy or neuralgia affecting multiple myeloma patients treated with bortezomib (Favis *et al.*, 2011).

The new mutation in the cytoplasmic dynein intermediate chain 1 lies within WD domain and this region is known to mediate binding to the dimer of heavy chains. We can hypothesise, that G482D substitution might affect intermolecular interactions, as structural features of the WD domains promote assembly of multisubunit complexes (Stirnimann *et al.*, 2010). Likewise, loss of dopaminergic neurons and locomotor deficits mimicking parkinsonism were observed in Zebrafish expressing leucine-rich repeat kinase 2 (LRRK2) lacking one of the WD40 repeats (Sheng *et al.*, 2010).

7.2 Mutation in the cytoplasmic dynein intermediate chain 2 *(Dync1i2)* perturbs molecular pathways involved in memory formation

The behavioural phenotype of animals homozygous for the mutant allele (*Dync1i2*$^{T172I/T172I}$) was related to an impairment in the hippocampus related short-term habituation. On the cellular level subtle deficits were observed in the dynamics of the trafficking of the EGF endosomes and Golgi membranes (in double homozygous *Dync1i1*$^{G482D/G482D}$ *Dync1i2*$^{T172I/T172I}$ cells). Furthermore, levels of *Dynlt3* and *Dynll2* transcripts were lower in the spinal cords and hippocampi isolated from homozygous *Dync1i2*$^{T172I/T172I}$ animals.

Mutation in the intermediate chain 2 was mapped to substitute second residue within the light chains *(Dynll1, Dynll2)* binding domain (Figure 7.1) (Hall *et al.,* 2009). Dimeric light chains were shown essential in the dimerisation of the intermediate chains and subsequent assembly of the complex (section 1.2.5). Furthermore, expression levels of *Dynlt3* and *Dynll2* varied from the wild type animals in the presence of the mutant allele. We can hypothesise, that the T172I mutation might affect the structure of the intermediate chain 2 thus disrupting interactions with light chains. Although the

regulation of expression of different subunits is not well known, depletion of the *Dync1h1* transcript resulted in simultaneous down-regulation of the *Dync1i* (Caviston *et al.*, 2007). Similar mechanisms might also govern the coexpression of the light chains. In addition, the dynein complex was proposed to be assembled via formation of sub-complexes with heavy and intermediate chains as a core subunits (King *et al.*, 2002). Furthermore, in the brain homogenates of the animals carrying a homozygous mutation in the dynein light intermediate chain 1 (*Dync1li1*^{N235Y}) the total level of the DYNLT3 was elevated while DYNLL were bound less tightly in the isolated dynein complexes (Banks *et al.*, 2011). These results suggest expression regulation mechanisms, which might be sensitive to structural changes in the complex. Based on observations from two different mutant mouse lines light chains might act as a hypothetical 'sensor', especially as DYNLL are known to be present ubiquitously in the cytoplasm, for example stabilising the structure of myosin Va dimers (Wagner *et al.*, 2006).

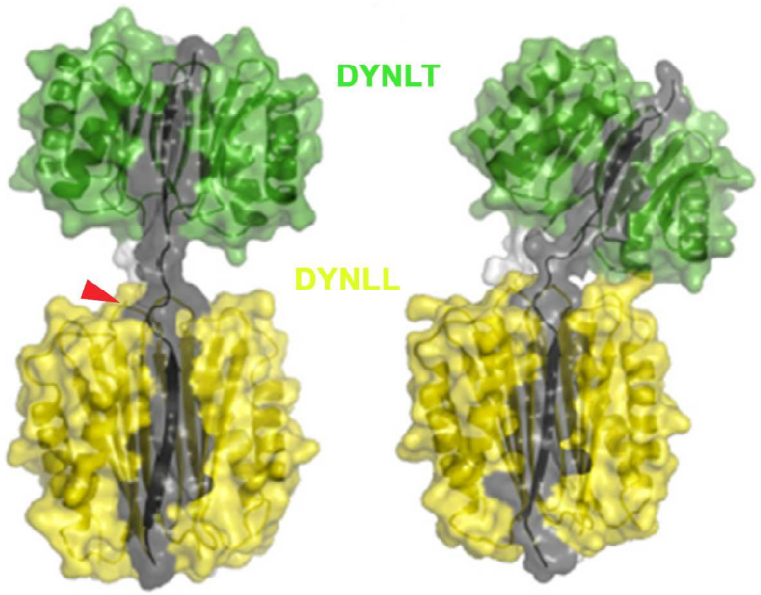

Figure 7.1. Crystal structure of the ternary complexes of intermediate chains (DYNC1I) with light chains (DYNLT, DYNLL)

Semi-transparent surface and secondary structural elements are shown for crystal structures of assembly intermediate chains (grey), light chains DYNLT (green) and DYNLL (yellow); the 'linker' between light chain binding domains is flexible and can adopt a range of conformations; approximate position of the T172I mutation marked with arrow

Dynein light chains DYNLT were also implicated in neurogenesis of the hippocampal neurons and axon formation (Conde *et al.*, 2010). In the rat brain DYNLT1 and DYNLT3 were found in mutually exclusive structures, with DYNLT3 enriched in the perikarya of pyramidal cell granule cell layers in the dentate hilus, and pyramidal cells of brain cortex (Chuang *et al.*, 2001). Likewise, DYNLT3 was found abundant in dendritic spines, postsynaptic structures, and vacuolar tubules of the Golgi complex, suggesting its function in membrane remodelling during long-term potentiation. In the homozygous *Dync1i2*$^{T172I/T172I}$ mice higher levels of DYNLT3 were detected in the spinal cord but not in other parts of the brain (Chapter 6). In spinal cord the expression pattern of both *Dync1i2* and *Dynlt3* overlaps, however no impairment in the locomotor functions were found. This result might suggest a mechanism 'buffering' imbalance of the subunits expressed, for example by degrading the excess of DYNLT3 transcript.

In the hippocampi isolated from homozygous *Dync1i2*$^{T172I/T172I}$ animals, the expression level of *Dynll2* was lower than observed in the wild type animals. DYNLL have been implicated in formation of synapses and they were found at the synaptic sites in the hippocampal neurons and at postsynaptic elements in the spinal cord (Fuhrmann *et al.*, 2002). Furthermore, direct interactions of DYNLL with gephyrin (GPHN), which acts as a scaffold for clusters of the glycine receptors at the inhibitory synapses, suggest the direct function of the light chains in trafficking of synaptic components. Bassoon (BSN) and Piccolo (PCLO) are another complex essential in the assembly of synapses and neurotransmitter release. After synthesis they are directed to synapses in Golgi-derived Piccolo – Bassoon transport vesicles (PTVs) (Fejtova *et al.*, 2009). In cultured hippocampal neurons PTVs were found associated with molecular motors, including the cytoplasmic dynein complex. Further analysis revealed that BSN interacts directly with DYNLL1 and DYNLL2, and the authors suggested its role as an adaptor binding dynein to PTVs via DYNLLs. Furthermore, disruption of BSN binding to the light chains affected trafficking of the PTVs and the distribution of the BSN – PCLO at the synapses. Taken together, we can hypothesise that observed impairment of the short-term habituation is a result of many cellular processes triggered by mutation in the intermediate chain 2. Both *Dync1i2* and *Dynll2* are highly expressed in the hippocampal formation, where structural abnormalities

in the light chain binding domain may affect complex stability and expression of the *Dynll2*. The decrease in amount of the DYNLL2 would then disrupt BSN – PCLO transport and synapse formation. It should also be noted that dynamics of Golgi and endocytic membranes was also impaired in the fibroblasts homozygous for mutant alleles (*Dync1i1*$^{G482D/G482D}$ *Dync1i2*$^{T172I/T172I}$ and *Dync1i2*$^{T172I/T172I}$ respectively). Finally, a decrease in the performance of the mutant *Dync1i2*$^{T172I/T172I}$ mice in the novelty preference task was a new feature not associated before with the dynein intermediate chains, whereas it was similar to the behaviour of the *Gria1*$^{-/-}$ animals (Sanderson *et al.*, 2009). The GRIA1 AMPA receptor subunit is a key mediator of hippocampal synaptic plasticity and is especially important for a rapidly-induced, short-lasting form of potentiation.

There is another line of evidence linking cytoplasmic dynein intermediate chain 2 with memory formation. DYNC1I2 was present in a complex with sorting nexin 4 (SNX4) and WWC1/KIBRA, which mediated trafficking of endosomal compartment (Traer *et al.*, 2007). In the human population, KIBRA was associated with synaptic plasticity and performance in a recall task (Yasuda *et al.*, 2010). Furthermore, patients with Alzheimer's disease showed up-regulation of the KIBRA in hippocampus and temporal cortex, which might correlate with observed memory impairment in the course of the disease (Corneveaux *et al.*, 2010).

7.3 What do double homozygous (*Dync1i1*$^{G482D/G482D}$ *Dync1i2*$^{T172I/T172I}$) mice show?

In this work we present initial results obtained with mouse embryonic fibroblasts (MEFs) isolated from animals carrying double homozygous mutations in the intermediate chains 1 and 2 (*Dync1i1*$^{G482D/G482D}$ *Dync1i2*$^{T172I/T172I}$), which displayed deficits in morphology of the Golgi apparatus. Deficits in trafficking of membranous organelles have been observed in hereditary spastic paraplegias (Blackstone *et al.*, 2011) therefore mutant animals might be useful in studying neurological deficits.

7.4 Why do *Dync1h1*^{Loa} mice get stressed?

The *Loa* mutant mouse line has been described in section 1.5.1.2. Using fibroblasts isolated from mutant *Dync1h1*^{Loa} mice we investigated a formation of stress granules. The *Dync1h1*^{Loa} mutation was mapped to be within a region where intermediate and light intermediate chains bind. It was found to affect the assembly of the complex and affinity of the distinct subunits (Deng *et al.*, 2010). By stronger binding of the DYNC1I associations with dynactin complex were impaired, which might correspond to the observed deficits in molecular transport (Hafezparast *et al.*, 2003).

Stress granules are heterogeneous assemblies of RNAs and RNA binding proteins which are formed in a dynein-dependent manner (Loschi *et al.*, 2009). Their composition is known to differ depending on the cell type or stress applied (Thomas *et al.*, 2011). In the homozygous *Dync1h1*$^{Loa/Loa}$ fibroblasts we observed an increased number of stress granules when cells were treated with sodium arsenite, whereas no differences were observed after treatment with thapsigargin. This discrepancy might correspond to different cellular mechanisms, which are activated depending on the stress applied, for example TDP-43 was shown to regulate granules induced by oxidative stress (McDonald *et al.*, 2011). Furthermore, our results also highlight a distinct role of cytoplasmic dynein in the assembly of the stress granules. In primary neurons treated with sodium arsenite DYNLRB1 was found in the structures positive for known stress granule markers (TIA-1, ELAVL1/HuR) (Tsai *et al.*, 2009). Stress granules are often compared to neuronal mRNA granules and they were proposed to have a neuroprotective role (Thomas *et al.*, 2011). We can hypothesise that disruption of the stress response pathway might result in neuronal cell death, which is observed in the *Dync1h1*^{Loa} animals.

7.5 Mice full of surprises

In the presented work we employed mouse mutant lines to study functions of the cytoplasmic dynein intermediate chains 1 and 2. As a result, distinct phenotypes were described, both suggesting neurological involvement, which are useful resources to study a specific deficits, for example short-term habitation. The role of a broad and

comprehensive behavioural analysis of mutant lines should be also stressed, which is essential in investigating mild behavioural deficits. Furthermore, we noted the influence of genetic background on the performance of animals, and it would be beneficial to examine more numerous cohorts of mice bred on at least 2 distinct genetic backgrounds. As an example, the modifying effects of genetic background on disease associated phenotype was recently described using transgenic model of amyotropic lateral sclerosis (ALS) (Acevedo-Arozena *et al.*, 2011).

7.6 Future work

Further characterisation of the *Dync1i1*^{G482D} mutant line would be advantageous, for instance, detailed histological analysis of NMJs and sensory neurons would be necessary to dissect the physiological basis of mutant phenotype. Mutations in both heavy (*Dync1h1*^{Loa}) and light intermediate 1 (*Dync1li1*^{N235Y}) chains were shown to disturb molecular organisation of the dynein complex, thus investigation of native dynein complex containing mutant intermediate chains would be important in the light of the assembly of the complex (Banks *et al.*, 2011; Deng *et al.*, 2010).

Deficits in the memory in the *Dync1i2*^{T172I} mutant mouse line suggest deregulation of the synaptic functions affecting mostly hippocampal neurons. Therefore, in parallel with detailed characterisation of animals, synapse formation and trafficking of dendritic components should be investigated.

Apart from intracellular transport, the cytoplasmic dynein complex is crucial for mitosis and chromosome separation, cell migration, and brain development (Friocourt *et al.*, 2011; Whyte *et al.*, 2008). Although there were no morphological abnormalities observed in either of the mutant mouse lines, the effects of both mutations (*Dync1i1*^{G482D}, *Dync1i2*^{T172I}) on the chromosome segregation and nuclear positioning should be examined.

8. Bibliography

Abrahams,G.L., Muller,P., and Hensel,M. (2006) Functional dissection of SseF, a type III effector protein involved in positioning the salmonella-containing vacuole. *Traffic*, **7**, 950-965.

Acevedo-Arozena,A., Kalmar,B., Essa,S., Ricketts,T., Joyce,P., Kent,R., Rowe,C., Parker,A., Gray,A., Hafezparast,M., Thorpe,J.R., Greensmith,L., and Fisher,E.M. (2011) A comprehensive assessment of the SOD1G93A low-copy transgenic mouse, which models human amyotrophic lateral sclerosis. *Dis Model Mech 4*.

Acevedo-Arozena,A., Wells,S., Potter,P., Kelly,M., Cox,R.D., and Brown,S.D. (2008) ENU mutagenesis, a way forward to understand gene function. *Annu Rev Genomics Hum Genet*, **9**, 49-69.

Aiastui,A., Pucciarelli,M.G., and Garcia-del,P.F. (2010) Salmonella enterica serovar typhimurium invades fibroblasts by multiple routes differing from the entry into epithelial cells. *Infect Immun*, **78**, 2700-2713.

Akhmanova,A. and Hammer,J.A., III (2010) Linking molecular motors to membrane cargo. *Curr Opin Cell Biol*, **22**, 479-487.

Alekseyenko,A.V., Kim,N., and Lee,C.J. (2007) Global analysis of exon creation versus loss and the role of alternative splicing in 17 vertebrate genomes. *RNA*, **13**, 661-670.

Alt,E., Yan,Y., Gehmert,S., Song,Y.H., Altman,A., Gehmert,S., Vykoukal,D., and Bai,X. (2011) Fibroblasts share mesenchymal phenotypes with stem cells, but lack their differentiation and colony forming potential. *Biol Cell*, **103**, 197-208.

Altria,K.D. (1996) Quantitation procedures. *Methods Mol Biol*, **52**, 49-60.

Anderson,P. and Kedersha,N. (2009) Stress granules. *Curr Biol*, **19**, R397-R398.

Angeby-Moller,K., Berge,O.G., and Hamers,F.P. (2008) Using the CatWalk method to assess weight-bearing and pain behaviour in walking rats with ankle joint monoarthritis induced by carrageenan: effects of morphine and rofecoxib. *J Neurosci Methods*, **174**, 1-9.

Angelastro,J.M., Klimaschewski,L., Tang,S., Vitolo,O.V., Weissman,T.A., Donlin,L.T., Shelanski,M.L., and Greene,L.A. (2000) Identification of diverse nerve growth factor-regulated genes by serial analysis of gene expression (SAGE) profiling. *Proc Natl Acad Sci U S A*, **97**, 10424-10429.

Banks,G.T. and Fisher,E.M. (2008) Cytoplasmic dynein could be key to understanding neurodegeneration. *Genome Biol*, **9**, 214.

Banks,G.T., Haas,M.A., Line,S., Shepherd,H.L., AlQatari,M., Stewart,S., Rishal,I., Philpott,A., Kalmar,B., Kuta,A., et,al., and Fisher,E.M. (2011) Behavioral and Other Phenotypes in a Cytoplasmic Dynein Light Intermediate Chain 1 Mutant Mouse. *J Neurosci*, **31**, 5483-5494.

Barbar,E. (2008) Dynein light chain LC8 is a dimerization hub essential in diverse protein networks. *Biochemistry*, **47**, 503-508.

Barlow,A.L., Macleod,A., Noppen,S., Sanderson,J., and Guerin,C.J. (2010) Colocalization analysis in fluorescence micrographs: verification of a more accurate calculation of pearson's correlation coefficient. *Microsc Microanal*, **16**, 710-724.

Bechler,M.E., Doody,A.M., Racoosin,E., Lin,L., Lee,K.H., and Brown,W.J. (2010) The phospholipase complex PAFAH Ib regulates the functional organization of the Golgi complex. *J Cell Biol*, **190**, 45-53.

Beuzon,C.R., Meresse,S., Unsworth,K.E., Ruiz-Albert,J., Garvis,S., Waterman,S.R., Ryder,T.A., Boucrot,E., and Holden,D.W. (2000) Salmonella maintains the integrity of its intracellular vacuole through the action of SifA. *EMBO J*, **19**, 3235-3249.

Beuzon,C.R., Salcedo,S.P., and Holden,D.W. (2002) Growth and killing of a Salmonella enterica serovar Typhimurium sifA mutant strain in the cytosol of different host cell lines. *Microbiology*, **148**, 2705-2715.

Bielli,A., Thornqvist,P.O., Hendrick,A.G., Finn,R., Fitzgerald,K., and McCaffrey,M.W. (2001) The small GTPase Rab4A interacts with the central region of cytoplasmic dynein light intermediate chain-1. *Biochem Biophys Res Commun*, **281**, 1141-1153.

Bilsland,L.G., Sahai,E., Kelly,G., Golding,M., Greensmith,L., and Schiavo,G. (2010) Deficits in axonal transport precede ALS symptoms in vivo. *Proc Natl Acad Sci U S A*, **107**, 20523-20528.

Birmingham,C.L. and Brumell,J.H. (2006) Autophagy recognizes intracellular Salmonella enterica serovar Typhimurium in damaged vacuoles. *Autophagy*, **2**, 156-158.

Blackstone,C., O'Kane,C.J., and Reid,E. (2011) Hereditary spastic paraplegias: membrane traffic and the motor pathway. *Nat Rev Neurosci*, **12**, 31-42.

Bolte,S. and Cordelieres,F.P. (2006) A guided tour into subcellular colocalization analysis in light microscopy. *J Microsc*, **224**, 213-232.

Boucrot,E., Henry,T., Borg,J.P., Gorvel,J.P., and Meresse,S. (2005) The intracellular fate of Salmonella depends on the recruitment of kinesin. *Science*, **308**, 1174-1178.

Bozkurt,A., Deumens,R., Scheffel,J., O'Dey,D.M., Weis,J., Joosten,E.A., Fuhrmann,T., Brook,G.A., and Pallua,N. (2008) CatWalk gait analysis in assessment of functional recovery after sciatic nerve injury. *J Neurosci Methods*, **173**, 91-98.

Brandt,M.D., Maass,A., Kempermann,G., and Storch,A. (2010) Physical exercise increases Notch activity, proliferation and cell cycle exit of type-3 progenitor cells in adult hippocampal neurogenesis. *Eur J Neurosci*, **32**, 1256-1264.

Bremner,K.H., Scherer,J., Yi,J., Vershinin,M., Gross,S.P., and Vallee,R.B. (2009) Adenovirus transport via direct interaction of cytoplasmic dynein with the viral capsid hexon subunit. *Cell Host Microbe*, **6**, 523-535.

Brooks,S.P. and Dunnett,S.B. (2009) Tests to assess motor phenotype in mice: a user's guide. *Nat Rev Neurosci*, **10**, 519-529.

Brown,S.D., Chambon,P., and de Angelis,M.H. (2005) EMPReSS: standardized phenotype screens for functional annotation of the mouse genome. *Nat Genet*, **37**, 1155.

Brown,S.D. and Nolan,P.M. (1998) Mouse mutagenesis-systematic studies of mammalian gene function. *Hum Mol Genet*, **7**, 1627-1633.

Buchan,J.R. and Parker,R. (2009) Eukaryotic stress granules: the ins and outs of translation. *Mol Cell*, **36**, 932-941.

Bush,J.R. and Wevrick,R. (2010) Loss of Necdin impairs myosin activation and delays cell polarization. *Genesis*, **48**, 540-553.

Caiazzo,M., Colucci-D'Amato,L., Esposito,M.T., Parisi,S., Stifani,S., Ramirez,F., and di Porzio,U. (2010) Transcription factor KLF7 regulates differentiation of neuroectodermal and mesodermal cell lineages. *Exp Cell Res*, **316**, 2365-2376.

Calarco,J.A., Xing,Y., Caceres,M., Calarco,J.P., Xiao,X., Pan,Q., Lee,C., Preuss,T.M., and Blencowe,B.J. (2007) Global analysis of alternative splicing differences between humans and chimpanzees. *Genes Dev*, **21**, 2963-2975.

Cano,D.A., Pucciarelli,M.G., Martinez-Moya,M., Casadesus,J., and Garcia-del,P.F. (2003) Selection of small-colony variants of Salmonella enterica serovar typhimurium in nonphagocytic eucaryotic cells. *Infect Immun*, **71**, 3690-3698.

Carninci,P. (2010) RNA dust: where are the genes? *DNA Res*, **17**, 51-59.

Carpenter,A.E., Jones,T.R., Lamprecht,M.R., Clarke,C., Kang,I.H., Friman,O., Guertin,D.A., Chang,J.H., Lindquist,R.A., Moffat,J., Golland,P., and Sabatini,D.M. (2006) CellProfiler: image analysis software for identifying and quantifying cell phenotypes. *Genome Biol*, **7**, R100.

Carter,A.P., Cho,C., Jin,L., and Vale,R.D. (2011) Crystal structure of the dynein motor domain. *Science*, **331**, 1159-1165.

Caviston,J.P. and Holzbaur,E.L. (2009) Huntingtin as an essential integrator of intracellular vesicular trafficking. *Trends Cell Biol*, **19**, 147-155.

Caviston,J.P., Ross,J.L., Antony,S.M., Tokito,M., and Holzbaur,E.L. (2007) Huntingtin facilitates dynein/dynactin-mediated vesicle transport. *Proc Natl Acad Sci U S A*, **104**, 10045-10050.

Caviston,J.P., Zajac,A.L., Tokito,M., and Holzbaur,E.L. (2011) Huntingtin coordinates the dynein-mediated dynamic positioning of endosomes and lysosomes. *Mol Biol Cell*, **22**, 478-492.

Charbonnier,F., Raux,G., Wang,Q., Drouot,N., Cordier,F., Limacher,J.M., Saurin,J.C., Puisieux,A., Olschwang,S., and Frebourg,T. (2000) Detection of exon deletions and duplications of the mismatch repair genes in hereditary nonpolyposis colorectal cancer families using multiplex polymerase chain reaction of short fluorescent fragments. *Cancer Res*, **60**, 2760-2763.

Chen,H., Yang,J., Low,P.S., and Cheng,J.X. (2008) Cholesterol level regulates endosome motility via Rab proteins. *Biophys J*, **94**, 1508-1520.

Chen,X.J., Levedakou,E.N., Millen,K.J., Wollmann,R.L., Soliven,B., and Popko,B. (2007) Proprioceptive sensory neuropathy in mice with a mutation in the cytoplasmic Dynein heavy chain 1 gene. *J Neurosci*, **27**, 14515-14524.

Chernov,K.G., Barbet,A., Hamon,L., Ovchinnikov,L.P., Curmi,P.A., and Pastre,D. (2009) Role of microtubules in stress granule assembly: microtubule dynamical instability favors the formation of micrometric stress granules in cells. *J Biol Chem*, **284**, 36569-36580.

Chevalier-Larsen,E.S., Wallace,K.E., Pennise,C.R., and Holzbaur,E.L. (2008) Lysosomal proliferation and distal degeneration in motor neurons expressing the G59S mutation in the p150Glued subunit of dynactin. *Hum Mol Genet*, **17**, 1946-1955.

Ching,Y.H., Munroe,R.J., Moran,J.L., Barker,A.K., Mauceli,E., Fennell,T., Dipalma,F., Lindblad-Toh,K., Abcunas,L.M., Gilmour,J.F., et,al., and Schimenti,J.C. (2010) High resolution mapping and positional cloning of ENU-induced mutations in the Rw region of mouse chromosome 5. *BMC Genet*, **11**, 106.

Chomczynski,P. (1992) Solubilization in formamide protects RNA from degradation. *Nucleic Acids Res*, **20**, 3791-3792.

Chuang,J.Z., Milner,T.A., and Sung,C.H. (2001) Subunit heterogeneity of cytoplasmic dynein: Differential expression of 14 kDa dynein light chains in rat hippocampus. *J Neurosci*, **21**, 5501-5512.

Chuang,J.Z., Yeh,T.Y., Bollati,F., Conde,C., Canavosio,F., Caceres,A., and Sung,C.H. (2005) The dynein light chain Tctex-1 has a dynein-independent role in actin remodeling during neurite outgrowth. *Dev Cell*, **9**, 75-86.

Clarkson,Y.L., Gillespie,T., Perkins,E.M., Lyndon,A.R., and Jackson,M. (2010) Beta-III spectrin mutation L253P associated with spinocerebellar ataxia type 5 interferes with binding to Arp1 and protein trafficking from the Golgi. *Hum Mol Genet*, **19**, 3634-3641.

Cole,N.B., Sciaky,N., Marotta,A., Song,J., and Lippincott-Schwartz,J. (1996) Golgi dispersal during microtubule disruption: regeneration of Golgi stacks at peripheral endoplasmic reticulum exit sites. *Mol Biol Cell*, **7**, 631-650.

Collinet,C., Stoter,M., Bradshaw,C.R., Samusik,N., Rink,J.C., Kenski,D., Habermann,B., Buchholz,F., Henschel,R., Mueller,M.S., Nagel,W.E., Fava,E., Kalaidzidis,Y., and Zerial,M. (2010) Systems survey of endocytosis by multiparametric image analysis. *Nature*, **464**, 243-249.

Conde,C., Arias,C., Robin,M., Li,A., Saito,M., Chuang,J.Z., Nairn,A.C., Sung,C.H., and Caceres,A. (2010) Evidence for the involvement of Lfc and Tctex-1 in axon formation. *J Neurosci*, **30**, 6793-6800.

Corneveaux,J.J., Liang,W.S., Reiman,E.M., Webster,J.A., Myers,A.J., Zismann,V.L., Joshipura,K.D., Pearson,J.V., Hu-Lince,D., Craig,D.W., Stephan,D.A., et,al., and Huentelman,M.J. (2010) Evidence for an association between KIBRA and late-onset Alzheimer's disease. *Neurobiol Aging*, **31**, 901-909.

Courchesne,S.L., Pazyra-Murphy,M.F., Lee,D.J., and Segal,R.A. (2011) Neuromuscular junction defects in mice with mutation of dynein heavy chain 1. *PLoS One*, **6**, e16753.

Crawley,J.N. (2008) Behavioral phenotyping strategies for mutant mice. *Neuron*, **57**, 809-818.

Culver-Hanlon,T.L., Lex,S.A., Stephens,A.D., Quintyne,N.J., and King,S.J. (2006) A microtubule-binding domain in dynactin increases dynein processivity by skating along microtubules. *Nat Cell Biol*, **8**, 264-270.

Deacon,R.M. (2006a) Assessing nest building in mice. *Nat Protoc*, **1**, 1117-1119.

Deacon,R.M. (2006b) Burrowing in rodents: a sensitive method for detecting behavioral dysfunction. *Nat Protoc*, **1**, 118-121.

Deacon,R.M., Bannerman,D.M., Kirby,B.P., Croucher,A., and Rawlins,J.N. (2002) Effects of cytotoxic hippocampal lesions in mice on a cognitive test battery. *Behav Brain Res*, **133**, 57-68.

Deacon,R.M. and Rawlins,J.N. (2005) Hippocampal lesions, species-typical behaviours and anxiety in mice. *Behav Brain Res*, **156**, 241-249.

Dedesma,C., Chuang,J.Z., Alfinito,P.D., and Sung,C.H. (2006) Dynein light chain Tctex-1 identifies neural progenitors in adult brain. *J Comp Neurol*, **496**, 773-786.

Deinhardt,K. and Schiavo,G. (2005) Endocytosis and retrograde axonal traffic in motor neurons. *Biochem Soc Symp*, 139-150.

Deng,W., Garrett,C., Dombert,B., Soura,V., Banks,G., Fisher,E.M., van der Brug,M.P., and Hafezparast,M. (2010) Neurodegenerative mutation in cytoplasmic dynein alters its organization and dynein-dynactin and dynein-kinesin interactions. *J Biol Chem*, **285**, 39922-39934.

Detzer,A., Engel,C., Wunsche,W., and Sczakiel,G. (2011) Cell stress is related to re-localization of Argonaute 2 and to decreased RNA interference in human cells. *Nucleic Acids Res*, **39**, 2727-2741.

Deumens,R., Jaken,R.J., Marcus,M.A., and Joosten,E.A. (2007) The CatWalk gait analysis in assessment of both dynamic and static gait changes after adult rat sciatic nerve resection. *J Neurosci Methods*, **164**, 120-130.

Dewey,C.M., Cenik,B., Sephton,C.F., Dries,D.R., Mayer,P., III, Good,S.K., Johnson,B.A., Herz,J., and Yu,G. (2011) TDP-43 is directed to stress granules by sorbitol, a novel physiological osmotic and oxidative stressor. *Mol Cell Biol*, **31**, 1098-1108.

Dixon,K.T., Cearley,J.A., Hunter,J.M., and Detloff,P.J. (2004) Mouse Huntington's disease homolog mRNA levels: variation and allele effects. *Gene Expr*, **11**, 221-231.

Driskell,O.J., Mironov,A., Allan,V.J., and Woodman,P.G. (2007) Dynein is required for receptor sorting and the morphogenesis of early endosomes. *Nat Cell Biol*, **9**, 113-120.

Dupuis,L., Fergani,A., Braunstein,K.E., Eschbach,J., Holl,N., Rene,F., Gonzalez de Aguilar,J.L., Zoerner,B., Schwalenstocker,B., Ludolph,A.C., and Loeffler,J.P. (2009) Mice with a mutation in the dynein heavy chain 1 gene display sensory neuropathy but lack motor neuron disease. *Exp Neurol*, **215**, 146-152.

Edgar,R.C. (2004) MUSCLE: multiple sequence alignment with high accuracy and high throughput. *Nucleic Acids Res*, **32**, 1792-1797.

Eickholt,B.J., Ahmed,A.I., Davies,M., Papakonstanti,E.A., Pearce,W., Starkey,M.L., Bilancio,A., Need,A.C., Smith,A.J., et,al., and Vanhaesebroeck,B. (2007) Control of axonal growth and regeneration of sensory neurons by the p110delta PI 3-kinase. *PLoS One*, **2**, e869.

Eschbach,J. and Dupuis,L. (2011) Cytoplasmic dynein in neurodegeneration. *Pharmacol Ther*, **130**, 348-363.

Eschbach,J., Fergani,A., Oudart,H., Robin,J.P., Rene,F., Gonzalez de Aguilar,J.L., Larmet,Y., Zoll,J., Hafezparast,M., Schwalenstocker,B., Loeffler,J.P., Ludolph,A.C., and Dupuis,L. (2011) Mutations in cytoplasmic dynein lead to a Huntington's disease-like defect in energy metabolism of brown and white adipose tissues. *Biochim Biophys Acta*, **1812**, 59-69.

Espindola,F.S., Suter,D.M., Partata,L.B., Cao,T., Wolenski,J.S., Cheney,R.E., King,S.M., and Mooseker,M.S. (2000) The light chain composition of chicken brain myosin-Va: calmodulin, myosin-II essential light chains, and 8-kDa dynein light chain/PIN. *Cell Motil Cytoskeleton*, **47**, 269-281.

Favis,R., Sun,Y., van,d., V, Broderick,E., Levey,L., Meyers,M., Mulligan,G., Harousseau,J.L., Richardson,P.G., and Ricci,D.S. (2011) Genetic variation associated with bortezomib-induced peripheral neuropathy. *Pharmacogenet Genomics*, **21**, 121-129.

Fejtova,A., Davydova,D., Bischof,F., Lazarevic,V., Altrock,W.D., Romorini,S., Schone,C., Zuschratter,W., Kreutz,M.R., Garner,C.C., Ziv,N.E., and Gundelfinger,E.D. (2009) Dynein light chain regulates axonal trafficking and synaptic levels of Bassoon. *J Cell Biol*, **185**, 341-355.

Feng,B., Jiang,J., Kraus,P., Ng,J.H., Heng,J.C., Chan,Y.S., Yaw,L.P., Zhang,W., Loh,Y.H., et,al., and Ng,H.H. (2009) Reprogramming of fibroblasts into induced pluripotent stem cells with orphan nuclear receptor Esrrb. *Nat Cell Biol*, **11**, 197-203.

Ferdinandusse,S., Zomer,A.W., Komen,J.C., van den Brink,C.E., Thanos,M., Hamers,F.P., Wanders,R.J., van der Saag,P.T., Poll-The BT, and Brites,P. (2008) Ataxia with loss of Purkinje cells in a mouse model for Refsum disease. *Proc Natl Acad Sci U S A*, **105**, 17712-17717.

Finn,R.D., Mistry,J., Tate,J., Coggill,P., Heger,A., Pollington,J.E., Gavin,O.L., Gunasekaran,P., Ceric,G., Forslund,K., Holm,L., Sonnhammer,E.L., Eddy,S.R., and Bateman,A. (2010) The Pfam protein families database. *Nucleic Acids Res*, **38**, D211-D222.

Flavell,S.J., Hou,T.Z., Lax,S., Filer,A.D., Salmon,M., and Buckley,C.D. (2008) Fibroblasts as novel therapeutic targets in chronic inflammation. *Br J Pharmacol*, **153 Suppl 1**, S241-S246.

Fletcher,P.A., Scriven,D.R., Schulson,M.N., and Moore,E.D. (2010) Multi-image colocalization and its statistical significance. *Biophys J*, **99**, 1996-2005.

Friedman,R.C., Farh,K.K., Burge,C.B., and Bartel,D.P. (2009) Most mammalian mRNAs are conserved targets of microRNAs. *Genome Res*, **19**, 92-105.

Friocourt,G., Marcorelles,P., Saugier-Veber,P., Quille,M.L., Marret,S., and Laquerriere,A. (2011) Role of cytoskeletal abnormalities in the neuropathology and pathophysiology of type I lissencephaly. *Acta Neuropathol*, **121**, 149-170.

Fuhrmann,J.C., Kins,S., Rostaing,P., El,F.O., Kirsch,J., Sheng,M., Triller,A., Betz,H., and Kneussel,M. (2002) Gephyrin interacts with Dynein light chains 1 and 2, components of motor protein complexes. *J Neurosci*, **22**, 5393-5402.

Fujita,P.A., Rhead,B., Zweig,A.S., Hinrichs,A.S., Karolchik,D., Cline,M.S., Goldman,M., Barber,G.P., Clawson,H., Coelho,A., et,al., and Kent,W.J. (2011) The UCSC Genome Browser database: update 2011. *Nucleic Acids Res*, **39**, D876-D882.

Futter,C.E., Pearse,A., Hewlett,L.J., and Hopkins,C.R. (1996) Multivesicular endosomes containing internalized EGF-EGF receptor complexes mature and then fuse directly with lysosomes. *J Cell Biol*, **132**, 1011-1023.

Garcia-del,P.F. (2001) Salmonella intracellular proliferation: where, when and how? *Microbes Infect*, **3**, 1305-1311.

Garcia-del,P.F., Nunez-Hernandez,C., Eisman,B., and Ramos-Vivas,J. (2008) Growth control in the Salmonella-containing vacuole. *Curr Opin Microbiol*, **11**, 46-52.

Gates,H., Mallon,A.M., and Brown,S.D. (2010) High-throughput mouse phenotyping. *Methods*.

Gauthier,L.R., Charrin,B.C., Borrell-Pages,M., Dompierre,J.P., Rangone,H., Cordelieres,F.P., De Mey,J., MacDonald,M.E., Lessmann,V., Humbert,S., and Saudou,F. (2004) Huntingtin controls neurotrophic support and survival of neurons by enhancing BDNF vesicular transport along microtubules. *Cell*, **118**, 127-138.

Gauthier-Fisher,A., Lin,D.C., Greeve,M., Kaplan,D.R., Rottapel,R., and Miller,F.D. (2009) Lfc and Tctex-1 regulate the genesis of neurons from cortical precursor cells. *Nat Neurosci*, **12**, 735-744.

George,C.X., Wagner,M.V., and Samuel,C.E. (2005) Expression of interferon-inducible RNA adenosine deaminase ADAR1 during pathogen infection and mouse embryo development involves tissue-selective promoter utilization and alternative splicing. *J Biol Chem*, **280**, 15020-15028.

Grigoriev,I., Splinter,D., Keijzer,N., Wulf,P.S., Demmers,J., Ohtsuka,T., Modesti,M., Maly,I.V., Grosveld,F., Hoogenraad,C.C., and Akhmanova,A. (2007) Rab6 regulates transport and targeting of exocytotic carriers. *Dev Cell*, **13**, 305-314.

Grimson,A., Farh,K.K., Johnston,W.K., Garrett-Engele,P., Lim,L.P., and Bartel,D.P. (2007) MicroRNA targeting specificity in mammals: determinants beyond seed pairing. *Mol Cell*, **27**, 91-105.

Groszer,M., Keays,D.A., Deacon,R.M., de Bono,J.P., Prasad-Mulcare,S., Gaub,S., Baum,M.G., French,C.A., Nicod,J., et,al., and Fisher,S.E. (2008) Impaired synaptic plasticity and motor learning in mice with a point mutation implicated in human speech deficits. *Curr Biol*, **18**, 354-362.

Grubb,S.C., Maddatu,T.P., Bult,C.J., and Bogue,M.A. (2009) Mouse phenome database. *Nucleic Acids Res*, **37**, D720-D730.

Guignot,J., Caron,E., Beuzon,C., Bucci,C., Kagan,J., Roy,C., and Holden,D.W. (2004) Microtubule motors control membrane dynamics of Salmonella-containing vacuoles. *J Cell Sci*, **117**, 1033-1045.

Ha,J., Lo,K.W., Myers,K.R., Carr,T.M., Humsi,M.K., Rasoul,B.A., Segal,R.A., and Pfister,K.K. (2008) A neuron-specific cytoplasmic dynein isoform preferentially transports TrkB signaling endosomes. *J Cell Biol*, **181**, 1027-1039.

Hafezparast,M., Klocke,R., Ruhrberg,C., Marquardt,A., Ahmad-Annuar,A., Bowen,S., Lalli,G., Witherden,A.S., Hummerich,H., et,al., and Fisher,E.M. (2003) Mutations in dynein link motor neuron degeneration to defects in retrograde transport. *Science*, **300**, 808-812.

Hall,J., Karplus,P.A., and Barbar,E. (2009) Multivalency in the assembly of intrinsically disordered Dynein intermediate chain. *J Biol Chem*, **284**, 33115-33121.

Hall,J., Song,Y., Karplus,P.A., and Barbar,E. (2010) The crystal structure of dynein intermediate chain-light chain roadblock complex gives new insights into dynein assembly. *J Biol Chem*, **285**, 22566-22575.

Hamers,F.P., Lankhorst,A.J., van Laar,T.J., Veldhuis,W.B., and Gispen,W.H. (2001) Automated quantitative gait analysis during overground locomotion in the rat: its application to spinal cord contusion and transection injuries. *J Neurotrauma*, **18**, 187-201.

Harada,A., Takei,Y., Kanai,Y., Tanaka,Y., Nonaka,S., and Hirokawa,N. (1998) Golgi vesiculation and lysosome dispersion in cells lacking cytoplasmic dynein. *J Cell Biol*, **141**, 51-59.

Hardy,S., Legagneux,V., Audic,Y., and Paillard,L. (2010) Reverse genetics in eukaryotes. *Biol Cell*, **102**, 561-580.

Harrison,R.E., Brumell,J.H., Khandani,A., Bucci,C., Scott,C.C., Jiang,X., Finlay,B.B., and Grinstein,S. (2004) Salmonella impairs RILP recruitment to Rab7 during maturation of invasion vacuoles. *Mol Biol Cell*, **15**, 3146-3154.

Hehnly,H. and Stamnes,M. (2007) Regulating cytoskeleton-based vesicle motility. *FEBS Lett*, **581**, 2112-2118.

Hirokawa,N., Niwa,S., and Tanaka,Y. (2010) Molecular motors in neurons: transport mechanisms and roles in brain function, development, and disease. *Neuron*, **68**, 610-638.

Hogg,J.R. and Collins,K. (2008) Structured non-coding RNAs and the RNP Renaissance. *Curr Opin Chem Biol*, **12**, 684-689.

Holleran,E.A., Ligon,L.A., Tokito,M., Stankewich,M.C., Morrow,J.S., and Holzbaur,E.L. (2001) beta III spectrin binds to the Arp1 subunit of dynactin. *J Biol Chem*, **276**, 36598-36605.

Hook,P. and Vallee,R.B. (2006) The dynein family at a glance. *J Cell Sci*, **119**, 4369-4371.

Horgan,C.P., Hanscom,S.R., Jolly,R.S., Futter,C.E., and McCaffrey,M.W. (2010a) Rab11-FIP3 binds dynein light intermediate chain 2 and its overexpression fragments the Golgi complex. *Biochem Biophys Res Commun*, **394**, 387-392.

Horgan,C.P., Hanscom,S.R., Jolly,R.S., Futter,C.E., and McCaffrey,M.W. (2010b) Rab11-FIP3 links the Rab11 GTPase and cytoplasmic dynein to mediate transport to the endosomal-recycling compartment. *J Cell Sci*, **123**, 181-191.

Hu,G. (1993) DNA polymerase-catalyzed addition of nontemplated extra nucleotides to the 3' end of a DNA fragment. *DNA Cell Biol*, **12**, 763-770.

Hutagalung,A.H. and Novick,P.J. (2011) Role of Rab GTPases in membrane traffic and cell physiology. *Physiol Rev*, **91**, 119-149.

Ikeda,K., Zhapparova,O., Brodsky,I., Semenova,I., Tirnauer,J.S., Zaliapin,I., and Rodionov,V. (2011) CK1 activates minus-end-directed transport of membrane organelles along microtubules. *Mol Biol Cell*, **22**, 1321-1329.

Ilangovan,U., Ding,W., Zhong,Y., Wilson,C.L., Groppe,J.C., Trbovich,J.T., Zuniga,J., Demeler,B., Tang,Q., Gao,G., Mulder,K.M., and Hinck,A.P. (2005) Structure and dynamics of the homodimeric dynein light chain km23. *J Mol Biol*, **352**, 338-354.

Jhuang,H., Garrote,E., Yu,X., Khilnani,V., Poggio,T., Steele,A.D., and Serre,T. (2010) Automated home-cage behavioural phenotyping of mice. *Nat Commun*, **1**.

Jin,Q., Gao,G., and Mulder,K.M. (2009) Requirement of a dynein light chain in TGFbeta/Smad3 signaling. *J Cell Physiol*, **221**, 707-715.

Johannes,L. and Popoff,V. (2008) Tracing the retrograde route in protein trafficking. *Cell*, **135**, 1175-1187.

Jordens,I., Fernandez-Borja,M., Marsman,M., Dusseljee,S., Janssen,L., Calafat,J., Janssen,H., Wubbolts,R., and Neefjes,J. (2001) The Rab7 effector protein RILP controls lysosomal transport by inducing the recruitment of dynein-dynactin motors. *Curr Biol*, **11**, 1680-1685.

Kan,Z., Garrett-Engele,P.W., Johnson,J.M., and Castle,J.C. (2005) Evolutionarily conserved and diverged alternative splicing events show different expression and functional profiles. *Nucleic Acids Res*, **33**, 5659-5666.

Kapitein,L.C., Schlager,M.A., Kuijpers,M., Wulf,P.S., van Spronsen,M., MacKintosh,F.C., and Hoogenraad,C.C. (2010) Mixed microtubules steer dynein-driven cargo transport into dendrites. *Curr Biol*, **20**, 290-299.

Karp,N.A., Baker,L.A., Gerdin,A.K., Adams,N.C., Ramirez-Solis,R., and White,J.K. (2010) Optimising experimental design for high-throughput phenotyping in mice: a case study. *Mamm Genome*, **21**, 467-476.

Kashuba,E., Pavan,Y.S., Deoram,D.S., Yurchenko,M., Kashuba,V., Klein,G., and Szekely,L. (2009) MRPS18-2 protein immortalizes primary rat embryonic fibroblasts and endows them with stem cell-like properties. *Proc Natl Acad Sci U S A*, **106**, 19866-19871.

Keays,D.A., Clark,T.G., and Flint,J. (2006) Estimating the number of coding mutations in genotypic- and phenotypic-driven N-ethyl-N-nitrosourea (ENU) screens. *Mamm Genome*, **17**, 230-238.

Kedersha,N. and Anderson,P. (2007) Mammalian stress granules and processing bodies. *Methods Enzymol*, **431**, 61-81.

Kent,W.J., Sugnet,C.W., Furey,T.S., Roskin,K.M., Pringle,T.H., Zahler,A.M., and Haussler,D. (2002) The human genome browser at UCSC. *Genome Res*, **12**, 996-1006.

Keren,H., Lev-Maor,G., and Ast,G. (2010) Alternative splicing and evolution: diversification, exon definition and function. *Nat Rev Genet*, **11**, 345-355.

Kieran,D., Hafezparast,M., Bohnert,S., Dick,J.R., Martin,J., Schiavo,G., Fisher,E.M., and Greensmith,L. (2005) A mutation in dynein rescues axonal transport defects and extends the life span of ALS mice. *J Cell Biol*, **169**, 561-567.

Kimura,K., Wakamatsu,A., Suzuki,Y., Ota,T., Nishikawa,T., Yamashita,R., Yamamoto,J., Sekine,M., Tsuritani,K., Wakaguri,H., et,al., and Sugano,S. (2006) Diversification of transcriptional modulation: large-scale identification and characterization of putative alternative promoters of human genes. *Genome Res*, **16**, 55-65.

King,S.J., Bonilla,M., Rodgers,M.E., and Schroer,T.A. (2002) Subunit organization in cytoplasmic dynein subcomplexes. *Protein Sci*, **11**, 1239-1250.

King,S.J., Brown,C.L., Maier,K.C., Quintyne,N.J., and Schroer,T.A. (2003) Analysis of the dynein-dynactin interaction in vitro and in vivo. *Mol Biol Cell*, **14**, 5089-5097.

Kolasinska-Zwierz,P., Down,T., Latorre,I., Liu,T., Liu,X.S., and Ahringer,J. (2009) Differential chromatin marking of introns and expressed exons by H3K36me3. *Nat Genet*, **41**, 376-381.

Koren,E., Lev-Maor,G., and Ast,G. (2007) The emergence of alternative 3' and 5' splice site exons from constitutive exons. *PLoS Comput Biol*, **3**, e95.

Kuhle,V., Abrahams,G.L., and Hensel,M. (2006) Intracellular Salmonella enterica redirect exocytic transport processes in a Salmonella pathogenicity island 2-dependent manner. *Traffic*, **7**, 716-730.

Kumar,P., Henikoff,S., and Ng,P.C. (2009) Predicting the effects of coding non-synonymous variants on protein function using the SIFT algorithm. *Nat Protoc*, **4**, 1073-1081.

Kuta,A., Deng,W., Morsi El-Kadi,A., Banks,G.T., Hafezparast,M., Pfister,K.K., and Fisher,E.M. (2010) Mouse cytoplasmic dynein intermediate chains: identification of new isoforms, alternative splicing and tissue distribution of transcripts. *PLoS One*, **5**, e11682.

Lai,C., Lin,X., Chandran,J., Shim,H., Yang,W.J., and Cai,H. (2007) The G59S mutation in p150(glued) causes dysfunction of dynactin in mice. *J Neurosci*, **27**, 13982-13990.

Lai,M., Wang,F., Rohan,J.G., Maeno-Hikichi,Y., Chen,Y., Zhou,Y., Gao,G., Sather,W.A., and Zhang,J.F. (2005) A Tctex1-Ca^{2+} channel complex for selective surface expression of Ca^{2+} channels in neurons. *Nat Neurosci*, **8**, 435-442.

Laird,F.M., Farah,M.H., Ackerley,S., Hoke,A., Maragakis,N., Rothstein,J.D., Griffin,J., Price,D.L., Martin,L.J., and Wong,P.C. (2008) Motor neuron disease occurring in a mutant dynactin mouse model is characterized by defects in vesicular trafficking. *J Neurosci*, **28**, 1997-2005.

Lalonde,R., Dumont,M., Paly,E., London,J., and Strazielle,C. (2004) Characterization of hemizygous SOD1/wild-type transgenic mice with the SHIRPA primary screen and tests of sensorimotor function and anxiety. *Brain Res Bull*, **64**, 251-258.

Lam,C., Vergnolle,M.A., Thorpe,L., Woodman,P.G., and Allan,V.J. (2010) Functional interplay between LIS1, NDE1 and NDEL1 in dynein-dependent organelle positioning. *J Cell Sci*, **123**, 202-212.

LaMonte,B.H., Wallace,K.E., Holloway,B.A., Shelly,S.S., Ascano,J., Tokito,M., Van,W.T., Howland,D.S., and Holzbaur,E.L. (2002) Disruption of dynein/dynactin inhibits axonal transport in motor neurons causing late-onset progressive degeneration. *Neuron*, **34**, 715-727.

Landmann,L. and Marbet,P. (2004) Colocalization analysis yields superior results after image restoration. *Microsc Res Tech*, **64**, 103-112.

Lane,J.D., Lucocq,J., Pryde,J., Barr,F.A., Woodman,P.G., Allan,V.J., and Lowe,M. (2002) Caspase-mediated cleavage of the stacking protein GRASP65 is required for Golgi fragmentation during apoptosis. *J Cell Biol*, **156**, 495-509.

Lewis,B.P., Burge,C.B., and Bartel,D.P. (2005) Conserved seed pairing, often flanked by adenosines, indicates that thousands of human genes are microRNA targets. *Cell*, **120**, 15-20.

Li,Q., Lee,J.A., and Black,D.L. (2007) Neuronal regulation of alternative pre-mRNA splicing. *Nat Rev Neurosci*, **8**, 819-831.

Li,Z., Wolff,K.C., and Samuel,C.E. (2010) RNA adenosine deaminase ADAR1 deficiency leads to increased activation of protein kinase PKR and reduced vesicular stomatitis virus growth following interferon treatment. *Virology*, **396**, 316-322.

Liu,Y., Bourgeois,C.F., Pang,S., Kudla,M., Dreumont,N., Kister,L., Sun,Y.H., Stevenin,J., and Elliott,D.J. (2009) The germ cell nuclear proteins hnRNP G-T and RBMY activate a testis-specific exon. *PLoS Genet*, **5**, e1000707.

Livingstone,C.D. and Barton,G.J. (1993) Protein sequence alignments: a strategy for the hierarchical analysis of residue conservation. *Comput Appl Biosci*, **9**, 745-756.

Lo,K.W., Kogoy,J.M., and Pfister,K.K. (2007a) The DYNLT3 light chain directly links cytoplasmic dynein to a spindle checkpoint protein, Bub3. *J Biol Chem*, **282**, 11205-11212.

Lo,K.W., Kogoy,J.M., Rasoul,B.A., King,S.M., and Pfister,K.K. (2007b) Interaction of the DYNLT (TCTEX1/RP3) light chains and the intermediate chains reveals novel intersubunit regulation during assembly of the dynein complex. *J Biol Chem*, **282**, 36871-36878.

Loschi,M., Leishman,C.C., Berardone,N., and Boccaccio,G.L. (2009) Dynein and kinesin regulate stress-granule and P-body dynamics. *J Cell Sci*, **122**, 3973-3982.

Louro,R., Smirnova,A.S., and Verjovski-Almeida,S. (2009) Long intronic noncoding RNA transcription: expression noise or expression choice? *Genomics*, **93**, 291-298.

Lu,W., Han,D.S., Yuan,J., and Andrieu,J.M. (1994) Multi-target PCR analysis by capillary electrophoresis and laser-induced fluorescence. *Nature*, **368**, 269-271.

Mallon,A.M., Blake,A., and Hancock,J.M. (2008) EuroPhenome and EMPReSS: online mouse phenotyping resource. *Nucleic Acids Res*, **36**, D715-D718.

Mandillo,S., Tucci,V., Holter,S.M., Meziane,H., Banchaabouchi,M.A., Kallnik,M., Lad,H.V., Nolan,P.M., Ouagazzal,A.M., et,al., and Wurst,W. (2008) Reliability, robustness, and reproducibility in mouse behavioral phenotyping: a cross-laboratory study. *Physiol Genomics*, **34**, 243-255.

Marsman,M., Jordens,I., Kuijl,C., Janssen,L., and Neefjes,J. (2004) Dynein-mediated vesicle transport controls intracellular Salmonella replication. *Mol Biol Cell*, **15**, 2954-2964.

Martinez-Moya,M., de Pedro,M.A., Schwarz,H., and Garcia-del,P.F. (1998) Inhibition of Salmonella intracellular proliferation by non-phagocytic eucaryotic cells. *Res Microbiol*, **149**, 309-318.

Mattsson,B., Sorensen,J.C., Zimmer,J., and Johansson,B.B. (1997) Neural grafting to experimental neocortical infarcts improves behavioral outcome and reduces thalamic atrophy in rats housed in enriched but not in standard environments. *Stroke*, **28**, 1225-1231.

Maunakea,A.K., Nagarajan,R.P., Bilenky,M., Ballinger,T.J., D'Souza,C., Fouse,S.D., Johnson,B.E., Hong,C., Nielsen,C., Zhao,Y., et,al., and Costello,J.F. (2010) Conserved role of intragenic DNA methylation in regulating alternative promoters. *Nature*, **466**, 253-257.

McEwen,E., Kedersha,N., Song,B., Scheuner,D., Gilks,N., Han,A., Chen,J.J., Anderson,P., and Kaufman,R.J. (2005) Heme-regulated inhibitor kinase-mediated phosphorylation of eukaryotic translation initiation factor 2 inhibits translation, induces stress granule formation, and mediates survival upon arsenite exposure. *J.Biol.Chem.,* **280(17)**, 16925-16933.

McDonald,K.K., Aulas,A., Destroismaisons,L., Pickles,S., Beleac,E., Camu,W., Rouleau,G.A., and Vande,V.C. (2011) TAR DNA-binding protein 43 (TDP-43) regulates stress granule dynamics via differential regulation of G3BP and TIA-1. *Hum Mol Genet*, **20**, 1400-1410.

Meiri,D., Greeve,M.A., Brunet,A., Finan,D., Wells,C.D., LaRose,J., and Rottapel,R. (2009) Modulation of Rho guanine exchange factor Lfc activity by protein kinase A-mediated phosphorylation. *Mol Cell Biol*, **29**, 5963-5973.

Modrek,B. and Lee,C.J. (2003) Alternative splicing in the human, mouse and rat genomes is associated with an increased frequency of exon creation and/or loss. *Nat Genet*, **34**, 177-180.

Mota,L.J., Ramsden,A.E., Liu,M., Castle,J.D., and Holden,D.W. (2009) SCAMP3 is a component of the Salmonella-induced tubular network and reveals an interaction between bacterial effectors and post-Golgi trafficking. *Cell Microbiol*, **11**, 1236-1253.

Motulsky,H. and Christopoulos,A. (2004) *Fitting models to biological data using linear and nonlinear regression: A practical guide to curve fitting*. Oxford University Press, 198 Madison Avenue, New York, NY, 10016, USA, 1-351 pp.

Munch,C., Sedlmeier,R., Meyer,T., Homberg,V., Sperfeld,A.D., Kurt,A., Prudlo,J., Peraus,G., Hanemann,C.O., Stumm,G., and Ludolph,A.C. (2004) Point mutations of the p150 subunit of dynactin (DCTN1) gene in ALS. *Neurology*, **63**, 724-726.

Myers,K.R., Lo,K.W., Lye,R.J., Kogoy,J.M., Soura,V., Hafezparast,M., and Pfister,K.K. (2007) Intermediate chain subunit as a probe for cytoplasmic dynein function: biochemical analyses and live cell imaging in PC12 cells. *J Neurosci Res*, **85**, 2640-2647.

Nguyen,D. and Xu,T. (2008) The expanding role of mouse genetics for understanding human biology and disease. *Dis Model Mech*, **1**, 56-66.

Nolan,P.M. (2000) Generation of mouse mutants as a tool for functional genomics. *Pharmacogenomics*, **1**, 243-255.

Nolan,P.M., Hugill,A., and Cox,R.D. (2002) ENU mutagenesis in the mouse: application to human genetic disease. *Brief Funct Genomic Proteomic*, **1**, 278-289.

Nolan,P.M., Peters,J., Strivens,M., Rogers,D., Hagan,J., Spurr,N., Gray,I.C., Vizor,L., Brooker,D., et,al., and Hunter,J. (2000) A systematic, genome-wide, phenotype-driven mutagenesis programme for gene function studies in the mouse. *Nat Genet*, **25**, 440-443.

Nurminsky,D.I., Nurminskaya,M.V., Benevolenskaya,E.V., Shevelyov,Y.Y., Hartl,D.L., and Gvozdev,V.A. (1998) Cytoplasmic dynein intermediate-chain isoforms with different targeting properties created by tissue-specific alternative splicing. *Mol Cell Biol*, **18**, 6816-6825.

Nyarko,A. and Barbar,E. (2011) Light chain-dependent self-association of dynein intermediate chain. *J Biol Chem*, **286**, 1556-1566.

Odell,A., Askham,J., Whibley,C., and Hollstein,M. (2010) How to become immortal: let MEFs count the ways. *Aging (Albany NY)*, **2**, 160-165.

Ohtsuka,M., Ogiwara,S., Miura,H., Mizutani,A., Warita,T., Sato,M., Imai,K., Hozumi,K., Sato,T., Tanaka,M., Kimura,M., and Inoko,H. (2010) Pronuclear injection-based mouse targeted transgenesis for reproducible and highly efficient transgene expression. *Nucleic Acids Res*, **38**, e198.

Okada,M., Sakai,T., Nakamura,T., Tamamori-Adachi,M., Kitajima,S., Matsuki,Y., Watanabe,E., Hiramatsu,R., Sakaue,H., and Kasuga,M. (2009) Skp2 promotes adipocyte differentiation via a p27Kip1-independent mechanism in primary mouse embryonic fibroblasts. *Biochem Biophys Res Commun*, **379**, 249-254.

Ori-McKenney,K.M., Xu,J., Gross,S.P., and Vallee,R.B. (2010) A cytoplasmic dynein tail mutation impairs motor processivity. *Nat Cell Biol*, **12**, 1228-1234.

Palmer,K.J., Hughes,H., and Stephens,D.J. (2009) Specificity of cytoplasmic dynein subunits in discrete membrane-trafficking steps. *Mol Biol Cell*, **20**, 2885-2899.

Pan,Q., Yu,Y., Chen,Q., Li,C., Wu,H., Wan,Y., Ma,J., and Sun,F. (2008) Sox9, a key transcription factor of bone morphogenetic protein-2-induced chondrogenesis, is activated through BMP pathway and a CCAAT box in the proximal promoter. *J Cell Physiol*, **217**, 228-241.

Pavlos,N.J., Cheng,T.S., Qin,A., Ng,P.Y., Feng,H.T., Ang,E.S., Carrello,A., Sung,C.H., Jahn,R., Zheng,M.H., and Xu,J. (2011) Tctex-1, a novel interaction partner of Rab3D, is required for osteoclastic bone resorption. *Mol Cell Biol*, **31**, 1551-1564.

Perlson,E., Jeong,G.B., Ross,J.L., Dixit,R., Wallace,K.E., Kalb,R.G., and Holzbaur,E.L. (2009) A switch in retrograde signaling from survival to stress in rapid-onset neurodegeneration. *J Neurosci*, **29**, 9903-9917.

Persico,A., Cervigni,R.I., Barretta,M.L., and Colanzi,A. (2009) Mitotic inheritance of the Golgi complex. *FEBS Lett*, **583**, 3857-3862.

Pfannkuche,K., Neuss,S., Pillekamp,F., Frenzel,L.P., Attia,W., Hannes,T., Salber,J., Hoss,M., Zenke,M., Fleischmann,B.K., Hescheler,J., and Saric,T. (2010) Fibroblasts facilitate the engraftment of embryonic stem cell-derived cardiomyocytes on three-dimensional collagen matrices and aggregation in hanging drops. *Stem Cells Dev*, **19**, 1589-1599.

Pfister,K.K., Shah,P.R., Hummerich,H., Russ,A., Cotton,J., Annuar,A.A., King,S.M., and Fisher,E.M. (2006) Genetic analysis of the cytoplasmic dynein subunit families. *PLoS Genet*, **2**, e1.

Piriyapongsa,J., Rutledge,M.T., Patel,S., Borodovsky,M., and Jordan,I.K. (2007) Evaluating the protein coding potential of exonized transposable element sequences. *Biol Direct*, **2**, 31.

Poh,J., Odendall,C., Spanos,A., Boyle,C., Liu,M., Freemont,P., and Holden,D.W. (2008) SteC is a Salmonella kinase required for SPI-2-dependent F-actin remodelling. *Cell Microbiol*, **10**, 20-30.

Potter,M., Yuan,C., Ottenritter,C., Mughal,M., and van,P.H. (2010) Exercise is not beneficial and may accelerate symptom onset in a mouse model of Huntington's disease. *PLoS Curr*, **2**, RRN1201.

Prostko,C.R., Dholakia,J.N., Brostrom,M.A., and Brostrom,C.O. (1995) Activation of the double-stranded RNA-regulated protein kinase by depletion of endoplasmic reticular calcium stores. *J Biol Chem*, **270**, 6211-6215.

Puls,I., Jonnakuty,C., LaMonte,B.H., Holzbaur,E.L., Tokito,M., Mann,E., Floeter,M.K., Bidus,K., Drayna,D., Oh,S.J., Brown,R.H., Jr., Ludlow,C.L., and Fischbeck,K.H. (2003) Mutant dynactin in motor neuron disease. *Nat Genet*, **33**, 455-456.

Quwailid,M.M., Hugill,A., Dear,N., Vizor,L., Wells,S., Horner,E., Fuller,S., Weedon,J., McMath,H., Woodman,P., et,al., and Cox,R.D. (2004) A gene-driven ENU-based approach to generating an allelic series in any gene. *Mamm Genome*, **15**, 585-591.

Radtke,A.L., Delbridge,L.M., Balachandran,S., Barber,G.N., and O'Riordan,M.X. (2007) TBK1 protects vacuolar integrity during intracellular bacterial infection. *PLoS Pathog*, **3**, e29.

Ramsden,A.E., Holden,D.W., and Mota,L.J. (2007a) Membrane dynamics and spatial distribution of Salmonella-containing vacuoles. *Trends Microbiol*, **15**, 516-524.

Ramsden,A.E., Mota,L.J., Munter,S., Shorte,S.L., and Holden,D.W. (2007b) The SPI-2 type III secretion system restricts motility of Salmonella-containing vacuoles. *Cell Microbiol*, **9**, 2517-2529.

Raney,B.J., Cline,M.S., Rosenbloom,K.R., Dreszer,T.R., Learned,K., Barber,G.P., Meyer,L.R., Sloan,C.A., Malladi,V.S., Roskin,K.M., et,al., and Kent,W.J. (2011) ENCODE whole-genome data in the UCSC genome browser (2011 update). *Nucleic Acids Res*, **39**, D871-D875.

Resch,A., Xing,Y., Alekseyenko,A., Modrek,B., and Lee,C. (2004) Evidence for a subpopulation of conserved alternative splicing events under selection pressure for protein reading frame preservation. *Nucleic Acids Res*, **32**, 1261-1269.

Reznikoff,C.A., Brankow,D.W., and Heidelberger,C. (1973) Establishment and characterization of a cloned line of C3H mouse embryo cells sensitive to postconfluence inhibition of division. *Cancer Res*, **33**, 3231-3238.

Richards M.P. (2005) Polymerase Chain Reaction Products: Analysis Using Capillary Electrophoresis. In: *Encyclopedia of chromatography* (Ed. Cazes J.), pp. 1318-1322. Taylor & Francis Group, Boca Raton, FL.

Rink,J., Ghigo,E., Kalaidzidis,Y., and Zerial,M. (2005) Rab conversion as a mechanism of progression from early to late endosomes. *Cell*, **122**, 735-749.

Rogers,D.C., Fisher,E.M., Brown,S.D., Peters,J., Hunter,A.J., and Martin,J.E. (1997) Behavioral and functional analysis of mouse phenotype: SHIRPA, a proposed protocol for comprehensive phenotype assessment. *Mamm Genome*, **8**, 711-713.

Rogers,D.C., Peters,J., Martin,J.E., Ball,S., Nicholson,S.J., Witherden,A.S., Hafezparast,M., Latcham,J., Robinson,T.L., Quilter,C.A., and Fisher,E.M. (2001) SHIRPA, a protocol for behavioral assessment: validation for longitudinal study of neurological dysfunction in mice. *Neurosci Lett*, **306**, 89-92.

Roghi,C. and Allan,V.J. (1999) Dynamic association of cytoplasmic dynein heavy chain 1a with the Golgi apparatus and intermediate compartment. *J Cell Sci*, **112 (Pt 24)**, 4673-4685.

Ron,D. and Walter,P. (2007) Signal integration in the endoplasmic reticulum unfolded protein response. *Nat Rev Mol Cell Biol*, **8**, 519-529.

Roy,M., Kim,N., Xing,Y., and Lee,C. (2008) The effect of intron length on exon creation ratios during the evolution of mammalian genomes. *RNA*, **14**, 2261-2273.

Rozeske,R.R., Greenwood,B.N., Fleshner,M., Watkins,L.R., and Maier,S.F. (2011) Voluntary wheel running produces resistance to inescapable stress-induced potentiation of morphine conditioned place preference. *Behav Brain Res*, **219**, 378-381.

Salazar,D.L., Uchida,N., Hamers,F.P., Cummings,B.J., and Anderson,A.J. (2010) Human neural stem cells differentiate and promote locomotor recovery in an early chronic spinal cord injury NOD-scid mouse model. *PLoS One*, **5**, e12272.

Sanderson,D.J. and Bannerman,D.M. (2010) The role of habituation in hippocampus-dependent spatial working memory tasks: Evidence from GluA1 AMPA receptor subunit knockout mice. *Hippocampus*, **21**, n/a

Sanderson,D.J., Good,M.A., Skelton,K., Sprengel,R., Seeburg,P.H., Rawlins,J.N., and Bannerman,D.M. (2009) Enhanced long-term and impaired short-term spatial memory in GluA1 AMPA receptor subunit knockout mice: evidence for a dual-process memory model. *Learn Mem*, **16**, 379-386.

Sartori,C.R., Vieira,A.S., Ferrari,E.M., Langone,F., Tongiorgi,E., and Parada,C.A. (2011) The antidepressive effect of the physical exercise correlates with increased levels of mature BDNF, and proBDNF proteolytic cleavage-related genes, p11 and tPA. *Neuroscience*, **180**, 9-18.

Schmidt-Glenewinkel,H., Reinz,E., Eils,R., and Brady,N.R. (2009) Systems biological analysis of epidermal growth factor receptor internalization dynamics for altered receptor levels. *J Biol Chem*, **284**, 17243-17252.

Schmitt,I., Bachner,D., Megow,D., Henklein,P., Hameister,H., Epplen,J.T., and Riess,O. (1995) Expression of the Huntington disease gene in rodents: cloning the rat homologue and evidence for downregulation in non-neuronal tissues during development. *Hum Mol Genet*, **4**, 1173-1182.

Schroeter,A., Walzik,S., Blechschmidt,S., Haufe,V., Benndorf,K., and Zimmer,T. (2010) Structure and function of splice variants of the cardiac voltage-gated sodium channel Na(v)1.5. *J Mol Cell Cardiol*, **49**, 16-24.

Schuster,M., Kilaru,S., Ashwin,P., Lin,C., Severs,N.J., and Steinberg,G. (2011) Controlled and stochastic retention concentrates dynein at microtubule ends to keep endosomes on track. *EMBO J*, **30**, 652-664.

Sena-Esteves,M., Saeki,Y., Camp,S.M., Chiocca,E.A., and Breakefield,X.O. (1999) Single-step conversion of cells to retrovirus vector producers with herpes simplex virus-Epstein-Barr virus hybrid amplicons. *J Virol*, **73**, 10426-10439.

Sheng,D., Qu,D., Kwok,K.H., Ng,S.S., Lim,A.Y., Aw,S.S., Lee,C.W., Sung,W.K., Tan,E.K., Lufkin,T., Jesuthasan,S., Sinnakaruppan,M., and Liu,J. (2010) Deletion of the WD40 domain of LRRK2 in Zebrafish causes Parkinsonism-like loss of neurons and locomotive defect. *PLoS Genet*, **6**, e1000914.

Shilyansky,C., Karlsgodt,K.H., Cummings,D.M., Sidiropoulou,K., Hardt,M., James,A.S., Ehninger,D., Bearden,C.E., Poirazi,P., et,al., and Silva,A.J. (2010) Neurofibromin regulates corticostriatal inhibitory networks during working memory performance. *Proc Natl Acad Sci U S A*, **107**, 13141-13146.

Silverman,J.L., Yang,M., Lord,C., and Crawley,J.N. (2010) Behavioural phenotyping assays for mouse models of autism. *Nat Rev Neurosci*, **11**, 490-502.

Smit,A.F. (1993) Identification of a new, abundant superfamily of mammalian LTR-transposons. *Nucleic Acids Res*, **21**, 1863-1872.

Solberg,L.C., Valdar,W., Gauguier,D., Nunez,G., Taylor,A., Burnett,S., Arboledas-Hita,C., Hernandez-Pliego,P., Davidson,S., et,al., and Flint,J. (2006) A protocol for high-throughput phenotyping, suitable for quantitative trait analysis in mice. *Mamm Genome*, **17**, 129-146.

Sorkin,A. and Duex,J.E. (2010) Quantitative analysis of endocytosis and turnover of epidermal growth factor (EGF) and EGF receptor. *Curr Protoc Cell Biol*, **Chapter 15**, Unit.15.14

Spano,S. and Galan,J.E. (2008) A novel pathway for exotoxin delivery by an intracellular pathogen. *Curr Opin Microbiol*, **11**, 15-20.

Spudich,J.A. (2011) Biochemistry. Molecular motors, beauty in complexity. *Science*, **331**, 1143-1144.

Stenmark,H. (2009) Rab GTPases as coordinators of vesicle traffic. *Nat Rev Mol Cell Biol*, **10**, 513-525.

Stirnimann,C.U., Petsalaki,E., Russell,R.B., and Muller,C.W. (2010) WD40 proteins propel cellular networks. *Trends Biochem Sci*, **35**, 565-574.

Sugnet,C.W., Kent,W.J., Ares,M., Jr., and Haussler,D. (2004) Transcriptome and genome conservation of alternative splicing events in humans and mice. *Pac Symp Biocomput*, 66-77.

Sun,F., Pan,Q., Wang,J., Liu,S., Li,Z., and Yu,Y. (2009) Contrary Effects of BMP-2 and ATRA on Adipogenesis in Mouse Mesenchymal Fibroblasts. *Biochem Genet*, **47**, 789-801

Tai,A.W., Chuang,J.Z., Bode,C., Wolfrum,U., and Sung,C.H. (1999) Rhodopsin's carboxy-terminal cytoplasmic tail acts as a membrane receptor for cytoplasmic dynein by binding to the dynein light chain Tctex-1. *Cell*, **97**, 877-887.

Tan,S.C., Scherer,J., and Vallee,R.B. (2011) Recruitment of dynein to late endosomes and lysosomes through light intermediate chains. *Mol Biol Cell*, **22**, 467-477.

Tanaka,C., Ito,S., Nishio,N., Kodera,Y., Sakurai,H., Suzuki,H., Nakao,A., and Isobe,K. (2010) GADD34 suppresses wound healing by upregulating expression of myosin IIA. *Transgenic Res*, **19**, 637-645.

Tao,S. and Sampath,K. (2010) Alternative splicing of SMADs in differentiation and tissue homeostasis. *Dev Growth Differ*, **52**, 335-342.

Thomas,M.G., Loschi,M., Desbats,M.A., and Boccaccio,G.L. (2011) RNA granules: the good, the bad and the ugly. *Cell Signal*, **23**, 324-334.

Todaro,G.J. and Green,H. (1963) Quantitative studies of the growth of mouse embryo cells in culture and their development into established lines. *J Cell Biol*, **17**, 299-313.

Torok,N., Urrutia,R., Nakamura,T., and McNiven,M.A. (1996) Upregulation of molecular motor-encoding genes during hepatocyte growth factor- and epidermal growth factor-induced cell motility. *J Cell Physiol*, **167**, 422-433.

Traer,C.J., Rutherford,A.C., Palmer,K.J., Wassmer,T., Oakley,J., Attar,N., Carlton,J.G., Kremerskothen,J., Stephens,D.J., and Cullen,P.J. (2007) SNX4 coordinates endosomal sorting of TfnR with dynein-mediated transport into the endocytic recycling compartment. *Nat Cell Biol*, **9**, 1370-1380.

Tsai,N.P., Tsui,Y.C., and Wei,L.N. (2009) Dynein motor contributes to stress granule dynamics in primary neurons. *Neuroscience*, **159**, 647-656.

Tucci,V., Achilli,F., Blanco,G., Lad,H.V., Wells,S., Godinho,S., and Nolan,P.M. (2007) Reaching and grasping phenotypes in the mouse (Mus musculus): a characterization of inbred strains and mutant lines. *Neuroscience*, **147**, 573-582.

Turner,J.D., Alt,S.R., Cao,L., Vernocchi,S., Trifonova,S., Battello,N., and Muller,C.P. (2010) Transcriptional control of the glucocorticoid receptor: CpG islands, epigenetics and more. *Biochem Pharmacol*, **80**, 1860-1868.

Tynan,S.H., Purohit,A., Doxsey,S.J., and Vallee,R.B. (2000) Light intermediate chain 1 defines a functional subfraction of cytoplasmic dynein which binds to pericentrin. *J Biol Chem*, **275**, 32763-32768.

Upchurch,M. and Schallert,T. (1983) A behavior analysis of the offspring of "haloperidol-sensitive" and "haloperidol-resistant" gerbils. *Behav Neural Biol*, **39**, 221-228.

Vadlamudi,R.K., Bagheri-Yarmand,R., Yang,Z., Balasenthil,S., Nguyen,D., Sahin,A.A., den Hollander,P., and Kumar,R. (2004) Dynein light chain 1, a p21-activated kinase 1-interacting substrate, promotes cancerous phenotypes. *Cancer Cell*, **5**, 575-585.

Vaisberg,E.A., Grissom,P.M., and McIntosh,J.R. (1996) Mammalian cells express three distinct dynein heavy chains that are localized to different cytoplasmic organelles. *J Cell Biol*, **133**, 831-842.

Valadkhan,S. and Jaladat,Y. (2010) The spliceosomal proteome: at the heart of the largest cellular ribonucleoprotein machine. *Proteomics*, **10**, 4128-4141.

Vale,R.D. (2003) The molecular motor toolbox for intracellular transport. *Cell*, **112**, 467-480.

Vaughan,K.T. (2005) Microtubule plus ends, motors, and traffic of Golgi membranes. *Biochim Biophys Acta*, **1744**, 316-324.

Vaughan,P.S., Leszyk,J.D., and Vaughan,K.T. (2001) Cytoplasmic dynein intermediate chain phosphorylation regulates binding to dynactin. *J Biol Chem*, **276**, 26171-26179.

Ventura-Lima,J., Bogo,M.R., and Monserrat,J.M. (2011) Arsenic toxicity in mammals and aquatic animals: a comparative biochemical approach. *Ecotoxicol Environ Saf*, **74**, 211-218.

Vinke,F.P., Grieve,A.G., and Rabouille,C. (2011) The multiple facets of the Golgi reassembly stacking proteins. *Biochem J*, **433**, 423-433.

Vokes,M.S. and Carpenter,A.E. (2008) Using CellProfiler for automatic identification and measurement of biological objects in images. *Curr Protoc Mol Biol*, **Chapter 14**, Unit 14.17.

vom Brocke J., Schmeiser,H.H., Reinbold,M., and Hollstein,M. (2006) MEF immortalization to investigate the ins and outs of mutagenesis. *Carcinogenesis*, **27**, 2141-2147.

Wadsworth,J.D., Powell,C., Beck,J.A., Joiner,S., Linehan,J.M., Brandner,S., Mead,S., and Collinge,J. (2008) Molecular diagnosis of human prion disease. *Methods Mol Biol*, **459**, 197-227.

Wagner,W., Fodor,E., Ginsburg,A., and Hammer,J.A., III (2006) The binding of DYNLL2 to myosin Va requires alternatively spliced exon B and stabilizes a portion of the myosin's coiled-coil domain. *Biochemistry*, **45**, 11564-11577.

Wang,E.T., Sandberg,R., Luo,S., Khrebtukova,I., Zhang,L., Mayr,C., Kingsmore,S.F., Schroth,G.P., and Burge,C.B. (2008) Alternative isoform regulation in human tissue transcriptomes. *Nature*, **456**, 470-476.

Wanschers,B., van,d., V, Wijers,M., Wieringa,B., King,S.M., and Fransen,J. (2008) Rab6 family proteins interact with the dynein light chain protein DYNLRB1. *Cell Motil Cytoskeleton*, **65**, 183-196.

Waterhouse,A.M., Procter,J.B., Martin,D.M., Clamp,M., and Barton,G.J. (2009) Jalview Version 2--a multiple sequence alignment editor and analysis workbench. *Bioinformatics*, **25**, 1189-1191.

Watson,P., Forster,R., Palmer,K.J., Pepperkok,R., and Stephens,D.J. (2005) Coupling of ER exit to microtubules through direct interaction of COPII with dynactin. *Nat Cell Biol*, **7**, 48-55.

Whyte,J., Bader,J.R., Tauhata,S.B., Raycroft,M., Hornick,J., Pfister,K.K., Lane,W.S., Chan,G.K., Hinchcliffe,E.H., Vaughan,P.S., and Vaughan,K.T. (2008) Phosphorylation regulates targeting of cytoplasmic dynein to kinetochores during mitosis. *J Cell Biol*, **183**, 819-834.

Williams,J.C., Roulhac,P.L., Roy,A.G., Vallee,R.B., Fitzgerald,M.C., and Hendrickson,W.A. (2007) Structural and thermodynamic characterization of a cytoplasmic dynein light chain-intermediate chain complex. *Proc Natl Acad Sci U S A*, **104**, 10028-10033.

Wilson,C., Venditti,R., Rega,L.R., Colanzi,A., D'Angelo,G., and De Matteis,M.A. (2010) The Golgi apparatus: an organelle with multiple complex functions. *Biochem J*, **433**, 1-9.

Wu,Y., Eghbali,M., Ou,J., Lu,R., Toro,L., and Stefani,E. (2010) Quantitative determination of spatial protein-protein correlations in fluorescence confocal microscopy. *Biophys J*, **98**, 493-504.

Xing,Y. and Lee,C. (2006) Alternative splicing and RNA selection pressure--evolutionary consequences for eukaryotic genomes. *Nat Rev Genet*, **7**, 499-509.

Yamada,M., Toba,S., Takitoh,T., Yoshida,Y., Mori,D., Nakamura,T., Iwane,A.H., Yanagida,T., Imai,H., et,al., and Hirotsune,S. (2010) mNUDC is required for plus-end-directed transport of cytoplasmic dynein and dynactins by kinesin-1. *EMBO J*, **29**, 517-531.

Yasuda,Y., Hashimoto,R., Ohi,K., Fukumoto,M., Takamura,H., Iike,N., Yoshida,T., Hayashi,N., Takahashi,H., Yamamori,H., Morihara,T., Tagami,S., Okochi,M., Tanaka,T., Kudo,T., Kamino,K., Ishii,R., Iwase,M., Kazui,H., and Takeda,M. (2010) Association study of KIBRA gene with memory performance in a Japanese population. *World J Biol Psychiatry*, **11**, 852-857.

Yuan,R., Tsaih,S.W., Petkova,S.B., Marin,d.E., Xing,S., Marion,M.A., Bogue,M.A., Mills,K.D., Peters,L.L., Bult,C.J., et,al., and Paigen,B. (2009) Aging in inbred strains of mice: study design and interim report on median lifespans and circulating IGF1 levels. *Aging Cell*, **8**, 277-287.

Zhang,X., Aubin,J.E., Kim,T.H., Payne,U., Chiu,B., and Inman,R.D. (2004) Synovial fibroblasts infected with Salmonella enterica serovar Typhimurium mediate osteoclast differentiation and activation. *Infect Immun*, **72**, 7183-7189.

Zylkiewicz,E., Kijanska,M., Choi,W.C., Derewenda,U., Derewenda,Z.S., and Stukenberg,P.T. (2011) The N-terminal coiled-coil of Ndel1 is a regulated scaffold that recruits LIS1 to dynein. *J Cell Biol*, **192**, 433-445.

9. Publications

Banks,G.T., Kuta,A., Isaacs,A.M., and Fisher,E.M. (2008) TDP-43 is a culprit in human neurodegeneration, and not just an innocent bystander. *Mamm Genome*, **19**, 299-305.

Kuta,A., Deng,W., Morsi El-Kadi,A., Banks,G.T., Hafezparast,M., Pfister,K.K., and Fisher,E.M. (2010) Mouse cytoplasmic dynein intermediate chains: identification of new isoforms, alternative splicing and tissue distribution of transcripts. *PLoS One*, **5**, e11682.

Banks,G.T., Haas,M.A., Line,S., Shepherd,H.L., Alqatari,M., Stewart,S., Rishal,I., Philpott,A., Kalmar,B., Kuta,A., Groves,M., Parkinson,N., cevedo-Arozena,A., Brandner,S., Bannerman,D., Greensmith,L., Hafezparast,M., Koltzenburg,M., Deacon,R., Fainzilber,M., and Fisher,E.M. (2011) Behavioral and other phenotypes in a cytoplasmic Dynein light intermediate chain 1 mutant mouse. *J Neurosci*, **31**, 5483-5494.

10. Appendices

10.1 CatWalk XT gait analysis - initial analysis of paw parameters

This section contains all the performed analyses of gait parameters, which did not vary in any cohort (*Dync1i1*^{G482D} or *Dync1i2*^{T172I}). The parameters for which *Dync1i1*$^{G482D/G482D}$ mice were different from wildtype *Dync1i1*$^{+/+}$ littermates are described in section 3.4.5 and Table 3.13. All the parameters were automatically calculated by the CatWalk XT software and for each mouse mean values from 4 successive runs were reported; for each pair of paws (**front, hind**) an average of left and right paw was calculated. In addition, the bias towards reporting higher values for one side than the other (e.g. print area for left/right paw) has been observed (Angeby-Moller *et al.*, 2008).

Parameters can be distinguished as static (measurements of the distance, area, etc) or dynamic (description of the movement in time units) and both categories were included in the analysis, starting from the static measurements:
Base of support (BOS) [mm] – an average width between front (left – right) or hind (left – right) paws; it is often used to describe stability of a moving animal
Stride length [mm] – distance between successive placements of the same paw, calculated for paw position at its maximum contact; **Stride length (F/H)** - stride length expressed as a fraction of distance covered by front paws in relation to hind paws
Print area [mm^2] – surface area of a complete print measured during stand phase and it corresponds to the area of a footprint left on paper if a paw was painted with ink; area ratio of front to hind paws was also calculated

Print length [mm] – length of a complete print (Figure 10.1)
Print width [mm] – width of a complete print (measured across the broadest region of a foot)
Moreover, the CatWalk XT enables measurements of dynamic parameters, which describe the movement of each paw in a domain of time:
Swing [ms] – phase of a step cycle when a paw is lifted and does not touch the glass walkway
Stand [ms] – phase of a step cycle describing the duration of paw contact with the glass walkway (phase when a print is recorded)
Swing and Stand are components of the Step cycle, which is the duration of a single step defined as two consecutive contacts of the same paw – the time of a single stride
Duty cycle – is used to express the duration of the stand in relation to the full step cycle

Maximum contact [ms] – time measured from the start of a run till a paw makes the biggest contact with the glass, described as the point at which a breaking phase of the step turns into a propulsion phase

Initial contact [ms] – time since the start of the run at which a paw makes contact with the glass.

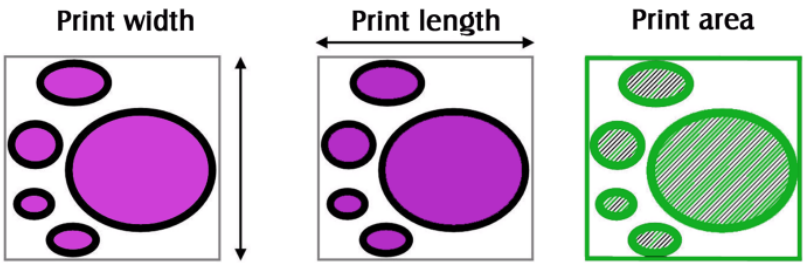

Figure 10.1. Schematic representation of relation between print parameters generated with CatWalk XT
A footprint is recorded for each paw when it is placed on the walkway; parameters described correspond to measurements taken during a stand phase: print width [mm] (vertical arrow) and length [mm] (horizontal arrow) parameters reflect the foot placement and toe spread. Print area [mm^2] corresponds to the total surface, adapted from 'CatWalk XT 8.1 Reference Manual', Noldus Information Technology

Table 10.1. Summary of analysed gait parameters calculated for the *Dync1i1*^{G482D} and *Dync1i2*^{T172I} mice
Raw or transformed data were analysed with either two-way repeated measures ANOVA (reports F and p) or unpaired *t*-test (p only), values for each parameter (with an unit) shown as mean ± SEM (standard error of the mean); genotypes annotated: wildtype *Dync1i1*$^{+/+}$, homozygous *Dync1i1*$^{G482D/G482D}$, wildtype *Dync1i2*$^{+/+}$, homozygous *Dync1i2*$^{T172I/T172I}$; n - number of animals tested; **F** and **H** correspond to front and hind paws while **WTH** and **LTH** correspond to width and length of a print respectively; mm – millimetre, mm^2 – squared millimetre, ms – milliseconds, F(DFn, DFd) is F ratio calculated for DFn: degrees of freedom for the numerator, DFd: degrees of freedom for the denumerator (shaded); two-tailed p value significant at p< 0.05

Parameter		*Dync1i1*$^{+/+}$ n=9	*Dync1i1*$^{G482D/G482D}$ n=10	*Dync1i2*$^{+/+}$ n=8	*Dync1i2*$^{T172I/T172I}$ n=8
Base of support [mm]	**F**	11.8 ± 0.3	10.8 ± 0.3	11.4 ± 0.5	11.8 ± 0.2
	H	20.0 ± 0.7	21.0 ± 0.6	22.8 ± 0.8	22.3 ± 0.6
		F(1,17)=0.0001, p=0.9907		F(1,14)=0.0329, p=0.8588	
Stride length [mm]	**F**	54.1 ± 2.5	50.9 ± 1.6	52.7 ± 1.9	51.4 ± 2.2
	H	54.0 ± 2.4	50.4 ± 1.6	51.9 ± 2.0	50.6 ± 2.2
		F(1,17)=1.4100, p=0.2514		F(1,14)=0.2133, p=0.6513	
Stride length F/H		1.003 ± 0.003	1.011 ± 0.006	1.016 ± 0.006	1.016 ±0.008
		p=0.2236		p=0.9413	
Print area [mm^2]	**F**	19.5 ± 1.8	15.8 ± 2.0	21.8 ± 1.7	21.8 ± 2.5
	H	29.8 ± 2.9	25.7 ± 2.8	28.6 ± 2.5	30.0 ± 2.8
		F(1,17)=1.3780, p=0.2566		F(1,14)=0.0393, p=0.8457	
Print area F/H		0.686 ± 0.044	0.635 ± 0.040	0.772 ±0.032	0.722 ± 0.047
		p=0.3159		p=0.3869	
Print widht [mm]	**F**	5.31 ± 0.19	4.79 ± 0.29	5.60 ± 0.17	5.49 ± 0.28
	H	6.32 ± 0.28	5.95 ± 0.28	6.33 ± 0.25	6.38 ± 0.26
		F(1,17)=1.5530, p=0.2296		F(1,14)=0.0077 p=0.9314	
Print length [mm]	**F**	5.30 ± 0.22	4.60 ± 0.31	5.69 ± 0.44	5.61 ± 0.37
	H	6.85 ± 0.29	6.08 ± 0.35	6.47 ± 0.30	6.56 ± 0.33
		F(1,17)=3.3410, p=0.0852		F(1,14)=0.0002, p=0.9889	
Swing [ms]	**F**	117.2 ± 4.8	133.9 ± 6.5	132.2 ± 5.0	126.9 ± 4.8
	H	106.2 ± 6.7	124.5 ± 7.3	128.4 ± 5.0	118.4 ± 8.0
		F(1,17)=3.9360, p=0.0636		F(1,14)=0.6018, p=0.4508	
Stand [ms]	**F**	87.4 ± 7.3	85.5 ± 6.2	102.2 ± 5.6	92.5 ± 6.2
	H	100.8 ± 8.4	95.8 ± 5.3	105.6 ± 6.8	101.6 ± 4.7
		F(1,17)=0.1361, p=0.7168		F(1,14)=0.7447, p=0.4027	
Duty cycle	**F**	0.417 ± 0.014	0.390 ± 0.020	0.422 ± 0.012	0.411 ± 0.018
	H	0.479 ± 0.026	0.438 ± 0.017	0.441 ± 0.017	0.456 ± 0.022
		F(1,17)=1.787, p=0.1990		F(1,14)=0.0068, p=0.9354	
Maximum contact [ms]	**F**	809.4 ± 136.2	945.7 ± 134.5	815.9 ± 96.3	921.9 ± 125.2
	H	858.1 ± 136.9	926.3 ± 112.1	839.7 ± 102.5	941.2 ± 125.0
		F(1,17)=0.4479, p=0.5123		F(1,14)=0.4218, p=0.5265	
Initial contact [ms]	**F**	705.6 ± 92.7	810.0 ± 78.8	785.9 ± 93.9	893.4 ± 124.2
	H	751.7 ± 95.0	846.3 ± 78.0	808.8 ± 101.1	905.9 ± 123.5
		F(1,17)=0.6743, p=0.4229		F(1,14)=0.4217, p=0.5266	
Maximum contact at	**F**	0.286 ± 0.017	0.299 ± 0.010	0.283 ± 0.023	0.321 ± 0.017
	H	0.294 ± 0.016	0.308 ± 0.006	0.286 ± 0.006	0.325 ± 0.013
		F(1,17)= 0.7698, p=0.3925		F(1,14)=3.7420, p=0.0735	

10.2 Detailed analysis of colocalisation

This section contains all the performed analyses of colocalisation parameters performed for wildtype *Dync1i1*$^{+/+}$ *Dync1i2*$^{+/+}$ and double homozygous *Dync1i1*$^{G482D/G482D}$ *Dync1i2*$^{T172I/T172I}$ cell lines. The analysis and summary are presented in section 4.4.1.2 and Table 4.1.

Cell images were annotated to relevant bins based on the value of pixel ratio (shaded pink), numbers of images from each cell line in **bold,** the results of statistical analysis and reported two-tailed p-values shaded grey; n - number of cell lines derived from animals; F(DFn, DFd) – F ratio calculated for DFn: degrees of freedom for the numerator, DFd: degrees of freedom for the denumerator; ANOVA – analysis of variance; * - unpaired *t*-test with Welch's correction for unequal variance.

Table 10.2. Analysis of colocalisation of MTs and dynein intermediate chains

Values of each parameter shown as mean and range (pixel ratio) or mean ± stanard deviation (SD) (PCC, M_{MTs}, M_{IC74}); genotypes annotated as follows: wildtype (*Dync1i1*$^{+/+}$ *Dync1i2*$^{+/+}$) double homozygous (*Dync1i1*$^{G482D/G482D}$ *Dync1i2*$^{T172I/T172I}$); for each genotype results shown as recorded for each cell line

Parameter		***Dync1i1*$^{+/+}$ *Dync1i2*$^{+/+}$ n=3**			***Dync1i1*$^{G482D/G482D}$ *Dync1i2*$^{T172I/T172I}$ n=3**		
Pixel ratio MTs/IC74	**Bin 1 (1-2)**	**10** 1.703 1.397-1.975	**8** 1.782 1.471-1.962	**5** 1.805 1.532-1.977	**3** 1.723 1.442-1.864	**4** 1.799 1.715-1.918	**4** 1.796 1.585-1.912
	Bin 2 (2-4)	**11** 2.317 2.005-2.992	**15** 2.482 2.011-3.644	**12** 2.753 2.142-3.598	**16** 2.720 2.171-3.878	**17** 2.581 2.067-3.990	**15** 2.500 2.042-3.209
	Bin 3 (4-6)	**1** 5.330		**4** 4.884; 4.109-5.619	**3** 4.633; 4.302-4.802		**1** 5.061
Pearson's colocalisation coefficient (PCC)	**Bin 1**	0.213± 0.090	0.242± 0.156	0.310± 0.204	0.209± 0.054	0.149± 0.134	0.249± 0.055
		Two-way ANOVA F(1,28)=1.1750, p=0.2876					
	Bin 2	0.117± 0.104	0.173± 0.096	0.168± 0.146	0.141± 0.082	0.159± 0.054	0.175± 0.103
		Two-way ANOVA F(1,80)=0.0639, p=0.8011					
	Bin 3	-0.005±0.115			0.113±0.120		
		Unpaired *t*-test, p=0.1768					
Mander's colocalisation coefficient MT intensities (M_{MTs})	**Bin 1**	0.683± 0.064	0.687± 0.059	0.696± 0.076	0.684± 0.035	0.632± 0.042	0.686± 0.048
		Two-way ANOVA F(1,28)=0.9604, p=0.3355					
	Bin 2	0.526± 0.075	0.539± 0.077	0.511± 0.082	0.460± 0.084	0.492± 0.074	0.535± 0.058
		Two-way ANOVA F(1,80)=3.2850, p=0.0737					
	Bin 3	0.276±0.045			0.278±0.036		
		Unpaired *t*-test, p=0.9504					
Mander's colocalisation coefficient IC74 intensities (M_{IC74})	**Bin 1**	0.968± 0.023	0.983± 0.014	0.975± 0.029	0.972± 0.033	0.982± 0.011	0.987± 0.002
		Two-way ANOVA F(1,28)=0.4201, p=0.5222					
	Bin 2	0.971± 0.012	0.990± 0.008	0.983± 0.019	0.971± 0.018	0.991± 0.012	0.981± 0.015
		Two-way ANOVA F(1,80)=0.0012, p=0.9729					
	Bin 3	0.976±0.026			0.995±0.006		
		Unpaired *t*-test, p=0.1745*					

10.3 Reassembly of Golgi comples after nocodazole treatment

This section contains all the performed analyses of the morphology of the Golgi complex was examined after nocodazole washout. Two experiments were performed and in each at least 300 cells were scored blindly to genotype and experiment for the appearance of the Golgi labelling. There were 3 types distinguished, corresponding to perinuclear complex (reticular or compact), and fragmented within a cytosol (Table 10.3). The results are summarised in section 4.4.2.1.

In addition, a detailed analysis of the Golgi structure at different time points was performed by comparing high resolution images of individual cells. For each cell image performed analysis was based on identification of objects positive for giantin labelling, for which a set of parameters was automatically calculated by the software (Cell Profiler). The parameters compared included: ratio of Golgi stacks number to their total area, form factor, eccentricity, and perimeter (in pixels). For each cell a mean value of a parameter was recorded and those were averaged giving a mean from a cell line. Means from each time point were normalised to mean values recorded for untreated cells. The final relative values were analysed using paired *t*-test (the genotype effect at different time points), repeated measures one-way ANOVA (the time point effect on results obtained) followed by Dunnett's multiple comparison test (results for each time point tested against results for untreated cells) (Table 10.4). The results are described in section 4.4.2.2.

Table 10.3. Analysis of Golgi apparatus reassembly after nocodazole treatment

Results obtained in 2 experiments were pooled and shown as fractions recorded for each cell line, total numbers of cells scored **(bold),** and mean±standard deviation; genotypes annotated as follows: wildtype (*Dync1i1*$^{+/+}$*Dync1i2*$^{+/+}$) double homozygous (*Dync1i1*$^{G482D/G482D}$ *Dync1i2*$^{T172I/T172I}$); results of statistical analysis and reported two-tailed p-values shaded grey; n - number of cell lines derived from animals

Morphology/ time point		***Dync1i1*$^{+/+}$ *Dync1i2*$^{+/+}$ n=3**			***Dync1i1*$^{G482D/G482D}$ *Dync1i2*$^{T172I/T172I}$ n=3**		
Reticular	Untreated	**799,** 0.532	**510,** 0.551	**569,** 0.425	**691,** 0.307	**751,** 0.478	**652,** 0.463
		0.503 ± 0.068			0.416 ± 0.095		
		Paired *t*-test, p=0.3732					
	0 min	**698**, 0.0	**544**, 0.0	**597**, 0.0	**668**, 0.0	**678**, 0.0	**646**, 0.0
	50 min	**747,** 0.390	**541,** 0.399	**561,** 0.349	**862,** 0.347	**809,** 0.428	**709,** 0.440
		0.379 ± 0.026			0.405 ± 0.051		
		Paired *t*-test, p=0.5767					
Compact	Untreated	0.392	0.367	0.476	0.624	0.471	0.417
		0.412 ± 0.057			0.504 ± 0.107		
		Paired *t*-test, p=0.3866					
	0 min	0.0	0.0	0.0	0.0	0.0	0.0
	50 min	0.347	0.347	0.396	0.447	0.333	0.313
		0.363 ± 0.028			0.364 ± 0.072		
		Paired *t*-test, p=0.9898					
Fragmented	Untreated	0.076	0.082	0.098	0.069	0.051	0.120
		0.086 ± 0.011			0.080 ± 0.036		
		Paired *t*-test, p=0.7412					
	0 min	1.0	1.0	1.0	1.0	1.0	1.0
	50 min	0.264	0.253	0.255	0.206	0.240	0.247
		0.257 ± 0.006			0.231 ± 0.022		
		Paired *t*-test, p=0.2338					

Table 10.4. Image based analysis of shape parameters of Golgi complex membranes

Digital images were taken and analysed at different time points after nocodazole washout; for each cell line mean values were normalised to values recorded for the untreated cells *(in italics)*, while raw data are shown as mean ± standard deviation (SD); genotypes annotated as follows: wildtype (*Dync1i1*$^{+/+}$ *Dync1i2*$^{+/+}$) double homozygous (*Dync1i1*$^{G482D/G482D}$ *Dync1i2*$^{T172I/T172I}$); results of repeated measures ANOVA or paired *t*-test and reported two-tailed p-values shaded grey, for **p< 0.05 in bold**; for time points shown p-values reported by Dunnett's multiple comparison test; n - number of cell lines derived from animals

Parameter/ time point		***Dync1i1*$^{+/+}$*Dync1i2*$^{+/+}$ n=3**			***Dync1i1*$^{G482D/G482D}$*Dync1i2*$^{T172I/T172I}$ n=3**		
Number of cells	0 min	5	6	5	5	5	6
	20 min	5	7	6	8	6	5
	50 min	5	5	6	5	7	5
	Untreated	7	6	6	6	5	6
Ratio number/ area	0 min	2.929±0.666	1.873±0.762	2.186±0.600	2.440±0.398	1.892±0.377	2.498±0.962
		3.275	*2.533*	*2.982*	*2.706*	*2.406*	*3.125*
		Paired *t*-test, p=0.4681					
	20 min	1.144±0.284	1.126±0.116	1.003±0.374	1.048±0.151	1.126±0.170	1.016±0.161
		1.280	*1.522*	*1.368*	*1.163*	*1.432*	*1.271*
		Paired *t*-test, p=0.0063					
	50 min	0.852±0.104	0.976±0.192	0.836±0.053	0.765±0.189	0.920±0.160	0.837±0.127
		0.953	*1.319*	*1.140*	*0.848*	*1.169*	*1.047*
		Paired *t*-test, p=0.0183					
	Untreated	0.894±0.209	0.740±0.081	0.733±0.106	0.902±0.186	0.787±0.168	0.799±0.165
		Paired *t*-test, p=0.1420					
Time points		**F(3,11)=38.25, p=0.0003**			**F(3,11)=43.70, p=0.0002**		
Untreated vs. 0 min		**p<0.001**			**p<0.001**		
Untreated vs. 20 min		p> 0.05			p> 0.05		
Untreated vs. 50 min		p> 0.05			p> 0.05		
Form factor	0 min	0.613±0.047	0.499±0.067	0.549±0.020	0.506±0.023	0.528±0.063	0.541±0.096
		1.432	*1.080*	*1.407*	*1.138*	*1.130*	*1.311*
		Paired *t*-test, p=0.3745					
	20 min	0.482±0.043	0.433±0.061	0.394±0.071	0.448±0.040	0.455±0.052	0.449±0.040
		1.125	*0.936*	*1.009*	*1.009*	*0.974*	*1.088*
		Paired *t*-test, p=0.9981					
	50 min	0.393±0.049	0.414±0.044	0.441±0.021	0.415±0.058	0.458±0.051	0.389±0.049
		0.917	*0.896*	*1.129*	*0.934*	*0.979*	*0.941*
		Paired *t*-test, p=0.7540					
	Untreated	0.428±0.062	0.463±0.050	0.390±0.035	0.444±0.040	0.467±0.036	0.413±0.074
		Paired *t*-test, p=0.1090					
Time points		**F(3,11)=6.186, p=0.0288**			**F(3,11)=11.17, p=0.0072**		
Untreated vs. 0 min		**p< 0.05**			**p< 0.05**		
Untreated vs. 20 min		p> 0.05			p> 0.05		
Untreated vs. 50 min		p> 0.05			p> 0.05		

Table 10.4. continued

Parameter/ time point		*Dync1i1*$^{+/+}$*Dync1i2*$^{+/+}$ n=3			*Dync1i1*$^{G482D/G482D}$*Dync1i2*$^{T172I/T172I}$ n=3		
Eccentri-city	0 min	0.703± 0.041 *0.910*	0.706± 0.028 *0.943*	0.704± 0.031 *0.900*	0.748± 0.026 *1.010*	0.711± 0.020 *0.978*	0.724± 0.015 *0.977*
		Paired *t*-test, p=0.0648					
	20 min	0.707± 0.035 *0.916*	0.750± 0.038 *1.001*	0.734± 0.027 *0.938*	0.733± 0.039 *0.991*	0.747± 0.045 *1.027*	0.744± 0.009 *1.004*
		Paired *t*-test, p=0.0684					
	50 min	0.749± 0.041 *0.970*	0.751± 0.047 *1.004*	0.714± 0.016 *0.912*	0.808± 0.042 *1.092*	0.755± 0.026 *1.038*	0.752± 0.024 *1.015*
		Paired *t*-test, p=0.0837					
	Untreated	0.772±0.060	0.749±0.044	0.782±0.067	0.740 0.055	0.727±0.046	0.741±0.036
		Paired *t*-test, p=0.0325					
Time points		**F(3,11)=5.439, p=0.0380**			F(3,11)=3.678, p=0.0819		
Untreated vs. 0 min		**p< 0.05**			p> 0.05		
Untreated vs. 20min		p> 0.05			p> 0.05		
Untreated vs. 50min		p> 0.05			p> 0.05		
Log of total peri-meter [a.u.]	0 min	3.616± 0.141 *0.998*	3.918± 0.102 *1.077*	3.788± 0.092 *1.050*	3.661± 0.107 *1.007*	3.963± 0.046 *1.113*	3.524± 0.339 *0.979*
		Paired *t*-test, p=0.8096					
	20 min	3.833± 0.165 *1.057*	3.885± 0.352 *1.068*	3.801± 0.237 *1.054*	3.579± 0.249 *0.984*	3.791± 0.353 *1.064*	4.034± 0.233 *1.121*
		Paired *t*-test, p=0.9426					
	50 min	3.818± 0.310 *1.053*	3.873± 0.116 *1.064*	3.983± 0.261 *1.104*	3.354± 0.197 *0.922*	3.726± 0.135 *1.046*	3.867± 0.133 *1.074*
		Paired *t*-test, p=0.2379					
	Untreated	3.625± 0.250	3.639± 0.126	3.607± 0.200	3.637± 0.133	3.562± 0.157	3.599± 0.214
		Paired *t*-test, p=0.4706					
Time points		**F(3,11)=5.974, p=0.0311**			F(3,11)=0.5749, p=0.6522		
Untreated vs. 0 min		**p> 0.05**			p> 0.05		
Untreated vs. 20 min		**p< 0.05**			p> 0.05		
Untreated vs. 50 min		**p< 0.05**			p> 0.05		

10.4 Analysis of EGF-uptake and endosomal trafficking

This section contains the performed analyses of the $EGF^{+/ve}$ endosomes in wildtype *Dync1i2*$^{+/+}$ and homozygous *Dync1i2*$^{T172I/T172I}$ fibroblasts. Cells were observed at different time points after EGF stimulation: 0 min, 15 min, 30 min, 45 min, and 60 min. Images of individual cells obtained from 2 experiments were analysed and parameters describing EGF-positive ($EGF^{+/ve}$) endosomes were calculated: the rate of translocation, endosome number and area. During the analysis the total number of vesicles was normalised relatively to the cytoplasm area. Because values of parameters obtained deviated from Gaussian distribution, raw data were transformed using: $f(x) = logY$ and *log* values were used. Furthermore, Pearson correlation between number and area of endosomes was calculated (Table 10.5). The results are discussed in section 4.4.3.

Table 10.5. Image based analysis of number and area of $EGF^{+/ve}$ endosomes
Digital images were taken and analysed at different time points after stimulation with EGF; due to a non-normal distribution of values all the data were transformed before analysis using: $f(x) = logY$; for each cell line raw data are shown as median and interquartile range (IQR) while *log* transformed as means ± standard deviation (SD) *(in italics)*; genotypes annotated as follows: wildtype (*Dync1i2*$^{+/+}$), homozygous (*Dync1i2*$^{T172I/T172I}$); result of ANOVA and reported two-tailed p-values shaded grey **(for p<0.05 in bold)**; R^2 - Pearson correlation coefficient squared, corresponds to goodness of linear fit (fraction of variance shared between both variables); n - number of cell lines derived from animals

Parameter/ time point		*Dync1i2*$^{+/+}$ *(n=2)*		*Dync1i2*$^{T172I/T172I}$ *(n=2)*	
Number/ cytosol area	0 min	1.786 (0.698 - 5.356) 0.285±0.508	6.106 (2.068 - 12.41) 0.673±0.453	2.013 (0.652 - 5.290) 0.254±0.549	2.472 (1.073 - 5.615) 0.362±0.590
		F(1,64)=1.718, p=0.1946			
	15 min	2.390 (1.643 - 3.310) 0.317±0.306	2.955 (2.101 - 7.430) 0.570±0.308	2.302 (1.175 - 3.297) 0.289±0.335	4.524 (2.272 - 5.430) 0.551±0.287
		F(1,92)=0.1288, p=0.7205			
	30 min	2.804 (2.010 - 3.843) 0.453±0.181	3.239 (1.717 - 6.663) 0.520±0.298	2.941 (2.416 - 4.405) 0.480±0.255	2.968 (1.869 - 6.054) 0.470±0.342
		F(1,109)=0.0477, p=0.8275			
	45 min	2.305 (1.768 - 3.120) 0.363±0.156	1.557 (0.738 - 2.108) 0.163±0.289	2.448 (1.321 - 2.759) 0.296±0.314	1.978 (1.115 - 2.739) 0.229±0.281
		F(1,103)=0.0, p=0.9998			
	60 min	1.435 (0.989 - 1.998) 0.125±0.269	0.522 (0.341 - 1.099) -0.211±0.328	1.744 (1.025 - 2.711) 0.214±0.287	0.857 (0.489 - 1.396) -0.084±0.316
		F(1,96)=3.188, p=0.0774			
Test for linear trend		F(4,9)=2.730, p=0.1501 **R^2=0.5068, p=0.0362**		F(4,9)=2.917, p=0.1355 R^2=0.2852, p=0.0811	

Table 10.5. continued

Parameter/ time point		*Dync1i2$^{+/+}$ (n=2)*		*Dync1i2$^{T172I/T172I}$ (n=2)*	
Perinuclear endosomes NUMBER	0 min	10 (5 - 33)	37 (14 – 194)	19 (11 – 45)	26 (6 – 52)
		1.148±0.622	1.667±0.709	1.314±0.399	1.366±0.633
		F(1,60)=0.1891, p=0.6653			
	15 min	52 (35 - 75)	64 (37 – 126)	34 (15 – 57)	72 (29 – 104)
		1.678±0.344	1.827±0.323	1.472±0.440	1.745±0.428
		F(1,91)=3.112, p=0.0811			
	30 min	65 (46 - 90)	78 (45 – 178)	54 (38 – 82)	77 (42 – 134)
		1.802±0.250	1.934±0.349	1.751±0.213	1.818±0.331
		F(1,109)=2.429, p=0.1220			
	45 min	50 (38 - 97)	40 (23 – 63)	82 (47 – 128)	51 (32 – 83)
		1.768±0.271	1.601±0.350	1.875±0.290	1.746±0.386
		F(1,102)=3.922, p=0.0503			
	60 min	52 (26 - 94)	19 (13 – 31)	60 (35 – 88)	24 (17 – 48)
		1.694±0.345	1.307±0.270	1.715±0.286	1.400±0.306
		F(1,94)=0.8291, p=0.3649			
Test for linear trend		F(4,9)=1.439, p=0.3443		F(4,9)=3.485, p=0.1017	
Perinuclear endosomes AREA [a.u.]	0 min	72 (47 - 294)	302 (108 - 1891)	154 (67 - 471)	207 (45 - 383)
		2.053±0.635	2.611±0.808	2.259±0.423	2.279±0.649
		F(1,58)=0.1450, p=0.7048			
	15 min	707 (331 - 1029)	829 (436 - 2007)	417 (156 - 807)	901 (296 - 1381)
		2.747±0.475	2.951±0.401	2.538±0.539	2.826±0.487
		F(1,91)=2.686, p=0.1047			
	30 min	861 (556 - 1383)	1563 (714 - 3585)	886 (523 - 1332)	1032 (431 - 2174)
		2.947±0.271	3.180±0.388	2.930±0.270	2.976±0.404
		F(1,109)=3.088, p=0.0817			
	45 min	756 (463 - 1573)	595 (228 - 893)	1346 (722 - 2086)	804 (408 - 1494)
		2.919±0.312	2.679±0.420	3.069±0.350	2.871±0.449
		F(1,102)=5.206, p=0.0246			
	60 min	812 (335 - 1119)	225 (117 - 356)	1007 (399 - 1340)	348 (207 - 765)
		2.808±0.414	2.328±0.312	2.888±0.374	2.479±0.402
		F(1,94)=2.195, p=0.1418			
Test for linear trend		F(4,9)=2.262, p=0.1973 R^2=0.0365, p=0.5062		**F(4,9)=5.525, p=0.0444 R^2=0.3154, p=0.0329**	
Pearson correlation coefficient *log(number) – log(area)*	0 min	0.9879	0.9972	0.9482	0.9767
		(0.9669 - 0.9956)	(0.9910 - 0.9992)	(0.8316 - 0.9847)	(0.9350 - 0.9918)
		R^2=0.9759	R^2=0.9945	R^2=0.8990	R^2=0.9540
	15 min	0.9622	0.9777	0.9887	0.9769
		(0.9201 - 0.9823)	(0.9417 - 0.9916)	(0.9758 - 0.9947)	(0.9378 - 0.9916)
		R^2=0.9258	R^2=0.9560	R^2=0.9775	R^2=0.9544
	30 min	0.9033	0.9586	0.8976	0.9532
		(0.8049 - 0.9533)	(0.9087 - 0.9815)	(0.8011 - 0.9486)	(0.8933 - 0.9798)
		R^2=0.8159	R^2=0.9189	R^2=0.8057	R^2=0.9086
	45 min	0.9270	0.9727	0.9159	0.9606
		(0.8528 - 0.9645)	(0.9309 - 0.9894)	(0.8385 - 0.9570)	(0.9011 - 0.9846)
		R^2=0.8594	R^2=0.9462	R^2=0.8388	R^2=0.9228
	60 min	0.9807	0.9416	0.9415	0.9581
		(0.9582 - 0.9911)	(0.8590 - 0.9764)	(0.8620 - 0.9758)	(0.9090 - 0.9809)
		R^2=0.9617	R^2=0.8866	R^2=0.8864	R^2=0.9179

10.5 Infection with *Salmonella enterica* ser. Typhimurium

This section contains the performed analyses of the phenotypes of the bacterial microcolonies observed in the MEF lines. Infection was carried out for 8 hours; intracellular bacteria were observed under fluorescent microscope and various features were scored by eye, from each line 120 infected MEFs were examined. There were 6 cell lines used in the experiments, including: one of wildtype *Dync1i1*$^{+/+}$ *Dync1i2*$^{+/+}$ and double homozygous *Dync1i1*$^{G482D/G482D}$ *Dync1i2*$^{T172I/T172I}$, two of wildtype *Dync1h1*$^{+/+}$ and homozygous *Dync1h1*$^{Loa/Loa}$. Cell lines derived from embryos with mutations in the intermediate chains (*Dync1i1*^{G482D} *Dync1i2*^{T172I}) were not tested statistically (n=1), cell lines with mutation in the *Dync1h1*^{Loa} were tested for n=2 with tests for categorical data (Fisher's exact test, Chi-squared). The efficiency of the infection was scored by 3 categorical parameters, which described the position and speed of replication of bacteria in each fibroblast. Those included: *(1)* position of bacteria in regards to nucleus (*perinuclear* or *periphery*), *(2)* ability to form micro colony (*clustered* or *scattered*), *(3)* and presence of *fewer* or *more* than 20 bacteria per fibroblast (Table 10.6). The results are discussed in section 4.4.4.

In addition, the *SifA*$^{-}$ mutant strain was used, in order to examine the dynamics of the SCV membranes. Stability of the bacterial vacuoles was investigated by following the distribution of LAMP-1 staining. A number of bacteria, which colocalised with LAMP-1 staining was scored and represented as a fraction of *Salmonella* found in LAMP-1$^{+/ve}$ compartment (Table 10.7).

Table 10.6. Distribution of microcolony features observed in MEFs infected with wildtype *Salmonella* typhimurium (next page)

Genotypes of cell lines correspond to wildtype (*Dync1i1*$^{+/+}$*Dync1i2*$^{+/+}$), double homozygous (*Dync1i1*$^{G482D/G482D}$ *Dync1i2*$^{T172I/T172I}$), wildtype (*Dync1h1*$^{+/+}$) and homozygous (*Dync1h1*$^{Loa/Loa}$) *Loa.*

Intracellular *Salmonella* were classified based on: (1) the position in regards to a nucleus, (2) micro colony formation, (3) evaluated number; categories graded as the most (**bold**) or least (*italics*) preferable (see paragraph for details); shaded area corresponds to the frequency distributions shown in Figure 4.11. In addition, parameters were analysed individually or combined in pairs; for each category number of cells is shown next to a relative fraction of population; because only 1 experiment was performed with 2 cell lines allelic in *Dync1i1*^{G482D} *Dync1i2*^{T172I} loci (n=1) the data were not tested for statistical significance, in case of *Loa* lines carrying a mutation in the dynein heavy chain (n=2) numbers are shown for both lines while a fraction is shown as an average value; * marks results of Chi-squared (χ^2) test, calculated after pooling values from individual MEF lines; in all cases reported two sided p-values; for clarification relevant panels in Figure 4.12 are also annotated for each comparison

Category			***Dync1i1*$^{+/+}$ *Dync1i2*$^{+/+}$**		***Dync1i1*$^{G482D/G482D}$ *Dync1i2*$^{T172I/T172I}$**		***Dync1h1*$^{+/+}$ *(n=2)***		***Dync1h1*$^{Loa/Loa}$ *(n=2)***	
Position (1)	*Microcolony (2)*	*Number (3)*	*Number of cells classified to each category and fraction it represents*							
Periphery	Scattered	<20	18	0.150	13	0.108	26, 21	0.196	31, 28	0.246
Periphery	Clustered	<20	27	0.225	12	0.100	16, 19	0.146	28, 22	0.208
Perinuclear	Scattered	<20	16	0.133	13	0.108	17, 20	0.154	11, 20	0.129
Perinuclear	**Clustered**	<20	**36**	**0.300**	**50**	**0.417**	**39, 30**	**0.288**	**24, 30**	**0.225**
Periphery	*Scattered*	*>20*	*7*	*0.058*	*7*	*0.058*	*8, 11*	*0.079*	*8, 9*	*0.071*
Periphery	Clustered	>20	5	0.042	7	0.058	7, 8	0.063	6, 6	0.050
Perinuclear	Scattered	>20	5	0.042	12	0.100	5, 5	0.042	7, 2	0.038
Perinuclear	Clustered	>20	6	0.050	6	0.050	2, 6	0.033	5, 3	0.033
Total MEFs scored			120	1.000	120	1.000	120	1.000	120	1.000
Periphery			57	0.475	39	0.325	57, 59	0.483	73, 65	0.575
Perinuclear			63	0.525	81	0.675	63, 61	0.517	47, 55	0.425
Figure 4.12A							Fisher's exact test, p=0.1958			
Scattered			46	0.383	45	0.375	56, 57	0.471	57, 59	0.483
Clustered			74	0.617	75	0.625	64, 63	0.529	63, 61	0.517
Figure 4.12B							Fisher's exact test, p=0.8240			
		< 20	97	0.808	88	0.733	98, 90	0.783	94, 100	0.808
		> 20	23	0.192	32	0.267	22, 30	0.217	26, 20	0.192
Figure 4.12C							Fisher's exact test, p=0.7490			
Periphery	Scattered		25	0.208	20	0.167	34, 32	0.275	39, 37	0.317
Periphery	Clustered		32	0.267	19	0.158	23, 27	0.208	34, 28	0.258
Perinuclear	Scattered		21	0.175	25	0.208	22, 25	0.196	18, 22	0.167
Perinuclear	Clustered		42	0.350	56	0.467	41, 36	0.321	29, 33	0.258
Figure 4.12D							$\chi^2(3)=4.172$, p=0.2435*			
Scattered		< 20	34	0.283	26	0.217	43, 41	0.350	42, 48	0.375
Scattered		> 20	12	0.100	19	0.158	13, 16	0.121	15, 11	0.108
Clustered		< 20	63	0.525	62	0.517	55, 49	0.433	52, 52	0.433
Clustered		> 20	11	0.092	13	0.108	9, 14	0.096	11, 9	0.083
Figure 4.12E							$\chi^2(3)=0.580$, p=0.9010*			
Periphery		< 20	45	0.375	25	0.208	42, 40	0.342	59, 50	0.454
Periphery		> 20	12	0.100	14	0.117	15, 19	0.142	14, 15	0.121
Perinuclear		< 20	52	0.433	63	0.525	56, 50	0.442	35, 50	0.354
Perinuclear		> 20	11	0.092	18	0.150	7, 11	0.075	12, 5	0.071
Figure 4.12F							$\chi^2(3)=6.551$, p=0.0877*			

Table 10.7. Summary of membrane dynamics observed in MEFs infected with wildtype (WT) and *SifA*$^{-}$ *Salmonella* typhimurium

Infections were carried out for 8 hours, intracellular bacteria were observed and association with LAMP-1$^{+/ve}$ compartment was scored by eye; genotypes of cell lines correspond to wildtype (*Dync1i1*$^{+/+}$*Dync1i2*$^{+/+}$), double homozygous (*Dync1i1*$^{G482D/G482D}$ *Dync1i2*$^{T172I/T172I}$), wildtype (*Dync1h1*$^{+/+}$) and homozygous (*Dync1h1*$^{Loa/Loa}$) *Loa;* from each line and bacterial strain 120 infected MEFs were examined; results are presented as relative fractions of population or number of cells displaying the feature, results of *Dync1h1*^{Loa} (n=2) as mean ± standard deviation, analysed with unpaired *t*-test, which reported two-tailed p-value; total number of intracellular *SifA*$^{-}$ bacteria was pooled and expressed as median and interquartile range

Phenotype observed		***Dync1i1*$^{+/+}$ *Dync1i2*$^{+/+}$**	***Dync1i1*$^{G482D/G482D}$ *Dync1i2*$^{T172I/T172I}$**	***Dync1h1*$^{+/+}$ n=2**	***Dync1h1*$^{Loa/Loa}$ n=2**
Salmonella in LAMP -1$^{+/ve}$ compartment	**WT**	0.991	0.990	0.989 ± 0.0001	0.986 ± 0.016
				Unpaired *t*-test, p=0.7767	
	***SifA*$^{-}$**	0.075	0.109	0.078 ± 0.047	0.091 ± 0.049
				Unpaired *t*-test, p=0.8964	
MEFs with *Salmonella* in 2 compartments	**WT**	5	6	10, 4	13, 2
		0.042	0.051	0.0583 ± 0.035	0.0665 ± 0.070
				Unpaired *t*-test p=0.8964	
	***SifA*$^{-}$**	30	29	50, 27	32, 22
		0.250	0.242	0.321 ± 0.136	0.225 ± 0.059
				Unpaired *t*-test, p=0.4560	
Salmonella with lost /retained LAMP -1$^{+/ve}$ membranes	**WT**	0.186	0.161	0.180 ± 0.087	0.194 ± 0.017
				Unpaired *t*-test, p=0.8459	
	***SifA*$^{-}$**	0.164	0.184	0.203 ± 0.059	0.151 ± 0.017
				Unpaired *t*-test, p=0.3580	
Median number of *SifA*$^{-}$ *Salmonella*		4.0 (1.0 - 8.0)	1.0 (1.0 - 5.0)	7.0 (4.3 - 9.0)	6.0 (4.0 - 8.0)

10.6 Formation of stress granules

This section contains detailed analyses of the cytoplasmic stress granules (SG). From each condition (sodium arsenite, thapsigargin) at least 20 pictures of each cell line were taken from 2 experiments, thus over 40 pictures of wildtype *Dync1i1*$^{+/+}$*Dync1i2*$^{+/+}$ (n=3), double homozygous *Dync1i1*$^{G482D/G482D}$ *Dync1i2*$^{T172I/T172I}$ (n=3), wildtype *Dync1h1*$^{+/+}$ (n=3), and homozygous *Dync1h1*$^{Loa/Loa}$ (n=3) fibroblasts were taken. The number and total area of G3BP$^{+/ve}$ objects were recorded for individual cells. Because values obtained for each cell line did not have Gaussian distribution, raw data were transformed ($f(x) = logY$) prior to statistical analysis. All the parameter were analysed with two-way ANOVA (Table 10.8, Table 10.9). The results are described in section 5.3.2.

Table 10.8. Analysis of stress granules in individual cells after sodium arsenite (SA) treatment
Images from 2 experiments were analysed and G3BP$^{+/ve}$ objects treated as stress granules; due to a non-normal distribution of values all the data were transformed before analysis using: $f(x) = logY$; for each cell line raw data are shown as median and interquartile range (IQR) while *log* transformed as means ± standard deviation (SD) *(in italics)*; genotypes annotated as follows: wildtype (*Dync1i1*$^{+/+}$*Dync1i2*$^{+/+}$), double homozygous (*Dync1i1*^{G482D}*Dync1i2*$^{T172I/T172I}$), wildtype (*Dync1h1*$^{+/+}$), and homozygous (*Dync1h1*$^{Loa/Loa}$); result of ANOVA and reported two-tailed p-values shaded grey **(for p<0.10 in bold)**; R^2 - Pearson correlation coefficient squared, corresponds to goodness of linear fit (fraction of variance shared between both variables); n - number of cell lines derived from animals; a.u. – arbitrary units

Parameter	***Dync1i1*$^{+/+}$ *Dync1i2*$^{+/+}$ n=3**			***Dync1i1*$^{G482D/G482D}$ *Dync1i2*$^{T172I/T172I}$ n=3**		
Number of cells	39	39	40	40	39	42
Number of G3BP$^{+/ve}$ foci	39 (32- 59)	46 (29 - 70)	49 (35 - 71)	42 (28 - 50)	55 (46 - 74)	50 (38 - 65)
	1.642±0.189	1.653±0.226	1.687±0.197	1.600 ±0.207	1.753 ±0.193	1.681 ±0.168
	F(1,233)=0.4717, p=0.4929					
Total area of G3BP$^{+/ve}$ foci [a.u.]	9308 (6879-12630)	9500 (6487-14313)	10010 (7843-16420)	8516 (5668-12397)	11291 (8104-15401)	9842 (7554-12760)
	3.957±0.187	3.986±0.214	4.028±0.217	3.909 ±0.247	4.063 ±0.193	3.985 ±0.160
	F(1,233)=0.0350, p=0.8517					
Parameter	***Dync1h1*$^{+/+}$ n=3**			***Dync1h1*$^{Loa/Loa}$ n=3**		
Number of cells	79	62	50	81	58	61
Number of G3BP$^{+/ve}$ foci	50 (28 - 82)	49 (35 - 65)	57 (35 -104)	64 (45 - 103)	64 (50 - 88)	62 (44 - 98)
	1.681±0.278	1.674±0.225	1.769±0.296	1.818 ±0.255	1.820 ±0.218	1.814 ±0.234
	F(1,385)=17.78, p< 0.0001					
Total area of G3BP$^{+/ve}$ foci [a.u.]	11796 (6527-19425)	12396 (8342 - 18230)	16556 (7735 - 26600)	16211 (10788-26177)	14519 (11309-21657)	15956 (9915 - 25230)
	4.050±0.284	4.065±0.268	4.154±0.324	4.197 ±0.270	4.169 ±0.216	4.192 ±0.259
	F(1,385)=11.97, p=0.0006					
Correlation log(number) – log(area)	0.9324	0.9108	0.9305	0.9290	0.9024	0.9532
	R^2=0.8694	*R^2=0.8296*	*R^2=0.8658*	*R^2=0.8631*	*R^2=0.8144*	*R^2=0.9086*

Table 10.9. Analysis of stress granule formation after thapsigargin (TG) treatment
Images from 2 experiments were analysed and G3BP$^{+/ve}$ objects treated as stress granules; due to a non-normal distribution of values all the data were transformed before analysis using: $f(x) = logY$; for each cell line raw data are shown as median and interquartile range (IQR) while *log* transformed as means ± standard deviation (SD) *(in italics)*; genotypes annotated as follows: wildtype (*Dync1i1*$^{+/+}$*Dync1i2*$^{+/+}$), double homozygous (*Dync1i1*^{G482D}*Dync1i2*$^{T172I/T172I}$), wildtype (*Dync1h1*$^{+/+}$), and homozygous (*Dync1h1*$^{Loa/Loa}$); result of ANOVA and reported two-tailed p-values shaded grey **(for p<0.10 in bold)**; R^2 - Pearson correlation coefficient squared, corresponds to goodness of linear fit (fraction of variance shared between both variables); n - number of cell lines derived from animals; a.u. – arbitrary units

Parameter	***Dync1i1*$^{+/+}$ *Dync1i2*$^{+/+}$ n=3**			***Dync1i1*$^{G482D/G482D}$ *Dync1i2*$^{T172I/T172I}$ n=3**		
Number of cells	40	42	39	41	38	39
Number of G3BP$^{+/ve}$ foci	40 (31 - 56) *1.620±0.156*	45 (34 - 58) *1.638±0.190*	50 (39 - 68) *1.736±0.181*	39 (31- 52) *1.596±0.188*	50 (35 - 59) *1.686±0.185*	52 (41 - 67) *1.717±0.164*
	F(1,233)=0.0041, p=0.9487					
Total area of G3BP$^{+/ve}$ foci [a.u.]	8462 (6583-12360) *3.942±0.185*	8723 (6334-12519) *3.944±0.197*	11659 (8119-14032) *4.078±0.194*	8988 (6665-12252) *3.931±0.208*	9519 (7258-11862) *3.973±0.172*	10386 (8747-13270) *4.018±0.173*
	F(1,233)=0.3408, p=0.5599					
Parameter	***Dync1h1*$^{+/+}$ n=3**			***Dync1h1*$^{Loa/Loa}$ n=3**		
Number of cells	61	62	60	61	60	64
Number of G3BP$^{+/ve}$ foci	64 (37 - 83) *1.752±0.231*	47 (34 - 57) *1.654±0.201*	46 (26 - 83) *1.671±0.308*	61 (47 - 91) *1.800±0.236*	48 (34 - 65) *1.668±0.206*	58 (40 - 71) *1.732±0.212*
	F(1,362)=2.806, p=0.0948					
Total area of G3BP$^{+/ve}$ foci	12342 (9447-19540) *4.103±0.256*	10903 (7817-13067) *4.027±0.213*	10988 (6638-17959) *4.006±0.306*	15156 (9519-22834) *4.162±0.273*	10523 (6780-14666) *4.007±0.236*	11183 (7924-15441) *4.018±0.224*
	F(1,362)=0.4153, p=0.5197					
Correlation log(number) – log(area)	0.9038 *R^2=0.8169*	0.8966 *R^2=0.8040*	0.9472 *R^2=0.8971*	0.9439 *R^2=0.8909*	0.9092 *R^2=0.8267*	0.9070 *R^2=0.8227*

10.7 Analysis of splicing pattern of the mouse *Dync1i1* and *Dync1i2* genes

This section contains detailed analyses of relative abundance of different isoforms of the cytoplasmic dynein intermediate chains 1 and 2.

Capillary gel electrophoresis with laser induced fluorescence (CGE-LIF) provided high efficiency separation of nucleic acids up to a single base resolution by combining polyacrylamide in capillaries as medium and fluorescence based detection for better resolution. Chromatograms recorded contained sets of peaks separated by their sizes with the accuracy to one bp. By comparison of expected sizes of amplified isoforms with peak positions on a chromatogram, five isoforms of each gene were annotated. Relative amounts were calculated as fraction of peak area to the total area of peaks identified and individual isoforms compared between samples (Table 10.10). The results are described in section 6.4.1.2.

Levels of transcripts of the subunits of the dynein complex were examined using real-time PCR. Relative quantification performed by calculating the ratio between the amounts of a target gene (dynein subunits) and a control gene (β-actin). Calculations were based on the values of threshold cycle ($\mathbf{C_T}$), which was number of cycle, when a fluorescence increased above a set threshold. Firstly, C_T values of β-actin were subtracted from values recorded for a dynein gene ($\mathbf{\Delta C_T}$). The ΔC_T values recorded for wildtype *Dync1i2*$^{+/+}$ mice (n=3) were averaged and used as 'calibrating' value when calculating $\mathbf{\Delta\Delta C_T}$ ($\Delta\Delta C_T$=ΔC_T 'calibrating' - ΔC_T sample). Finally, normalised expression levels of dynein subunits were calculated as $\mathbf{2^{-\Delta\Delta CT}}$ and those values were tested for statistical significance using unpaired *t*-test with reported two-tailed p-values (Table 10.10). Detailed description of the quantitative real-time PCR can be found in Qiagen handbook (Critical Factors for Successful Real-Time PCR). Each sample was run in triplicate and values averaged before analysis. The results are discussed in section 6.4.2.

Table 10.10. Relative abundance of individual isoforms of *Dync1i1* and *Dync1i2* (exon 1a, exon 1b) in mouse neural tissues

Results shown as mean ± standard error (SEM); PCR products were amplified using reverse primers conjugated with 5-FAM (Appendix 10.12.4) and isoforms detected shown; isoforms *Dync1i1.E*, and *Dync1i2.D* were not observed due to low sensitivity of the assay; values were compared using paired *t*-test or one-way ANOVA, reported two-tailed p-values; transcripts detected at levels below 2% were not considered in the analysis and marked in *italics*; the most abundant isoforms shaded pink; values from parts of brain were compared against samples from hippocampus and underlined when significantly different; isoforms showing different levels within the sample in green, nd – not detected, n=4 in all samples except for * (n=3) and $ (n=2)

Tissue/ Isoform	*Dync1i1*				
	1.A	***1.B***	***1.D***	***1.C***	***1.F***
Brain	0.018±0.002	0.502±0.016	0.310±0.013	0.134±0.021	0.036±0.006
Spinal cord	0.055±0.011	0.477±0.024	0.398±0.007	0.048±0.004	0.022±0.006
Statistics	p=0.0314	p=0.4127	p=0.0068	p=0.0337	p=0.2056
Embryonic brain$	nd	0.647±0.008	0.112±0.006	0.220±0.014	0.021±0.000
Embryonic sp. cord$	nd	0.721±0.008	0.148±0.003	0.115±0.000	0.009±0.002
	-	p=0.0208	p=0.0374	p=0.0163	p=0.0351
Cortex	0.005±0.004	0.585±0.006	0.273±0.020	0.106±0.005	0.031±0.006
Hippocampus *	0.004±0.002	0.493±0.051	0.298±0.018	0.160±0.024	0.045±0.007
Olfactory bulbs	0.018±0.003	0.289±0.008	0.130±0.008	0.437±0.023	0.126±0.005
Cerebellum	0.035±0.005	0.572±0.029	0.334±0.017	0.044±0.006	0.014±0.004
Brain stem	0.069±0.030	0.455±0.028	0.410±0.027	0.048±0.018	0.018±0.007
Tissue/ Isoform	***Dync1i2 exon 1a***				
	2.E	***2.A***	***2.B***	***2.F***	***2.C***
Brain	nd	0.359±0.010	0.313±0.007	nd	0.328±0.014
Spinal cord	nd	0.125±0.006	0.329±0.022	nd	0.545±0.024
Statistics	-	p=0.0002	p=0.5521	-	p=0.0039
Embryonic brain$	0.009±0.001	0.083±0.019	0.633±0.025	nd	0.274±0.009
Embryonic sp. cord$	0.009±0.003	0.245±0.005	0.551±0.010	nd	0.195±0.008
	-	p=0.0144	p=0.0936	-	p=0.0219
Cortex	0.004±0.001	0.333±0.061	0.301±0.007	0.003±0.001	0.359±0.068
Hippocampus *	nd	0.390±0.052	0.255±0.014	0.004±0.000	0.351±0.065
Olfactory bulbs	0.005±0.003	0.121±0.005	0.479±0.002	nd	0.394±0.005
Cerebellum	0.002±0.001	0.417±0.015	0.267±0.012	nd	0.313±0.011
Brain stem	nd	0.204±0.015	0.358±0.009	0.002±0.000	0.435±0.007
Tissue/ Isoform	***Dync1i2 exon 1b***				
	2.E	***2.A***	***2.B***	***.2F***	***2.C***
Brain	nd	0.382±0.009	0.357±0.013	0.003±0.001	0.258±0.017
Spinal cord	nd	0.206±0.009	0.398±0.014	nd	0.396±0.011
Statistics	-	p< 0.0001	p=0.0902	-	p=0.0017
Embryonic brain$	0.008±0.001	0.050±0.002	0.699±0.015	nd	0.244±0.014
Embryonic sp. cord$	nd	0.191±0.010	0.647±0.010	nd	0.157±0.003
	-	p=0.0055	p=0.1058	-	p=0.0270
Cortex	nd	0.489±0.031	0.310±0.018	nd	0.200±0.014
Hippocampus *	nd	0.484±0.017	0.253±0.017	0.003±0.001	0.259±0.008
Olfactory bulbs	0.012±0.001	0.232±0.008	0.499±0.014	nd	0.256±0.010
Cerebellum	nd	0.317±0.031	0.316±0.029	nd	0.367±0.045
Brain stem	nd	0.225±0.009	0.370±0.008	0.002±0.000	0.403±0.008

Table 10.11. Quantitative analysis of expression levels of dynein subunits in wildtype *Dync1i2*$^{+/+}$ and homozygous *Dync1i2*$^{T172I/T172I}$ mice

Results shown as mean ± standard error (SEM); real-time PCRs were run using primers designed to detect 1 population of cDNAs (Appendix 10.12.5) and subunits detected shown; isoforms of intermediate chains: *Dync1i1.E*, *Dync1i1.F, Dync1i2.D, Dync1i2.E,* and *Dync1i2.F* were not observed due to low sensitivity of the assay; genotypes correspond to wildtype *Dync1i2*$^{+/+}$ and homozygous *Dync1i2*$^{T172I/T172I}$ animals; *Dync1li1* – dynein light intermediate chain1, *Dynlt1, Dynlt3* – dynein light chains Tc-tex1, RP3, *Dynll1, Dynll2* – dynein light chains LC8-1 and 2

Gene		*Dync1i2*$^{+/+}$ *(n=3)*			*Dync1i2*$^{T172I/T172I}$ *(n=3)*		
		Cortex	Hippocampus	Spinal cord	Cortex	Hippocampus	Spinal cord
Dync1i1.A	ΔC_T	12.57	9.943	8.167	11.79±0.415	10.38±0.372	9.307±0.318
	$\Delta\Delta C_T$	0.000±0.543	0.000±0.326	0.000±0.360	-0.778±0.415	0.441±0.372	1.141±0.318
	$2^{-\Delta\Delta CT}$	1.148±0.416	1.055±0.256	1.063±0.260	1.846±0.447	0.783±0.177	0.475±0.093
		p=0.3167	p=0.4311	p=0.1000			
Dync1i1.B	ΔC_T	4.776	3.010	3.761	4.325±0.508	3.628±0.732	4.071±0.335
	$\Delta\Delta C_T$	0.000±0.257	0.000±0.152	0.000±0.024	-0.451±0.508	0.619±0.732	0.310±0.335
	$2^{-\Delta\Delta CT}$	1.032±0.178	1.011±0.103	1.000±0.016	1.523±0.431	0.800±0.282	0.849±0.177
		p=0.3515	p=0.5209	p=0.4427			
Dync1i1.D	ΔC_T	5.076	4.651	4.544	4.386±0.439	4.953±0.155	4.264±0.128
	$\Delta\Delta C_T$	0.000±0.496	0.000±0.069	0.000±0.041	-0.690±0.439	0.302±0.155	-0.280±0.128
	$2^{-\Delta\Delta CT}$	1.115±0.338	1.002±0.048	1.001±0.029	1.754±0.452	0.820±0.083	1.224±0.113
		p=0.3214	p=0.1316	p=0.1283			
Dync1i1.C	ΔC_T	7.511	6.590	8.044	7.697±0.745	6.836±0.273	8.583±0.446
	$\Delta\Delta C_T$	0.000±0.170	0.000±0.139	0.000±0.089	0.186±0.745	0.245±0.273	0.539±0.446
	$2^{-\Delta\Delta CT}$	1.014±0.118	1.009±0.092	1.004±0.063	1.119±0.498	0.875±0.172	0.760±0.247
		p=0.8478	p=0.5313	p=0.3925			
Dync1i2.A	ΔC_T	4.246	2.249	5.438	3.804±0.435	2.990±0.407	4.975±0.165
	$\Delta\Delta C_T$	0.000±0.278	0.000±0.261	0.000±0.072	-0.443±0.435	0.741±0.407	-0.462±0.165
	$2^{-\Delta\Delta CT}$	1.039±0.206	1.031±0.168	1.002±0.051	1.479±0.401	0.650±0.194	1.396±0.165
		p=0.3836	p=0.2125	p=0.0852			
Dync1i2.B	ΔC_T	3.976	2.725	3.699	3.453±0.331	3.104±0.320	3.545±0.335
	$\Delta\Delta C_T$	0.000±0.124	0.000±0.343	0.000±0.203	-0.522±0.331	0.380±0.320	-0.154±0.335
	$2^{-\Delta\Delta CT}$	1.008±0.090	1.059±0.254	1.021±0.152	1.509±0.313	0.809±0.187	1.169±0.242
		p=0.1987	p=0.4724	p=0.6309			
Dync1i2.C	ΔC_T	5.836	4.956	4.028	5.756±0.141	5.245±0.267	3.868±0.183
	$\Delta\Delta C_T$	0.000±0.087	0.000±0.275	0.000±0.196	-0.081±0.141	0.289±0.267	-0.160±0.183
	$2^{-\Delta\Delta CT}$	1.004±0.062	1.036±0.189	1.019±0.140	1.068±0.104	0.847±0.157	1.135±0.145
		p=0.6243	p=0.4855	p=0.5947			
Dync1li1	ΔC_T	3.607	3.443	4.644	3.915±0.661	3.519±0.143	4.487±.184
	$\Delta\Delta C_T$	0.000±0.599	0.000±0.195	0.000±0.744	0.308±0.661	0.076±0.143	-0.157±0.184
	$2^{-\Delta\Delta CT}$	1.198±0.523	1.018±0.131	1.306±0.667	1.011±0.497	0.958±0.094	1.132±0.135
		p=0.8087	p=0.7280	p=0.8107			
Dynlt1	ΔC_T	13.38	12.90	12.88	12.26±0.489	12.65±0.262	12.08±0.230
	$\Delta\Delta C_T$	0.000±1.124	0.000±0.092	0.000±0.383	-1.119±0.489	-0.252±0.262	-0.805±0.230
	$2^{-\Delta\Delta CT}$	1.523±0.656	1.004±0.063	1.066±0.242	2.437±0.824	1.230±0.217	1.790±0.268
		p=0.4346	p=0.3739	p=0.1153			
Dynlt3	ΔC_T	3.354	3.795	3.168	3.680±0.065	3.911±0.042	2.695±0.084
	$\Delta\Delta C_T$	0.000±0.176	0.000±0.073	0.000±0.135	0.325±0.065	0.116±0.042	-0.473±0.084
	$2^{-\Delta\Delta CT}$	1.015±0.129	1.003±0.051	1.009±0.090	0.800±0.036	0.924±0.027	1.392±0.079
		p=0.1824	p=0.2429	**p=0.0329**			

Gene		*Dync1i2*$^{+/+}$ *(n=3)*			*Dync1i2*$^{T172I/T172I}$ *(n=3)*		
		Cortex	Hippocampus	Spinal cord	Cortex	Hippocampus	Spinal cord
	ΔC_T	-0.415	-0.462	1.218	0.051±0.497	-0.478±0.179	1.212±0.333
Dynll1	$\Delta\Delta C_T$	0.000±0.289	0.000±0.044	0.000±0.327	0.466±0.497	-0.016±0.179	-0.006±0.333
	$2^{-\Delta\Delta CT}$	1.040±0.201	1.001±0.030	1.056±0.257	0.823±0.310	1.027±0.127	1.056±0.227
		p=0.5877	p=0.8522	p=0.9985			
	ΔC_T	-0.046	0.641	0.528	0.012±0.565	0.969±0.111	-0.330±0.135
Dynll2	$\Delta\Delta C_T$	0.000±0.483	0.000±0.058	0.000±0.379	0.058±0.565	0.329±0.111	-0.858±0.135
	$2^{-\Delta\Delta CT}$	1.127±0.408	1.002±0.040	1.072±0.282	1.128±0.465	0.801±0.060	1.828±0.168
		p=0.9985	**p=0.0491**	p=0.0823			

10.8 Alignment of human, rat, and mouse protein sequences of identified isoforms of DYNC1I1

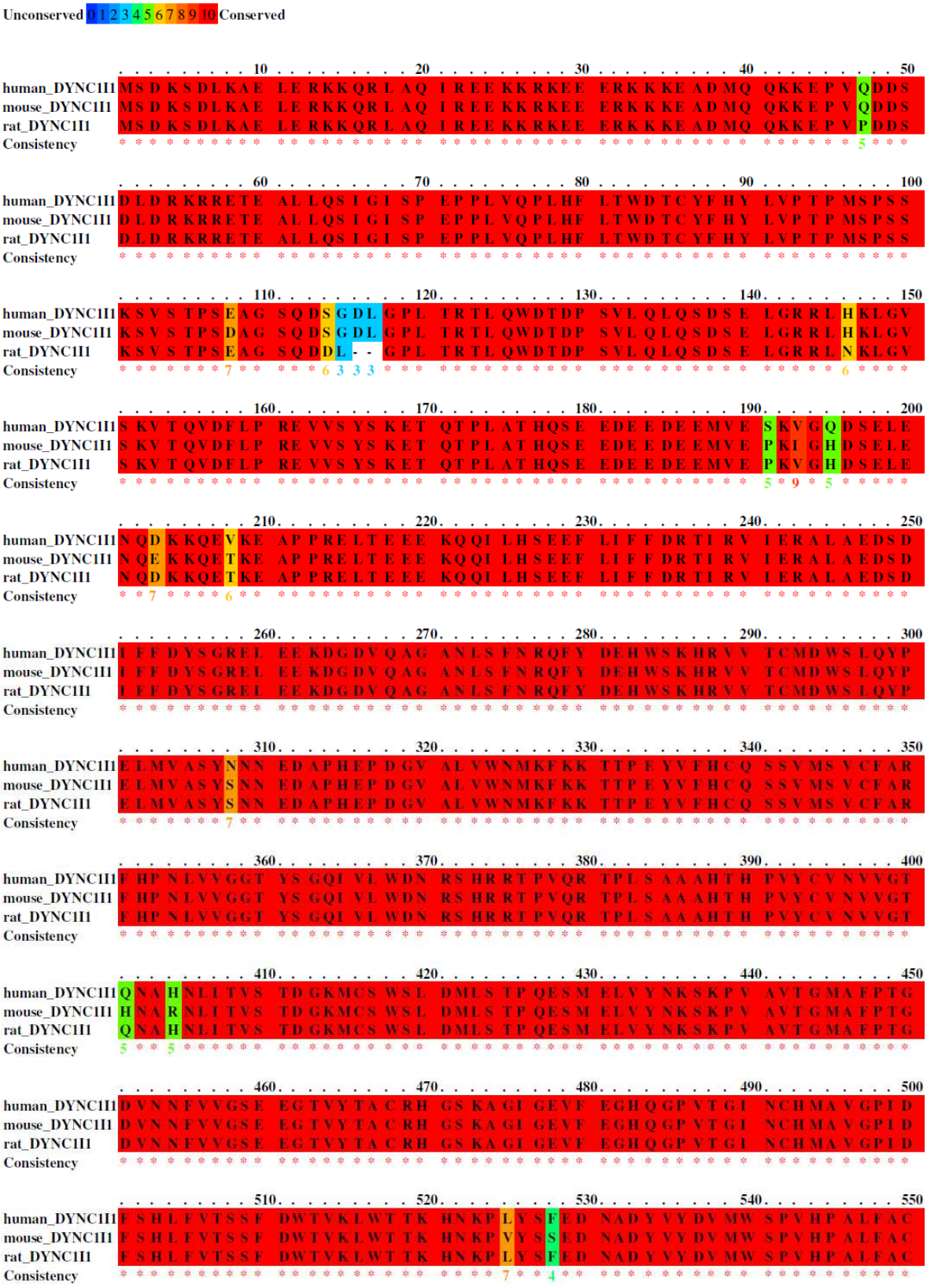

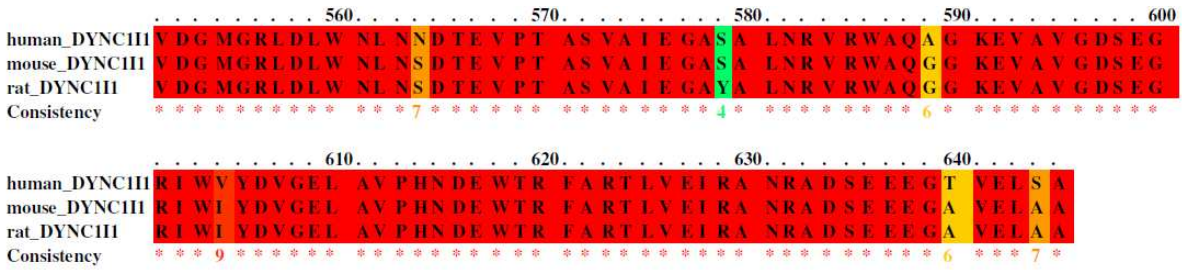

The above alignment corresponds to the isoform DYNC1I1.A, which is the longest isoform found in human, mouse, and rat.

10.9 Alignment of human, rat, and mouse protein sequences of identified isoforms of DYNC1I2

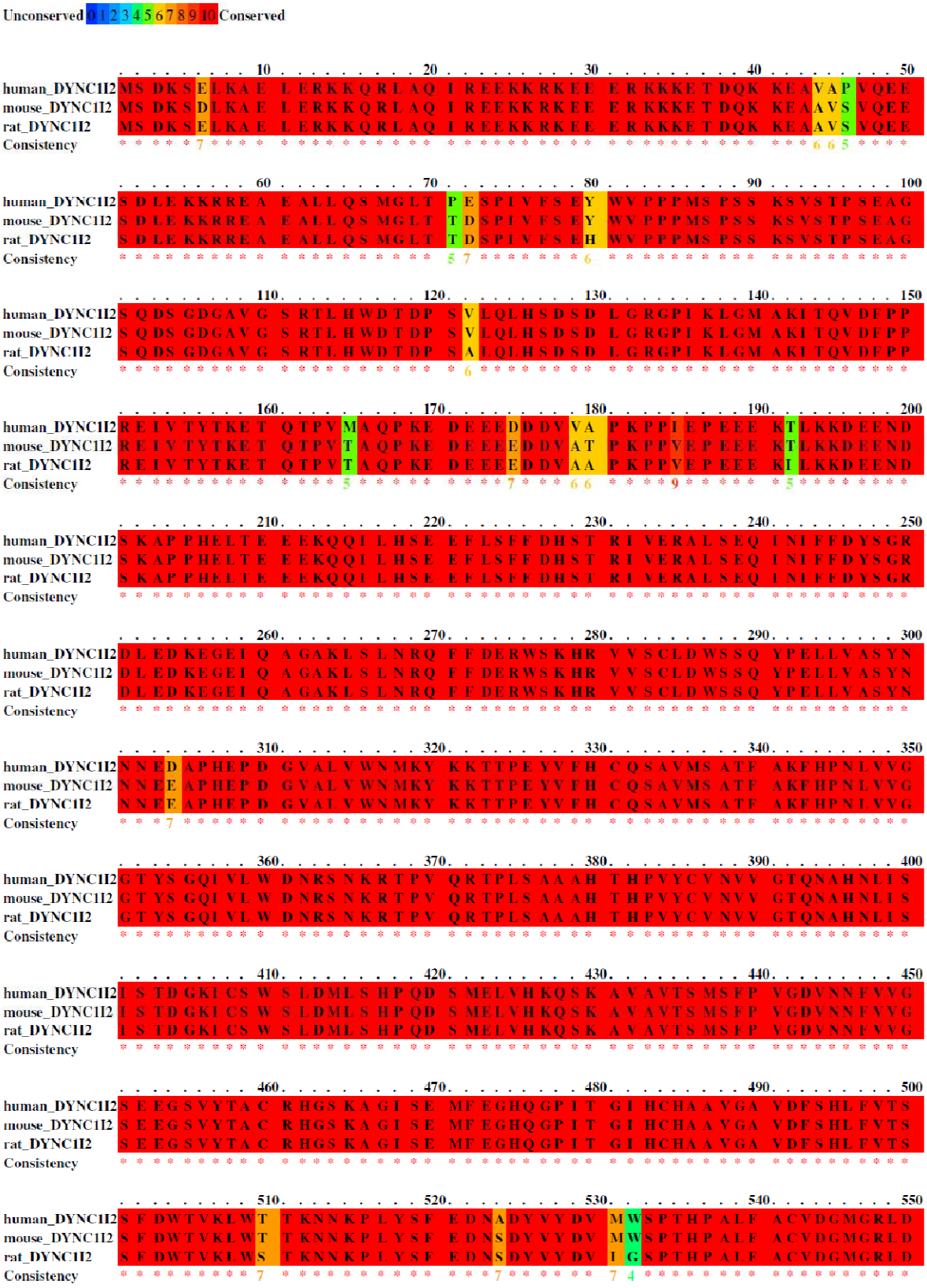

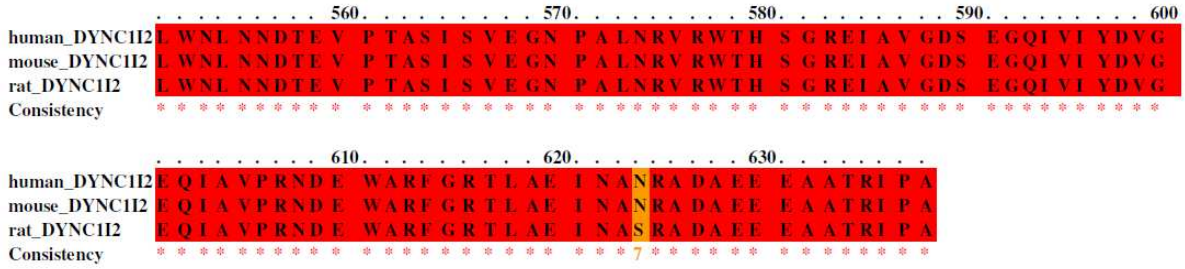

The above alignment correspond to the isoform DYNC1I2.C, which is the longest isoform found in human, mouse, and rat.

10.10 General consumables

10.10.1 Chemicals and reagents

Agarose (electrophoresis grade)	Invitrogen
Agarose, High Resolution	Ambion
Benzonase	Roche
Better Buffer	Microzone
Bovine Serum Albumin (BSA)	Sigma – Aldrich
Bromo-chloro-propane (BCP)	Sigma – Aldrich
BSA (10mg/ml)	NEB
Deoxycholate	Sigma – Aldrich
Deoxyribonuclease I (DNase I)	Invitrogen
DEPC-treated water	Invitrogen
Dimethyl sulfoxide (DMSO)	Sigma – Aldrich
DNA loading buffer (5x)	Qiagen
Ethanol (absolute, >99%)	VWR
Ethidium bromide	Sigma - Aldrich
Foetal Bovine Serum (FBS)	Invitrogen
Fluorescence Mounting Medium	DakoCytomation
Glutaraldehyde (25%, EM grade)	Sigma - Aldrich
Glycerol	Sigma - Aldrich
Hyperladder I	Bioline
Hyperladder IV	Bioline
Isopropanol	VWR
Kanamycin	Sigma – Aldrich
LB Agar, Miller	Sigma – Aldrich
LB Broth, Miller	Sigma – Aldrich
Leibovitz's L-15 GlutaMAX I	Gibco Invitrogen
Lipofectamine 2000 (LFA)	Invitrogen
MboII (5000 U/ml)	NEB
MegaMix Blue	Microzone
MegaMix Gold	Microzone
Methanol (Normapur)	VWR
$MgCl_2$ (25 mM)	NEB
Paraformaldehyde (PFA)	Sigma - Aldrich
NEB Buffers (10x)	NEB
Nocodazole	Calbiochem
NP-40	Sigma – Aldrich
NuPAGE LDS Sample Buffer (4x)	Invitrogen
NuPAGE Novex Bis-Tris gel	Invitrogen
NuPAGE Reducing Agent (10x)	Invitrogen
NuPAGE Transfer Buffer (20x)	Invitrogen
Oligo dT primer	Qiagen
Penicillin – streptomycin (100x)	Gibco Invitrogen
Quick Load 50 bp DNA ladder	NEB
RNAlater	Qiagen
RNase-free Mussel Glycogen	Sigma – Aldrich
RNAZap	Ambion
RsaI (10 000 U/µl)	NEB
Saponin (from quillaja bark)	Sigma – Aldrich
Sodium acetate (NaAc, 3M)	Sigma – Aldrich
Sodium arsenite (SA, 0.05M)	VWR
Sodium cacodylate	Agar Scientific
Sodium chloride (NaCl)	Sigma – Aldrich
Sodium citrate	Sigma – Aldrich
Sodium dodecylsulfate (SDS)	Sigma – Aldrich
Sodium hydroxide (NaOH, 1M)	VWR
Taq DNA polymerase (5 U/µl)	Fermentas
Thapsigargin (1mM in DMSO)	Calbiochem
Tris-HCl (1M, pH 7.0)	Sigma - Aldrich
Triton X-100	Sigma – Aldrich
TrypLE Express	Gibco Invitrogen
Trypsin 0.25%	Gibco Invitrogen
Tsp45I (4000 U/ml)	NEB
Tween-20	Sigma – Aldrich
Water nuclease-free	Ambion
β-mercaproethanol (β-ME)	Sigma – Aldrich

4-(2-hydroxyethyl)-1-piperazineethanesulfonic acid (HEPES, 1M)	Gibco Invitrogen
4',6-diamidino-2-phenylindole (DAPI)	Sigma-Aldrich
AccuScript High Fidelity Reverse Transcriptase	Stratagene
Deoxyadenosine triphosphate (dATPs)	Invitrogen
Deoxyribonucleotide triphosphate (dNTP)	Invitrogen
Dulbecco's Modified Eagle Medium (D-MEM GlutaMAX I)	Gibco Invitrogen
Dulbecco's PBS (with Ca^{2+}/Mg^{2+})	Gibco, Invitrogen
Dulbecco's PBS (without Ca^{2+}/Mg^{2+})	Gibco Invitrogen
EGF Alexa Fluor 555 conjugate	Molecular Probes Invitrogen
Emetine dihydrochloride hydrate	Sigma – Aldrich
Ethylenediaminetetraacetic acid (EDTA, 0.5M)	Sigma – Aldrich
GeneScan – Liz 1200 Size Standard	Applied Biosystems
Halt Protease and Phosphatase Inhibitor Cocktail	Thermo Scientific
Hi-Di Formamide	Applied Biosystems
Horse Serum (with 0.09% sodium azide)	AbD Serotec
N, N-Dimethylformamide (DMF, >99%)	Sigma - Aldrich
Normal Horse Serum	Jackson Immuno Research Laboratories
NuPAGE MOPS SDS Running Buffer (20x)	Invitrogen
Oligonucleotyde primers	Eurofins MWG Operon, Sigma

Opti-MEM I Reduced Serum Medium	Gibco Invitrogen
PCR Buffer IV	Applied Biosystems
PfuUltra High Fidelity DNA polymerase	Stratagene
Phosphate buffered saline (PBS, 10x)	Fisher Scientific
ProLong Gold Antifade Reagent with DAPI	Invitrogen
PVDF membrane	ImmobilonP, Milipore
SeeBlue Plus2 Pre-Stained Standard	Invitrogen
TRIreagent	Sigma – Aldrich, Ambion
Tris/Borate/EDTA (TBE, 10x)	National Diagnostic
X-Gal (5-Bromo-4-chloro-3-indolyl b-D-galactopyranoside)	Sigma – Aldrich

10.10.2 Commercial kits

BigDye Terminator Ready Reaction Kit	Applied Biosystems
DNeasy Blood & Tissue Kit	Qiagen
GenElute Plasmid Miniprep Kit	Sigma-Aldrich
Multiplex PCR Kit	Qiagen
QIAquick PCR Purification Kit	Qiagen
QIAshredder	Qiagen
QuantiTect Reverse Transcription Kit	Qiagen
RNase-free DNase Set	Qiagen
RNeasy Mini Kit	Qiagen
TOPO TA Cloning Kit for Sequencing	Invitrogen
DC Protein Assay	Bio-Rad Laboratories

10.10.3 Equipment

3130XL Genetic Analyser	Applied Biosystems	Microscope slides	VWR
5 and 15 ml tubes	Falcon	Microwave	Proline
96-well PCR microplate	ABgene, StarLab	Odyssey Imager	LI-COR Biosciences
Bright-Line Haemocytometer	Sigma - Aldrich	PCR plate seal	Thermo Scientific
Centrifuge Allegra 25R	Beckman Coulter	Phase contrast microscope	Olympus CK40
Cryo-freezing container	Nalge Nunc	Plastic spreaders	VWR
Cryogenic vials (1.8 ml)	Corning Life Science	Shaking incubator	Orbital
Dounce Tissue Grinder	Wheaton Industries	Tissue culture flasks	Nunc
Electrophoresis power pack	Bio-Rad Laboratories	Plastic Petri dishes	Sarstedt
Electrophoresis tank	Life Technologies Inc	UV transluminator	Bio-Rad Laboratories
Gilson pipettes	Anachem	Water bath	Grant Instruments
Glass coverslips (d. 12 mm)	VWR	XCell SureLock Mini-Cell	Invitrogen
Heat block	Grant Instruments	Microcentrifuge	Eppendorf S415C
Incubator	LTE Scientific		

DH Autoflow Air-Jacketed Incubator	Nuaire
DNA Engine Tetrad 2 Peltier Thermal Cycler	Bio-Rad Laboratories
NanoDrop® ND-1000 Spectrophotometer	Labtech
RNase-free tubes (1.5 ml, 2.0 ml)	Biopur, Eppendorf
Tissue culture multi-well plates	TTP, Corning Life Science, Nunc

10.10.4 Software

BioEdit Sequence Alignment Editor v5.0.9 (freeware)			
Gene Mapper	Applied Biosystems	Volocity	Perkin Elmer
GraphPad Prism v5.02	GraphPad Software	Photoshop CS3	Adobe
Sequence Analysis 5.2	Applied Biosystems	Odyssey Imaging Software	LI-COR Biosciences
UCSC Genome Browser	www.genome.ucsc.edu		

10.11 Antibodies

PRIMARY ANTIBODIES USED IN IMMUNOFLUORESCENCE			
Antigen/Antibody	Host	Dilution	Supplier
Dynein intermediate chain 1 DIC1 (51/52)	Rabbit	1:100	Affinity purified, generated by G. Banks
Dynein intermediate chain 2 DIC2 (60)	Rabbit	1:100	Affinity purified, generated by A. Kuta
Dynein intermediate chain (IC74)	Mouse	1:200	Chemicon (Milipore)
G3BP	Mouse	1:200	BD Transduction Laboratories
GIANTIN	Rabbit	1:600	Covance
GM130	Mouse	1:250	BD Transduction Laboratories
LAMP1 (1D4B)	Rat	1:1000	Developmental Studies Hybridoma Bank, Iowa University
TIAR (C-18)	Goat	1:50	Santa Cruz Biotechnology
α-tubulin Alexa Fluor 488	Mouse	1:200	Milipore
SECONDARY ANTIBODIES USED IN IMMUNOFLUORESCENCE			
Antigen/Antibody	Host	Dilution	Supplier
anti – rat Rhodamine Red-X IgG	Donkey	1:400	Jackson ImmunoResearch Lab.
anti – goat Alexa Fluor 546 IgG	Donkey	1:600	Molecular Probes, Invitrogen
anti – mouse Alexa Fluor 488 IgG	Donkey	1:200	Molecular Probes, Invitrogen
anti – mouse Alexa Fluor 633 IgG	Donkey	1:200	Molecular Probes, Invitrogen
anti – mouse Alexa Fluor 647 IgG	Donkey	1:400	Molecular Probes, Invitrogen
anti – rabbit Alexa Fluor 546 IgG	Donkey	1:500	Molecular Probes, Invitrogen
PRIMARY ANTIBODIES USED IN WESTERN BLOTTING			
Antigen/Antibody	Host	Dilution	Supplier
[pSer52]EIF2α	Rabbit	1:1000	Assay Designs, Stressgen
β-actin	Mouse	1:15000	Sigma - Aldrich
Dynein intermediate chain 1 DIC1 (51/52)	Rabbit	1:1000	Affinity purified, generated by G. Banks
Dynein intermediate chain 2 DIC2 (59)	Rabbit	1:250	Affinity purified, generated by A. Kuta
Dynein intermediate chain 2 DIC2 (58, 59, 60)	Rabbit	1:300	Affinity purified, glycerol stock
Dynein intermediate chain (IC74)	Mouse	1:1000	Chemicon (Milipore)
SECONDARY ANTIBODIES USED IN WESTERN BLOTTING			
Antigen/Antibody	Host	Dilution	Supplier
anti – mouse IR Dye 800	Goat	1:7000	LI-COR Biosciences
anti – mouse IR Dye 680	Goat	1:7000	LI-COR Biosciences
anti – rabbit IR Dye 680	Goat	1:7000	LI-COR Biosciences
anti – rabbit IR Dye 680	Goat	1:7000	LI-COR Biosciences

10.12 Primer sequences

10.12.1 Genotyping primers

Gene	Primer	Sequence
Dync1i1	DIC1_Mbo_FOR1	5': TTG CTT TGC AAA GGT CAC TG
	DIC1_Mbo_REV2	5': TTG CCC AGA TAG ATG GAG TTC
Dync1i2	DICg2_FOR	5': TTC ACT TAT TTA GAC GAG GAC C
	DICg2_REV	5': ACT CCC TCA CCA CTA AAT GC
Dync1h1	Loa_F_MDN1767	5': ATT GAG GAG GTG AAC CTG GCC
	Loa_R_MDN2313	5': CAG TCA TCG AAG ATC TCC TGG G

10.12.2 Primers used during cloning

Ex' refers to the number of the exon containing the primer binding site e.g. Ex 1 is exon 1.

Gene/Vector	Primer	Sequence
Dync1i1	DIC1_Ex 1 for	5': CTC CAC GAC CTC CAG TGA G
	DIC1_Ex 17 rev	5': ACG CAC ATG CTC TAA GAT CG
Dync1i2	DIC2_Ex1a for	5': GGC CGG TGT ATC TGT TTC AAC
	DIC2_Ex1b for	5': CAG TTG GAG AGG GAC GTT C
	DIC2_Ex18 rev	5': AGA AGG GAA ATG GCA TCA AC
Gapdh	Gapdh for	5': ACT CCA CTC ACG GCA AAT TC
	Gapdh rev	5': ATG TAG GCC ATG AGG TCC AC
pCR4-TOPO®	M13_FOR	5': GTA AAA CGA CGG CCA G
	M13_REV	5': CAG GAA ACA GCT ATG AC

10.12.3 *Dync1i1* and *Dync1i2* sequencing primers

Ex' refers to the number of the exon containing the primer binding site e.g. Ex 1 is exon 1.

Gene	Primer	Sequence
Dync1i1	DIC1_Ex 1 for	5': CTC CAC GAC CTC CAG TGA G
	DIC1_Ex 3 rev	5': CTC CGG TGA TAT GCC AAT GC
	DIC1_Ex 9 for	5': TGA ACA TTG GTC TAA GCA TCG G
	DIC1_Ex 10 rev	5': TGG AAG ACA TAT TCT GGT GTG G
	DIC1_Ex 16 for	5': AGG AGC ATC TGC CCT AAA C
Dync1i2	DIC2_Ex1a for	5': GGC CGG TGT ATC TGT TTC AAC
	DIC2_Ex1b for	5': CAG TTG GAG AGG GAC GTT C
	DIC2_Ex9 for	5': CGA GAA TTG TAG AAA GAG CC
	DIC2_Ex14 for	5': GTT GTG GGC AGT GAA GAA G

10.12.4 *Dync1i1* and *Dync1i2* primers used in the PCR based survey of the alternative splicing

Ex' refers to the number of the exon containing the primer binding site e.g. Ex 1 is exon 1.

Gene	Primer	Sequence
Dync1i1	DIC1_Ex 1 for	5': CTC CAC GAC CTC CAG TGA G
	DIC1_1.1 for	5': CTC TAG TGC AGC CGT TGC AT
	DIC1_AS4 rev	5': GGG AGT GCT CAC TGA TTT GG
	DIC1_5 rev	5': AAG TTC TGA GTC TGA CTG CAG
	DIC1_iso14 rev	5': GCA GTC GTC TCC TTG TTA ATG G
	DIC1_R rev	5': CTA GGC AGG AAA TCC ACC TG
Dync1i2	DIC2_Ex1a for	5': GGC CGG TGT ATC TGT TTC AAC
	DIC2_Ex1b for	5': CAG TTG GAG AGG GAC GTT C
	DIC2_N4 rev	5': GAG GGA CCC AGT ACT CAG
	DIC2_6 rev	5': AAA TCG GAA TCT GAG TGA AGC
	DIC2_iso24 rev	5': CAA GTT TAA TAG GTC CTC GTC TA
	DIC2_2.1 rev	5': AAC TTG ATT GAA GCT AGA ATC CTC
	DIC2_R rev	5': CTC GAG GGG GAA AGT CAA C

10.12.5 Primers used in the quantitative real time PCR

Gene	Primer	Sequence
Dync1i1	DIC1_A_for	5': CTC TAG TGC AGC CGT TGC AT
	DIC1_B_for	5': CTC TAG TCC CAA CCC CTA TGT
	DIC1_C_for	5': CTC TAG TGA GCA CTC CCA GT
	DIC1_R	5': CAG TCG TCT CCC AAG TTC TG
Dync1i2	DIC2_D_for	5': CCC TAT TGG CTT CCT CCT TTC
	DIC2_E_for	5': CCC TAT TGA GGA TTC TAG CTT C
	DIC2_A_for	5': CCC TAT TGT TTT TTC TGA GTA CTG
	DIC2_B_for	5': CC T ATT GTC CCT CCT CCT ATG
	DIC2_R	5': ATA GGT CCT CGT CCC AAA TCG
Dync1li1	Forward	5': GTG CAA GCC CCA GTT TGC
	Reverse	5': GTG AAC ATC TGA AAG CAC AGG TTT
Dynlt1	Forward	5': TTT CAG CCA ACT CAC CAA TC
	Reverse	5': TGG TCT TGT TCT CCC ATC GG
Dynlt3	Forward	5': CAA TGC TGA TGA AGC CCA TAA TAT A
	Reverse	5': GCT TGC AGT CCA TTG GTT GA
Dynll1	Forward	5': AAG GCG GTG ATC AAA AAT GC
	Reverse	5': ATG GGC CGC AAT ATC CTT CT
Dynll2	Forward	5': GTG ATC AAG AAC GCA GAC ATG TC
	Reverse	5': GAT ATA GGC AGC AAT GTC CTT CTC T.
Rpl L13A	Forward	5': GGA AGC GGA TGA ATA CCA AC
	Reverse	5': GGA TCC CAT CCA ACA CCT T